Chemical pressure-induced transition of the magnetic ground state from ferromagnetic to antiferromagnetic order in CeCuGe and DyCuIn alloys

By

Anas Alamin Hassan Altayeb

Thesis submitted in the fulfilment of the requirement for the degree of Doctor of Philosophy at the University of The Western Cape.

Department: Physics and Astronomy

Faculty: Natural Science

Supervisor(s):

Prof. M.B. Tchoula Tchokonté, University of the Western Cape

Co-Supervisor(s):

Dr. B.M. Sondezi, University of Johannesburg

November 2023

Declaration

I declare that this thesis is my own independently researched work conducted in the Physics Department of the University of the Western Cape, South Africa. It is being submitted for the degree of Doctor of Philosophy in Science, and is the first time this work is being submitted for this degree.

_____

Anas Alamin Hassan Altayeb

…… day of ……..2023

List of Publications

1- Evolution from 4*f*-electron antiferromagnetic to ferromagnetic order in the $CeCu(Ge_{1-x}Sn_x)$ alloy series ($0 \leq x \leq 1$), A. Altayeb, B. M. Sondezi, M. B. Tchoula Tchokonté, A. M. Strydom, T. B. Doyle and D. Kaczorowski. AIP ADVANCES 7, 055714 (2017).

2- Critical properties of the 3D-Mean-field ferromagnet GdPdIn, (Accepted by Journal of Magnetism and Magnetic Materials).

Acknowledgements

First, I thank Allah who made this work possible.

I would like to convey my deepest gratitude to my supervisor, Professor M. B. Tchoula Tchokonté for offering me this great opportunity to commence my doctoral study at the University of the Western Cape (UWC).

My sincere gratitude extends to Professor M. B. Tchoula Tchokonté and to my Co-Supervisor Dr. Buyisiwe Mavis Sondezi, for their valuable suggestions, guidance, discussions, advice and encouragements which they have given to me during the course of my PhD. I also give special thanks to Dr B. M. Sondezi for some experimental measurements performed in the Department of Physics at the University of Johannesburg. Moreover, I sincerely thank both of them, for spending their valuable time on assisting me to learn the research techniques of my work, data analysis and interpretation of results. On the other hand, I express my heartfelt thanks to Prof A. M. Strydom at University of Johannesburg (UJ) for giving me the chance to perform some of my experiments in his laboratory, especially, electrical, magnetic and thermo dynamics transport properties.

My deepest gratitude goes to Prof D. Kaczorowski and his team at the Institute of Low Temperature and Structure Research, Polish Academy of Sciences, for facilitating the magnetic measurements of my samples in their laboratory.

Also, I wish to convey my warm gratitude to my colleagues at University of the Western Cape, for their kind support and continuous encouragement.

I would like to express my deepest gratitude to my family and colleagues in Sudan, Sudanese Community in Gauteng province for their continuous contact, encouragement and support they provided me, while away from home.

Abstract

Rare-earth intermetallic compounds continue to attract considerable attention, due to their fundamental importance in understanding physical properties and potential applications based on a variety of phenomena. The ternary intermetallic compounds of the RTX series (R = rare-earth element, T = 3*d* / 5*d* transition element, X = *p*-block element) in particular, were studied extensively for the past two decades. A number of interesting magnetic and electrical properties of practical and fundamental importance, were found in different compounds of the RTX series, including giant and large magnetocaloric effects and magnetoresistivity, antiferromagnetic (AFM) to ferromagnetic (FM) order transitions and rich magnetic transition phase diagrams. Most of these properties are related to the interaction between the R-4*f* (localized) electronic states and other (itinerant) electronic states in the electronic system.

Several experiments have provided evidence for magnetic ground state switching between FM and AFM ordering, driven by pressure or chemical substitution in *d* and *f* electron compounds. The methods used to investigate the magnetic phase transitions could be divided into macroscopic and microscopic ones. The macroscopic method relied on the temperature dependences of magnetization, magnetic susceptibility and specific heat measurements while the microscopic method relied on neutron diffraction and Mössbauer effect.

The present thesis reports on the magnetic ground state switching between FM and AFM ordering driven by chemical substitution in *d* and *f* electron compounds such as DyCuIn and DyPdIn. The method used to investigate the magnetic phase transition in this thesis, is that of the macroscopic method. The focus of this project is to employ three families of rare-earth intermetallic systems: $CeCu(Ge_{1-x}Sn_x)$, $(Ce_{1-x}Nd_x)CuGe$ and $Dy(Cu_{1-x}Pd_x)In$ to uncover the underlying ground state properties that result in a strong coupling between the conduction electrons of transition metals and the 4*f*-electrons of the rare-earth ions, and study the transition of its magnetic states from AFM to FM.

At the onset of the research project the focus was on sample synthesis using arc- melting and sample characterization using X-ray powder diffraction. The elemental sample and homogeneity of the prepared samples was checked by scanning electron microscopy (SEM), energy dispersion spectroscopy (EDS) and micro-probe detection. The physical properties (electrical resistivity, $\rho(T)$, heat capacity, $C_P(T)$, magnetic susceptibility, $\chi(T)$ and magnetization, $M(\mu_0 H)$) were investigated as a function of temperature and magnetic field. All

these properties were measured using the physical property measurement system (PPMS) and the magnetic property measurement system (MPMS) supplied by Quantum Design, USA.

X-ray diffraction (XRD) studies of $CeCu(Ge_{1-x}Sn_x)$ alloy series indicate that all samples crystallize in the hexagonal ZrBeSi-type structure with space group $P6_3/mmc$. Magnetic and heat capacity measurements of this alloy series indicate that FM ordering extends up to 60% Sn content. The AFM ordering is observed for samples with $x \geq 0.7$ with a kind of spin - reorientation in the ordered region. C_P (T) data below T_C can be well described assuming spin - waves excitations.

XRD studies of $(Ce_{1-x}Nd_x)CuGe$ alloy series indicate that except for the CeCuGe which crystallize in the hexagonal ZrBeSi-type structure as mentioned above, all the other samples crystallize in the hexagonal AlB_2-type structure with space group $P6/mmm$. The χ (T) results of $(Ce_{1-x}Nd_x)CuGe$ alloy series indicate that FM ordering extends up to 60% Nd content. Below T_C, ρ (T) data can be well described with the FM spin-waves with energy gaps Δ_R = 15.24 (1) K, 1.906 (2) K and 7.629 (2) K for x = 0, 0.1 and 0.2, respectively. The transition from FM to AFM ordering is observed for samples with $x \geq 0.7$. At low-temperature ρ (T) data can be well described by AFM superzone pseudogap at the Fermi surface for $0.4 \leq x \leq 1$ with superzone band gap Δ = 3.403 (6) K, 6.289 (5) K, 14.318 (4) K and 4.121 (5) K for x = 0.4, 0.6, 0.7 and 1, respectively.

XRD studies of $Dy(Cu_{1-x}Pd_x)In$ alloys series indicate that all samples crystallize in the hexagonal ZrNiAl – type structure with space group P-62m. The results of χ (T) and C_P (T), of $Dy(Cu_{1-x}Pd_x)In$ alloys series indicate that the AFM ordering extended up to 50 % Pd content. For samples $0.6 \leq x \leq 1$ showing FM ordering, an additional magnetic phase transition below T_C was observed and attributed to AFM rearrangement of the magnetic moment of Dy ion. C_P (T) data below T_C, can be well described in terms of FM spin-wave dispersion with an energy gap Δ_E. The crystalline electric field (CEF) was observed at low temperature in the C_p (T) data which plays an influential role in the ground state for this system. The CEF parameters have been estimated from the LSQ fits of the Schottky anomaly to the C_p (T) data. Furthermore, C_p (T) data confirm the FM and AFM phase transition at T_C and T_N, respectively. On the other hand, the non-magnetics homologues YCuIn and YPdIn can be described by the Debye - Einstein model, giving a Debye and Einstein temperature values of θ_D = 232.8 (3) K and θ_E = 26.5 (5) K and θ_D = 273.6 (2) K and θ_E = 191.8 (4) K, respectively. The 4f-electron specific heat, C_{4f}(T), of the two end compounds DyCuIn and DyPdIn show a Schottky-type anomalies around 55.1 K and 60 K, respectively associated with CEFs, with energy splitting Δ_1 = 77 (2)

K, Δ_2 = 140 (2) K and Δ_1 = 96 (2) K, Δ_2 = 202 (3) K, respectively of Dy^{3+} (J = 15/2) multiplet, that are associated with the first and second excited state of Dy^{3+} ion. The low temperature C_{4f} (T) for samples exhibiting FM behaviour, can be well described assuming spin-waves excitation with an energy gap Δ_C.

Table of Contents

List of figures

List of Tables

Chapter 1

Introduction

1.1 Rare-earth intermetallic compounds

Rare earths are defined as the group of elements with atomic number 57-71, from the periodic table. The outer electron shell determining the number and nature of the valences is much the same for these 15 elements.

The chemical similarity leads to more or less uniform behaviour when the rare-earth metals are combined with other metals. One can say that if one member of the group forms an intermetallic compound of a given sample and crystal structure, all the other members will act in the same way. On the other hand, the physical properties may vary remarkably within such a series of isotropic compounds. The 4*f*-electron shell of the rare-earth elements are gradually filled up from 0-14; as a result, spin and orbital moment will show a large variation as one proceeds from La compound to the corresponding Lu compound [1].

Due to the variety of interesting properties in the ground state of the intermetallic compounds containing rare earth elements, such as Kondo effect, heavy-fermion (HF) behaviour, intermediate valence, superconductivity, single and multiple magnetic transitions, spin glass, metamagnetism and large magnetocaloric effect (MCE), make the compounds technologically important, and have attracted the interest of the experimental as well and theoretical researchers over the past decade. The compounds composed of the rare earth elements and transition metals shows peculiar characteristics like good oxidation resistance and excellent strength [1].

The family of compounds formed between rare-earths and 3*d*-transition metals of particular interest in this research project. Such compounds include binary intermetallic compounds where the combination of one rare-earth element and 3*d*-element gives rise also to many different compounds and the ternary intermetallic compound where the one rare-earth element, one 3*d*-element and one element of the *p*-block of the periodic table gives rise to a large number of compounds. The majority of investigations of rare earth-transition metal compounds reported in the literature so far, deal with the magnetic properties of these compounds, and other few physical properties of compounds were reported to obtain a better understanding of the nature of the

magnetic interactions [2]. The magnetic properties of binary and ternary rare-earth compounds are due primarily to the electrons in the incomplete shell. In fact the magnetic moment is determined by the number of electrons in the 4*f* shell according to the Russell-Saunders coupling scheme. These materials have a metallic character and the interatomic distance between the rare-earth are fairly large [2]. The magnetic interactions between the highly localized 4*f*-electrons are being realized by their conduction electrons mediating in an exchange interaction, and the effect of crystal-electric-field acting on the 4*f*-electrons. In rare-earth intermetallic compounds, exchange interactions between rare-earth moments are mediated by spin polarization of conduction electrons. This mechanism leads to long-range exchange interaction with an oscillatory dependence of the interaction strength on the distance between the moments and is known as the Ruddermann-Kittel-Kasuya-Yosida (RKKY) interaction. Intermetallic compounds in which the rare-earth partner bears no magnetic moment such as La, Lu, Y and tetravalent Ce have received much attention as they provide a good opportunity to investigate the origin and the nature of the 4*f*-electron magnetism [3].

In recent years, interest in intermetallic compounds between rare-earths and transition metals has increased rapidly from the discovery that several of its members can be used as a magnetic refrigerants and as starting materials for permanent magnets of outstanding quality [4].

1.2 Motivation

The magnetic ground state properties of rare-earth intermetallic compounds are a matter of interest for two reasons. Firstly, their study helps to elucidate some of the fundamental principles of magnetism (RKKY interaction, crystal electric field, magnetoelastic properties, coexistence of superconductivity and long-range magnetic order). Secondly, from an application point of view, they are of technical interest in the development of magnetic refrigeration technology, based upon the MCE. They have brought an alternative to the conventional gas compression technique. As a result of this, many new materials with large MCE have been discovered and a very good understanding of this magnetothermal property, has been achieved [5].

The transition of the magnetic states has become an incredibly important area of physics due to the change in properties during the transition between different magnetic ordered states, in addition to the critical behaviour around the transition temperature. This include a variety of materials involving second-order and first-order magnetic transitions and experimental attempts to achieve different properties [6, 7, 8, 9, 10].

The choice of the parent compounds CeCuGe, NdCuGe and DyCuIn, was motivated by the fact that these compounds belong to the family of compound RTX where R is the rare-earth element, T is d-electron element (group VIIIA, IB or IIB) and X is a main group (IIIB or IVB), which is one of the simplest classes of intermetallic compounds to afford systematic studies of rare-earth element (R) physics in the solid state. Furthermore, the choice of the chemical substitutions viz: Sn and Pd is based on the magnetic state (ferromagnetic or antiferromagnetic) of the two end compounds upon substitution. For instance, substitution of Ge with Sn, the magnetic state of the two end compounds is different viz: ferromagnetic (FM) for CeCuGe and antiferromagnetic (AFM) for CeCuSn. This is similar to DyCuIn, which is FM and DyPdIn, which is AFM. The difference in the magnetic states of the compounds, allow us to investigate the transition from one state to another, by substitution of one of the constituent elements. It should also be noted that, these choices were also based on the constituent elements available in the laboratory, where the research was carried out.

The work in this thesis is presented as follows:

- Chapter 1 presents the introduction and an overview of rare-earth intermetallic compounds. This is followed by the definition, preparation and metallurgical aspects of RE intermetallic compounds and ends with a motivation of the work carried out in this thesis.
- Chapter 2 presents various theoretical concepts, which have been used to analyze and interpret the experimental results discussed in this thesis. These are among others: the different magnetic interactions which allow the generation of magnetism in intermetallic compounds, the different kinds of magnetism present in compounds, the spin wave theory, and the phase transition, as well as the concepts of critical behaviour. The theoretical concepts of the physical properties of rare-earth intermetallic compounds are also presented in this chapter.
- In chapter 3, the experimental methods used in this study are presented. Sample synthesis, characterization and measurement techniques are discussed.
- Chapters 4, 5, and 6 report the experimental results obtained for the hexagonal systems $CeCu(Ge_{1-x}Sn_x)$, $(Ce_{1-x}Nd_x)CuGe$ and $Dy(Cu_{1-x}Pd_x)In$. A brief discussion of the results studied in these families of compounds is also presented.
- Chapter 7 presents the conclusion of the thesis and further works.

Chapter 2

Theoretical concepts

2.1 Introduction

One of the important problems in solid state physics is the investigation of magnetic phase transitions in materials. The methods used to investigate such transitions can be divided into two categories namely the macroscopic and the microscopic methods. The macroscopic method involves the temperature and magnetic field dependences of magnetic susceptibility, magnetization and heat capacity measurements while the microscopic method involves neutron diffraction and the Mössbauer effect.

Below characteristic temperatures of magnetic materials, i.e. the Curie temperature (T_C) for ferromagnets and the Néel temperature (T_N) for antiferromagnets, the magnetic moments of atoms order. The transition from the paramagnetic to the magnetically ordered phase is a second order phase transition and a characteristic maximum in the temperature dependence of the specific heat is observed [11]. On the other hand, Neutron diffraction, provides information on the symmetry of the magnetic structure from the intensities of the magnetic peaks. The thermal dependence of the intensities of magnetic peaks gives information on the critical temperature of the magnetic ordering (T_C or T_N), as well as of the magnetic phase transitions i.e. changes in the magnetic structure [12]. Intensive development of these methods in recent years, in particular the neutron diffraction experiments with multidetectors, allows to obtain new information on phase transitions. However, information from different experimental data does not always provide similar results.

The transition from AFM to FM ground state was reported in literature. For instance, field-induced transition of the magnetic ground state from A-type antiferromagnetic to ferromagnetic order in $CsCo_2Se_2$ was reported through a series of magnetization and neutron diffraction measurements [13]. First order AFM-FM transitions in $Fe_{49}(Rh_{0.93}Pd_{0.07})_{51}$ under simultaneous applications of magnetic fields (up to 8 T) and external pressure (up to 20 kbar) was reported using resistivity measurements [14]. The theoretical model describing the mechanism for pressure induced transitions between ferromagnetic and antiferromagnetic orders in *d*-electron metallic magnets was also reported [15]. It was proposed that, this mechanism relies on a competition between characteristic energy scales, ubiquitous among

d-electron metallic magnetic compounds. Furthermore, the principles behind the mechanism are demonstrated in the example of the minimal two-orbital *p-d* lattice model [15].

In this chapter, the theoretical concepts of the macroscopic method will be discussed, as well as the origin of magnetism, the magnetic state in crystals, the theory of magnetism and phase transitions.

2.2 Origin of magnetism: General concepts

Magnetism is a property characteristic of all materials that contain electrically charged particles. A moving electrical charge gives rise to a magnetic field in a material. The contribution of nucleons to the magnetic field in substances is small and requires special instrumentation to be observed. Thus, magnetism may be considered to be entirely dependent on the number of unpaired electron(s). The states of atom are characterized by the following quantum numbers:

- The total quantum number (n) which determines the size of the orbit and its energy. The maximum number of electrons occupying a given shell according to Pauli's principle is given by [16]:

$$2\sum_{l=0}^{n-1}(2l+1) = 2n^2\,, \tag{2.1}$$

where l is orbital angular momentum.

The orbital angular momentum quantum number, l, describes the angular momentum of the orbital motion, and the magnetic quantum number, m_l, describes the component of the angular orbital momentum l along a particular direction, while the spin quantum number, m_s, describes the component of the electron spin, *s* along a particular direction.

For this study, the effect from nucleons is neglected, since the macroscopic magnetic properties of a substance are a consequence of magnetic moments associated with individual electrons. Each electron in an atom has magnetic moments that originate from the orbital motion and electron spin. In an atom, the magnetic moment is due to the coupled orbital and spin magnetic moments associated with the motion of electrons. The orbital magnetic moment is due to the motion of electrons around the nucleus. An electron with orbital angular momentum along a fix axis has an associated magnetic moment along the *z*-axis as follows [17,18]:

$$\mu_{lz} = -m_l\mu_B, \tag{2.2}$$

and the total magnetic moment is given by:

$$\mu_l = \sqrt{l(l+1)}\mu_B, \tag{2.3}$$

where μ_B is the Bohr magneton defined as follows:

$$\mu_B = \frac{e\hbar}{2m}, \tag{2.4}$$

with e is the electron charge, m is the electron mass and ħ is the Planck's constant.

The electron spin *s* along a particular direction is given by $m_s\hbar$ with $m_s = \pm\frac{1}{2}$. The electron spin s is the intrinsic angular momentum corresponding with the rotation (or spinning) of each electron about an internal axis . The magnetic moment associated with the spin angular momentum can have a component along a particular axis (in this case *z*-axis) given by [19]:

$$\mu_{sz} = -gm_s\mu_B, \tag{2.5}$$

where g is constant known as the Landé g-factor. This g-factor takes a value of approximately 2 so that the *z*-component of the spin magnetic moment is $\approx \mp\mu_B$. The magnitude of the spin magnetic moment is then given as:

$$\mu_s = \sqrt{s(s+1)}\mu_B. \tag{2.6}$$

The magnitude of the spin angular momentum for an electron is $\sqrt{s(s+1)}\hbar = \frac{\sqrt{3}}{2}\hbar$. In the presence of an external magnetic field *B* the electron acquires an energy given by:

$$E = -g\mu_B m_s B. \tag{2.7}$$

From the values of m_s, it is observed that the energy levels of an electron is split in a magnetic field by an energy difference $\Delta E = g\mu_B B$, called Zeeman splitting [19].

The total orbital (*L*) and spin (*S*) angular momenta are weakly coupled, via the spin-orbit interaction, which act as a perturbation on the states with well-defined *L* and *S*. Therefore, the magnetic moment on an atom is associated with the total angular momentum $\vec{J}$ which is the sum of $\vec{L}$ and $\vec{S}$, so that:

$$\vec{J} = \vec{L} + \vec{S}. \tag{2.8}$$

This is known as the Russel-Saunders coupling. It should be noted that the orbital and spin angular momentum gives rise to paramagnetic behaviour of a material [20]. The best-known examples of paramagnetic materials are the transition and rare-earth metals. The incomplete atomic shells of these metals are responsible for their paramagnetic behaviour. On the other hand, ionic and covalent crystals have atoms or ions with complete shells as a result of that they exhibit a diamagnetic behaviour which is due to the fact that a magnetic

field acts to distort the orbital motion of the electrons.

As mentioned above, the magnetic moment of a free atom originates from the spin angular momenta associated with electrons, and the orbital angular momenta as a result of the movement of the electrons around the nucleus, where both effects give paramagnetic contributions to magnetization. The third principle is the change in the orbital momenta induced by an applied magnetic field which causes a diamagnetic contribution to magnetization.

Magnetism in rare-earth (RE) compounds originates from rare-earth atoms where the open 4*f* shell has a variety of spin and orbital moments. Due to localized 4*f*-electrons the value of the effective magnetic moments μ_{eff} is in good agreement with the values for the free RE^{3+} ions, which can be obtained from [20, 21]:

$$\mu_{eff} = g_J \sqrt{J(J+1)}\ \mu_B, \tag{2.9}$$

The theoretical values of μ_{eff} of RE elements are listed in table 2.1 and plotted in figure 2.1 The rare-earth elements have an electronic structure expressed by $4f^n5s^25p^65d^16s^2$. The incomplete 4*f* shell is protected from outside disturbance by the outer $5s^25p^6$ shell so that its orbital magnetic moment is well preserved or 'unquenched' by the crystalline field [22,23]. The outermost electrons $5d^16s^2$ can be easily removed the neutral atoms produce trivalent ions in ionic crystals, and conduction electrons in metals or alloys. In metallic state, 4*f*-electrons of the RE elements are subjected to two interactions with their surroundings, which are [23]:

- The single-ion interactions act independently at each ionic site, so that their influence on the state of the 4*f*-electrons at a particular site is unaffected by the magnetic state of its neighbours.
- The two-ion interactions couple the 4*f*-electron clouds at pairs of ions, giving terms that involve two sites i and j.

The charge distribution around an ion produces an electric field, with the local point-symmetry, which acts on the 4*f*-electrons and gives rise to the large magnetic anisotropies which are characteristic of the RE metals. This crystal field contributes to the potential energy of a 4 *f*-electron with charge-e [24] as follows:

$$v_{cf}(r) = \int -\frac{e\rho(R)}{|r-R|}\,dR, \tag{2.10}$$

where $\rho(R)$ is the charge density of the surrounding electrons and nuclei. If these do not penetrate the 4*f* charge cloud, $v_{\text{cf}}(r)$ is a solution of Laplace's equation and may be expanded

in spherical harmonics which is a special case of the multipole expansion [24]. As the crystal-field energy is small compared to the spin-orbit splitting, its effects on the eigenstates of the system are adequately accounted for by first-order perturbation theory. As first pointed out by Stevens (1952) [16], provided that to remain within a manifold of constant *J*, in the case the ground-state multiplet, the matrix elements of $v_{cf}(\boldsymbol{r})$ are proportional to those of operator equivalents, written in terms of the ***J***, and the crystal field Hamiltonian can be written using the Stevens operator $O_l^m(J)$ and crystal field parameterB_l^m:

$$\mathcal{H}_{\mathrm{cf}} = \sum_i \sum_{lm} B_l^m O_l^m J_i \quad . \tag{2.11}$$

Table 2.1 Ionic properties of RE ions with their splitting factors and their theoretical magnetic moments (μ_{eff}).

RE-ion	Ground Term	*S*	*L*	*J*	g_J	$\mu_{eff} = g_J \mu_B [J(J+1)]^{1/2}$	$g_J J$
La^{3+}	$4f^0$ $^1S_0$	0	0	0	—	0	0
Ce^{3+}	$4f^1$ $^2F_{5/2}$	1/2	3	5/2	6/7	2.54	2.14
Pr^{3+}	$4f^2$ $^3H_4$	1	5	4	5/4	3.58	3.20
Nd^{3+}	$4f^3$ $^4I_{9/2}$	3/2	6	9/2	8/11	3.62	3.28
Pm^{3+}	$4f^4$ $^5I_4$	2	6	4	3/5	2.68	2.40
Sm^{3+}	$4f^5$ $^6H_{5/2}$	5/2	5	5/2	2/7	0.840	0.72
Eu^{3+}	$4f^6$ $^7F_0$	3	3	0	0	0	0
Gd^{3+}	$4f^7$ $^8S_{7/2}$	7/2	0	7/2	2	7.94	7
Tb^{3+}	$4f^8$ $^7F_6$	3	3	6	3/2	9.72	9
Dy^{3+}	$4f^9$ $^6H_{15/2}$	5/2	5	15/2	4/3	10.63	10
Ho^{3+}	$4f^{10}$ $^5I_8$	2	6	8	5/4	10.60	10
Er^{3+}	$4f^{11}$ $^4I_{15/2}$	3/2	6	15/2	6/5	9.59	9
Tm^{3+}	$4f^{12}$ $^3H_6$	1	5	6	7/6	7.57	7
Yb^{3+}	$4f^{13}$ $^2F_{7/2}$	1/2	3	7/2	8/7	4.54	4
Lu^{3+}	$4f^{14}$ $^1S_0$	0	0	0	—	0	0

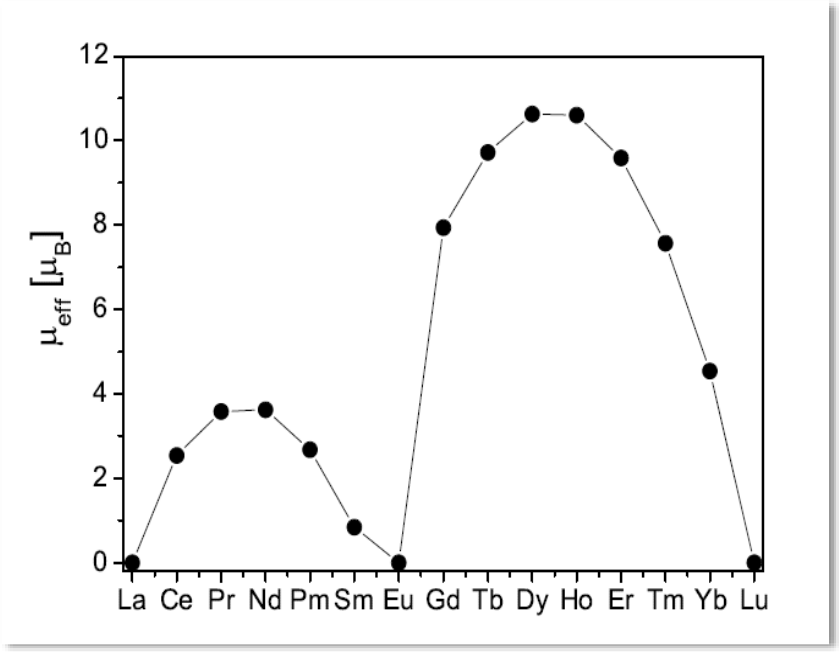

Figure2.1: Theoretical effective magnetic moments μ_{eff} of the free RE^{3+} ions obtained from Eq. 2.9 [21].

2.3 Magnetic states in materials

2.3.1 Diamagnetism

Diamagnetism is a quantum mechanical effect that occurs in all materials when subjected to an applied magnetic field. In diamagnetic materials, all electrons are paired leading to zero net magnetic moment. The applied magnetic field tends to deform orbitals so that the motion of electrons creates a magnetic field that opposes the external magnetic field in accordance with Lenz' law and results in the decrease of the magnetic field within the material [25]. The diamagnetic behaviour gains its origin from the induction associated with the orbital motion due to paired electrons. Therefore, the magnetic induction increases linearly with the magnitude of the external magnetic field. It should be noted that all materials are inherently diamagnetic, but this contribution to the magnetism of the materials are very small and overshadowed by other phenomena such as paramagnetism, ferromagnetism and antiferromagnetism. The theoretical treatment of diamagnetism of atoms and ions makes use of the Lamor theorem which states that: for electrons moving in a single central field of force, the motion in a uniform magnetic field *H* is, to first order in *H*, the same as a possible motion in the absence of *H* except for the superposition of a common precession of angular frequency: $\omega = \frac{eB}{2m}$, with *B* being the external magnetic field,

e and *m* being the charge and the mass of the electron. The magnetic susceptibility of diamagnetic materials is given by [25]:

$$\chi = -\mu_o N \left(\frac{e^2}{6m}\right) \sum \langle r^2 \rangle \ , \tag{2.12}$$

where $\langle r^2 \rangle$ is the average square radii of an electron orbit and *N* is the number of atoms per unit volume. The negative sign of the diamagnetic susceptibility is a direct consequence of Lenz's law. The magnitude of χ is very small of the order ~ -10^{-5} [26]. Diamagnetism is a weak effect that can only be detected by sensitive laboratory instruments. Diamagnetic susceptibility is observed most clearly in those solids in which the atomic shells are completely filled. Examples of these are provided by the noble gas crystals and also ionic crystals. Diamagnetic susceptibility of materials is almost temperature independent.

2.3.2 Paramagnetism

Paramagnetic materials include most chemical elements and some compounds; they have a relative magnetic permeability slightly greater than 1 i.e. a small positive magnetic susceptibility of the order of 10^{-5}-10^{-2}, and hence are attracted to magnetic fields. Substances are considered paramagnetic when there is an intrinsic non zero magnetic moment on each of their atoms, which is independent of the applied magnetic field [27]. The magnetic moment induced by the applied magnetic field is linear in the field strength and rather weak. The coefficient of this linear behaviour is known as the volume susceptibility. It typically requires a sensitive analytical balance to detect the effect and modern measurements on paramagnetic materials and are often conducted with a SQUID (superconducting quantum interference device) magnetometer.

Paramagnetism is due to the presence of unpaired electrons in the material, so most atoms with incompletely filled atomic orbitals are paramagnetic, although exceptions such as copper exist. Due to their spin, unpaired electrons have a magnetic dipole moment and act like tiny magnets. An external magnetic field causes the electrons' spins to align parallel to the field, causing a net attraction.

When studying the magnetic properties of materials by applying an external magnetic field, *H* and measuring the induced magnetization, in these materials, the magnetic induction *B* that the materials experience is given by the expression:

$$B = H + 4\pi M, \tag{2.13}$$

where M is the magnetic moment per unit volume of the materials also known as the magnetization. The volume susceptibility of the materials is defined as the ratio of the magnetization to the applied magnetic field:

$$\chi_v = \frac{M}{H} \tag{2.14}$$

χ_v measures the ease with which a material acquires a magnetization under an external applied magnetic field. Unlike ferromagnets, paramagnets do not retain any magnetization in the absence of an externally applied magnetic field because thermal motion randomizes the spin orientations [27].

For low levels of magnetization, the magnetization of paramagnetic substances follows what is known as Curie's law, at least approximately. This law indicates that the susceptibility, χ, of paramagnetic materials is inversely proportional to their temperature, i.e. that the materials become more magnetic at lower temperatures. The susceptibility is expressed as:

$$\chi = \frac{C}{T} \tag{2.15}$$

where C is a material-specific Curie constant with a unit of Kelvin (K). Hence, the observed paramagnetic susceptibility of the material increases with decreasing temperature, since the effect of thermal motion is minimized at low temperature [28, 29]. For a paramagnetic ion with noninteracting magnetic moments with angular momentum J, the Curie constant is related the individual ions' magnetic moments is given by the expression:

$$C = \frac{n\mu_0\mu_{eff}^2}{3k_BT}; \tag{2.16}$$

where $\mu_{eff} = g_J\mu_B\sqrt{J(J+1)}$, n is the number of atoms per unit volume. The parameter μ_{eff} is interpreted as the effective magnetic moment per paramagnetic ion. The constant g_J denotes the Landé g-value given by:

$$g_J = \frac{3}{2} + \frac{S(S+1)-L(L+1)}{2J(J+1)}. \tag{2.17}$$

Thus a measurement of χ allows one to deduce the value of the effective moment μ_{eff}. The Curie's law dependence of the susceptibility leads to $\chi \propto \frac{1}{T}$ so that the graph of $1/\chi$ versus T is a straight line and a graph of $\chi(T)$ is a constant versus T as shown in figure 2.2.

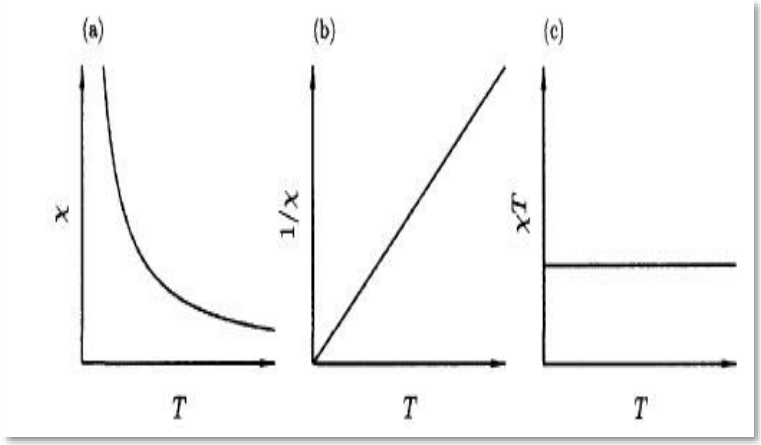

Fig 2.2: Curie's law states that $\chi \propto \frac{1}{T}$ as shown in (a). Thus, a straight-line graph is obtained by plotting $1/\chi$ versus T as shown in (b). A graph of χ (T) versus T is a constant as shown in (c) [30].

2.3.3 Curie-Weiss law

Paramagnetic substances, besides having unpaired electrons, contain paired electrons in the inner shells of the constituent atoms. The presence of these paired electrons makes diamagnetism an inherent property of all materials. Thus, the magnetic moment measured is the sum of both paramagnetic (positive quantity) and the associated diamagnetic (negative quantity) moment. Since the presence of intrinsic magnetic moment in a substance results in a large paramagnetic moment. The diamagnetic effects are often neglected in the calculations. However, magnetic moments of individual atoms in many substances do interact with each other in several different ways. In these materials, Curie's law is not obeyed: often, the magnetic behaviour of these substances is best described by a Curie-Weiss law which takes into account the interactions among the individual magnetic moments. Thus, the Curie-Weiss law described magnetic susceptibility, χ of a ferromagnet or an antiferromagnet in the paramagnetic region above the Curie or the Néel point is given by [30, 31, 32]:

$$\chi = \frac{\mathrm{C}}{T-\theta} \quad , \tag{2.18}$$

where θ is the Weiss constant (or paramagnetic Curie temperature). Interactions of magnetic

moments in condensed matter systems (solids) will in most cases lead to different types of magnetic ordering, characteristic of the substance. The type of magnetic interactions present in a particular substance is primarily determined by the nature of the constituent ions and chemical bonds. The magnetic interactions between the individual magnetic moments result in net stabilization energy. The two most common types of magnetic ordering or interactions are called ferromagnetism and antiferromagnetism. Figure 2.3 illustrates the temperature dependence of the inverse magnetic susceptibility of three types of magnetism, Paramagnetism (PM), ferromagnetism (FM), and antiferromagnetism (AFM) [33].

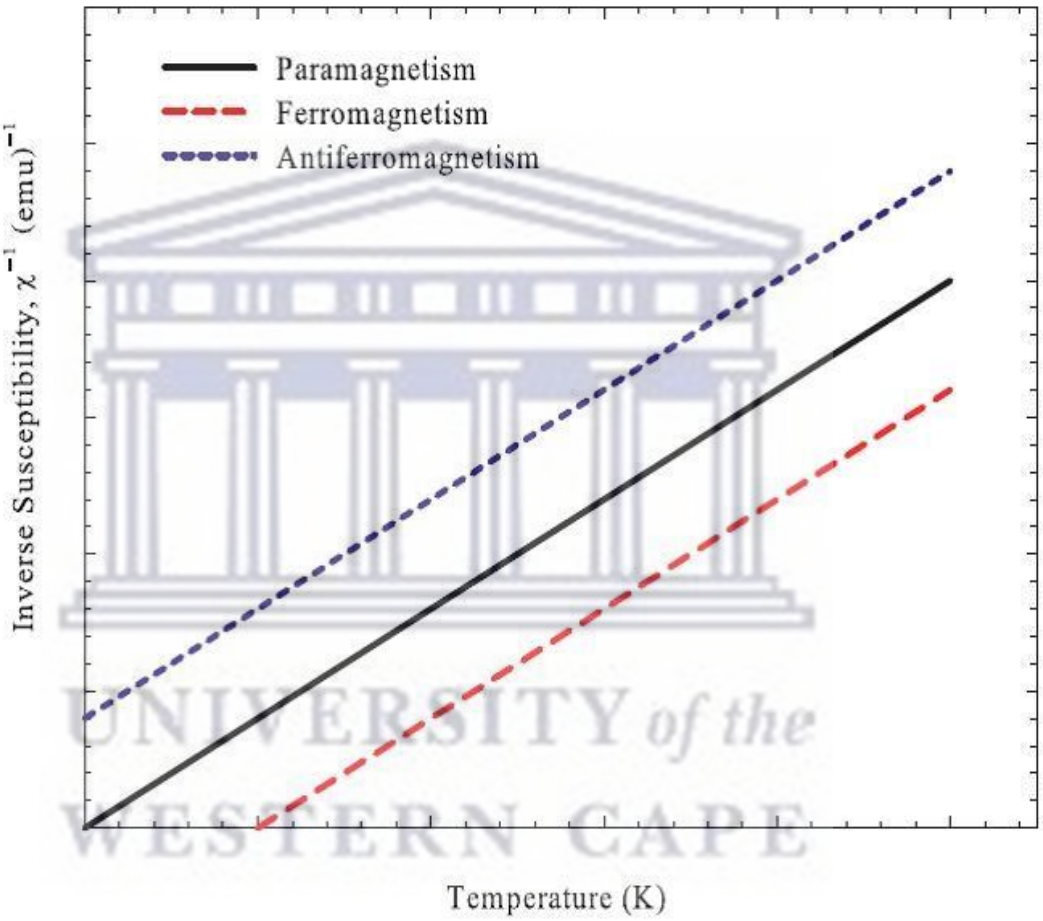

Figure 2.3: Temperature- dependence of the inverse magnetic susceptibility simulation curves showing three types of magnetism that can be exhibited by materials, blue dashed line (antiferromagnetism), black solid line (paramagnetism), and red dashed line (ferromagnetism) [33].

2.3.4 Ferromagnetism

In ferromagnetic substances, the magnetic moments of adjacent atoms are aligned parallel to one another below a certain critical temperature known as the Curie temperature (T_c), as shown in figure .2.4, which represents parallel aligned unpaired electron spins in ferromagnetically-ordered material. This type of magnetic ordering is characterized by a spontaneous magnetization of the substance below T_c, even in the absence of an external magnetic field. Iron, nickel and cobalt, some RE metals, as well as some compounds of these elements, are typical examples that show ferromagnetic ordering [34, 35, 36]. Compounds that exhibit ferromagnetic or antiferromagnetic type of magnetic ordering often obey the Curie-Weiss law Eq. 2.18 at temperatures well above the transition temperatures (ordering temperature, T_c or T_N) [37, 38].

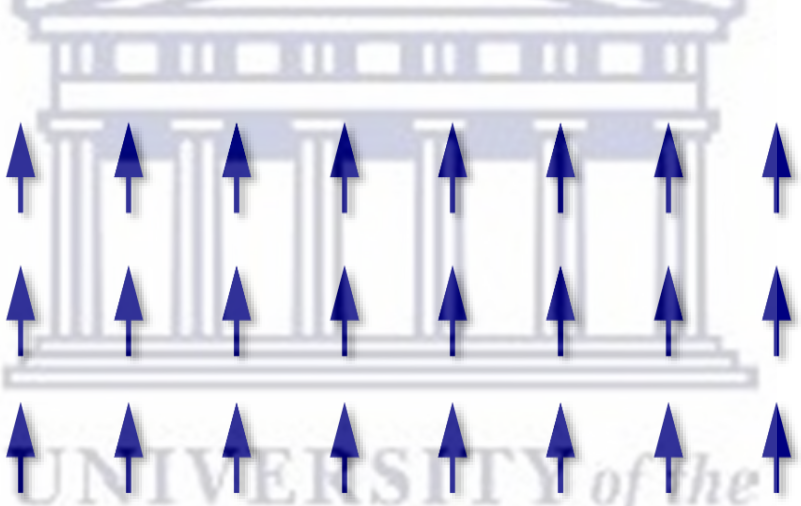

Figure 2.4: A figure representing parallel aligned unpaired electron spins in ferromagnetically-ordered material.

2.3.5 Antiferromagnetism

In antiferromagnetic materials, the interaction between the magnetic moments tends to align adjacent moments antiparallel to each other [39] as in figure 2.5, which shows the antiparallel aligned unpaired electron spins in an antiferromagnetically-ordered material. In

an antiferromagnet, the atomic moments form two equivalents but oppositely oriented magnetic sublattices. The material nonetheless exhibits a phase transition with a λ-shaped specific heat anomaly where the moments begin to order [40]. The antiferromagnetic transition occurs at the Néel temperature, T_N. Occasionally it is possible to switch an antiferromagnet into a ferromagnet if a sufficiently large field is applied. This discontinuous change of magnetic order is known as a metamagnetic transition [41, 42].

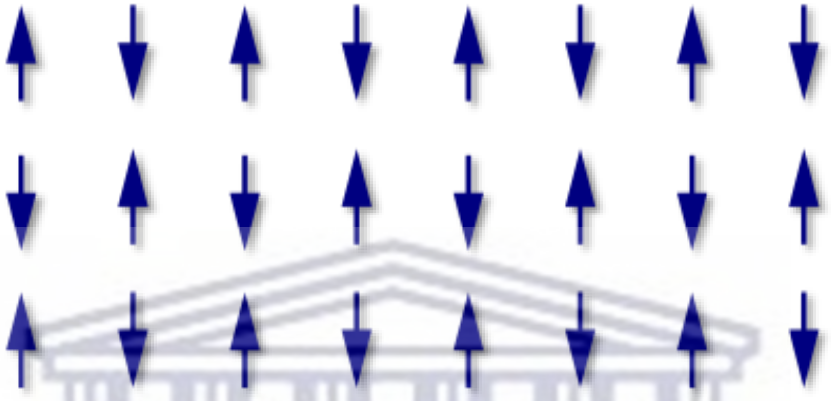

Figure 2.5: A figure representing antiparallel aligned spins in an antiferromagnetically-ordered material.

2.3.6 Ferrimagnetism

Ferrimagnetism is another prevalent type of ordering of the magnetic moments. In ferrimagnetic substances, although individual magnetic moments of adjacent atomic particles are aligned antiparallel, they are not of equal magnitude when the types of interacting neighbouring atoms are different. Exchange coupling between adjacent magnetic ions leads to antiparallel alignment of the localized moments as appears in figure 2.6 which represents antiparallel aligned spins with unequal magnitude in the two orientations ferrimagnetically-ordered materials. The overall magnetization occurs because the magnetization of one sublattice is greater than that of the oppositely oriented sublattice. As the magnetic moments are of different magnitude in opposite directions, there is still a spontaneous magnetization and an internal magnetic field is present [43, 44]. Similar to ferromagnetic materials the magnetic interactions are held together by exchange interactions. The orientation of moments however, are antiparallel which results in net magnetization

[45]. The magnetization and magnetic susceptibility behaviour of ferrimagnetic materials are similar to that of ferromagnetic materials. In general, ferrimagnetic materials are poor conductors compared to ferromagnetic materials.

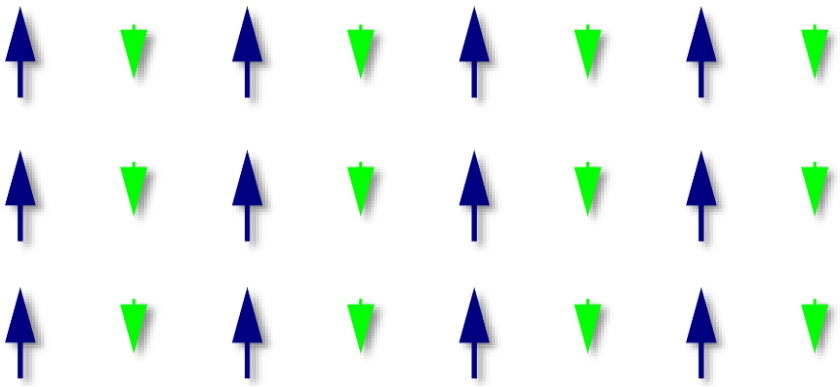

Figure 2.6: A figure representing antiparallel aligned spins with unequal magnitude in the two orientations ferrimagnetically-ordered material.

2.3.7 Spin-glass behaviour

Spin-glass is a magnetic state characterized by randomness, besides cooperative behaviour in freezing of spins at a temperature called 'freezing temperature' T_f [46, 47]. It considers a possible configuration with a form of magnetic state with inadequate populated magnetic atoms in a non-magnetic lattice with dilute and random distribution [48]. Figure 2.7 represents the random spin structure of a Spin-glass (top) and the ordered one of a ferromagnet (bottom).

The metastable state formed has no tendency towards ordering uniformly like ferromagnets, nor in a spatially ordered way like in antiferromagnets [49, 50]. The two key factors that lead to spin glass are structural disorder and/or competing ferromagnetic and antiferromagnetic interactions which produce a magnetically frustrated state. As a result of the conflict between these two types of interaction, neither of the two states can be satisfied by the interaction of the neighbouring spins [51].

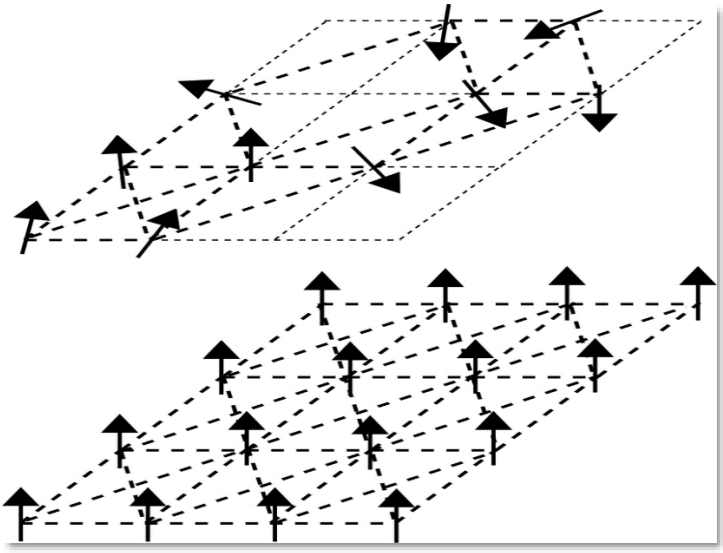

Figure 2.7: Schematic diagram representing the random spin structure of a spin glass (top) and the ordered one of a ferromagnet (bottom) [49].

2.4 Theory of magnetism

2.4.1 Exchange interactions

The exchange interaction was first treated by Heisenberg in 1928 to interpret the origin of the enormously large internal molecular magnetic fields acting in ferromagnetic materials. The interaction lies at the heart of the phenomenon of long-range magnetic order [52]. It is considered as an electrostatic interaction, arising because charges of the same sign cost energy when they are close together and save energy when they are apart [52]. It should be noted that the dipole-dipole interaction between magnetic moments of electrons is much too weak to explain magnetic order at high temperatures. This means we have to find a strong interaction between electrons. Heisenberg realized that the responsible interaction is the Coulomb repulsion between electrons which is strong, but does not explicitly depend on the spin. The spin selectively is coming from quantum mechanics, specifically from the Pauli exclusion principle: two electrons with parallel or antiparallel spins behave differently, even though the fundamental interaction is the same, because the (spatial) wave function $\psi(\overrightarrow{r_1}, \overrightarrow{r_2})$ has to be antisymmetric and symmetric in this case, respectively. This means for instance two electrons with parallel spins cannot be at the same place.

2.4.2 Direct exchange interaction

Magnetism is a macroscopic phenomenon that at the microscopic level occurs due to exchange interactions, whose typical range (length scale), is determined by the spatial extent of the quantum mechanical wave function [52, 53]. Confinement of these wave functions for example; the presence of a surface leads to many unusual magnetic phenomena [54, 55]. The mechanism of spin alignment is not magnetic in origin; it is essentially the effect of the Pauli exclusion principle tending to keep parallel spins apart and known as an exchange interaction. The interaction is a result of the fact that the wave function of two electrons must be antisymmetric under the exchange of all electron coordinates, space, and spin [56, 57, 58]:

$$\psi(\vec{r_1}, \vec{s_1}; \vec{r_2}, \vec{s_2}) = -\psi(\vec{r_2}, \vec{s_2}; \vec{r_1}, \vec{s_1}) \ . \tag{2.19}$$

From this relation, it follows that the wave function vanishes when the coordinates of two electrons are identical: $\vec{s_1} = \vec{s_2}$, $\vec{r_1} = \vec{r_2}$. The overall antisymmetry of the wave function, therefore, tends to keep electrons of parallel spin apart so that the expectation of the Coulomb repulsion energy $e^2/4\pi\varepsilon_0|\vec{r_1} - \vec{r_2}|$ of both electrons are reduced for parallel spin than that of antiparallel spin. This represents the exchange interaction between the two electrons and can be expressed as; $J_{12}\ \vec{s_1} \ . \ \vec{s_2}$, which corresponds to the Coulomb energy of the parallel spin state being 2 J_{12} smaller than that of the antiparallel spin state. It is from this interpretation that $J_{12} > 0$ is associated with ferromagnetic alignment of spins and $J_{12} < 0$ is ascribed to antiferromagnetic alignment of spins. The exchange interaction between the electrons of the same atoms explain Hund's rule [59, 60]. On the other hand, Coulomb interaction between two electrons on different atoms depends on their relative spin orientation as a result of the antisymmetry of the wave function. The resulting exchange energy decreases rapidly with increasing distance between the two atoms. This type of interaction is known as direct interaction which cannot explain magnetic ordering in RE metals due to the small overlap of the 4*f* wave functions on neighboring atoms [61].

2.4.3 Indirect interaction: Rudderman-Kittel-Kasuya Yosida (RKKY) interaction

Another type of interaction still observed in RE metals is the indirect exchange. This is the indirect exchange interaction between magnetic ions which is mediated by the conduction electrons. Indeed, a localized magnetic moment spin-polarizes the conduction electrons and this polarization in turn couples to a neighbouring localized magnetic moment a distance away. This interaction does not involve direct coupling between magnetic moments and is known as the RKKY interaction (or also as itinerant exchange). This interaction results from the limited spatial extent of the 4*f* wave function of adjacent RE centres which may turn out to be a negligible contribution to the inter-atomic coupling. It should be noted that this interaction leads to a magnetic ordering of the RE 4*f* moments especially at low temperatures. The Interaction between them can only be possible via polarized conduction electrons that leads to magnetic ordering of 4*f* moments at low temperatures. In contrast to the 3*d* metals, the 3*d* wave functions are spatially more extended and one can expect to find both direct and indirect interactions. The coupling between the localized magnetic moments via the polarized conduction electrons takes the form of an *r*-dependent exchange interaction $J_{RKKY}(r)$ given by [62, 63]:

$$J_{RKKY}(r) \propto \frac{\cos(2k_F r)}{r^3}, \tag{2.20}$$

At large r ($r \gg k_F^{-1}$), assuming a spherical Fermi surface of radius k_F, $J_{RKKY}(r)$ is oscillatory. The interaction in this case is long range and has an oscillatory dependence on the distance between the magnetic moments. As a result, depending on the separation it may be either ferromagnetic or antiferromagnetic. The coupling is oscillatory with wavelength $\frac{\pi}{k_F}$ because of the sharpness of the Fermi surface [64]. The RKKY interaction for the magnetic exchange described by the Hamiltonian:

$$H = -J_{ij}.\vec{S}_i.\vec{S}_j; \tag{2.21}$$

where $\vec{S}_i$ and $\vec{S}_j$ are the total spins of the localized 4*f* electrons located at *i* and *j* positions,

respectively, and separated by a distance $\vec{r}_{ij}$. J_{RKKY}^{ij} is the coupling constant found to be between the two spins $\vec{S}_i$ and $\vec{S}_j$ and takes the form [64, 65]:

$$J_{RKKY}^{ij} = 6\pi Z J^2 N(E_F) \left(\frac{sin(2\,k_F r_{ij})}{(2k_F r_{ij})^4} - \frac{cos(\,2k_F r_{ij})}{(2k_F r_{ij})^3} \right), \tag{2.22}$$

with Z being the number of conduction electrons per atom, k_F the Fermi wave number, $N(E_F)$ is the density of state at the Fermi level and J is the exchange integral defined according to the Schrieffer-Wolff transformation as follows [66, 67]:

$$J = -\frac{|V_{sf}|^2}{|\varepsilon_{4f} - \varepsilon_F|}, \tag{2.23}$$

V_{sf} is the hybridization matrix element between the 4f electrons and the conduction band so $|\,V_{sf}\,|^2$ will describe the strength of the hybridization between the itinerant conduction electrons and the localized 4f electrons. ε_{4f} denotes the position of the 4f energy level relative to the Fermi energy level ε_F. The negative sign indicates that the coupling between the conduction electrons and the local moment is antiparallel. The RKKY exchange coefficient J_{RKKY}^{ij}, oscillates from positive to negative as the separation of ions changes and has a damped oscillatory nature. The energy scale connected to the RKKY interaction is given by [68]:

$$k_B T_{RKKY} \propto J^2 N(E_F), \tag{2.24}$$

The real-space susceptibility is given by [62]:

$$\chi(r) = \frac{2k_F^3 \chi_P}{\pi} \left(\frac{\sin(2k_F r)}{(2k_F r)^4} - \frac{\cos(2k_F r)}{(2k_F r)^3} \right), \tag{2.25}$$

where χ_P is the Pauli paramagnetic susceptibility. $\chi(r)$ follows the same behaviour like the coupling constant at large r. At small r the susceptibility diverges. The RKKY interaction provides an important mechanism for magnetic coupling between localized electronic moments in metals. One moment produces an oscillatory magnetization of the electron gas which can interact with a second moment [67]. As mentioned above the interaction can be ferromagnetic or antiferromagnetic depending on the distance between the two moments.

2.4.4 Spin-wave theory

Spin waves are another interesting dynamic aspect of the spin motion in a ferromagnet. Spin waves are the analog in solid systems for magnetically ordered lattice wave systems. Just as a "phonon" is called the quantized lattice wave, a quantized spin wave is called "magnon"[68].

The determination of the low-temperature thermal behaviour of the heat capacity, magnetization and electrical resistivity important to this thesis, are also discussed.

A semi classical approach calculation of a chain of ferromagnetically aligned spins' low-lying excited states, assumed that the spins behave as classical angular momenta. This calculation is similar to one used in a solid system to measure the vibrations of the lattice. Considering only the exchange interaction between nearest neighbour, and using the Hamiltonian of the Heisenberg model [68, 69]:

$$\hat{H} = -\sum_i \sum_{j \neq i} J_{ij} \hat{S}_i . \hat{S}_j \,, \tag{2.26}$$

J_{ij} is the exchange interaction between the total spin momenta, $\hat{S}_i$ and $\hat{S}_j$ of the i and j atoms. Considering a one-dimensional chain, each spin has two nearest neighbours and the Hamiltonian is reduced to:

$$\hat{H} = -2J \sum_i \hat{S}_i . \hat{S}_{i+1}. \tag{2.27}$$

The time dependence of the wave function, ψ in the absence of a measurement is given by the Schrödinger equation:

$$\hat{H}\psi = i\hbar \frac{d\psi}{dt}.$$

Using the time dependence of the expected value of an operator, $\hat{A}$ given by:

$$\frac{d\langle \hat{A} \rangle}{dt} = \frac{1}{i\hbar} \langle [\hat{A}, \hat{H}] \rangle$$

if the operator $\hat{A}$ itself is not time dependent, one can calculate the time dependence of $\langle \hat{S}_j \rangle$ (note the subscript j is used here to avoid confusion with i the complex number) given by [69]:

$$\frac{d\langle \hat{S}_j \rangle}{dt} = \frac{2J}{\hbar} \langle \hat{S}_j \times \left(\hat{S}_{j-1} + \hat{S}_{j+1} \right) \rangle. \tag{2.28}$$

Taking the spins at each site as classical vectors and assuming that the ground state of the system has all the spins aligned along the z-axis, the Eq. 2.28 leads to:

$$\hbar\omega_k = 4JS(1 - \cos(ka)) \,. \tag{2.29}$$

The corresponding exchange energy of the j^{th} spin in the chain within the semiclassical approach is given by:

$$E_j = -2J\hat{S}_j.\left(\hat{S}_{j-1} + \hat{S}_{j+1}\right). \tag{2.30}$$

2.4.4.1 Quantum mechanical approach

It is important to derive the dispersion relation (Eq. 2.28) using the quantum mechanical model. In the analogy with the semiclassical model we used of the derivation taking the spin S =1/2. However this can be generalized for all spins. We begin to consider the ground state of the system, $|\phi\rangle$, which involves all the spins lying in the z-axis. Similar to the semiclassical model, the one-dimensional Hamiltonian for the Heisenberg model as given in Eq. 2.27 can now be written as:

$$\widehat{H} = -2J\sum_i \left[\hat{S}_i^z S_{i+1}^z + \frac{1}{2}\left(\hat{S}_i^+ S_{i+1}^- + \hat{S}_i^- S_{i+1}^+\right)\right], \tag{2.31}$$

so that when the Hamiltonian operator operates on the wave function of the ground state the system one obtains $\widehat{H}|\phi\rangle = -NS^2J|\phi\rangle$. Note that S^+ and S^- denotes spin up and spin down, respectively and N the total number of spins. To create an excitation, we must flip the spin at a site j. For that we consider the ground state with the spin at site j flipped given by $|j\rangle = S_j^-|\phi\rangle$ as shown in figure 2.8.

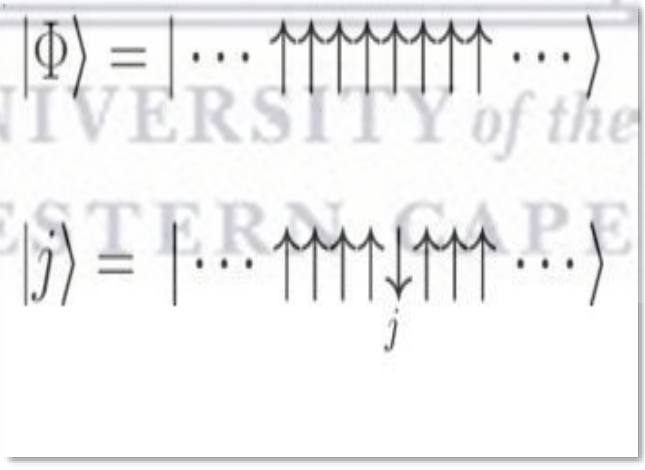

Figure 2.8: The state $|\phi\rangle$ involving all the spins lying in the z- axis. The State $|j\rangle$ is the ground state with spin j [70].

By flipping the spin, the total spin of the system change $\frac{1}{2} - \left(-\frac{1}{2}\right) = 1$. Such an excitation has an integer spin and is known as boson. Now let the Hamiltonian operator, $\widehat{H}$ operate on the state $|j\rangle$, one obtains:

$$\widehat{H}|j\rangle = 2[(-NS^2J + 2SJ)|j\rangle - SJ|j+1\rangle - SJ|j-1\rangle]. \quad (2.32)$$

It should be noted that the result is not a constant multiplied by $|j\rangle$, which means the eigenvalue of $\widehat{H}$ in the above equation is not a constant. Consequently, this state is not an eigenstate of $\widehat{H}$. However, to overcome this situation one can diagonalize $\widehat{H}$ by looking for plane wave solutions of the form [70]:

$$|k\rangle = \frac{1}{\sqrt{N}} \sum_i e^{ikR_j} |j\rangle, \quad (2.33)$$

where R_j is the position of the spin at the site j. It should be noted that the state $|k\rangle$ is basically a flipped spin smeared out through all the sites. It can be shown that the eigenvalue equation of $\widehat{H}$ can now be written as:

$$\widehat{H}|k\rangle = E(k)|k\rangle, \quad (2.34)$$

where the energy takes the form:

$$E(k) = -2NS^2J + 4JS(1 - \cos(ka)). \quad (2.35)$$

From the above expression of $E(k)$, it is clear that the energy is then $\hbar\omega = 4JS(1 - \cos(ka))$ which is the same as the result obtained using the semiclassical model (Eq.2.28).

From the dispersion relation given by $\hbar\omega_k = 4JS(1 - \cos(ka))$, the magnon energy ε for small value of k leads to a quadratic dependence of ε in the form:

$$\varepsilon = \hbar\omega_k = 2JSa^2k^2 \quad (2.36)$$

so that $\omega_k \sim k^2$.

The contribution of the spin waves to the heat capacity of ferromagnetic materials at low temperature is then obtained using the number of spin-wave modes with wavenumber between k and $k + dk$ and the number of modes with a frequency between ω and $\omega + d\omega$. The energy associated with each mode is related to the average

number of magnons at temperature T given by the Bose-Einstein distribution function. Thus, the contribution of the magnons to the total energy is given by [70, 71]:

$$E = E_0 + \frac{V}{4\pi^2}\left(\frac{\hbar}{2JSa^2}\right)^{3/2}\left(\frac{k_BT}{\hbar}\right)^{5/2}\int_0^{\infty}\frac{x^{3/2}}{e^x-1}dx\,, \tag{2.37}$$

where E_0 is the zero-point energy, V is the volume of the crystal and $x = \hbar\omega/k_BT$. Eq. 2.37 leads to the spin-wave contribution to the heat capacity at low temperatures in the form [69]:

$$C_M = \frac{dE}{dT} \propto k_BT^{3/2}\,. \tag{2.38}$$

Similar to the heat capacity, the magnetization can be expressed in the form [70]:

$$M = M_S\left[1 - \frac{1}{NS4\pi^2}\left(\frac{k_BT}{2JSa^2}\right)^{3/2}\int_0^{\infty}\frac{x^{1/2}}{e^x-1}dx\right], \tag{2.39}$$

where $M_S = Ng\mu_BS$ is the saturation magnetization and the integral gives a constant number. It follows from Eq. 2.39 that the decrease in magnetization at low temperature is proportional to $T^{3/2}$. This result is known as the Bloch $T^{3/2}$ law, and it fits the experimental data in the low temperature region. It is expected to be a much better fit with the experimentally observed behaviour than predicted by the mean-field theory. For an anisotropic ferromagnet material, the magnon dispersion relation is given in the limit of small wave number k in the form [71]:

$$\omega_k = \Delta + Dk^2\,, \tag{2.40}$$

where Δ accounts for an anisotropy frequency gap and D is the spin-wave stiffness. The electrical resistivity resulting from the scattering of conduction electrons due to the spin-wave modes is given by [71]:

$$\rho_M = \frac{A}{k_BT}\int\frac{\omega}{\sinh^2(\omega/2k_BT)}d\omega\int k^3\mathrm{Im}\chi(k,\omega)dk\,, \tag{2.41}$$

where $A = (1/3n)(4\pi mG^2/ne)$ with m, e, and n being the mass, charge, and the number of conduction electrons per unit volume, respectively. G is the coupling constant between the conduction electrons and the RE moments. The imaginary part of the transverse dynamic susceptibility, $\mathrm{Im}\chi(k,\omega)$, associated with the spin waves is given by:

$$\mathrm{Im}\chi(k,\omega) = \pi[\delta(\omega - E_k) + \delta(\omega + E_k)], \tag{2.42}$$

with E_k the energy of the magnetic excitation responsible for the scattering of the conduction electrons. For anisotropy ferromagnetic materials or when a symmetry lifting external magnetic field is applied, there is a gap in the spectrum and the resistivity can be obtained for $k_BT \ll \Delta$, given by [70, 71, 72]:

$$\rho_M(T) = a\Delta_{FM}T\left[1 + 2\frac{k_BT}{\Delta_{FM}}\right]\exp\left(-\frac{\Delta_{FM}}{k_BT}\right), \tag{2.43}$$

where a is a constant that depends on the material. In the isotropic ferromagnet case $\Delta = 0$ (gapless dispersion in k-space), one obtains $\rho_M \sim T^2$. The spin-wave contribution to the heat capacity at low temperatures expected for an energy gapped ferromagnetic spin-wave to be given by [72]:

$$C_M(T) \approx \gamma T + BT^{3/2}\, exp\left(-\frac{\Delta_{FM}}{k_BT}\right), \tag{2.44}$$

where γ is the Sommerfeld coefficient and B a constant that defines the stiffness of the sample.

For antiferromagnetic materials, Yamada and Takada [73] suggest a new expression for the transverse dynamic susceptibility, Imχ(k, ω) associated with spin-waves given by :

$$\mathrm{Im}\chi(k,\omega) = \frac{\pi}{\varepsilon_k}[\delta(\omega - \omega_k^+) + \delta(\omega + \omega_k^-)]; \tag{2.45}$$

$$\omega_k^{\pm} = -\mu_{eff}H \pm \varepsilon_k,$$

with:

$$\varepsilon_k = \frac{1}{2}(\omega_k^+ - \omega_k^-) = (\Delta^2 + Dk^2)^{1/2}. \tag{2.46}$$

The resistivity then follows:

$$\rho_M(T) \approx b\Delta_{AFM}^2\left(\frac{k_BT}{\Delta_{AFM}}\right)^{\frac{1}{2}} exp\left(-\frac{\Delta_{AFM}}{k_BT}\right) \times \left[1 + \frac{2}{3}\left(\frac{k_BT}{\Delta_{AFM}}\right) + \frac{2}{15}\left(\frac{k_BT}{\Delta_{AFM}}\right)^2\right], \tag{2.47}$$

where b is a constant. The spin-wave contribution to the heat capacity at low temperatures expected for energy gapped antiferromagnetic spin-wave having the same dispersion relation given by Eq. 2.47 takes the form [74, 75]:

$$C_M(T) = \Delta_{AFM}^{7/2}T^{1/2}\, exp\left(-\frac{\Delta_{AFM}}{k_BT}\right) \times \left[1 + \frac{39}{20}\left(\frac{k_BT}{\Delta_{AFM}}\right) + \frac{51}{32}\left(\frac{k_BT}{\Delta_{AFM}}\right)^2\right]. \tag{2.48}$$

2.5 Crystal electric field effect and Schottky anomaly

So far, we have discussed that the magnetic properties of materials containing rare earth elements can be deduced by bearing in mind the rare earth ions behave as completely free ions without interacting with each other or their surroundings. In fact, for magnetic ions in some crystals one cannot neglect or ignore such interactions. In this section, we will discuss the interactions between an atom and its intermediate surroundings.

Crystal electric field arises from the surrounding electrons and ions in the crystal [76]. In a compound, a 4*f*-ion is exposed to a crystal-electric-field, which reflects the symmetry at the RE ion site. This crystal-electric-field completely or partially lifts the degeneracy of the $4f$ free-ion ground state multiplet ($2J + 1$), J being the total angular momentum [77, 78]. It should be noted that the ground state of a free-ion or atom with a partially filled $4f$ shell can be derived using Hund's rules. Ground state multiplets generally denote the lowest lying multiplets in the presence of a crystal-electric-field. The resulting number of multiplets is determined by the local crystal symmetry and their relative energy levels depends on the exact form and magnitude of the crystal-electric-field [79].

In RE compounds, crystal - electric - fields are likely responsible for the magnetocrystalline anisotropy [80], but may themselves cause the splitting of the $(2J + 1)$-fold degenerate manifold. For a system with a field excited level at $k_B T_{\Delta CEF}$ ($T_{\Delta CEF}$ denotes the temperature corresponding to the crystal-electric-field) above the ground state, only the lowest lying multiplet has a high probability of occupancy for $T \ll T_{\Delta CEF}$. Therefore, the properties of the system are determined by the ground state multiplet. With increasing temperature, the state above the ground state becomes populated. The corresponding increase of entropy shows up as an extra contribution to the 4*f*-electron specific heat of the system in the form of Schottky anomaly in the region $T_{\Delta CEF}$, expressed for m number of levels in the form [80, 81, 82]:

$$C_{Sch}(T) = \frac{R\sum_{i=0}^{m} g_i\left(\frac{\Delta_i}{T}\right)^2 exp\left(-\frac{\Delta_i}{T}\right)}{\left[\sum_{i=0}^{m} g_i\left(-\frac{\Delta_i}{T}\right)\right]^2} \times \left[\sum_{i=0}^{m} g_i exp\left(-\frac{\Delta_i}{T}\right) - \sum_{i=0}^{m} g_i\left(\frac{\Delta_i}{T}\right)^2 exp\left(-\frac{\Delta_i}{T}\right)\right] \quad (2.49)$$

where level i with degeneracy of g_i is situated at energy Δ_i above the ground state. The change of the effective moment with increasing occupancy of higher energy levels becomes evident in the magnetic susceptibility. Transport properties reflect the enhanced scattering on crystal-electric-field excitation around $T_{\Delta CEF}$. In the case of

the temperature variation of the electrical resistivity, the crystal-electric-field is sometimes characterized by a broad curvature at high temperatures around $T_{\Delta CEF}$ [83].

2.6 Phase transition

Phase can be defined as a region with homogeneous physical properties. It forms uniform crystal structure and properties through interaction among component elements, and has regions with homogeneous sample. Phases in an alloy can be divided into four types: solid solution, pure monomeric component substance, order solid solution, and metallic compound [84, 85].

In thermodynamic systems, there are a number of physical parameters that are characterized by their state variables such as temperature, pressure, and magnetization density. If the metallic compound has magnetic properties, it indicates that the variables are dependant on the conditions applied to the system, in particular the temperature, the pressure, and the applied magnetic field. The possibility of sudden variation of one of the state parameters on the macroscopic scale is called "Phase Transition" [86]. One can define phase transitions as transitions between different physical states (phases) of the same substance. It occurs when there is a discontinuity in the free energy [87]. In fact, the phase transition results from a broken symmetry. In this situation the system will have a sharp change of behaviour at a temperature T_C for ferromagnetic materials. One describes this by saying that the system has changed phase (e.g. paramagnet to ferromagnet, solid to liquid etc.). The region near the phase transition is known as the critical region. A phase transition from a magnetically ordered state into a paramagnetic state at 0 K is considered as an example of a quantum phase transition (QPT) [88, 89] as in figure 2.9 [33].

The order of the transition is defined by the lowest discontinuous derivative of the free energy function. The first-order phase transition (FOPT) which is accompanied by discontinuities of the first derivatives of the free energy taken with respect to the thermodynamic variables that trigger the phase transition. When control variables are temperature (T) and magnetic field (H) at atmospheric pressure, one can state that a FOPT occurs across a T_C (H_C) boundary, where T_C is the critical transition temperature at the critical field (H_C), if one observes a discontinuous change in entropy, S, or a discontinuous change in magnetization, M [90].

Second-order phase transitions or continuous phase transitions, are characterized by

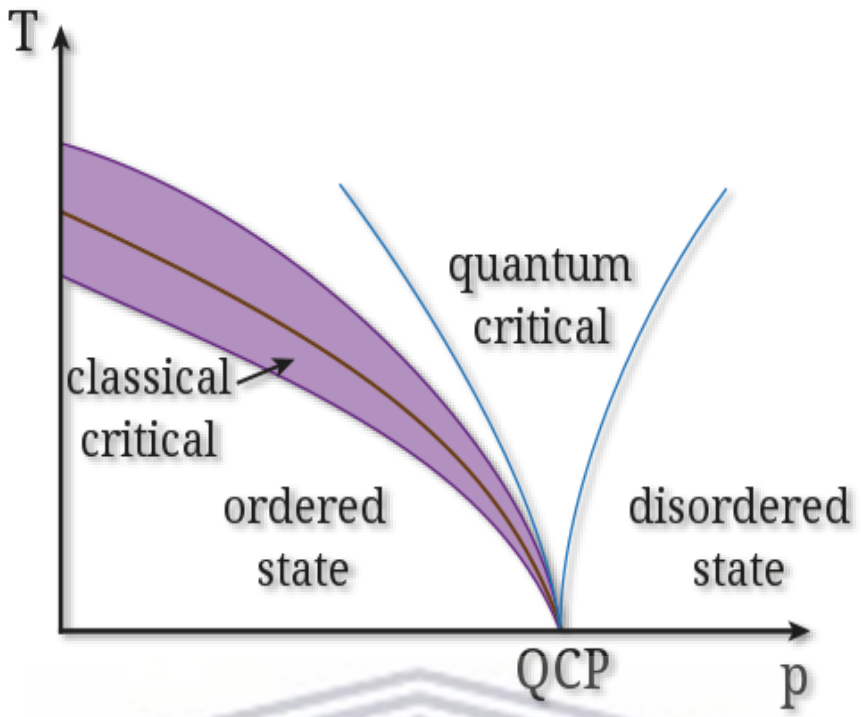

Figure 2.9: Diagram of temperature (*T*) and pressure (*P*) showing the quantum critical point (QCP) and quantum phase transitions [33].

a continuity of all the first derivatives of the potential. The second-order phase transitions include transitions associated with the emergence of magnetism, superconductivity and orientational order. Since second-order phase transitions were customarily defined as a cooperative, continuous, homogeneous processes, involving all constituent particles in the bulk, it became almost exclusively the subject of interest.

2.6.1 Landau theory of second-order phase transition

The Landau theory is a conventional model which simply produces a phase transition and arises from some very general considerations. The Landau theory of second-order phase transition is based on the existence of order parameter such as the spontaneous magnetization, thus, the value characterizes the phase present in the considered system. At high temperatures, this parameter is zero, whereas at low-temperatures, a spontaneous symmetry break occurs at about the critical point and the order parameter takes a non-zero value in the ordered phase.

In the vicinity of the critical point, Landau suggested developing the free energy of the system in the powers of the order parameter. From this development, the critical exponents based on the mean-field model can be deduced. In this model, the succession of the phases when the temperature increases is understood by a competition between the internal energy *U* (which favour order in the system) and the entropy *S* (source of disorder) in the Gibbs free energy *G* and in which the minimum value of the order parameter denotes the thermodynamic equilibrium [91, 92, 93].

Landau suggested that near a phase transition an approximate form for the free energy can be constructed without first calculating the microscopic states, and it is always possible to identify an order parameter that is zero on the high temperature side of the phase transition and nonzero on the low temperature side of the phase transition [94, 95]. For instance, the magnetization can be considered to be the order parameter at a ferromagnetic - paramagnetic phase transition. At a second-order phase transition, the order parameter increases continuously from zero starting at the critical temperature of the phase transition. An example of this is the continuous increase of the magnetization at a ferromagnetic-paramagnetic phase transition. Since the order parameter is small near the phase transition, to a good approximation, the free energy of the system can be approximated by the first few terms of the Taylor expansion of the free energy [96, 97, 98]:

$$f(T) = f_0(T) + \alpha\eta^2 + \frac{1}{2}\beta\eta^4 \qquad \alpha > 0, \ \ \beta > 0, \qquad (2.50)$$

where η is the order parameter, α and β are coefficients of the second order and fourth order terms, and $f_0(T)$ describes the temperature dependence of the high-temperature phase near the phase transition. It should be noted that this power series cannot contain any odd power of η because there is no energetic difference between "up" and "down" spins. It can be shown that the system yields an appropriate phase transition if one allows α to change sign at the transition temperature T_C. It is assumed that $\beta > 0$, so that the free energy has a minimum for finite values of the order parameter. When $\alpha > 0$, there is only one minimum at $\eta = 0$, whilst when $\alpha < 0$ there are two minima with $\eta \neq 0$. Thus, in the region of interest, near the transition, one can write $\alpha(T) = \alpha_0(T - T_C)$ where α_0 is a positive constant. The free energy can then be written as [98, 99]:

$$f(T) = f_0(T) + \alpha_0(T - T_C).\eta^2 + \frac{1}{2}\beta\eta^4 \qquad (2.51)$$

where $\alpha_0 > 0,\ \beta > 0.$

Figure 2.10 shows the free energy as a function of the order parameter η. To obtain the ground state of the system, it is necessary to minimize the free energy so we look for solutions based on $\frac{\partial f}{\partial \eta} = 0$. This condition implies that:

$$\frac{df}{d\eta} = 0 = 2\alpha_0(T - T_C).\eta + 2\beta\eta^3, \tag{2.52}$$

Hence for $T > Tc$, $\eta = 0$ and.

The right-hand side of Eq. 2.52 is a product of two terms, so either of them could be zero. However, there are three possible roots for η namely $\eta = 0$ and

$$\eta = \pm\sqrt{\frac{\alpha_0(T_C - T)}{\beta}} \qquad \text{with} \quad T < T_c \tag{2.53}$$

For $T < Tc$. By substituting the expression for the order parameter back into the expression above for the free energy, the temperature dependence of the free energy near the phase transition can be shown to be:

$$f(T) = f_0(T) - \frac{\alpha_0^2(T - T_C)^2}{\beta} \tag{2.54}$$

For $T < Tc$.

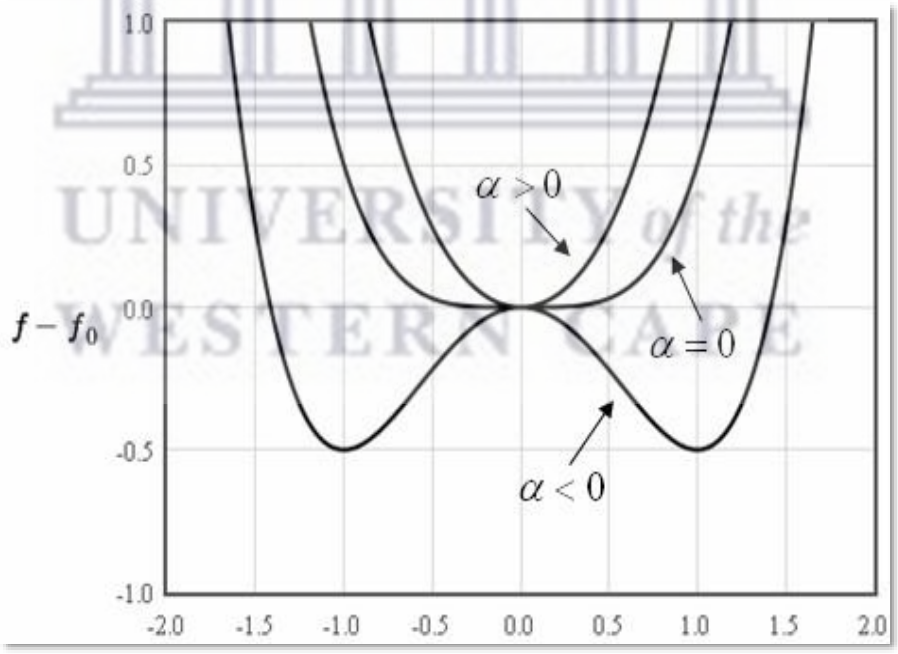

Figure 2.10: The free energy of a ferromagnet as a function of order parameter [29].

The entropy is the derivative of the free energy with respect to temperature, therefore;

$$S = -\frac{df}{dT} = S_0(T) + 2\frac{\alpha_0^2(\mathrm{T}-T_C)}{\beta} \tag{2.55}$$

For $T < Tc$

and the specific heat can be determined from the entropy using the relation [96, 98]:

$$C_v = C_{v0}(T) + \frac{2\alpha_0^2 T}{\beta} \tag{2.56}$$

The order parameter and specific heat as a function of temperature are shown in figure 2.11. To calculate the magnetic susceptibility, a term that couples the field, *B*, to the order parameter is added to the free energy,

$$f(T) = f_0(T) + \alpha_0(T - T_C).\eta^2 + \frac{1}{2}\beta\eta^4 - \eta B, \tag{2.57}$$

minimizing the free energy with respect to η, yields,

$$\frac{df}{d\eta} = 2\alpha_0(T - T_C).\eta + 2\beta\eta^3 - B = 0.$$

Since η is small, by ignoring the $2\beta\,\eta^3$ term and solve for η, yields

$$\eta = \frac{B}{2\alpha_0(T-T_C)}.$$

This formula is valid for small η (T near T_c) for temperatures above the critical temperature. The susceptibility above *Tc* is then [29]:

$$\chi = \frac{\eta}{B} = \frac{1}{2\alpha_0(T-T_C)}. \tag{2.58}$$

This is consistent with Curie-Weiss law.

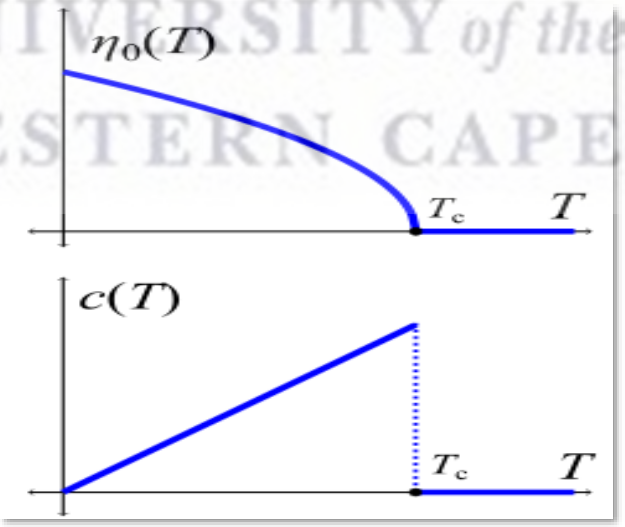

Figure 2.11: The order parameter and specific heat as a function of temperature [91].

Below the critical temperature, there is a finite magnetization, $\eta^* = \sqrt{\frac{\alpha_0(T_C - T)}{\beta}}$. The free energy can be written as a Taylor expansion around this energy, resulting [100, 101]

$$f \approx f(\eta^*) + \frac{df}{d\eta}\Big|_{\eta^*} \eta + \frac{1}{2}\frac{d^2 f}{d\eta^2}\Big|_{\eta^*} \eta^2 + \cdots . \tag{2.59}$$

Adding the field term and minimizing as before yields,

$$\frac{df}{d\eta}\Big|_{\eta^*} + \frac{d^2 f}{d\eta^2}\Big|_{\eta^*} \eta = B,$$

which results in the magnetic susceptibility,

$$\chi = \frac{\eta}{B} = \frac{1}{\frac{d^2 f}{d\eta^2}\Big|_{\eta^*}} = \frac{1}{4\alpha_0(T_C - T)} . \tag{2.60}$$

The magnetic susceptibility below *Tc* has also got a Curie-Weiss form, but *T* > *Tc*. Figure 2.12 shows Zero-field susceptibility as a function of temperature near the critical temperature.

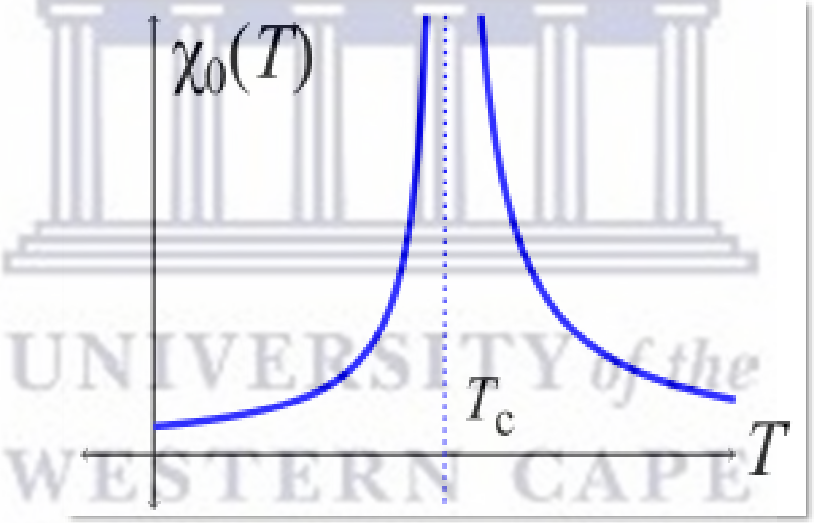

Figure 2.12: Zero-field susceptibility as a function of temperature near the critical temperature [91].

2.6.2 Heisenberg and Ising models

These models are an alternative approach to the understanding of the magnetic behaviour of materials by considering a particular microscopic model of the magnetic interactions. The

commonly studied model is the nearest neighbour Heisenberg model with a Hamiltonian given by [101, 102]:

$$\hat{H} = -\sum_{i,j} J\hat{S}_i.\hat{S}_j \ ,$$

where the constant J is the exchange integral. The spins $\hat{S}_i$ are treated as three dimensional vectors because we allow them to point in any direction in three dimensional space, but the sum can be taken over a lattice of 1, 2 or 3 dimensions. It is important to differentiate between the dimensionality "*d"* of the lattice on which the spins sit and the dimensionality "*D*" of the spins themselves which is also known as the dimensionality of the order parameter. In the case of the Heisenberg model $D = 3$ because the spins are three dimensional vectors [102].

A related model is the Ising model in which the spins are only allowed to point up or down which means we only consider the *z*-component of the spin. Therefore, the Hamiltonian of this model is given by [103]:

$$\hat{H} = -\sum_{i,j} JS_i^z.S_j^z. \tag{2.61}$$

Here, the dimensionality of the order parameter D is equal to 1. Nevertheless we could arrange these one dimensional spins on a lattice with $d = 1, 2, 3,\ldots$

2.6.3 Metamagnetism

In his early study of antiferromagnetism, Néel predicted the magnetic field conditions under which an antiferromagnet would show an abrupt decoupling between the direction of antiferromagnetism and the easy axis, known as spin-flopping or magnetization turnover. He later extended this analysis to the behaviour termed metamagnetic transition in which an antiferromagnetic array abruptly transforms to a fully aligned ferromagnetic array at a critical field [104].

Metamagnetism is defined as a transition from an antiferromagnetic to a ferromagnetic spin arrangement [105, 106]. This can occur by applying a magnetic field or by changing temperature, and may be associated with a first-order phase transition, or continuous phase transition at a critical point. When a magnetic field is applied to an antiferromagnetic material with a small anisotropy, the spin axis flops to the direction perpendicular to the magnetic field, because susceptibility, $\chi_{\perp}$, is larger than that, $\chi_{\parallel}$ in the case with the spin axis parallel to the magnetic field. This phenomenon is called spin-axis flopping. Further increase

in the magnetic field results in the magnetization increasing with a constant susceptibility given by [102]:

$$\chi = -\frac{1}{w_2}, \tag{2.62}$$

where w_2 is the molecular field coefficient acting between the A and B sublattices. The magnetization curve in this case is shown in figure 2.13. Along the linear magnetization curve, the two sublattice magnetizations rotate towards the direction of the field and reach a saturation magnetization, I_S, at a field given by [102]:

$$H_s = -w_2\, I_s. \tag{2.63}$$

When the spin axis is held in the *z*-axis by a strong anisotropy, an increasing magnetic field applied parallel to the z-axis increases the sublattice moment parallel to the field gradually, thus the susceptibility, $\chi_{\parallel}$ increases until the spin axis flops at a critical field H_c. The critical field, H_c can be found by assuming that the anisotropy energy density is to be uniaxial, thus given by [102, 103, 104]:

$$E_a = -K_u cos^2\theta, \tag{2.64}$$

where K_u is the anisotropy constant, and θ is the angle between the spin axis and the z-axis

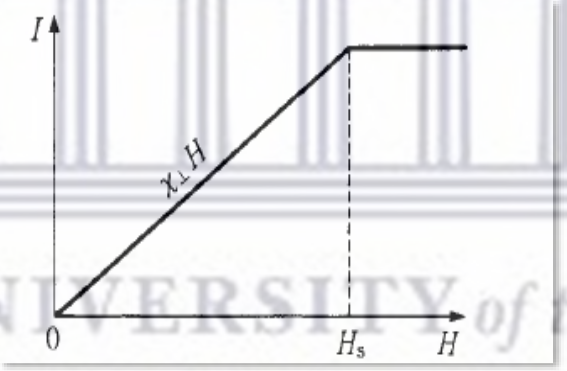

Figure 2.13: Magnetization curve of antiferromagnetic material with magnetic field applied perpendicular to the spin-axis [21].

When the spin axis makes an angle, θ, with the z-axis (figure. 2.14), the susceptibility is given by [104] :

$$\chi = \chi_{\parallel} cos^2\theta + \chi_{\perp} sin^2\theta \tag{2.65}$$

Therefore the field energy density is given by;

$$E_H = -\frac{1}{2}\chi H^2 = -\frac{1}{2}(\chi_{\parallel} cos^2\theta + \chi_{\perp} sin^2\theta)H^2. \tag{2.66}$$

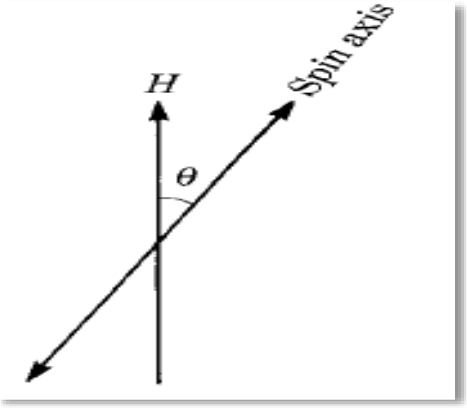

Figure 2.14: Magnetic field *H* applied at the spin axis [21].

Spin-axis flopping occurs when the total energy;

$$E = E_a + E_H \tag{2.67}$$

reaches an unstable equilibrium, that is:

$$\frac{\partial E}{\partial \theta} = \{2K_u + (\chi_{\parallel} - \chi_{\perp})H^2\} \sin\theta \cos\theta = 0, \tag{2.68}$$

$$\frac{\partial^2 E}{\partial \theta^2} = \{2K_u + (\chi_{\parallel} - \chi_{\perp})H^2\} \cos 2\theta \gtrless 0. \tag{2.69}$$

From (2.65) we have θ = 0° or 90°. The condition (2.66) lead to the critical field formula [104]:

$$H \gtrless \sqrt{\frac{2K_u}{\chi_{\perp} - \chi_{\parallel}}} = H_{C,} \tag{2.70}$$

Depending on the coefficient within braces in (2.69) $\gtrless$ 0, where H_C is the critical field for the spin-axis flopping.

2.7 Physical properties

This section discusses the standard theoretical results for the temperature-and magnetic field dependence of the electrical resistivity, heat capacity, magnetic susceptibility and magnetization investigated in this thesis.

2.7.1 Electrical resistivity

In metallic materials, conduction electrons govern transport properties. Therefore, the determination of the density of free electrons, and the energy associated with free electrons is essential to study transport properties relevant to the work done in this research. In metals,

free electrons obey the Fermi-Dirac statistics, where the Fermi surface separates the unoccupied state above the Fermi level to the occupied states below the Fermi level. As a result, the electrons near the Fermi surface are responsible for transport properties of a given material [105].

Electrical resistivity measurement is important to understand the properties of the RE intermetallic compounds, as it originates from various types of scattering processes that conduction electrons experience along their motion in the crystals. These scattering processes can be due to:

- The presence of impurities either accidental or deliberate in the samples, and imperfections in crystals such as grain boundaries.
- The temporal displacement of ions from their fixed positions due to thermally excited lattice vibrations. This effect increases largely as the temperature rises.
- Deviation from perfect magnetic order caused by spin disorder in magnetic materials as the temperature is increased towards their ordering temperatures.
- The localized magnetic moments of 4*f* or 5*f* atoms in dilute systems, especially, concentrated Kondo systems, HF materials, intermediate valence and spin fluctuation systems.
- Electrons also scatter from each other but for normal metals, this effect is very small. At higher temperatures, this effect is negligible due to the dominance of electron-phonon scattering [29].

Due to the electron-electron scattering process, the transport properties such as electrical resistivity, $\rho(T)$, thermoelectric power, $S(T)$ and thermal conductivity, $\lambda(T)$ may be described using the linearized Boltzmann Equation [105, 106], and can be expressed as follows:

$$\frac{1}{\rho(T)} = e^2 K_0; \;\; S(T) = -\frac{K_1}{|e|TK_0}; \;\; \lambda(T) = \frac{1}{T}\left(K_2 - \frac{K_1^2}{K_0}\right). \quad (2.71)$$

The integrals K_n are given by:

$$K_n = \frac{k_F^2}{3\pi^2 m}\int \varepsilon_k^n \tau(\varepsilon_k)\left(-\frac{\partial f_k}{\partial \varepsilon}\right) d\varepsilon_k, \quad (2.72)$$

where k_F is the wave vector at the Fermi surface, f_k the Fermi-Dirac distribution function, $\tau(\varepsilon_k)$ the relaxation time and ε_k the energy of the conduction electrons in a state k.

The determination of the relaxation time gives the difference in transport properties. In the case of the scattering of conduction electrons from each other, Fermi-Dirac statistics is

used to describe the transport properties. However, normal electron-electron scattering cannot contribute to the total resistivity; this results in the fact that in such a collision, charge and momentum must be conserved. However, if Umklapp processes are included, momentum can be conveyed to be the lattice as a whole, through electron-electron collision and as a result, can contribute to the total resistivity [107].

At a given set of conditions (temperature (*T*), magnetic field (*H*) and pressure (*P*)), the resistivity measures the combined effect of scattering processes in which the conduction electrons are involved. Experimentally, for the measurement of the electrical resistivity of material a charge *dQ* passes in a time *dt* through a cross – sectional *A* of a sample of length ℓ (see figure 2.15) and a simple measurement of the voltage difference *V* across the two ends of the sample gives the resistivity through the relation $\rho = A\frac{V}{(dQ/dT)l}$. Reliable values of the resistivity can be obtained if a uniform current density $j = dQ/dt$ throughout the length ℓ of the sample is set up and this can be accomplished only if $\frac{A}{\ell} \ll 1$.

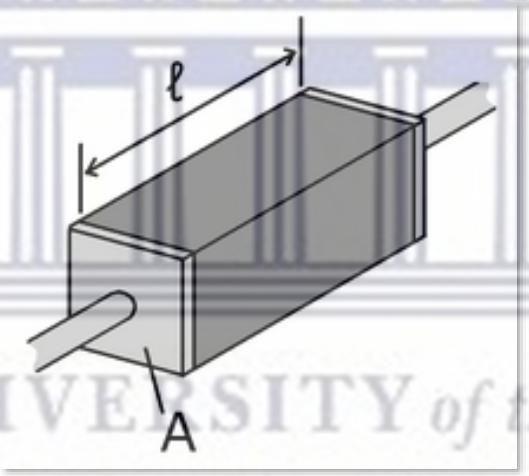

Figure 2.15: Experimental measurement of the electrical resistivity of material a charge *dQ* passes in a time *dt* through a cross-sectional are *A* of sample of length ℓ.

In the following section we will discuss the temperature variation of the electrical resistivity of nonmagnetic and magnetic materials.

2.7.1.1 Linear approximation

In general, the electrical resistivity of most materials varies with temperature. In case the change in temperature is too small, a linear approximation is typically used, given in form of:

$$\rho(T) = \rho_0[1 + \alpha(T - T_0)], \tag{2.73}$$

where α is called the temperature coefficient of the electrical resistivity, T_0 is a fixed reference temperature (usually room temperature), and ρ_0 is the resistivity at temperature T_0. The parameter α is an empirical parameter fitted from measurement data. Since the linear fitting is only an approximation, α is different for different reference temperatures. As a result of that, it is usual to specify the temperature that α was measured at with a suffix, such as α_{15}, and the relationship only holds in a range of temperatures around the reference [108]. When the temperature varies over a large temperature range, the linear approximation is inadequate and a more detailed analysis and understanding should be used.

2.7.1.2 Electrical resistivity of materials

The electrical resistivity of materials originates from the contribution of different scattering processes that an electron experiences along its motion in a crystal as mentioned earlier. If states of collisions from these different scattering processes are taken as independent in the first approximation this leads to Matthiessen's rule. This rule states that the temperature dependence of the total resistivity given by:

$$\rho\,(T) = \rho_0 + \rho_{ph}(T) + \rho_{mag}(T). \tag{2.74}$$

The contribution originating from defects or imperfections in the crystal is known as the residual resistivity, ρ_0. It shows a constant value when the temperature is lowered towards absolute zero. For normal metals, ρ_0 arises from scattering of conduction electrons by stationary imperfections or impurities. It should be noted that ρ_0 is a sensitive measure of the degree of imperfection of a sample. It is usual practice to specify the overall purity and perfection of a metal crystal by quoting the ratio of its resistivity at room temperature to that extrapolated at the lowest measure temperature (2 K in our case) as $RRR = \rho_{300K}/\rho_{2K}$. It is evident from this relation that the highest purity of the specimen corresponds to the highest value of the ratio. Overall, imperfections enhance the residual resistivity and can change the band structure, the Fermi energy, the density of states, and the effective mass and also

influence the elastic constant, which in turn modify the lattice vibration spectrum. These parameters have a significant influence on the magnitude of the *RRR* for a sample [109]. A decrease of the *RRR* magnitude in order to reduce ρ_{300K}/ρ_{2K} can be achieved by annealing the sample at a sufficiently high temperature for a period of time, generally two to four weeks.

At finite temperature, the second term ρ_{ph} describes the temperature dependence of the resistivity due to the thermal vibrations of ions around their equilibrium positions which is called electron-phonon scattering. Following the Debye model [110], the term phonon is allocated to the thermal vibrations and the highest frequency in the Brillouin zone ω_{max} can be obtained roughly from the relation $\hbar\omega_{max} \approx k\theta_D$, where θ_D is the Debye temperature also obtained from heat capacity. The procedure for calculating the scattering probability due to phonons as a function of temperature is mainly to find the number of available states into which an electron may be scattered and the number of suitable phonons available for scattering [107]. For an electron in a spherical Fermi surface, however, the density of available states is practically independent of the energy of the electron compared to the Fermi energy but depend strongly on the occupation probability [107]. The general result of ρ_{ph}(T) in this case is given by the Bloch-Grüneisen law [108]:

$$\rho\,(T) = A\,(\frac{T}{\theta_R})^n \int_0^{\theta_R/T} \frac{x^n}{(e^{x-1})(1-e^{-x})}\,dx, \tag{2.75}$$

where A is a constant that depends on the velocity of electrons at the Fermi surface, the Debye radius (the Debye radius also called the Debye length in plasma and electrolytes is a measure of a charge carrier's net electrostatic effect in solution and how far its electrostatic effect persists), and the number density of electrons in metals as well as the strength of the electron-phonon coupling. θ_R is the Debye temperature as obtained from electrical resistivity measurements and matches closely with the values of Debye temperature obtained from heat capacity measurements [109]. The parameter, *n* is an integer that depends upon the nature of interaction:

- *n* = 5 implies that the electrical resistivity is due to the scattering of electrons by phonons (as it is for simple metals).
- *n* = 3 implies that the electrical resistivity is due to *s-d* inter-band scattering (as in the case for transition metals).
- *n* = 2 implies that the electrical resistivity is due to the electron-electron interaction.

If more than one source of scattering is simultaneously present, Matthiessen's

rule must be applied, that the total phonon resistivity can be approximated by adding up several different terms, each with the appropriate value of *n*. At high temperatures and low-temperatures, Eq. 2.75 can be approximated by:

$$\rho_{\mathrm{ph}} \propto \left(\frac{T}{\theta_R}\right) \quad (T \gg \theta_R); \quad \rho_{\mathrm{ph}} \propto \left(\frac{T}{\theta_R}\right)^5 \quad (T \ll \theta_R). \tag{2.76}$$

The contribution ρ_{mag} in Eq. 2.74 relates to the scattering associated with magnetic 4*f* ions. Firstly, we may have ordered magnetism, e.g. ferromagnetic, antiferromagnetism or helical ordering as in the heavy RE metals. Perfect magnetic order well below the ordering temperature as $T \rightarrow 0$K results in no scattering of the conduction electrons. ρ_{mag} is characterized by the following traits:

i) A temperature independent behaviour above the ordering temperature T_{ord} ($T > T_{\mathrm{ord}}$: paramagnetic regime).

ii) A pronounced kink at $T = T_{\mathrm{ord}}$.

iii) A strong decrease for $T < T_{\mathrm{ord}}$ with decreasing temperature.

In the paramagnetic regime, several authors [111, 112, 113] were able to solve the conduction scattering problem. The resulting magnitude of ρ_{mag} ($T > T_{\mathrm{ord}}$), ρ_{spd} is then given by:

$$\rho_{spd} = \frac{3\pi N m^*}{2\hbar e^2 E_F} |\Gamma|^2 \left(g_J - 1\right)^2 J(J+1) \tag{2.77}$$

This equation was obtained by solving the Boltzmann equation in the relaxation time approximation. The conduction electrons were considered to be free particles with an effective mass m*, E_F is the Fermi energy, *e* is the electron charge, *N* is the number of atoms per unit volume and Γ is the measured strength of *s-f* interaction. Eq. 2.78 shows that spin disorder resistivity, ρ_{spd}, is proportional to the de Gennes factor $\left(g_J - 1\right)^2 \times J(J+1)$. ρ_{spd} provides a large additive contribution to the total resistivity as shown in figure (2.16).

At low temperature, magnetic ordering is described in terms of the concept of magnon excitations. The dispersion relation $\omega(q)$ for ferromagnetic magnons is proportional to the square of the magnon wave vector, $\omega(q) \propto q^2$, leading to a T^2 dependent resistivity [114]. In the case of antiferromagnetic magnons, $\omega(q) \propto q$ leading to a T^4 dependent resistivity. It should be noted that the influence of crystal electric field (CEF) modified the preceding expectations for the resistivity, for instance for a ferromagnet with an anisotropy gap Δ in the spin-wave dispersion, the resistivity takes the form [115]:

$$\rho_{mag} \sim T^2 \exp\left(-\frac{\Delta}{k_B T}\right)$$

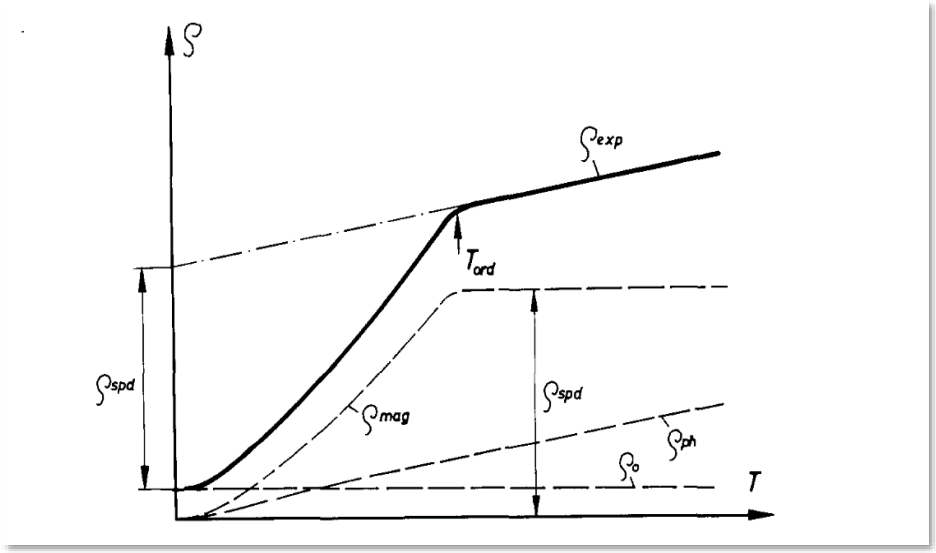

Figure 2.16 Temperature dependence of the electric resistivity of magnetic compounds with negligible of *d*-electron contribution [72].

Furthermore, at a magnetic phase transition, anomalous behaviour in ρ (T) is observed reflecting critical behaviour or in antiferromagnetic or helical magnets also super-zone boundary effects. Several theoretical results have been suggested for ρ_{mag}. Vonsovski [116, 117] was the first to recognize that an additional contribution to the resistivity would occur in ferromagnetic materials as a result of the exchange interaction between the conduction electrons and localized magnetic moments known as the s-f interaction. Subsequently, Kasuya [111] suggested a qualitative description of the temperature dependence of ρ_{mag} by representing the s-f interaction with a molecular field. He obtained an expression which describes the main features of the variation of ρ_{mag} from low temperatures to temperatures above T_C. Later on, Kasuya [114] made use of the spin wave description of the interactions to derive a low temperature expression for ρ_{mag}. Taking a spin-wave dispersion relation of the form $\omega(q) \sim q^2$, he obtained:

$$\rho_{mag}(T) = \frac{\pi^2}{8}\frac{Vm^*}{Ne^2}\frac{J^2(0)}{\hbar E_F}\left(g_J - 1\right)^2 J\left(\frac{k_B T}{k_F J(0)}\right)^2 \qquad (2.78)$$

where J (0) ≡ Γ is a parameter which describes the strength of the s-f interaction, V is the volume of the crystal and the other parameters have been defined earlier.

In the case of antiferromagnetic materials, a T^4 dependence of ρ_{mag} at low temperature was obtained [118, 119, 120, 121] using the antiferromagnetic magnon spectrum dispersion $\omega(q) \sim q$. Another calculation of the electrical resistivity of

antiferromagnetic materials at low temperatures was suggested by Yamada and Takada [122]. They made use of the variational approach to the Boltzmann equation. The resulting temperature dependence of ρ_{mag} can be written as follows:

$$\rho_M(T) = \begin{cases} \sim T^5, & \text{for } \Delta \ll T \ll T_N \\ \sim T exp\left(-\frac{\sqrt{T_N \Delta}}{T}\right), & \text{for } T \ll T_N, \Delta' \end{cases} \quad (2.79)$$

where Δ is the anisotropy energy of the spin system.

2.7.2 Magnetization and magnetic susceptibility

The magnetization (*M*) of a material is defined as the magnetic moments per unit volume. Hence $n = \frac{N}{N_A} = \frac{m}{M}$

$$M = \frac{N\mu}{V}$$

where *V* the volume of the sample. The magnetization can also be per unit mass or per mole defined by:

$$\sigma = \frac{M}{\rho} = \frac{N_A \mu}{M_o}$$

Where ρ is density of the sample, M_o is molar mass and N_A is the Avogadro's number. The magnetization is usually measured as a function of temperature (*T*) and magnetic field (*H*).

Experimentally, the magnetization curve as a function of the applied magnetic field for a ferromagnet exhibits a hysteresis loop and saturates with an increasing magnetic field. The magnetization may remain present in the system even when the magnetic field is reduced to zero. This magnetization is known as remanence magnetization M_r.

The temperature dependence of the magnetization of a system of N moments per unit volume is given by [32]:

$$M = N \frac{\sum_{m_j=-J}^{+J} -g_J \mu_B B m_j exp\left[-\frac{g_J \mu_B m_j}{k_B T}\right]}{\sum_{m_j=-J}^{+J} exp\left[-\frac{g_J \mu_B m_j}{k_B T}\right]}. \quad (2.80)$$

To obtain an expression of the magnetization it is convenient to express it in terms of the partition function, *Z* given by:

$$Z = \sum_{m_j=-J}^{+J} exp\left[-\frac{g_J \mu_B m_j}{k_B T}\right]. \quad (2.81)$$

Therefore, the magnetization can be deduced from:

$$M = -\frac{Nk_B T^2}{B}\frac{1}{Z}\left(\frac{\partial Z}{\partial T}\right)_B = -\frac{Nk_B T^2}{B}\left(\frac{\partial \ln Z}{\partial T}\right)_B \quad (2.82)$$

If we let $y = \frac{g_J \mu_B B J}{k_B T}$, we find:

$$M = M_s B_J(y)$$

where the saturation magnetization is:

$$M_s = N g_J \mu_B J.$$

The function $B_J(y)$ is known as the Brillouin function which can be shown to be:

$$B_J(y) = \frac{2J+1}{2J}\coth\left[\left(\frac{2J+1}{2J}\right)y\right] - \frac{1}{2J}\coth\left(\frac{y}{2J}\right). \quad (2.83)$$

This function is plotted in figure 2.17 for various values of J [123].

The behaviour of the magnetization is similar to that of the Brillouin function which increases linearly at low fields and tends to saturate at high fields, which correspond to the maximum possible alignment of the dipole moments with the field.

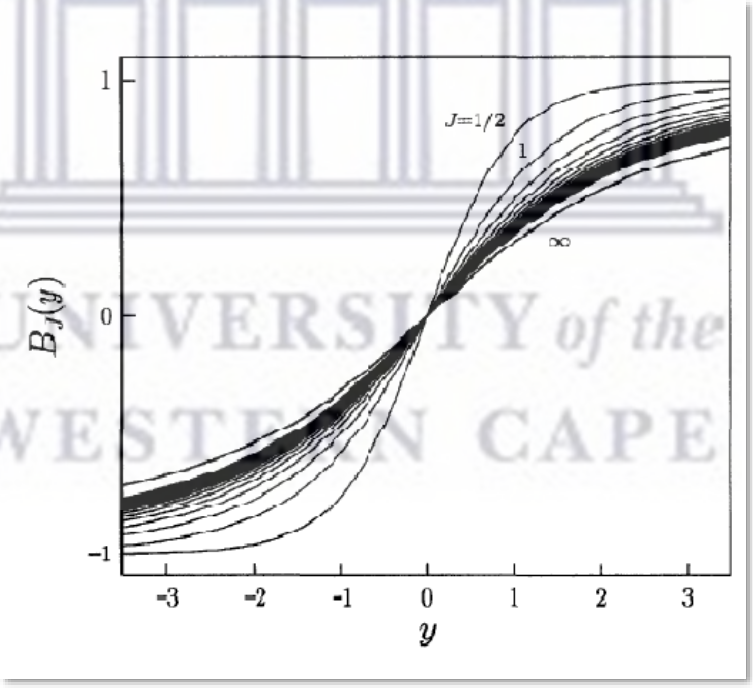

Figure 2.17: The magnetization of paramagnet with magnetic quantum number J follows a Brillouin function, $B_J(y)$, which is plotted here for different values of J. The values of J are $\frac{1}{2}, 1, \frac{3}{2}, 2, \frac{5}{2}, \ldots and\ J = \infty$ [123].

A typical value of y can be estimated as follows: for $J = 1/2$, $g_J = 2$ with $B = 1$ T, the value y is $\sim 2 \times 10^{-3}$ at room temperature. Thus, except at very low temperature and / or very large magnetic field, the experimental situation will correspond to $y << 1$. In this situation $B_J(y)$ can be approximated using the Maclaurin expression of coth (y) in the form:

$$B_J(y) = \frac{(J+1)}{3J} y + O(y^3). \tag{2.84}$$

Hence for low magnetic field the magnetization can be written as:

$$M(B) = \frac{Ng^2\mu_B^2 J(J+1)}{3k_B T} B; \tag{2.85}$$

The magnetic susceptibility can be deduce to be:

$$\chi = \frac{M}{H} = \frac{\mu_0 M}{B} = \frac{N\mu_0\mu_{eff}^2}{3k_B T} = \frac{C}{T}. \tag{2.86}$$

This is the classical Curie law. μ_0 is the permeability of the free space or vacuum, μ_{eff} is the effective magnetic moment defined in section 2.3.3 and C is the Curie constant. It should be noted that for ferromagnetic and antiferromagnetic materials, there is some spontaneous interaction between the neighbouring magnetic moments at low temperature. As a result of that the Curie's law is changed to Curie-Weiss relationship (see section 2.3.3).

2.7.3 Heat capacity

The heat capacity of a material is the amount of heat needed to raise its temperature per degree temperature increase [124] defined as:

$$C = \frac{Q}{\Delta T}. \tag{2.87}$$

Q is the amount of heat needed to raise a material's temperature to ΔT. It also depends on whether we are doing work on the material. Therefore, using the first law of thermodynamics, Eq.2.87 can be written as:

$$C = \frac{\Delta U - W}{\Delta T}. \tag{2.88}$$

In practice, there are two types of circumstances that are most likely to occur. The first one is the case when $W = 0$ when no work is being done on the system. Usually this means that

the system's volume is constant. So the heat capacity for a particular case is called heat capacity at constant volume, denote C_V and given by:

$$C_v = \left(\frac{\Delta U}{\Delta T}\right)_v = \left(\frac{\partial U}{\partial T}\right)_v \quad (2.89)$$

where ΔU the change in the internal energy of a closed system. The second case is when the work is done to the surroundings, so we need to add additional heat to compensate for the energy lost as work. If the pressure surrounding the materials happens to be constant, we refer to the heat needed per degree as C_p known as the heat capacity at constant pressure [124] which can be expressed as:

$$C_p = \left(\frac{\Delta U-(-P\Delta V)}{\Delta T}\right)_p = \left(\frac{\partial U}{\partial T}\right)_p + P\left(\frac{\partial V}{\partial T}\right)_p. \quad (2.90)$$

In the present study, the specific heat capacity was measured at constant pressure and the term C_p will be used throughout the thesis. At high temperature (near room temperature), the specific heat of materials is explained by the classical concept of degrees of freedom. For a solid, there are six degrees of freedom per atom, so the heat capacity per mole should be $\frac{6}{2}R = 3R = 29.9$ mJ/(mole/K). This general result called the rule of Dulong and Petit [124].

The heat capacity of metals results from various contributions. These are the lattice or phonon contribution C_{ph}, the electronic contribution C_e, the magnetic contribution C_{mag}, the nuclei contribution C_{nucl} and the Schottky term C_{sch}. Therefore, the total heat capacity is given by the sum of all the contributions and can be written as:

$$C_{tot}(T) = C_{ph}(T) + C_e(T) + C_{mag}(T) + C_{nucl}(T) + C_{sch}(T) \quad (2.92)$$

2.7.3.1 Phonon heat capacity

The calculation of the phonon heat capacity of solids falls into 2 parts: (i) evaluation of the contribution of a single mode known as the Einstein model and (ii) summation over the frequency distribution of the modes known as the Debye model [124].

(i) Einstein model

In this model the atoms are treated as independent oscillators, but their energies is given by quantum mechanics in terms of:

$$E_n = \left(n + \frac{1}{2}\right)\hbar\omega. \tag{2.92}$$

The energy levels are evenly spaced and one can define a quantum of energy $\epsilon = \hbar\omega$.

The phonon heat capacity obtained from the derivative of the average energy with respect to the temperature can be written as [124]:

$$C_{ph,E}(T) = \frac{d\bar{\varepsilon}}{dT} = 3R\left(\frac{\Theta}{T}\right)^2 \frac{e^{\frac{\Theta}{T}}}{(e^{\frac{\Theta}{T}}-1)^2}, \tag{2.93}$$

Where $\Theta = \frac{\hbar\omega_E}{k_B}$.

The temperature Θ is an adjustable parameter chosen to produce the best fit to the measured values over the whole temperature range. The Einstein frequency can be deduced from Θ. At high temperature, T >> Θ, $C_{ph,E}$ tends to a constant given by: $C_{ph,E} = 3R = 3N_A k_B$ which is the classical result known as the Dulong and Petit value. In the low temperature range, T << Θ, the exponent is much larger than unity, and $C_{ph,E}$ become:

$$C_{ph,E}(T) = 3R\left(\frac{\Theta}{T}\right)^2 e^{-\frac{\Theta}{T}} \approx B(T)e^{-\frac{\Theta}{T}}. \tag{2.94}$$

The $B(T)$ is relatively insensitive to temperature. Because of the exponent, $C_{ph,E}$ approaches zero very rapidly exponentially and vanishes at $T = 0$ K. Although $C_{ph,E} \rightarrow 0$ at $T \rightarrow 0$ K agrees with the experiment, but the manner in which this is approaches zero is not in agreement with experimental results. $C_{ph,E}$ in this model approach zero exponentially, while experiments show that $C_{ph,E}$ approaches zero as T^3. Einstein model is in good agreement with experiment over most of the temperature range, but incorrect at very low temperatures. Correction is given by the Debye model [124].

(ii) Debye model

The more exact solution of the phonon heat capacity is given by the Debye theory. According to this theory, the crystal is considered as a system of coupled harmonic

oscillators with energy given by the Planck's formula [124]:

$$U(\omega,T)=\frac{\hbar\omega}{e^{\hbar\omega/k_BT}-1}, \tag{2.95}$$

where ω is the frequency of the harmonic oscillator. The total energy of vibrations for all harmonic oscillators is now given by:

$$E=\int \bar{\varepsilon}(\omega)\,\mathrm{g}(\omega)d\omega, \tag{2.96}$$

where the integration is taken over all the allowed frequencies. $\mathrm{g}(\omega)d\omega$ is the number of modes in the range $(\omega,\omega+d\omega)$ and the energy of each of these modes is $<\varepsilon>$.

The specific heat found by differentiating E with respect to T is:

$$C_{ph,D}=\frac{3V}{2\pi^2v_s^3}\frac{\hbar^2}{k_BT^2}\int_0^{\omega_D}\frac{\omega^4e^{\hbar\omega/k_BT}}{(e^{\hbar\omega/k_BT}-1)^2}, \tag{2.97}$$

where v_s is the velocity of sound which is related to the Debye frequency: $\omega_D=v_s(6\pi^2n)^{\frac{1}{3}}$. We can simplify the appearance of C_V by changing to dimensionless variable: $x=\frac{\hbar\omega}{k_BT}$ and define the Debye temperature: $\theta_D=\frac{\hbar\omega_D}{k_B}$. The specific heat is then given by:

$$C_{ph,D}=9R\left(\frac{T}{\theta_D}\right)^3\int_0^{\theta_D/T}\frac{x^4e^x}{(e^x-1)^2}dx. \tag{2.98}$$

In the low temperature limit ($T\ll\theta_D$) the upper limit of the integral approaches infinity. The ensuing integral may be evaluated analytically to give $\int_0^{\infty}\frac{x^4e^x}{(e^x-1)^2}dx=\frac{4\pi^2}{15}$ hence

$$C_{ph,D}(T)=\frac{12\pi^2}{5}R\left(\frac{T}{\theta_D}\right)^3. \tag{2.99}$$

This relation shows a T^3 – dependence as predicted by the experimental results.

In a few cases, the phonon contribution is also described by both the Einstein and Debye models. The resulting phonon contribution described by the two models can be approximated by the formula [124]:

$$C_{ph}(T)=kC_{ph,D}(T)+(1+k)C_{ph,E}(T) \tag{2.100}$$

where the parameter k is a mutual weight of phonon modes of two models.

Experimentally, the results of phonon heat capacity of rare earth compounds are obtained from their La, Y or Lu non-magnetic based counterparts.

2.7.3.2 Electronic heat capacity

The electronic heat capacity is dominant at low temperatures and classified if the

material is in the heavy fermion state or is a normal metal. At high temperature, this contribution is very small. In metals, only electrons close to the Fermi level, within the approximate range $k_B T$ of the energy, contribute to the heat capacity. Assuming that the density of state $N(E)$ is a slowly varying function with E near the Fermi energy, $N(E) = N(E_F)$, the electronic heat capacity can be expressed in the form [124]:

$$C_e(T) = \frac{2}{3}\pi^2 k_B^2 N(E_F) T = \gamma T; \tag{2.101}$$

with $N(E_F)$ given by:

$$N(E_F) = \frac{m^* k_F}{2\pi^2 \hbar^3}). \tag{2.102}$$

γ denotes the electronic or Sommerfeld coefficient and it is proportional to the density of states at the Fermi level. At low temperature for normal metals, the total heat capacity can be approximated by the formula:

$$C_{tot}(T) = \gamma T + \beta T^3. \tag{2.103}$$

The second term represents the Debye heat capacity with β a parameter that characterizes the lattice vibrations, given by:

$$\beta = \frac{12\pi^2}{5}\frac{R}{\theta^3}\ . \tag{2.104}$$

It should be mentioned that the coefficient γ of typical heavy fermion materials is temperature dependent and becomes more enhanced as the temperature decreases. This indicates that the effective mass of the conduction electrons become more enhanced [109]. In the case of magnetic materials, in addition to lattice and electronic contributions, the different magnetic excitations can also contribute to the total heat capacity. The thermal excitation of spin waves results in such magnetic heat capacity, C_{mag}. Quantized spin waves are called magnons. According to the magnetic order, there are two types of magnons viz. FM and AFM magnons (see 2.4.4: spin-wave theory).

Another important quantity that is related to the magnetic heat capacity is the magnetic entropy (S_{mag}). This quantity provides information about the degeneracy of the system and is defined by integrating the magnetic heat capacity to give [124]:

$$S_{mag}(T) = \int_0^T \frac{C_{mag}(T')}{T'}\, dT'. \tag{2.105}$$

Due to the weakly-interacting local magnetic moments between the RE atoms, each ion has an intrinsic total angular momentum J which results in the ground state being $(2J+1)$ fold degenerate. With an increase in temperature all these states can be populated and

the magnetic entropy saturates to a constant value given by:

$$S_{\mathrm{mag}} = R\ln(2J+1). \tag{2.106}$$

2.7.3.2 Schottky heat capacity

It should be noted that the temperature at which the entropy saturates gives information about the crystal electric fields (CEFs). The CEF leads to the splitting of the ground state into different discrete energy levels and the occupation of these levels gives rise to an additional contribution to the total heat capacity known as the Schottky heat capacity, C_{Sch}. C_{Sch} has entropy contributions coming from magnetic ordering temperature at T_{N} or T_{C} as well as from splitting of the ground multiplet under the presence of a crystal field. For instance, in the case of two energy levels ε_0 and ε_1 with a degeneracies g_0 and g_1, respectively, the entropy is defined as [124]:

$$S_{sch}(T) = R\left(\frac{\Delta}{T}\right)^2\left(\frac{g_0}{g_1}\right)\frac{exp\left(\frac{\Delta}{T}\right)}{\left(1+\left(\frac{g_0}{g_1}\right)exp\left(\frac{\Delta}{T}\right)\right)^2}\ , \tag{2.107}$$

where $\Delta = \frac{\varepsilon_1}{k_B}$ is the energy separation between the two energy levels and R is the gas constant. The Schottky term is characterized by a broad maximum at high temperature known as the Schottky – type anomaly due to CEF effect.

2.7.3.4 Nuclear heat capacity

The final contribution is the nuclear heat capacity, C_{nucl} which arise from the RE nuclear Schottky anomaly and enhanced due to the hyperfine interaction. This contribution takes the form [32]:

$$\frac{C_{\mathrm{nucl}}(T)}{R} = \frac{I(I+1)g_{\mathrm{N}}^2\mu_{\mathrm{N}}^2(1+K^2)}{3k_{\mathrm{B}}^2}\left(\frac{B_{\mathrm{eff}}}{T}\right)^2. \tag{2.108}$$

In this equation B_{eff} represents the effective magnetic field acting on the RE nuclei, I is the nuclear spin, g_{N} is the gyromagnetic coefficient of the RE atom, μ_{N} is the nuclear magnetic moment of the RE atom and K is the enhancement factor proportional to the magnetic susceptibility which also expresses the hyperfine interaction. This contribution is characterized by an increase in the total heat capacity with decreasing temperature well below the ordering temperature, T_{C} or T_{N}.

Chapter 3

Experimental procedures and facilities

3.1 Introduction

This chapter illustrates the experimental procedures used from sample preparation and characterization right through to the physical properties measurements. We furthermore give a description of all equipment used for the study that includes synthesis, characterization and the physical properties measurements. The method used for sample synthesis rely on arc- melting of high-purity elements to obtain polycrystalline specimens of the designated stoichiometry and compound formulae. Heat treatment was performed for some systems. The method used for sample characterization relied on a Bruker D8 advance diffractometer, scanning electron microscope (SEM) and energy dispersive spectroscopy (EDS). Transport and magnetic properties as well as heat capacity measurements were performed using the physical property measurement system (PPMS) as well as the magnetic property measurement system (MPMS), both supplied by Quantum Design. The motivation behind the use of Quantum Design PPMS and MPMS is that, they represent a unique concept in laboratory equipment that consist of an open architecture, variable temperature and magnetic field systems designed to perform a variety of automated measurements. Furthermore, using the PPMS and MPMS with its many purpose-built measurement options, allowed for easy adaptation to our own experiments.

3.2 Sample synthetization

Polycrystalline samples of $CeCu(Ge_{1-x}Sn_x)$, $(Ce_{1-x}Nd_x)CuGe$ and $Dy(Cu_{1-x}Pd_x)In$ alloys series were prepared using the arc-melting furnace in figure 3.1. All the alloy series were synthesized from high purity elements bought from Alfa Aesar company. The purity of the elements is given in Table 3.1. The RE elements were firstly etched in a 50:50 nitric acid: deionized water solution. This was done to ensure that the thin alkaline oxide layer is removed from the surfaces of the elements. The etched elements were

then rinsed and dried in acetone.

Figure 3.1: Arc-furnace melting chamber at the University of the Western Cape.

Table 3.1: Purity of the starting elements in *wt.*%.

Element	Purity (*wt.* %).
Ce	99.98
Nd	99.99
Ge	99.9999
Dy	99.99
Y	99.99
Cu	99.995
Pd	99.99
In	99.999
Sn	99.999

Stoichiometric quantities of all elements were carefully weighed to the accuracy of 2×10^{-4} g using a microbalance (OHAUS crop. Pine Brook, NJ USA) for a starting sample mass of 2.0 g. All polycrystalline samples investigated, were prepared by arc-melting the constituent elements on a water-cooled copper plate in the arc-furnace in a titanium gettered high purity argon atmosphere (50 kPa below atmospheric pressure) at the Department of Physics and Astronomy, University of the Western Cape. The sample was melted three to four times to ensure good homogeneity. The weight losses after final melting were usually less than 1%. The resulting oblate shaped ingots had a typical mass of 2 to 3g. Measurements were performed on as-cast and annealed samples.

3.3 Diamond blade technique

Cutting the sample using this technique starts with the gluing of the sample onto the dressing stick using Beuhler thermoplastic cement. This is done by firstly warming both the dressing stick and the glue on the hot plate before placing the sample onto the stick. As soon as the glue melts the sample is carefully placed on the melt and allowed to cool before taking it onto the diamond cutter. It is important that a large fraction of the sample is covered with thermoplastic cement to avoid it from dropping during cutting. A small wedge which is used for powder X-ray diffraction (XRD) is firstly cut from the side of the sample. It is of utmost importance that every sample be proven to be structurally homogeneous before the other pieces for physical properties measurements are cut. The annealing process were performed in all compounds before proceeding with other measurements. The XRD piece is firstly cleaned by soaking it in acetone to dissolve all thermoplastic cement and other impurities. The samples for X-ray diffraction, electrical resistivity, magnetic susceptibility, magnetization and heat capacity measurements were cut using a Micracut 125 low speed precision cutter with a diamond coated blade of thickness 0.381 mm as show in figure. 3.2. The samples for resistivity measurement were cut in the form of a parallelepiped rectangle with typical dimension $1\times1\times6$ mm^3 and the samples for magnetic susceptibility, magnetization and heat capacity were cut in the form of a cube with a typical dimension of $1\times1\times1$ mm^3.

These dimensions were measured using a travelling microscope to an accuracy of ±5 μm with geometrical uncertainty of $\frac{A}{l} \pm 2\%$ where A is the cross-sectional area and l is the length of the resistivity sample. All the samples for resistivity, magnetic

property and heat capacity were cut out of the center of the ingot in order to avoid the bottom surface and the top layer where the stress in the material as evidenced by hairline cracks was sometimes found. Parts of the ingot were used for X-ray diffraction, SEM and EDS measurements.

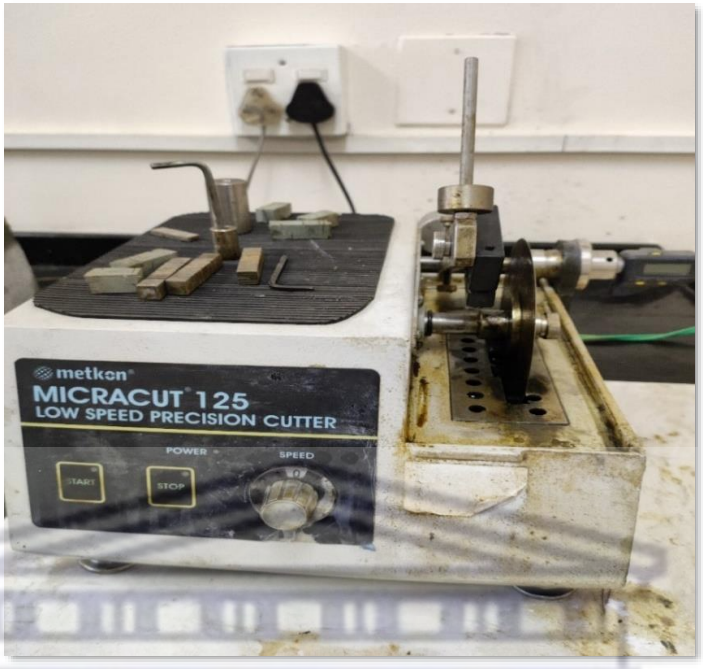

Figure 3.2: Micracut 125 low speed precision cutter with a diamond coated blade of thickness 0.381 mm at the University of the Western Cape.

3.4 Annealing procedure

Heat treatment is done to equalize small shifts in chemical homogeneity of the compound and to eliminate possible parasitic phases that co-melt with the desired phase during the arc melting process. For the heat treatment, the samples were wrapped in tantalum foil (purity of 99.99 wt-%) and sealed off in an evacuated quartz tube. A neck (constriction in the tube) was formed on the tube to make the flushing with argon and the sealing afterwards, quicker. The tube was subsequently attached to the argon gas supply which was linked to diffusion pump system. The tube was then flushed many times with high-purity argon gas (99.999 %) to remove all other gases in the ampoule. The tube was sealed by melting the neck with oxyacetylene flame and the finished tube was placed into a tube furnace and samples were annealed at 850 °C for 15 days.

3.5 Sample characterization

3.3.1 Powder X-ray diffraction

All the samples thus prepared for this project were characterized by X-ray powder diffraction using a Bruker D8 advance diffractometer with a CuKα radiation (λ = 1.540698 Å) located at iThemba LABS, Cape Town (figure 3.3). A small piece of each prepared ingot was finely ground in an agate mortar and spread out in a hollow rectangular sample holder and carefully inserted into the sample stage of the diffractometer so that they can be irradiated by the X-ray diffractometer figure 3.3. Measurements were performed by scanning through a 2 theta (2θ) angle between 10° and 80° in steps of approximately 0.034°, which correspond to the range where reflections from the planes are expected for most of the *d*-spacings found in intermetallic compounds. A potential difference of 40 kV was applied between the filament and the anode target. The data was collected using a computer supplied with EVA software from Bruker, equipped with the diffractometer. The room temperature X-ray diffraction pattern was refined using the cell and intensity least square (CAILS) Pawley and the full profile Rietveld refinement programme both from TOPAS ACADEMIC software.

Figure 3.3: The Bruker D8 Advance diffractometer at iThemba LABS.

3.3.1.a Cell and Intensity Least Square (CAILS)-Pawley and Rietveld refinement method

The CAILS-Pawley refinement method is used to get lattice parameters of the crystal structure. In this refinement only the cell parameters, peak width parameters and integrated intensities are refined. This refinement method is independent of the atomic position parameters (or structural model) and only depends on the space group symmetry. Furthermore, the intensities of all different peaks in the CAILS method vary independently [125, 126].

The Rietveld refinement method also depends on the space group symmetry. The difference in their level of complexity and application. Rietveld is a powerful tool for detailed crystal structure determination and quantitative phase analysis, while CAILS-Pawley is a faster, profile-based method that is particularly useful for time-resolved or in situ studies and can handle complex structures with simpler parameterization [126, 127].

3.3.1.b Criteria of fit

The Rietveld refinement method uses selected parameters to considerably reduce the difference between experimental pattern (observed data, y_o) and a model based on the hypothesized crystal structure and instrumental parameters (calculated pattern, y_c). The use of full profile fitting and crystallographic constraints (lattice parameters and space groups to constrain peak positions, crystal structure to constrain peak intensities) are carefully considered. The Rietveld refinement analysis the whole diffraction pattern by including the profile fitting, the refinement of the structure parameters from diffraction data (lattice parameters, atomic positions and site occupancies). TOPAS ACADEMIC is a graphics based profile analysis program built around a non-linear least squares fit. Its main focus is in crystallography, solid state chemistry and optimization. At the core of this program is its superb minimization routines wrapped by a computer algebra system [128, 129]. The quality of the fit is defined by the refine agreement indices of the sample defined as follows [128]:

- *R* -pattern (R_p) and *R*'-pattern background corrected (R'_P) which is an indicator of the goodness of fit (GOF) given by:

$$R_p = \frac{\sum|Y_{o,m}-Y_{c,m}|}{\sum|Y_{o,m}|}\ ,\ R'_P = \frac{\sum|Y_{o,m}-Y_{c,m}|}{\sum|Y_{o,m}-GKg_m|}. \quad (3.1)$$

- *R*-weighted pattern (R_{wp}) and *R'*-weighted pattern background corrected (R'_{wp}): it is a measure of the *GOF*, calculated point by point and weighted by a standard deviation of the data, given by:

$$R_{\text{wp}} = \sqrt{\frac{\sum w_m (Y_{o,m} - Y_{c,m})^2}{\sum w_m Y_{o,m}^2}}, \quad R'_{\text{wp}} = \sqrt{\frac{\sum w_m (Y_{o,m} - Y_{c,m})^2}{\sum w_m (Y_{o,m} - BKg_m)^2}}, \quad (3.2)$$

- *R*-expected (R_{exp}) and *R*'-expected background corrected (R'_{wp}): It is an expected value of R_{wp}, given by:

$$R_{\text{exp}} = \sqrt{\frac{\sum M - P}{\sum w_m Y_{o,m}^2}}, \quad R'_{\text{exp}} = \sqrt{\frac{\sum M - P}{\sum w_m (Y_{o,m} - BKg_m)^2}}; \quad (3.3)$$

- The goodness of fit (GOF) based on statistics is expressed by:

$$GOF = \chi^2 = \frac{R_{\text{wp}}}{R_{\text{exp}}} \quad (3.4)$$

- *R*-Bragg (R_B or intensity factor): It is a measure of the quality of the structural model related to the peak shape and not the area. It is given by:

$$R_B = \frac{\sum |I_{o,k} - I_{c,k}|}{\sum |I_{o,k}|} \quad (3.5)$$

- The Durbin-Watson parameter (*DW*): It is a measure of the fit model, given by [130, 131]:

$$DW = \frac{\sum_{m=2}^{M} (\Delta Y_m - \Delta Y_{m-1})}{\sum_{m=1}^{M} (\Delta Y_m)^2}, \quad \Delta Y_m = Y_{o,m} - Y_{c,m}\,. \quad (3.6)$$

In these relations, $Y_{o,m}$ and $Y_{c,m}$ are the observed and calculated data, respectively at data point *m*, Bkg_m is the background at data point *m*, *M* and *P* are respectively the number of data points and parameters, w_m the weighting given to data point *m*, $I_{o,k}$ and $I_{c,k}$ are the observed and calculated intensities of the k^{th} reflection.

3.3.2 Energy Dispersive Spectroscopy (EDS)

For further characterization, electron micro-probe analysis was performed to obtain the chemical sample of the parent compounds of the alloy systems in this study. The energy dispersive spectroscopy analysis has been performed using Field Emission Gun Scanning Electron Microscope (FEGSEM) Auriga (see figure 3.4). Generally, the EDS analysis involves the generation of an X-ray spectrum from the entire scan area

of the scanning electron microscopy. To perform this, the samples were all mounted on a sample holder aluminum stub with carbon sticky tapes and were inserted in FEGSEM. The carbon tapes help the sample to stick well on the stub. They also prevent the sample from charging up and reducing the effective electron energy thus enhancing the secondary electron yield during the analysis. In the Detector Secondary Electron (DSE) the samples were magnified differently in the range 100 to 250 times, the Electron High Tension (EHT) was set at 20 kV and the working distance was 9.2 mm. Images were analyzed and recorded using an energy dispersive spectroscopy software Aztec Energy. The SEM images were taken by either backscattering electron (BSE) or secondary electron (SE) modes for different zooming scales.

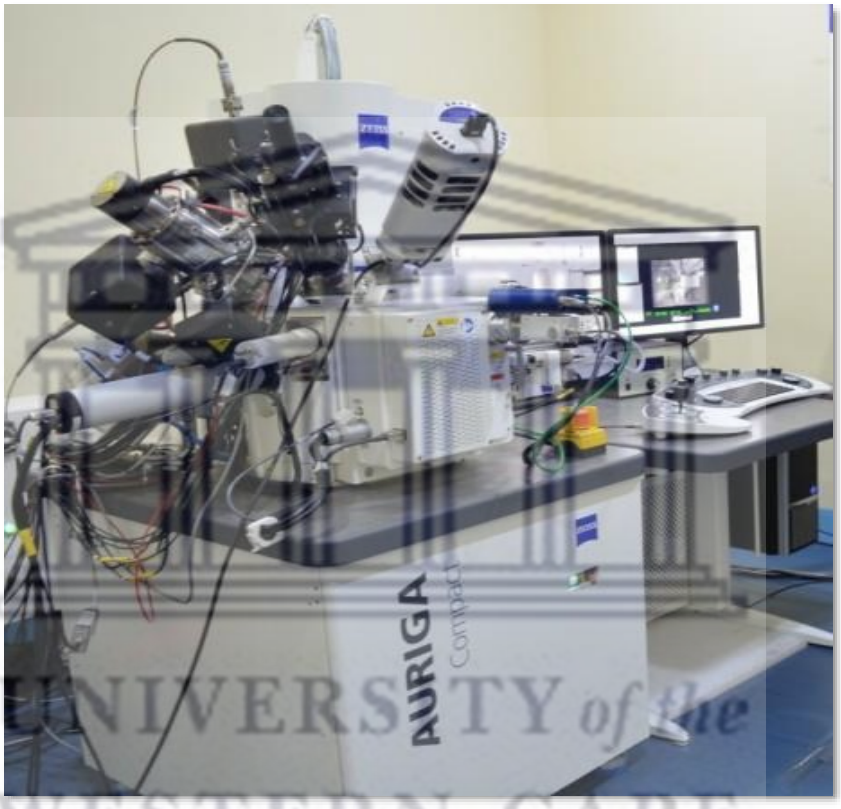

Figure 3.4: Photograph of Field Emission Gun Scanning Electron Microscope, at the Electron Microscope Unit (EMU), University of the Western Cape.

3.4 Physical Property Measurement System (PPMS)

PPMS is an open architecture, variable temperature-field system, designed to perform a variety of automated measurements, including resistivity, heat capacity, ac/dc magnetometry, and thermal transport. In this work electrical resistivity and heat capacity measurements were performed using a commercial device Quantum Design Physical

Property Measurement System (PPMS), San Diego (USA) shown in figures 3.5 and 3.6. The measured temperature and magnetic field ranges are 400 K to 1.8 K and 0 T to 9 T. Further, low temperatures down to 50 mK can be achieved by inserting the Helium-3 (^{3}He) cryogenic system also from Quantum Design. In this equipment, the magnet is in axial solenoid configuration, with the center of the magnet corresponding to the sample position. However, the PPMS can also allow the measurement of magnetic properties (MPMS) by using the vibrating sample magnetometer (VSM) techniques [132, 133]. In these techniques, the magnetic field and ramp rate are determined by the magnetic power supply. The Magnetic properties measurements (Magnetic susceptibility and magnetization) in this study were performed using a Superconducting Quantum Interference Device (SQUID) magnetometer in a Quantum Design Magnetic Property Measurement System (QD MPMS-5), San Diego (USA) (see figure 3.7).

Figure 3.5: A Commercial Device Quantum Design Physical Property Measurement System (QD PPMS), San Diego (USA), University of Johannesburg, Department of Physics.

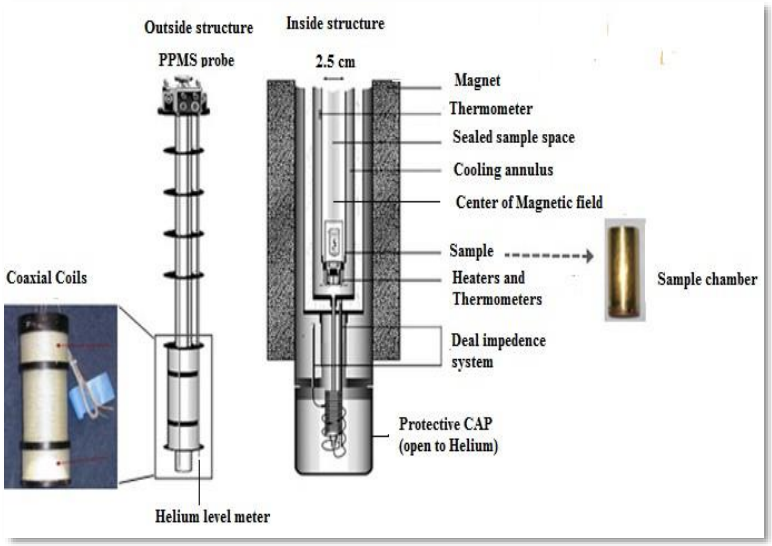

Figure 3.6: Cross section of Physical Properties Measurements System (PPMS).

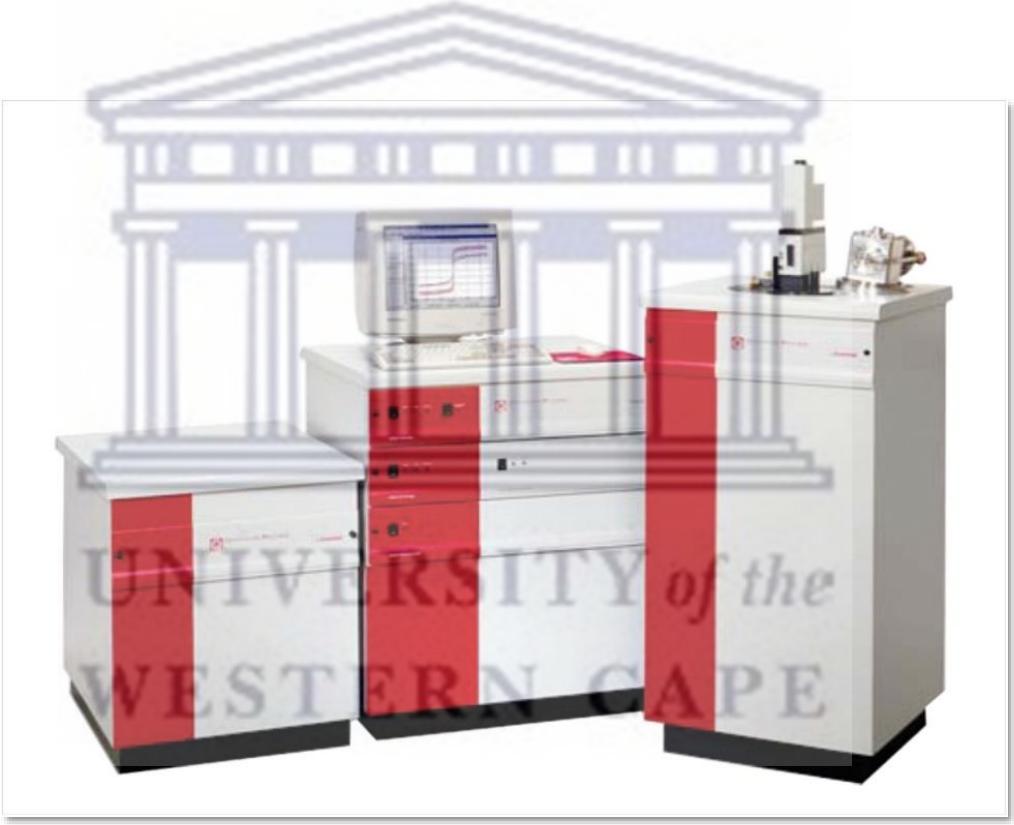

Figure 3.7: A Superconducting Quantum Interference Device (SQUID) magnetometer in a Quantum Design Magnetic Property Measurement System (QD MPMS-5), San Diego (USA), University of Johannesburg, Department of Physics.

3.4.1 Electrical resistivity

Electrical resistivity measurements were done using the PPMS, by standard four probe technique over the temperature range 1.8 to 300 K on a bar shape specimen of a typical dimension 1×1×6 mm^3. The bar sample was mounted on an AC resistivity puck after the surface of the puck was firstly cleaned with ethanol then the sample was attached to the kapton tape by G.E. (general electric) vanish glue (C5-101 from Oxford instrument). This process was done to electrically insulate the samples from the puck, the four point probe technique as presented in figure 3.8 was used, which were made from 50 μm gold wire and were spot welded on the sample corresponding to the following channels I^+, V^+, V^- and I^-. In this technique, 2 current contacts attached at the side of the sample pass the current through the sample, while 2 voltage contacts were attached at the surface of the sample, measuring the potential difference drop across a section of the sample. The G.E. vanish glue was used because of its excellent adhesive properties at very low temperature and its good thermal conductivity and electrical insulating properties.

In general, the PPMS eliminates the thermoelectric effects that arise from the current and voltage leads by using a fast current reversal technique in which the current polarity in the sample continuously flips, and measuring the resistivity as the average of two readings of positive and negative currents. Indeed, the PPMS measures electric resistance as a function of temperature of the sample R (T) and then evaluates the resistivity ρ (T) using the geometry of the sample such as the cross sectional area and the voltage leads separation between V^+ and V^- (l). The value of the input current and the sample geometry during each measurement were set to I = 4500 μA, cross sectional area A = 1 mm^2 and the length, l = 1 mm. The PPMS software measure $\Delta V_{sample} = RI = I\frac{l\rho}{A}$ to compute the resistance and the resistivity of the sample [132].

The actual value of the resistivity of sample is to manually calculate using the measured cross sectional area of the sample and the voltage contact length. The measurements were done in the following sequences: the temperature range from 300 K down to 100 K at the cooling rate of 1.5 K/min, from 99 K to 11 K, at the rate of 1 K/min in 90 steps and from 10 K to 1.8 K at 0.5 K/min in 41 steps.

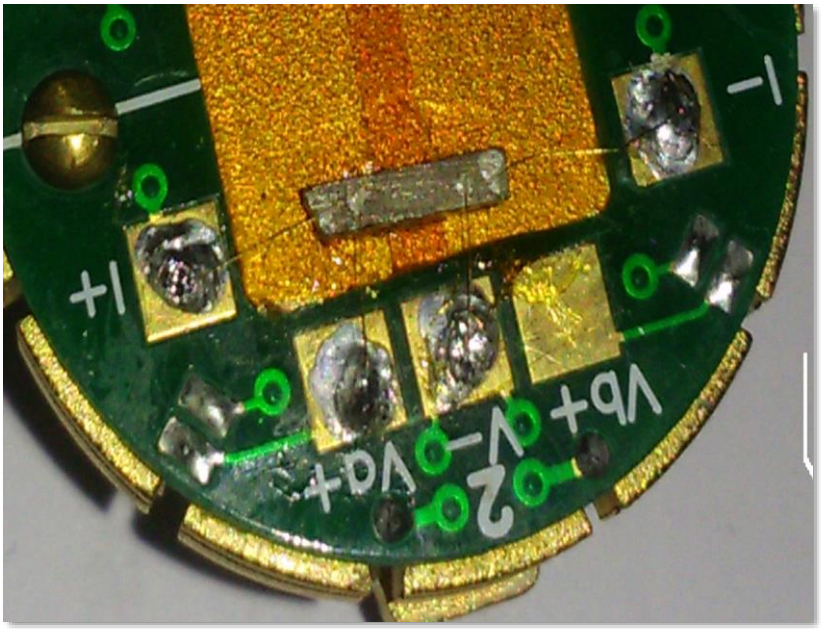

Figure 3.8: Photograph of a sample mounted on puck using spot welding techniques for the electrical resistivity measurements.

3.4.2 Specific heat

The PPMS uses a relaxation-time method to measure the specific heat in the temperature range 400 K-1.8 K. The measurements of the heat capacity were run at constant pressure and changes in sample volume were negligible according to the change rate of the measured temperature. On the specific heat measurement puck, a heater and a thermometer are attached below the sample platform as shown in figure. 3.9 (schematic representation of the platform). Small wires provide the electrical connection to the heater and thermometer as well as to provide thermal connection and mechanical support to the sample platform.

The measurements were first done by mounting the Apiezon N grease on the specific heat puck (sapphire specimen holder) in order to ensure good thermal contact and was loaded onto the PPMS. The specific heat measurements of the grease plus puck (Addenda measurements) were carried out before each measurement. The appropriate sequence was set and run at the same range of temperature as the data would be recorded. The addenda measurement was followed by a sample measurement where a typical sample mass used was between 9 mg-11 mg. This was placed on the Apiezon N grease to ensure a good signal to noise ratio as shown in the schematic representation of the heat capacity puck in figure 3.9 [132]. This

measurement of the heat capacity first used a heating period which was followed by a cooling period, after which the capacity option fits the entire temperature response of the sample platform to a model that accounts for the thermal relaxation of the sample platform to the bath temperature and the relaxation between the sample platform and the sample itself. Moreover, the specific heat measurements were done, with a heat pulse of around 1% of the current puck temperature. The contribution of the platform and sample gives the total specific heat. This latter contribution is determined from a *two-τ* model which simulates the effect of heat flowing between the sample and the platform, and the effect of heat flowing between the platform and the puck. The contribution of the grease and platform to the total specific heat was determined by a separate measurement using a one-τ model fitting [132]:

$$C_{total}\frac{dT_p}{dT} = -K_w(T - T_b) + P(t) \tag{3.7}$$

with:

$$\tau = C_{total}/K_w\,, \tag{3.8}$$

where τ is the relaxation time and K_w is the thermal conductance of the supporting wires, T_b is the constant related to puck temperature and $P(t)$ is the heater power.

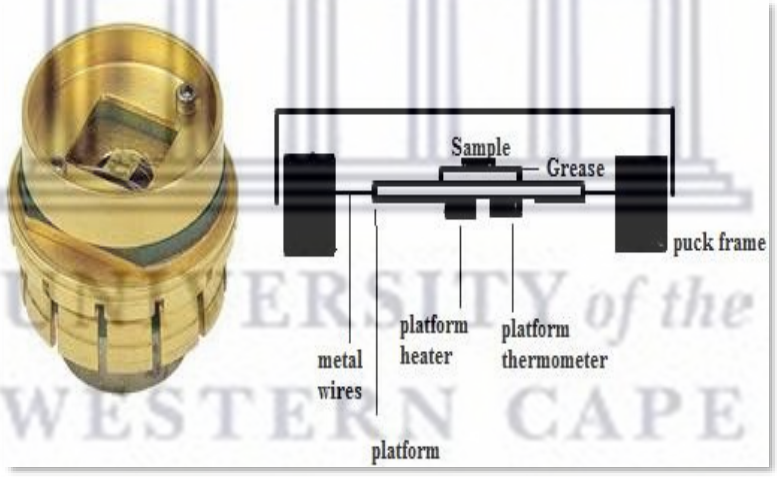

Figure 3.9: ^{4}He specific heat puck and its schematic representation of the platform [132].

3.5 Magnetic Property Measurement System (MPMS)

The magnetic properties of all samples studied in this work were measured using the QD MPMS-5 (figure 3.10) [133]. This MPMS has three main modes of measurements consisting of the reciprocating sample option (RSO), alternative

current (AC), and direct current (DC) measurement methods. In the DC method, two Josephson junctions (that consists of two weakly coupled superconducting electrodes) are connected parallel onto two superconductors with an insulating gap in between. In the case where the gap is thin enough, electron pairs can tunnel from one superconductor across the gap to the other superconductor, utilizing quantum tunneling, a resistanceless current flow across the insulator [133].

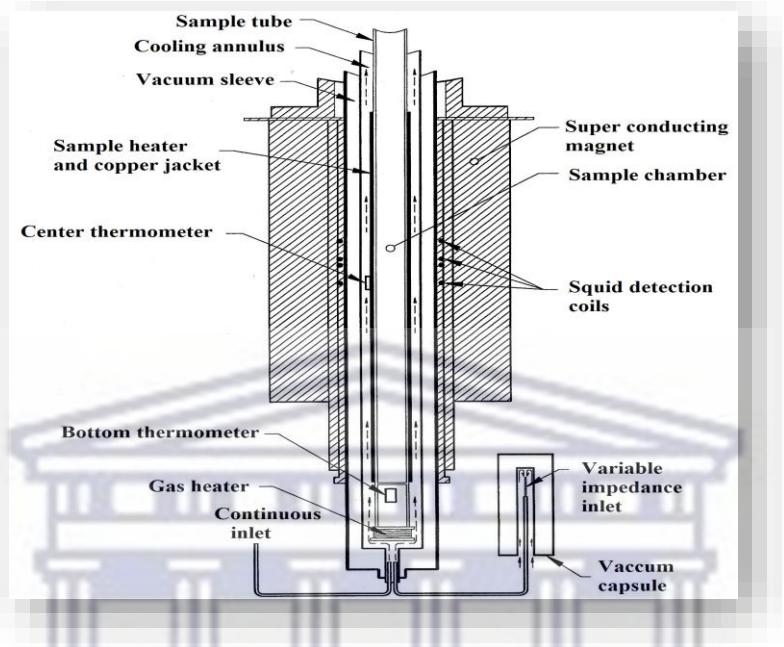

Figure 3.10: Schematic representation of Magnetic Properties Measurement System (MPMS) [134].

The MPMS measures the magnetic properties such as magnetic susceptibility and magnetization with a field range of up to 7 T produced by a highly uniform axial solenoid magnet. The working frequency in this system is given as $\omega j = 2\pi V/\Phi_0$, where Φ_0 is the magnetic flux quantum and V is the applied voltage [132, 133].

The DC option mentioned above, was used to perform magnetic properties measurements of samples studied in this thesis. Here, the magnetometer is very accurate so as to easily detect a high magnetic moment of diamagnetic, paramagnetic, ferromagnetic and antiferromagnetic materials [133].

3.5.1 Magnetic measurements

Magnetic susceptibility and magnetization isotherm measurements were performed on a single piece of each sample with mass approximately 15 mg of each polycrystalline alloy series in the temperature range 1.7-400 K and in fields up to 7 T. The sample was cleaned with acetone and inserted into a regular plastic straw (figure 3.11) used as a sample holder. This sample holder was used because of its low mass and less diamagnetic background signal. The sample was cut into a cubic shape to minimize the demagnetization field. The auto centering of the sample was continually performed at periodic intervals during the measurements. As shown in figure 3.12, the VSM option has two gradiometer pick-up coils where the sample can sit deep within the dewar (see figure 3.12(a)) at the center of the magnet. The sample is held inside the coil-set (see figure 3.12(c) by a long rod (see figure 3.12(b)) that is driven by a linear motor transport.

Figure 3.11: Picture showing sample mounted in the straw for the magnetization and magnetic susceptibility measurements on MPMS.

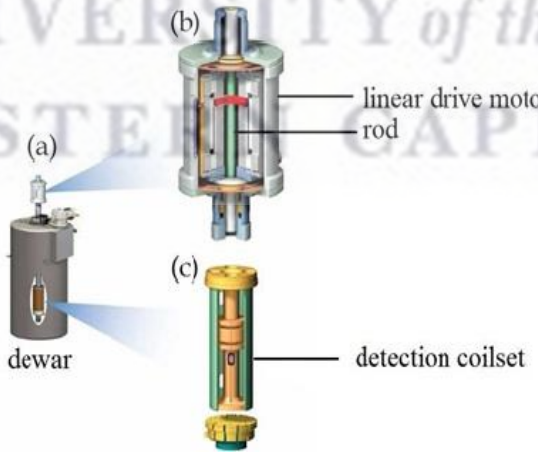

Figure 3.12: (a) A picture of PPMS dewar showing VSM linear drive motor with (b) the motor showing the rod that hold the sample and (c) the pickup coil set at the bottom of the dewar [134].

The sample was oscillated through superconducting detection coils at a constant speed at a given temperature and in a homogeneous magnetic field. During the oscillation movement of the sample, the magnetization of the space within the pick-up coils of the SQUID (figure 3.13) changed producing an electrical current in the detection coils. This induced current was not attenuated and any change in magnetic flux produced a proportional change of current in the detection circuit according to Faraday's principle ($\nabla \times E = -\frac{\partial B}{\partial t}$). The coils were inductively coupled to the SQUID, through a flux gate transformer. Therefore, by moving the sample on either side of the detection coils, an integration of the magnetic field was realized and the flux transformer was used to transmit the signal to the SQUID [134, 135].

From the phase difference across the junction of the SQUID, the magnetic moment in emu (electromagnetic unit) is obtained from the SQUID response. The amplitude of the measured signal is proportional to the magnetization of the sample. These measurements can be carried out by varying the temperature (magnetic susceptibility measurements) or maintaining the temperature constant, and vary the applied magnetic field (magnetization measurements) [135].

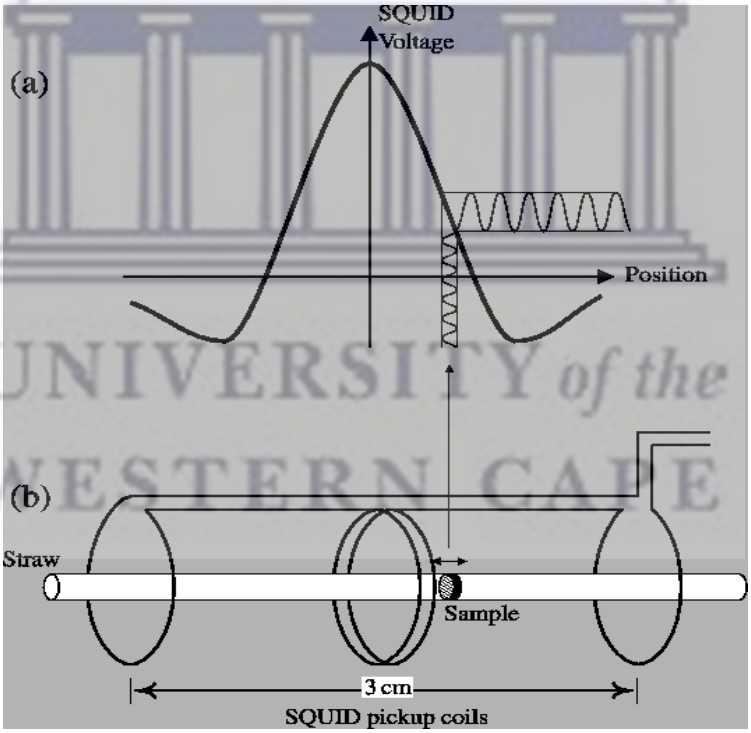

Figure 3.13.Illustration of an RSO measurement with a small amplitude. (a) shows the ideal SQUID response for a dipole and (b) shows the movement of the sample within the SQUID pickup coils [135].

Chapter 4
Chemical substitution-induced transition of the magnetic ground state from ferromagnetic to antiferromagnetic order in $CeCu(Ge_{1-x}Sn_x)$

Abstract

This chapter reports the evolution from ferromagnetic (FM) to antiferromagnetic (AFM) state in $CeCu(Ge_{1-x}Sn_x)$ investigated by means of magnetic and heat capacity measurements. X-ray diffraction studies for all samples indicate the ZrBeSi-type hexagonal crystal structure with space group $P6_3/mmc$ (No. 194). The magnetic susceptibility, $\chi(T)$ at high temperature follows the Curie-Weiss relation with an effective magnetic moment close to of 2.54 μ_B expected for free Ce^{3+}-ion. At low temperatures, $\chi(T)$ data indicate AFM transition for alloys in the concentration range $0.7 \leq x \leq 1$ and FM for $x \leq 0.6$. The magnetization ($M(\mu_0 H)$) of samples exhibiting AFM behaviour show metamagnetic transition at low magnetic fields with some irreversibility in the process of increasing and decreasing magnetic field. In turn, $M(\mu_0 H)$ of samples exhibiting FM behaviour show saturation in high magnetic fields. Heat capacity, $C_p(T)$ data confirm the AFM and FM transitions observed in magnetic measurements. An additional anomalies below T_C and T_N are observed in $C_p(T)/T$, which likely arises from spin reorientation or rearrangement in FM or AFM structure. $\rho(T)$ data confirm the magnetic phase transition temperature at T_C and T_N and revealed the occurrence of a second magnetic phase transition below T_C and T_N which may be attributed to spin reorientation or rearrangement of the magnetic moments of Ce ions. Furthermore, $C_p(T)$ and $\rho(T)$ data below T_C are well described by the spin-wave excitations with energy gap Δ_C and Δ_R in the FM spin-wave spectrum.

4.1 Introduction

A large number of experimental investigations have provided evidence of magnetic ground state switching between FM and AFM ordering driven by magnetic field, pressure or chemical substitution in *d* and *f* electron compounds [136-141]. But only a few theoretical studies aimed at describing these magnetic transitions have been reported in the literature

between FM and AFM phases [142, 143]. One of these theoretical studies has been provided within extended Landau theory [143]. The experimental methods used to investigate the magnetic phase transitions could be divided into macroscopic and microscopic ones [144]. The macroscopic method involves the temperature dependences of magnetization, magnetic susceptibility and heat capacity, while the microscopic one involves neutron diffraction and Mössbauer effect. The present chapter is based on the experimental studies of the magnetic ground state transition between FM and AFM ordering driven by chemical substitution in *p*-block elements such as Ge and Sn, in 4*f* electron compounds such as Ce and Nd (chapter 5) and in 3*d* electron compounds such as Cu and Pd (Chapter 6) using the macroscopic method.

The compounds RTX (R = *f*-electron, T = *d*-electron, X = *p*-electron) crystallize in different crystal structures depending on the constituent elements and order magnetically in a wide temperature range from very low temperatures to temperatures about 510 K [145]. Depending on the crystal structure, they show a variety of magnetic and electrical properties. A large amount of experimental research was devoted to the compounds CeCuGe [146, 147] and CeCuSn [148, 149] probing their magnetic and electronic properties. Both compounds were found to crystallize in structures derived from various hexagonal-type such AlB_2-type with Ce atoms located on the Al site, ZrBeSi-type or $CaIn_2$-type [150-157].

The compound CeCuGe has been reported to order ferromagnetically at T_C = 10 K [33, 158]. In the paramagnetic state it exhibits Curie-Weiss behaviour with an effective magnetic moment (μ_{eff}) per Ce of 2.50 μ_B that is close to the value of 2.54 μ_B expected for free Ce ion [158]. At low temperature the effective moment decreases to about 2.20 μ_B per Ce. This decrease was attributed to crystalline electric field (CEF) effect [148]. Below T_C, in the ferromagnetic region, the magnetization exhibits hysteresis loop which indicates a rather small anisotropy with a coercive field less than 20 Oe as reported by Oner *et al*. [148]. Furthermore, very little remanence was observed (the ratio of the remanence to the technical saturation magnetization per Ce concentration about 0.05), implying that this material is magnetically soft, with a very small magnetocrystalline anisotropy. The resistivity data of this compound follows the T^2-power law in the temperature range 10-30 K, consistent with the appearance of spin fluctuations above T_C [148]. In the ordered state, the resistivity behaviour can be interpreted in terms of scattering of conduction electrons on magnons. In the same temperature range, the thermoelectric power exhibits a linear rise in addition to a T^2 term, anomalous behaviour which

was also attributed tentatively to the development of spin fluctuations [148]. The heat capacity of CeCuGe shows a Schottky-type anomaly around 68 K associated with CEF effects [33]. The presence of CEF was confirmed by inelastic neutron scattering excitation [147]. Critical behaviour studies of ferromagnetic CeCuGe using magnetocaloric effect was also reported [159]. The resulting critical exponents, β, γ and δ indicated that CeCuGe behaved as a mean-field ferromagnet.

The CeCuSn compound has been reported to order below 8.6 K with a complex AFM – type structure [149]. In the ordered state, the heat capacity exhibited a maximum near 7.4 K, signaling a rearrangement of the AFM structure [160]. Two structural modifications of CeCuSn were synthesized by Sebastian *et al*. [161]. The high-temperature β-CeCuSn phase crystallized with the hexagonal NdPtSb-type structure, while the low-temperature α-CeCuSn phase adopted the hexagonal structure of the ZrBeSi-type. In view of the different magnetic states in CeCuGe and CeCuSn, it is interesting to investigate a solid solution of the alloys series $CeCu(Ge_{1-x}\ Sn_x)$ in order to probe the transition from FM to AFM ordering using the macroscopic method which involved magnetic and heat capacity measurements of this alloy series.

4.2 Experimental details

Polycrystalline samples of $CeCu(Ge_{1-x}\ Sn_x)$ were prepared as indicated in chapter 3, by arc - melting stoichiometric amounts of the elements Ce (99.98%), Cu (99.995%) Ge and Sn (99.999%) under ultra - high purity argon atmosphere. The samples were overturned and remelted three times to promote good homogeneity. The weight losses after final melting were always less than 1 wt.%. Subsequently, the sample ingots were wrapped in tantalum foil, encapsulated in evacuated quartz tubes and annealed at 850 ^{o}C for two weeks.

The products were checked by powder X-ray diffraction using a Bruker D8 ADVANCE diffractometer with CuKα radiation ($\lambda = 1.5406$ Å). The X-ray diffraction spectra were analyzed by using the cell and intensity least-squares (CAILS)-Pawley and the Full-profile Rietveld refinement method both from TOPAS ACADEMIC [162].

Temperature and magnetic field-dependent properties of the prepared alloys were measured by using Quantum Design Physical Property Measurement System (PPMS) and a Magnetic Property Measurement System (MPMS) described in chapter 3.

4.3 Results and discussion

4.3.1 X - ray diffraction: Crystallography

X-ray diffraction results obtained for the two end compounds as well as two other samples in the series together with the CAILS refinement fits to the data, are shown in figures 4.1, 4.2. The space group setting used in the CAILS-Pawley refinement, and Rietveld refinement in figure 4.3, was $P6_3/mmc$ (No. 194) hexagonal ZrBeSi-type structure. The results of the refinements are shown by black solid lines through the measured data and the Sn content (x) dependence of the lattice parameters (a and c) and unit cell volume (V) are shown in figure 4.4. It is observed that V and a increase linearly with x. The linear increase in V is consistent with Vegard's law which suggests the stability of the Ce valence across the series as well as no change in the number of conduction electrons, which ensures metallic bonding of the alloy system. Furthermore, the linear increase in V with increase in Sn content x also corroborated with the large atomic radius of Sn (r = 1.45 Å) compared to that of Ge (r = 1.25 Å). The room temperature lattice parameters and unit cell volume of the two-end compounds are: $a_{Ge} = b_{Ge}$ = 4.3031 (2) Å, c_{Ge} = 7.9673 (5) Å and V_{Ge} = 127.76 (4) Å^3 for CeCuGe compound; $a_{Sn} = b_{Sn}$ = 4.5867 (3) Å, c_{Sn} =7.9079 (5) Å and V_{Sn} = 144.09 (2) Å^3 for CeCuSn compound.

These values are in good agreement with those reported in the literature [151-155]. In the space group setting used in the Rietveld refinement ($P6_3/mmc$ hexagonal ZrBeSi-type structure) the Ce atoms occupy the crystallography site 2a, Cu atoms occupy the crystallography site 2c, and Ge or Sn occupy the crystallographic site 2d. The resulting hexagonal crystal structure is depicted in figure 4.5.

The refinement instrumental parameters for the two-end compounds are listed in Table 4.1 and the atomic coordinates in CeCuX (X = Ge or Sn) are listed Table 4.2. During the refinement, the occupancy fraction of all atoms was kept fixed to 100% (fully occupied) as well as the equivalent isotropic temperature factor (beq). The resulting phase density amount to 7.1813 (7) g/cm^3 for CeCuGe compound and 7.4303 (9) g/cm^3 for CeCuSn compound.

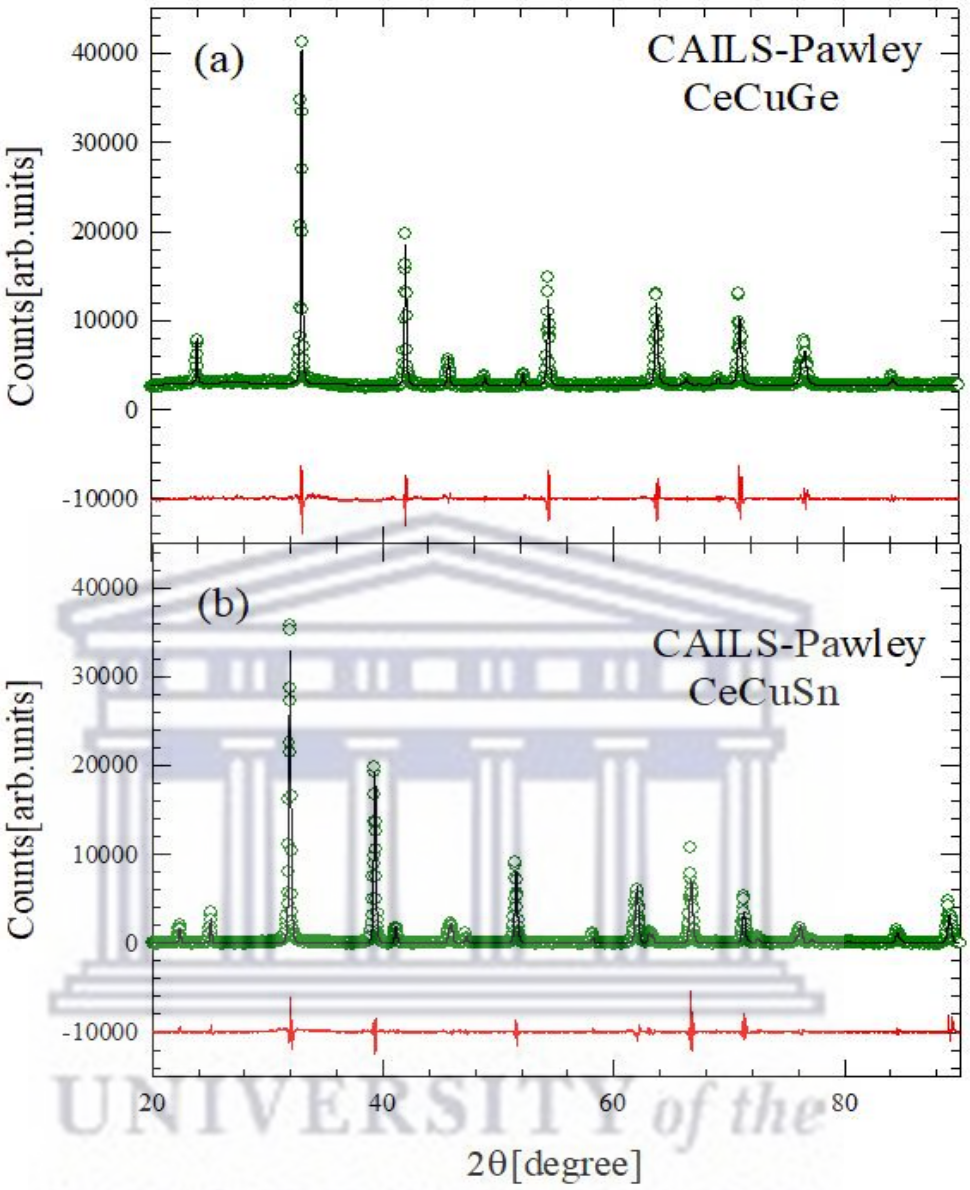

Figure 4.1. CAILS-Pawley analysed spectra of (a) CeCuGe and (b) CeCuSn. The observed data are shown by green symbols and the solid black lines through the data represent the result of the CAILS refinement. The lower red curves are the difference curves between the experimental data and the calculated curves.

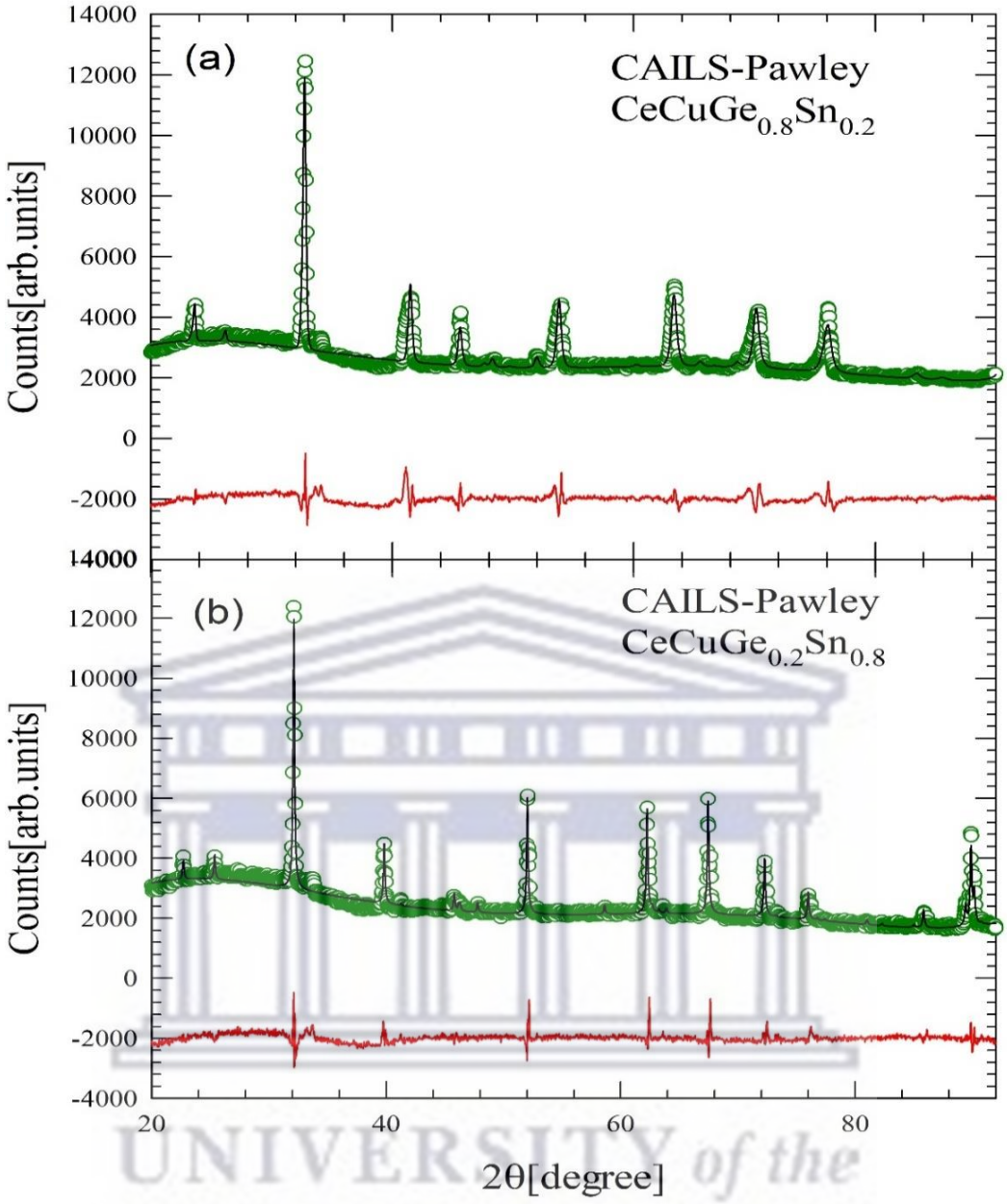

Figure 4.2. CAILS-Pawley analysed spectra of selected samples in $CeCu(Ge_{1-x}Sn_x)$. The observed data are shown by green symbols and the solid black lines through the data represent the result of the CAILS refinement. The lower red curves are the difference curves between the experimental data and the calculated curves.

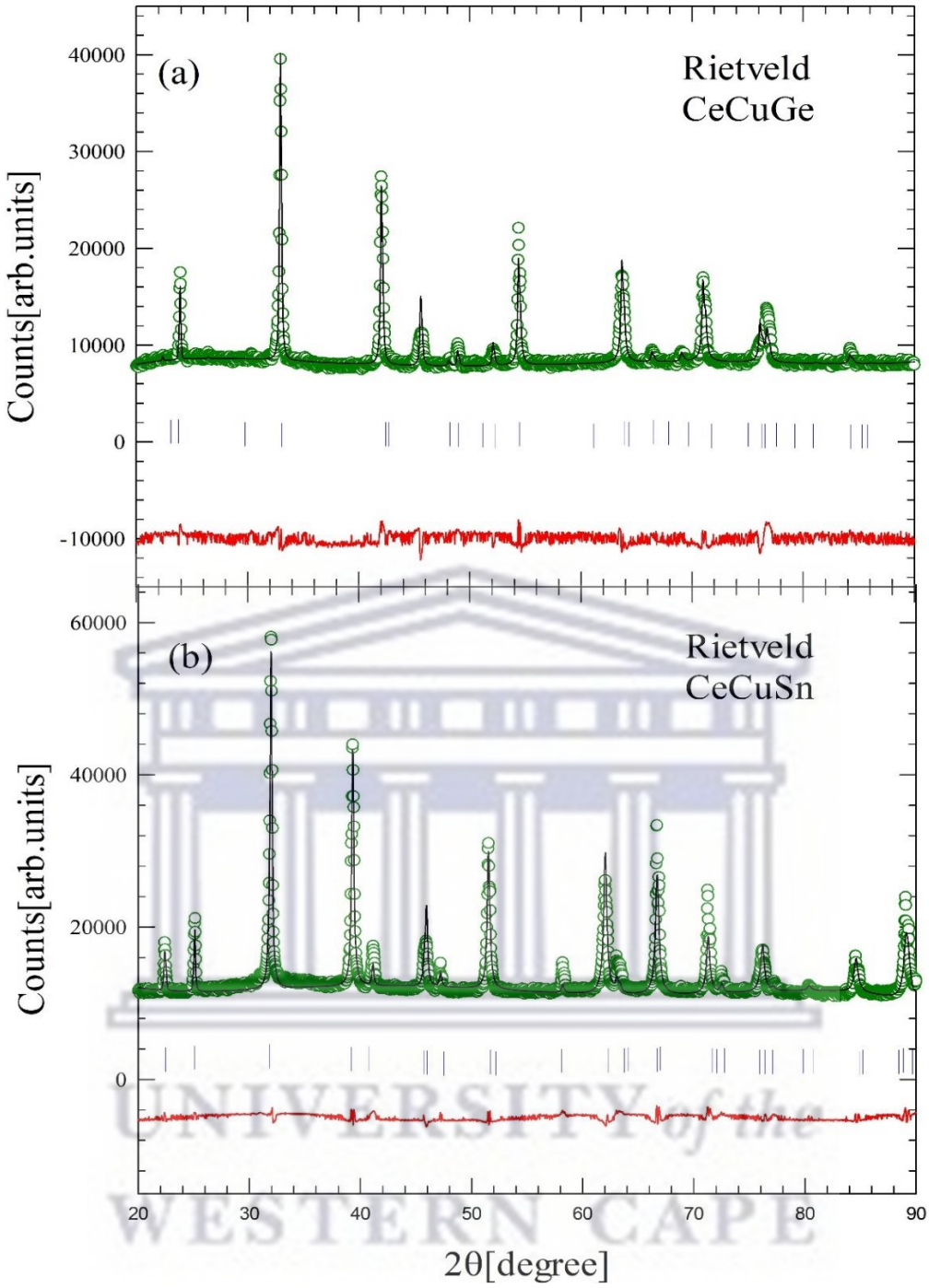

Figure 4.3. Rietveld analysed spectra of (a) CeCuGe, (b) CeCuSn. The observed data are shown by green symbols and the solid black lines through the data represent the result of the CAILS refinement. The lower red curves are the difference curves. The vertical blue lines represent Bragg's reflection.

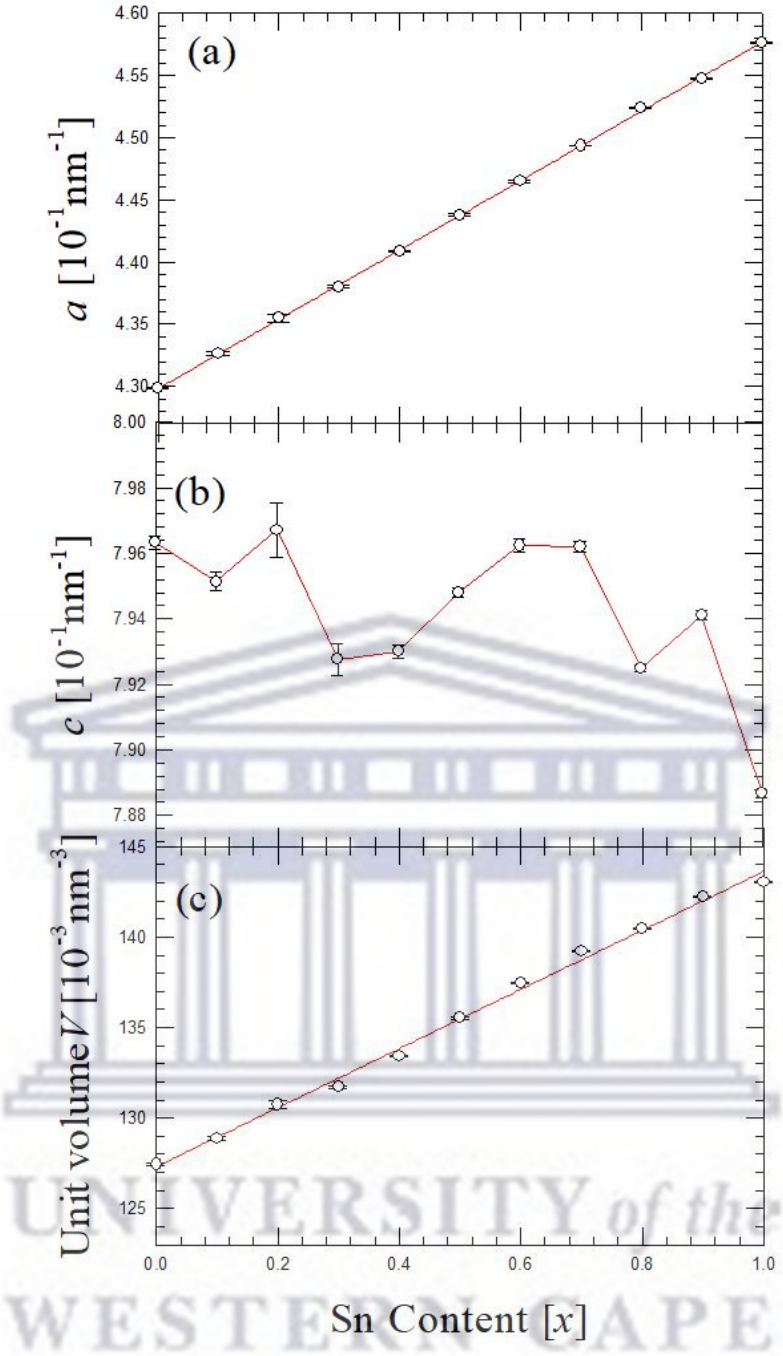

Figure 4.4. The figure shows the Sn content *x* dependence of the lattice parameters *a* and *c* and the unit cell volume *V* in the CeCu(Ge1−*x* Sn*x*) alloys series. The Solid red lines in the lattice parameters *a* and the unit cell volume *V* Panels is LSQ fit of the data to the linear equation. The red line in the middle panel is is a guide to the eye.

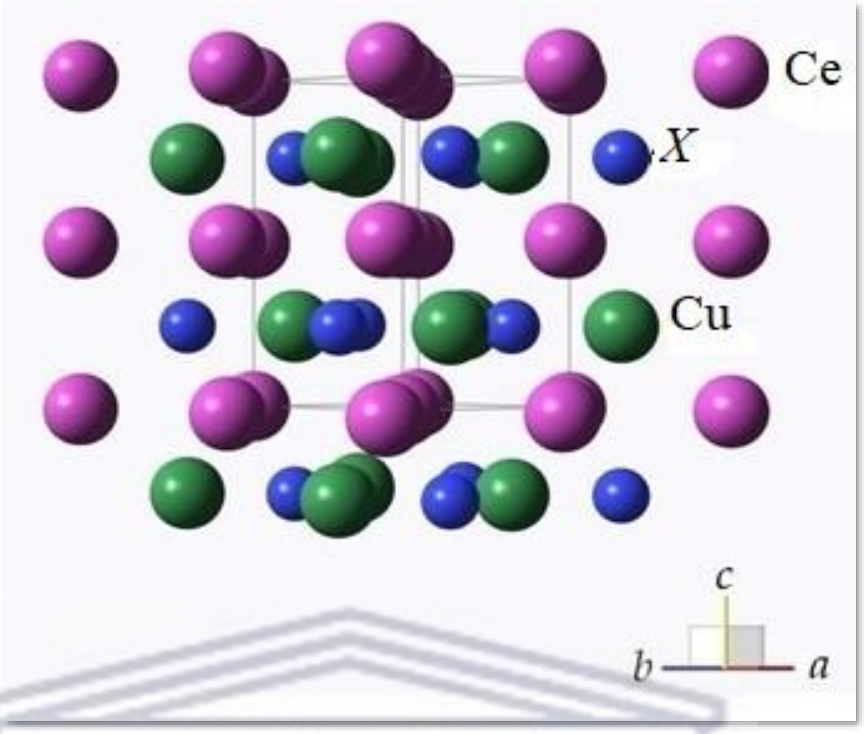

Figure 4.5 Crystal structure of CeCuX (X: Ge, Sn) with Cu X layer sandwiched between the Ce-layers [33].

Table 4.1: The refined instrumental parameters of the (1) CAILS and (2) Full-structure Rietveld refinement method (for comparison only) for the two-end compounds.

Parameters	CAILS (1)		Rietveld (2)	
	CeCuGe	CeCuSn	CeCuGe	CeCuSn
Rp [%]	4.022	26.349	5.696	9.076
Rwp [%]	6.251	51.629	8.671	12.268
Rexp [%]	1.771	4.026	3.350	2.232
$X^2 = GOF$	3.53	4.621	2.588	3.496
DW [%]	0.793	1.409	0.455	0.201

Table 4.2: Atomic coordinates, the site occupancy (S.O.) and the equivalent isotropic temperature factor (beq) for CeCuX (X = Ge or Sn) obtained for the full-structure Rietveld refinement method using the space group $P6_3/mmc$. The S.O. and the beq were kept fixed.

Atoms	Wyckoff site	*x*	*y*	*z*	S.O	beq
Ce	2a	0	0	0	1	1
Cu	2c	1/3	2/3	1/4	1	1
X	2d	1/3	2/3	3/4	1	1

The observed values of the *R*-factors and χ^2 (goodness of fit) obtained from the CAILS and Rietveld refinement methods are relatively good as observed from the good quality of the fits in figures 4.1 and 4.3.

Furthermore, the values of *DW* for all investigated samples are less than the value of 2 % in agreement with the ideal range value of $0 < DW < 2\%$ [25, 26] which indicate that the quality of the fit model is good.

4.3.2 Magnetic susceptibility and magnetization

The dc-inverse magnetic susceptibility, $\chi^{-1}(T)$ of the $CeCu(Ge_{1-x}Sn_x)$ alloys series, measured in applied field of 0.1 T in the temperature range $1.7 \leq T \leq 400$ K, are shown in figure 4.6. At temperatures above 100 K, $\chi^{-1}(T)$ exhibits Curie-Weiss (CW) behaviour:

$$\chi^{-1}(T) = \frac{3k_B(T-\theta_P)}{N_A\mu_{eff}^2}, \tag{4.1}$$

where all the parameters are defined in chapter 2. Least squares (LSQ) fits against the experimental data are shown as solid lines in figure 4.6. The obtained parameters from the LSQ fits are gathered in Table 4.3.

The obtained values of the effective magnetic moment, μ_{eff} are reasonably close to those predicted within a Russel-Saunders coupling scenario for the trivalent Ce^{3+}-ion (2.54 μ_B). The slight excess in the measured effective moment of the compound CeCuSn may be attributed to the polarization of the conduction electron band by Ce magnetic moments also observed in other rare-earth compounds such as PrCuSi [163]. At lower temperature below about 100 K, $\chi^{-1}(T)$ data deviated from CW linear behaviour and this is usually the first indication of structure in the 4*f*-electronic level distribution under the action of a CEF or may be attributed to the onset of magnetic ordering. This finding indicates fairly stable 4*f*-electronic state of the cerium atoms dominated by AFM exchange interactions. At low temperatures, $\chi(T)$ data measured in field of 0.1 T are displayed in figures 4.7 (a), 4.7 (b), 4.7 (c) and 4.7 (d) (left axis) for selected samples showing AFM and FM behaviour.

Table 4.3. LSQ fits parameters of the high temperatures magnetic susceptibility data of the CeCu($Ge_{1-x}Sn_x$) alloys series according to the Curie-Weiss relationship (Eq. 4.1).

Sn Content x	$\mu_{eff}(\mu_B)$	$-\theta_P[K]$	T_C^{χ} (T_C^{cp})$[K]$	T_N^{χ} (T_N^{cp})$[K]$
1	2.629(4)	18.9(8)		8.6
0.9	2.307(2)	29.3(6)		10
0.8	2.319(2)	4.3(8)		9.5 (7.3)
0.7	2.287(2)	6.2(5)		8.6
0.6	2.444(1)	6.3(4)	10 (9.2)	
0.5	2.201(1)	12.7(3)	10	
0.4	2.346(3)	12(1)	9.5 (8.7)	
0.3	2.253(1)	4.0(4)	9.7	
0.2	2.441(3)	22(1)	9.7 (9)	
0.1	2.450(4)	21(1)	10	
0	2.500(3)	25(2)	11	

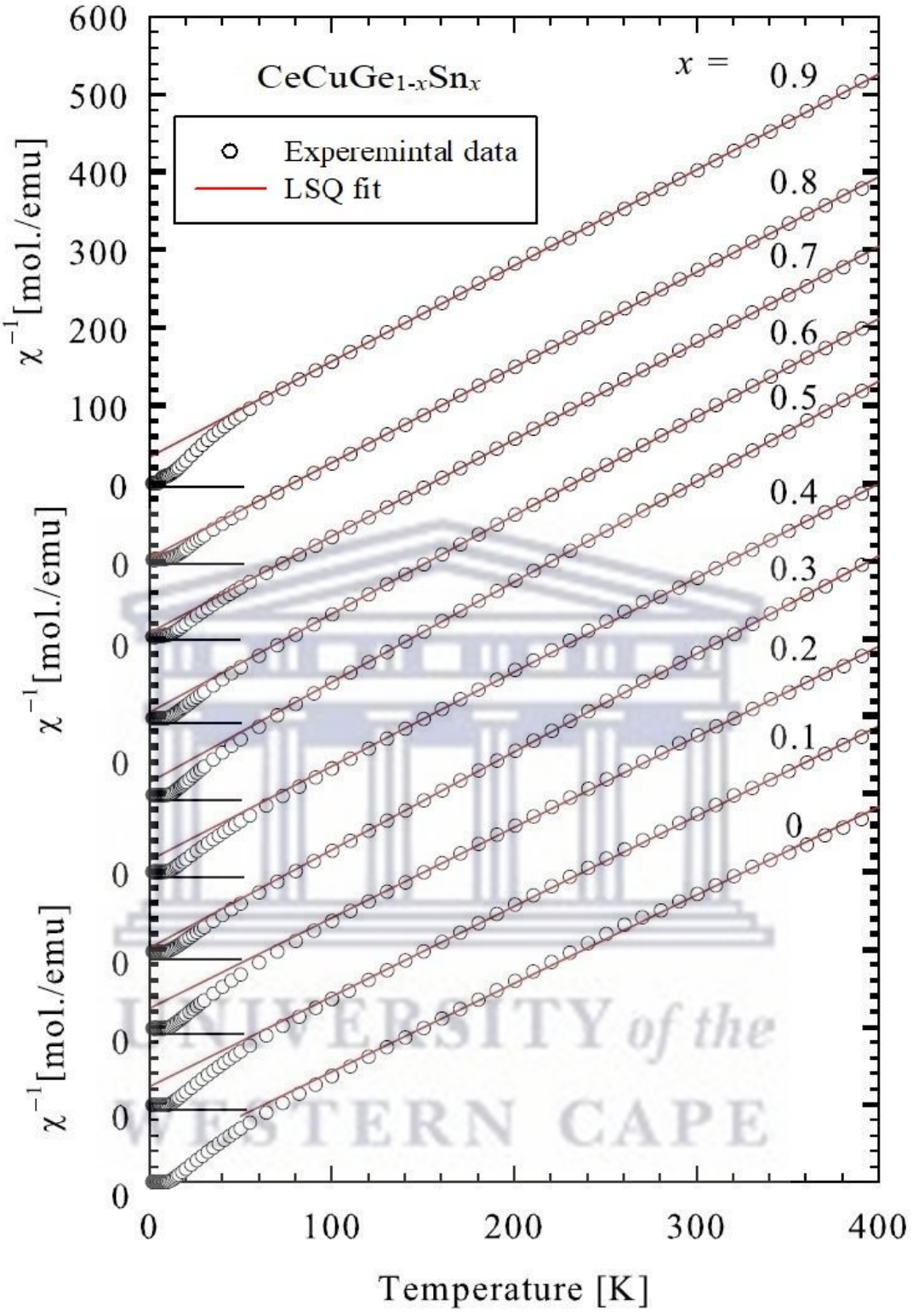

Figure 4.6: DC-inverse magnetic susceptibility of $CeCu(Ge_{1-x}Se_x)$ alloys with the least-square (LSQ) fits of the Curie-Weiss law to the data points above 100 K.

For all samples, the Weiss temperatures (θ_P) were found to be negative. These indicate that regardless of the FM ordering, these systems are for samples in the range $0.7 \leq x \leq 1$ (AFM region, figure 4.7 (a)), χ (T) data show kinks associated to PM-AFM transition at T_N as indicated by arrows in figure 4.7 (a). Below T_N, an abrupt rise in χ (T) data is observed, which may be associated with the coexistence of AFM and FM exchange interactions or canting of the AFM structure. As shown in figures 4.7 (b), 4.7 (c), and 4.7 (d), χ (T) data of the samples with $x \leq 0.6$ exhibits a typical FM-like behaviour. The PM-FM transition around T_C was estimated from the minimum value of dχ (T)/dT curves (right axis) for each sample as indicated by arrows in the figures 4.7 (b), 4.7 (c), 4.7 (d). The estimated values of T_N and T_C from χ (T) data are listed in Table 4.1. The obtained values of T_N and T_C for the two end compounds are in good agreement with previously reported values of T_C = 10 K [33, 149, 163] for CeCuGe and T_N = 8.6 K for CeCuSn [160, 163].

The field-dependent magnetization, M ($\mu_o H$) was measured in fields up to 5 T. Hysteresis was observed for some samples in the process of increasing and decreasing field. As shown in figures 4.8 (a), and 4.8. M ($\mu_o H$) of samples with $0 \leq x \leq 0.6$ exhibited typical FM-like behaviour characterized by an abrupt rise of M ($\mu_o H$) upon application of weak magnetic field, followed by a tendency towards saturation in high fields.

For all samples, the magnetization measured in fields of 5 T at 1.7 K is less than $1.1\mu_B$, which is approximately half the theoretical value for free Ce^{3+}-ion ($g_J J = 2.14\mu_B$). In the present case of a polycrystal in which the applied field is inevitably directed along arbitrary crystallographic directions in the sample, this shortfall may be explained by virtue of magnetocrystalline anisotropy. A similar shortfall was also observed in PrCuSi polycrystalline sample [164].

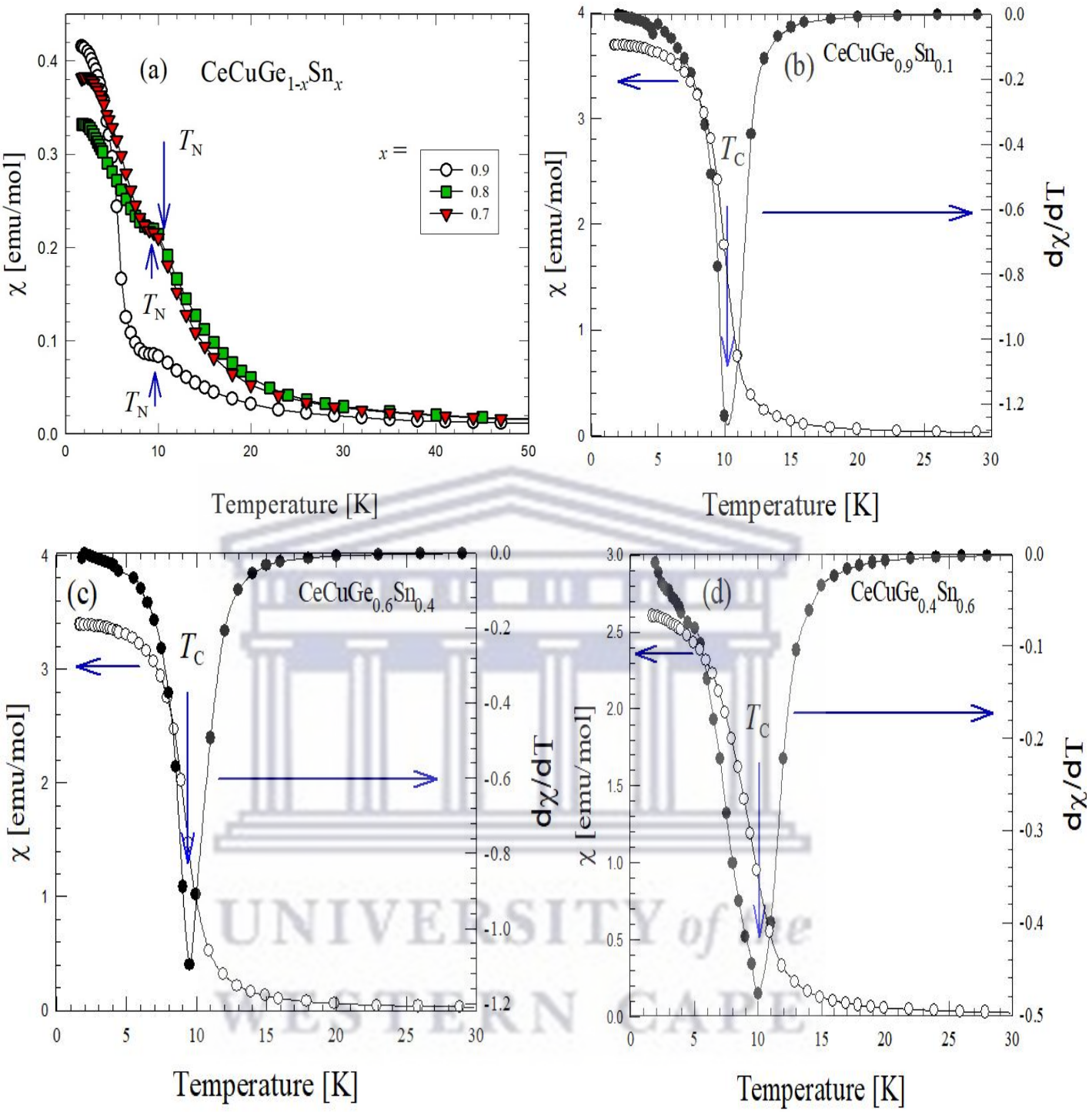

Figure 4.7: The low temperature χ (*T*) data of selected samples of CeCu($Ge_{1-x}Sn_x$) alloy series (a) in the AFM region, (b), (c) and (d) in the FM region (left axis). The right axis of (b), (c) and (d) display dχ/d*T* with the arrows indicating the FM phase transition temperature, T_C at the minimum of dχ/d*T* curve.

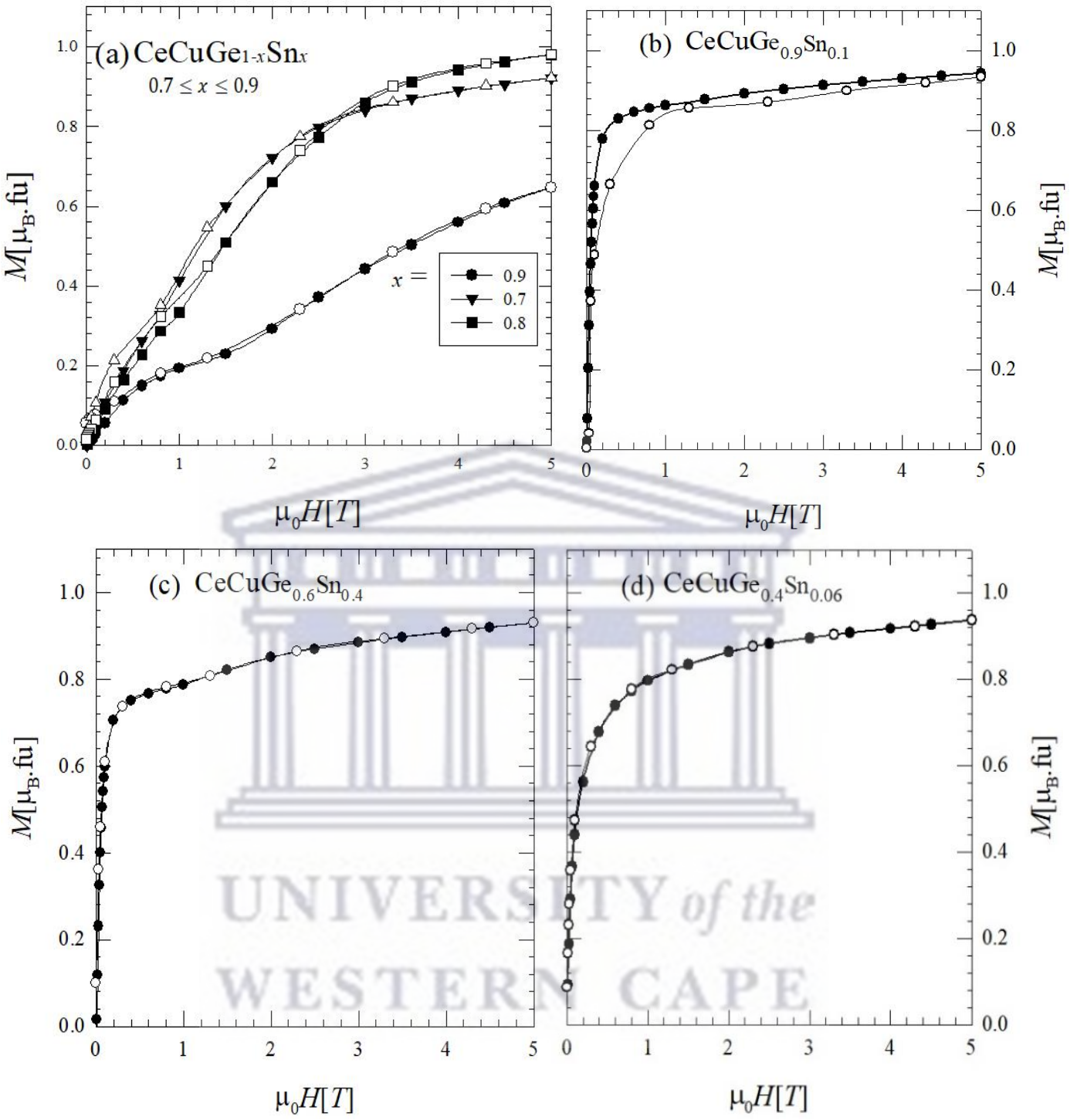

Figure 4.8: The field-dependent magnetization, M ($\mu_0 H$) of selected sample in the alloy series $CeCu(Ge_{1-x}Sn_x)$ measured in increasing (closed symbols) and decreasing (open symbols) field at 1.7 K.

4.3.3 Heat capacity

The low temperature heat capacity at constant pressure, $C_p(T)/T$ data of selected samples in the FM and AFM regions are shown in figures 4.9 and 4.10. $C_p(T)$ was measured at zero applied magnetic field in the temperature range 2 to 30 K. For all measured samples, the magnetic phase transitions manifest themselves as sharp anomalies in the $C_p(T)/T$ curves. The so-derived magnetic phase transition temperatures, T_C and T_N listed in Table 4.1, are close to those obtained from $\chi(T)$ and $\rho(T)$ data (see section 4.3.4). A second anomaly below T_C and T_N at T_1 = 4.6 K and 3.2 K for samples with x = 0.4 and 0.8 respectively were observed. These anomalies may be associated with spin reorientation or rearrangement of the FM and AFM structures also observed in CeCuSn [160]. In the case of x = 0.4, another anomaly was observed above T_C at T_2 = 11.2 K.

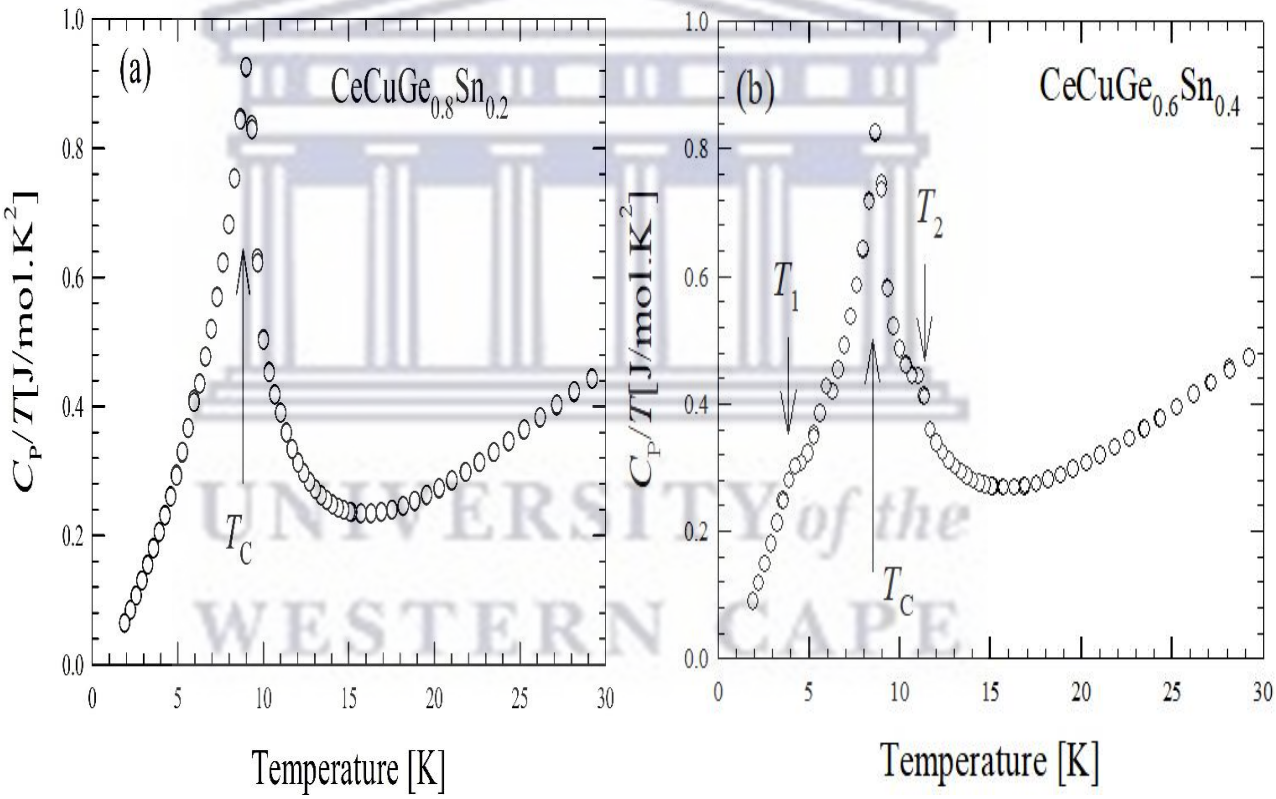

Figure 4.9: Specific heat $C_p(T)/T$ of selected samples in the FM and AFM region in the alloy series $CeCu(Ge_{1-x}Sn_x)$, measured in zero external magnetic and in the temperature range 2 to 30 K. The arrows indicate the magnetic phase transition temperatures.

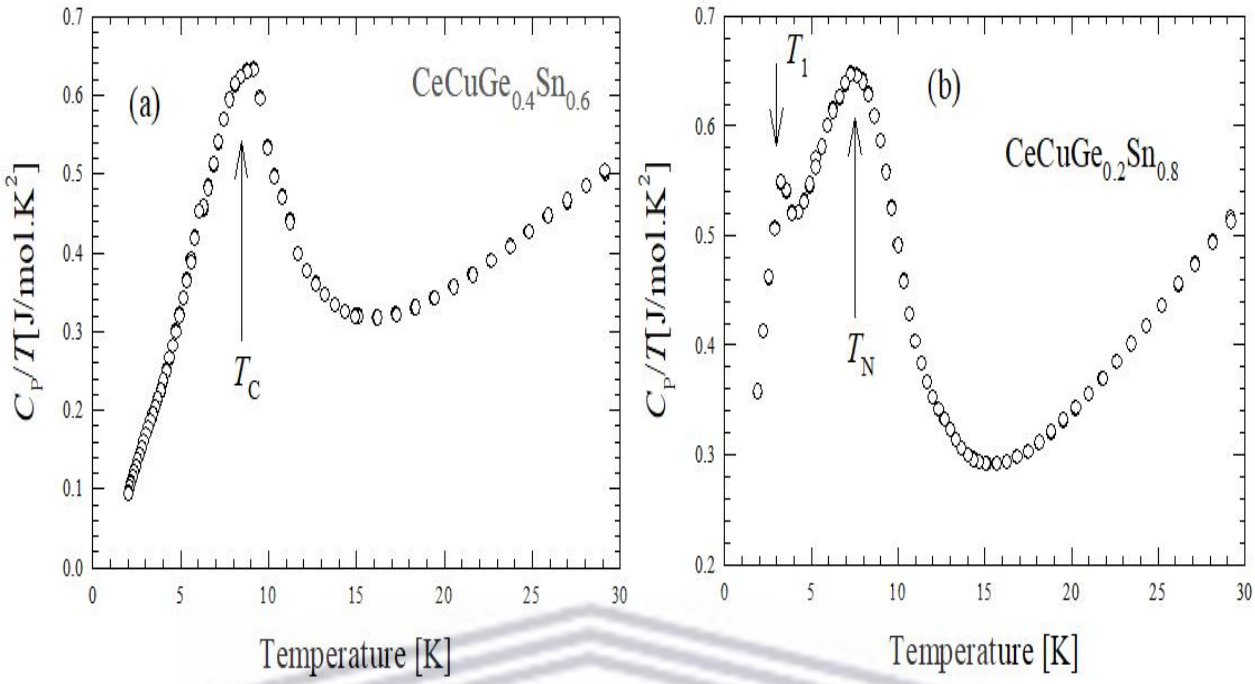

Figure 4.10: Specific heat $C_p(T)/T$ of selected samples in the FM and AFM region in the alloy series CeCu($Ge_{1-x}Sn_x$), measured in zero external magnetic field and in the temperature range 2 to 30 K. The arrows indicate the magnetic phase transition temperatures.

Figure 4.11 display $C_p(T)/T$ versus T^2. The solid line through the data points represents the least square fits (LSQ) of the conventional Debye equation for the specific heat of a metal at temperature well above T_C and T_N defined as:

$$\frac{C_p(T)}{T} = \gamma^{conv} + \beta T^2. \qquad (4.2)$$

The resulting LSQ fit parameters, γ^{conv} and β values (see Table 4.4) of the selected samples measured were used to derive the 4*f*-electron contribution to the total specific heat, $C_{4f}(T)$. The data was obtained by subtracting from the measured $C_p(T)$ curves the phonon contribution resulting from the fit.

Table 4.4: LSQ fits parameters of the heat capacity data of selected samples of the CeCu($Ge_{1-x}Sn_x$) alloy series well above their phase transition temperatures, T_C and T_N, according to the conventional Debye equation (Eq. 4.2).

Sn content *x*	γ^{conv}	β
0.2	0.117(1)	0.0004(1)
0.4	0.156(1)	0.0004(2)
0.6	0.215(2)	0.0003(2)
0.8	0.184(2)	0.0004(2)

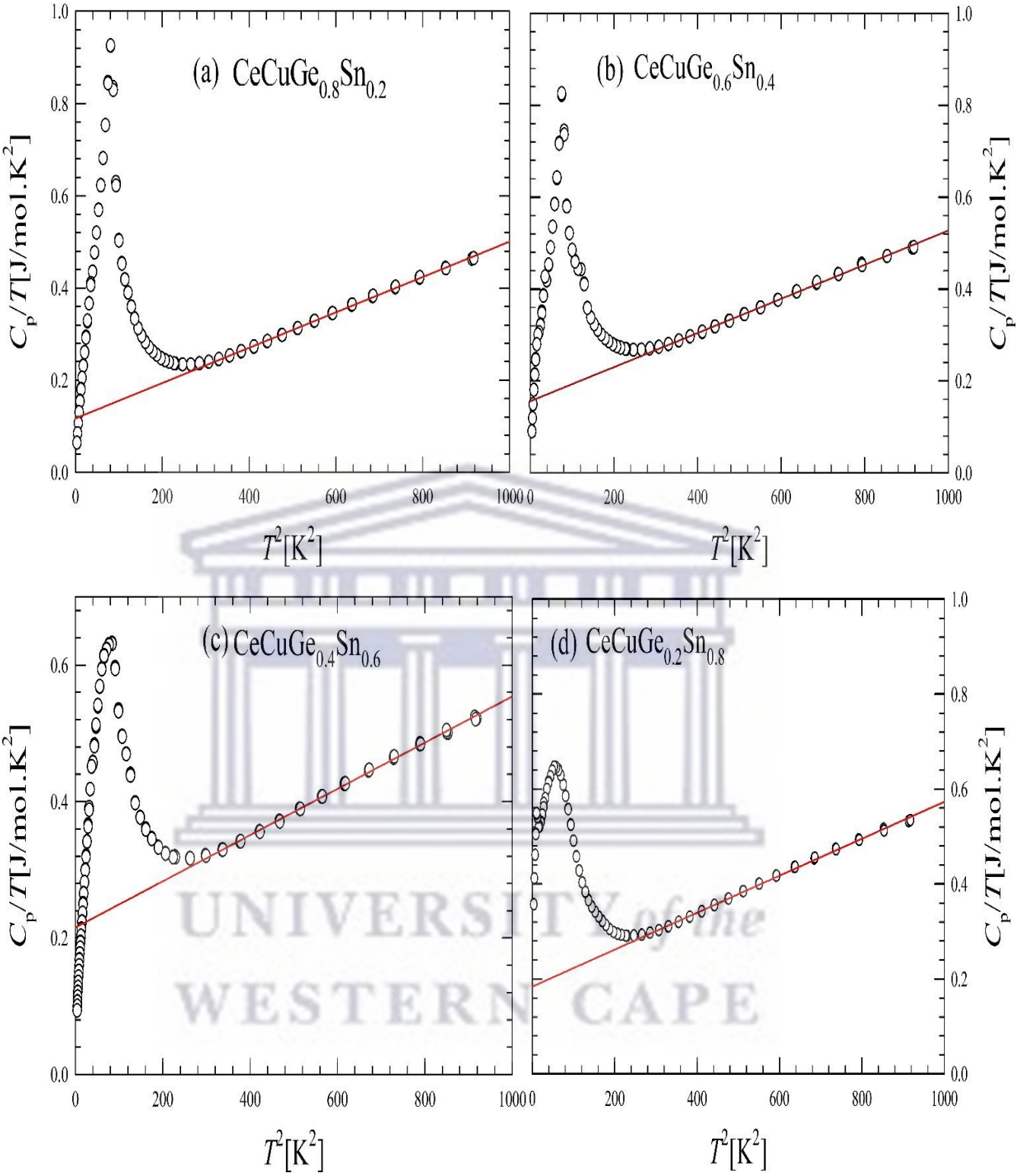

Figure 4.11: The plots of $C_p(T)/T$ versus T^2 of some samples in the alloy series $CeCu(Ge_{1-x}Sn_x)$. The red solid lines through the data point are the LSQ of the conventional equation (Eq. 4.2) for the specific heat of metals well above T_C and T_N (see text page 82).

Figure 4.12 shows $C_{4f}(T)$ results. In the ordering region below T_C, it is appropriate to consider to what extent $C_{4f}(T)$ data could be ascribed to the cooperative effect of spin-wave excitations. Assuming magnon excitations, with an energy gap, Δ_C in the FM spin-waves spectrum, the solid red curves in figure 4.12 depict LSQ fits of $C_{4f}(T)$ below T_C according to the formula [163, 164, 165]:

$$C_{sw}(T) = \gamma T + AT^{3/2} exp\left(-\frac{\Delta_C}{T}\right), \tag{4.3}$$

where γ is the Sommerfeld coefficient which represent the free-electron contribution to the specific heat and *A* is a constant. The resulting LSQ fits parameters are gathered in Table 4.5. The values of Δ_C and *A* for $x = 0.2$ are of the same order of magnitude as those reported before for CeCuGe [33, 163].

Table 4.5: LSQ fit parameters of the low temperature heat capacity data of selected samples of the CeCu($Ge_{1-x}Sn_x$) alloy series according to the spin-wave descriptions.

Sn content *x*	γ [J/mol.K^2]	*A* [J/mol.K$^{5/2}$]	Δ_C [K]
0.2	0.112(9)	0.91(6)	12.4(6)
0.4	0.17(2)	0.59(8)	11(1)
0.6	0.086(3)	0.450(7)	7.2(2)

As can be inferred from Table 4.5, Δ_C and *A* decrease with increasing the Sn content *x* as one moves toward the AFM region.

Figure 4.13 displays the temperature dependence of the total entropy $S(T)$ calculated from the $C_p(T)$ data of each measured sample using the relation:

$$S(T) = \int_0^T \left[\frac{C_p(T')}{T'}\right] dT. \tag{4.4}$$

For all samples, $S(T)$ reaches a value of $Rln2$ expected for doublet ground state somewhat above their respective transition temperature (Black dashed lines figure 4.13).

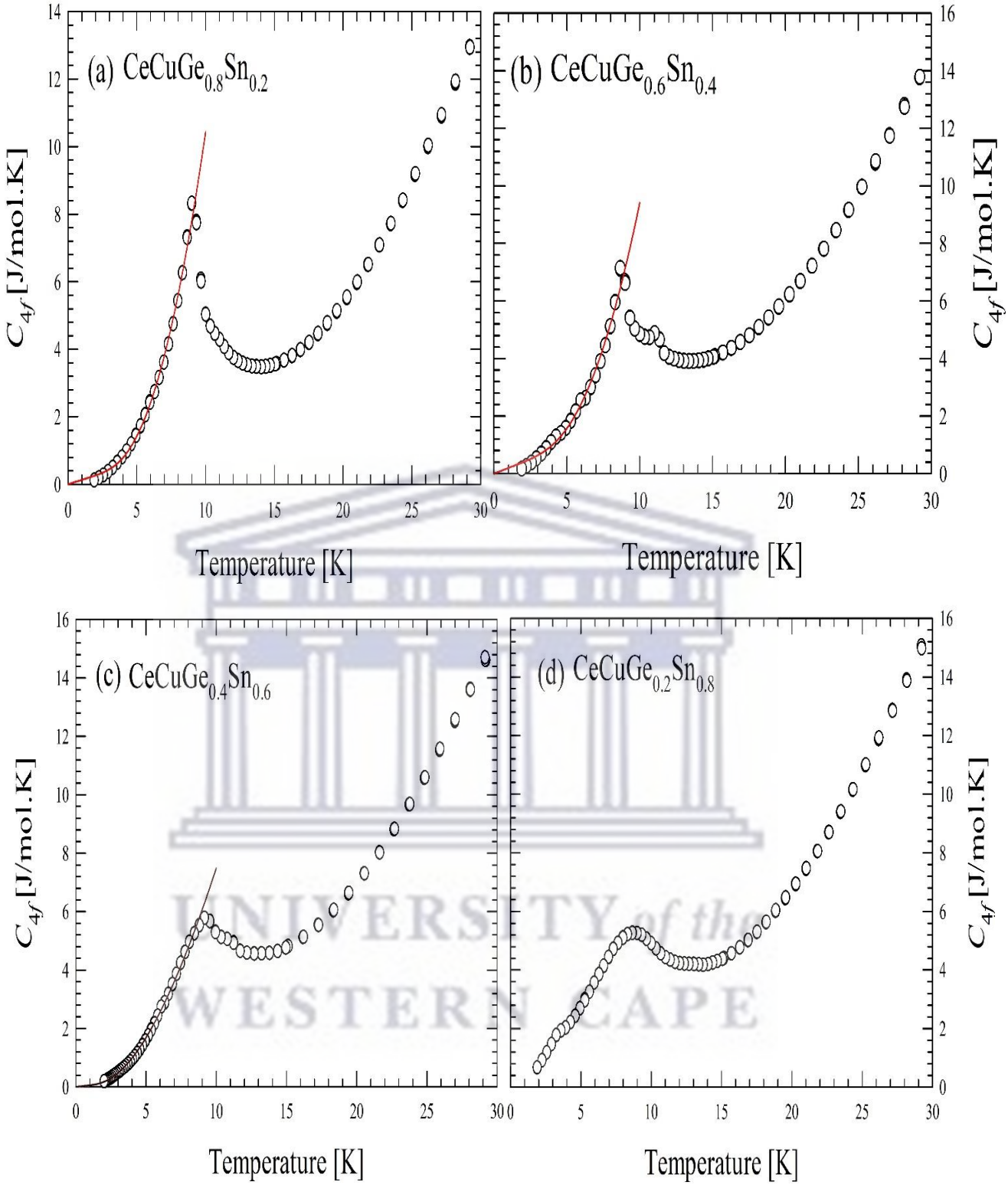

Figure 4.12: The low temperature of the 4*f*-electron specific heat, $C_{4f}(T)$ of selected samples in the FM and AFM region in the alloy series $CeCu(Ge_{1-x}Sn_x)$. The red solid curves through the data points are LSQ fits of the spin-wave spectrum (Eq. 4.3).

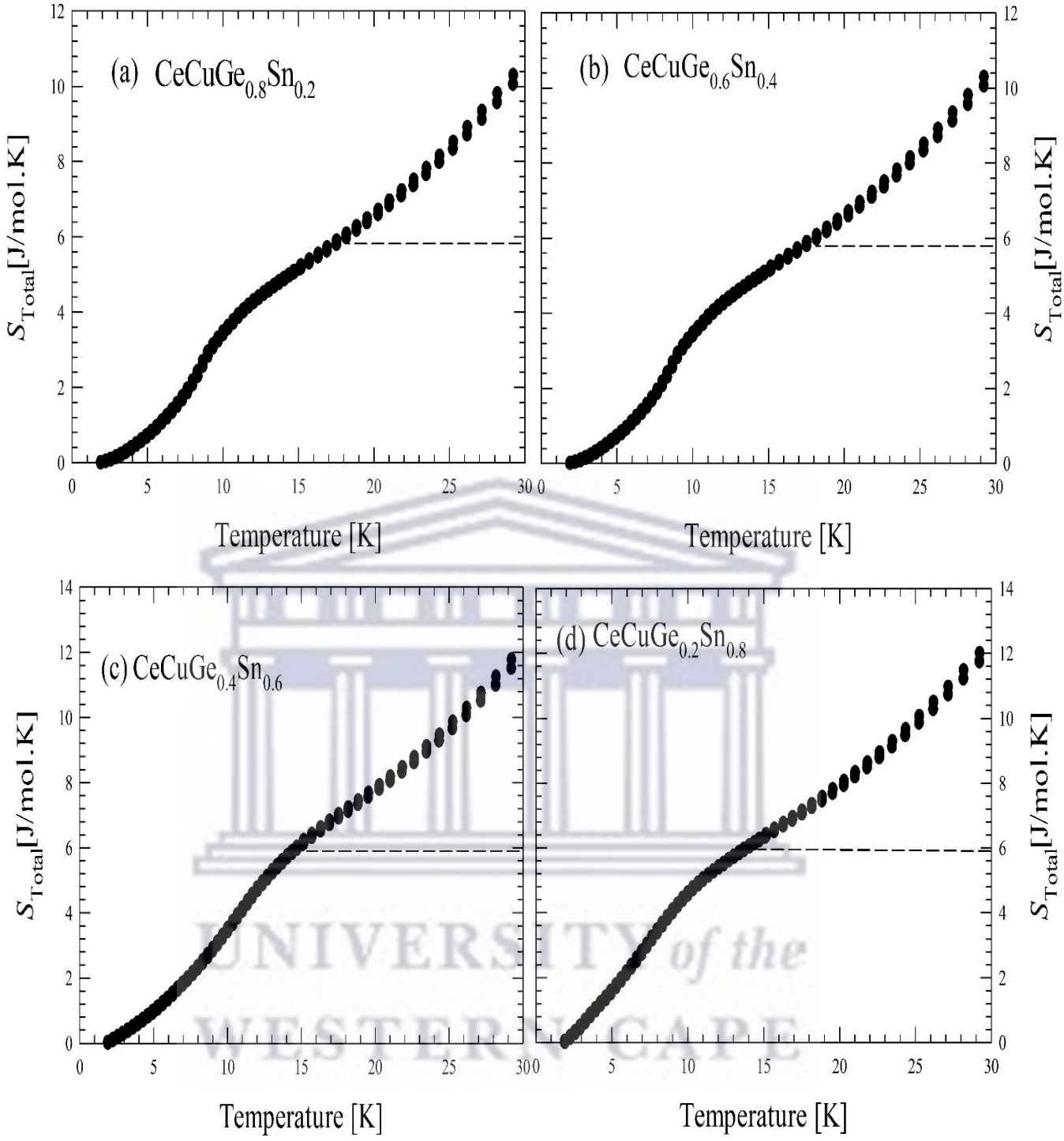

Figure 4.13: The temperature dependence of the total entropy, *S* (*T*) with the dashed line indicating the value of *Rln*2 expected for a doublet ground state in some samples in the alloy series $CeCu(Ge_{1-x}Sn_x)$.

4.3.4 Electrical resistivity

The temperature dependence of the electrical resistivity, ρ (*T*) of selected samples in CeCu($Ge_{1-x}Sn_x$) alloy series ($0.1 \leq x \leq 0.8$) are shown in figure 4.14. ρ (*T*) was measured in zero external magnetic field in the temperature range 2 to 300 K. All measured samples exhibited a metallic behaviour with a quasi-linear behaviour of ρ (*T*) over an extended temperature interval. Above 20 K, the resistivity data can be well described by the Bloch-Grüneisen-Mott (BGM) formula [166]:

$$\rho(T) = (\rho_0 + \rho_0^{\infty}) + 4AT(\frac{T}{\theta_R})^4 \int_0^{\theta_R/T} \frac{x^5}{(e^{x-1})(1-e^{-x})} dx - KT^3, \quad (4.5)$$

where the first term is a sum of the residual resistivity, ρ_0 due to scattering of the conduction electrons on static defects and imperfections in the crystal lattice and the spin-disorder resistivity, ρ^{∞} due to scattering on disordered magnetic moments. The second term represents the electron-phonon scattering processes with θ_R a rough measure of the Debye temperature, while the third one accounts for Mott-type *s-d* interband scattering. The constants *A* and *K* are related to the strengths of the electron-phonon and the *s-d* interactions respectively. It should be noted that the BGM approach is applicable only in the temperature range in which the CEF effect can be neglected (ρ^{∞} is assumed temperature independent). In the case of CeCu($Ge_{1-x}Sn_x$) alloy series, the χ (*T*) data (see section 4.3.2) indicated that the CEF interactions are indeed almost irrelevant in the region considered in the numerical evaluation of ρ (*T*). LSQ fits of the BGM formula to the experimental data are shown as red solid curves in figure 4.14. The resulting parameters obtained from the fits are listed in Table 4.6. At temperatures well below 20 K, in the magnetically ordered state, the electrical resistivity of all investigated samples drop suddenly owing to reduction in conduction electron scattering on the magnetic moments.

As inferred in Table 4.6, θ_R values decrease with increasing Sn content *x*, which suggests the increase in the lattice vibrations as a result of the large atomic mass of Sn atom compared to the atomic mass of Ge atom.

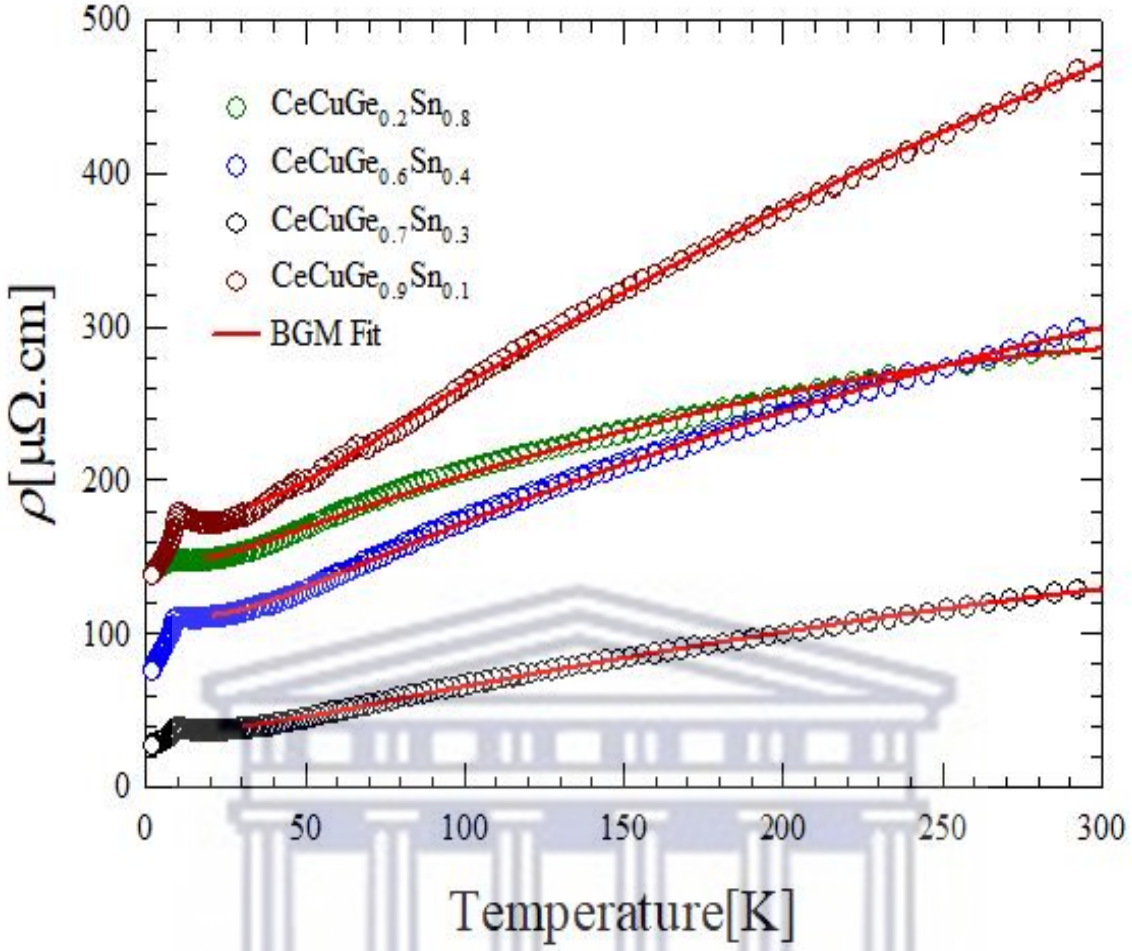

Figure 4.14: Temperature dependence of the electrical resistivity, ρ (*T*) of selected Samples in CeCu($Ge_{1-x}Sn_x$) alloy series ($0.1 \leq x \leq 0.8$). The solid red curves represent the Bloch-Grüneisen-Mott (BGM) fits (Eq. 4.5).

Table 4.6: LSQ fit parameters of the BGM formula (Eq. 4.5) to the measured ρ (*T*) data above 20 K of selected samples in CeCu($Ge_{1-x}Sn_x$) alloy series ($0.1 \leq x \leq 0.8$).

Sn content (x)	$(\rho_0 + \rho_0^{\infty})$[μΩ.cm]	A [μΩ.cm/K]	θ_R [K]	K [$\times 10^{-6}$ μΩ.cm/K^3]
0.1	183.1(1)	1.1200(4)	225(1)	1.20(6)
0.3	39.2(1)	0.352(2)	209(2)	0.44(2)
0.4	111.6(1)	0.750(3)	185(2)	1.18(4)
0.8	148.6(1)	0.632(3)	135(2)	1.834(5)

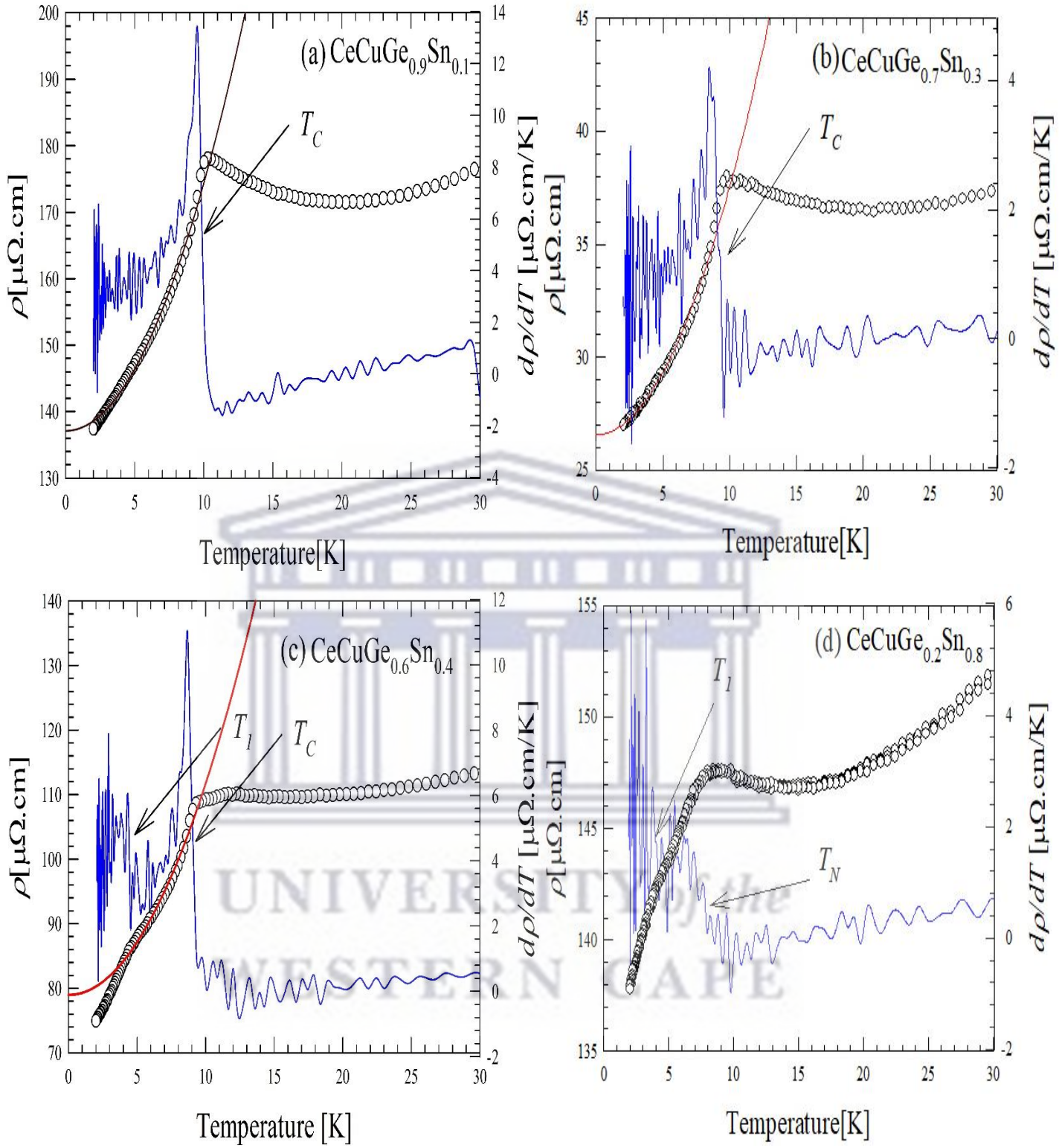

Figure 4.15: The left axis displays the low temperature ρ (*T*) data of selected samples in CeCu($Ge_{1-x}Sn_x$) alloy series ($0.1 \leq x \leq 0.8$). The right axis shows the derivative, $d\rho/dT$ which illustrates the magnetic phase transition at T_N and T_C as indicated by arrows. The red solid curves to the data points represent the LSQ fits to the spin-wave spectrum (Eq 4.6).

Figure 4.15, right axis shows the derivative, $d\rho/dT$ which illustrate the magnetic phase transition at T_N and T_C as indicated by arrows and listed in Table 4.7. Similar to the heat capacity results, a second magnetic phase transition was observed below T_C and T_N for the x = 0.4 and 0.8 alloys, respectively which indicated the spin reorientation of the magnetic moments of Ce ion. These values have been estimated in accordance with the criterion given by Sato *et al*. [167], which is at the midpoint of the anomaly produced due to the large drop in the $d\rho/dT$. The left axis of figure 4.15 displays the low temperature $\rho(T)$ data. As mentioned above, below the magnetic phase transition, a steep decrease bears testimony to the effects of long-range ordering in the spin sublattice on the electronic scattering. This sudden decrease in $\rho(T)$ of a ferromagnet within the ordering depends on whether the spin arrangement is spatially isotropic with a gapless dispersion in k-space or not. In the case of spatial isotropy, the energy gap, $\Delta_{FM} = 0$ and $\rho(T) \sim T^2$ is expected. In the case of spatially anisotropic ferromagnets or when a symmetry-lifting external field is applied, a gap may persist in the spectrum and the resistivity can be well described by the formula that accounts for scattering conduction electrons on ferromagnetic spin-waves excitation with energy gap Δ_{FM} in the magnon spectrum [168] given by:

$$\rho\,(T) = \rho_0 + A\Delta_{FM}T\left[1 + 2\frac{T}{\Delta_{FM}}\right]\exp\left(-\frac{\Delta_{FM}}{T}\right); \qquad (4.6)$$

where A is a prefactor that determines the stiffness of the sample. The red solid curves to the data points represent the LSQ fits of the Eq. 4.6 to the data points. The resulting LSQ fit parameters are gathered in Table 4.7. Using the results of the LSQ fits of Eq. 4.5 listed in Table 4.6, the spin-disorder resistivities are listed in Table 4.7 together with their respective transition temperature. For the sample with x = 0.8 in the AFM state, the low temperature ρ (T) data below T_N exhibit almost linear behaviour with decrease temperature down to 2 K. Such linear decrease has been observed in many Gd based rare-earth compounds showing AFM behaviour below T_N, such as $Gd_8Pd_{24}Al$ [169], $GdCu_4Au$ [170], $GdPd_3$ [171], $Gd_8Pd_{24}Ga$ [172].

As inferred from Table 4.7, the value of the energy gap obtained from the resistivity, Δ_R for the sample with x = 0.4 is of the same order of magnitude with the value of the energy gap obtained from the heat capacity, Δ_C. Furthermore, in contrast to the behaviour of Δ_C with respect to Sn content, the values of Δ_R increase with Sn content x.

Table 4.7: LSQ fit parameters of the spin-wave dispersion relation (Eq. 4.6) to the measured ρ (*T*) data below T_C of selected sample in CeCu($Ge_{1-x}Sn_x$) alloy series ($0.1 \leq x \leq 0.4$).

Sn content (*x*)	ρ_0 [$\mu\Omega$.cm]	*A* [$\mu\Omega$.cm/K^2]	Δ_R[K]	T_C , (T_N) [K]	ρ_0^{∞}[$\mu\Omega$.cm]
0.1	137.4 (1)	0.193 (2)	0.7 (2)	9.8	45.6(1)
0.3	27.0 (1)	0.073 (1)	3.8 (2)	9.4	12.2(1)
0.4	86.4 (1)	0.42 (3)	17.5 (7)	9	25.2(1)
0.8	-	-	-	(8.8)	-

Below 30 K, shallow minima are observed in ρ (*T*) data for samples with *x* = 0.1, 0.3 and 0.8. These minima occur at T_{min} = 20.3, 13.8 and 16.2 K for *x* = 0.1, 0.3 and 0.8, respectively and furthermore shift to lower temperatures with increasing Sn content *x*. Below these minima, ρ (*T*) data increase toward T_C and T_N with a further decrease in temperature. Such an increase was observed in several rare – earth compounds such as $RE_8Pd_{24}Ga$ (RE = Gd and Tb) [172], $GdPd_3$ [171], $RE_8Pd_{24}Al$ (RE = Gd, Tb, Dy and Ho) [169]. In the case of $GdPd_3$, it was reported that the observed minimum was possibly due to the opening of antiferromagnetic superzone gap (pseudogap for $T \geq T_N$ = 6.5 K and gap for T < 6.5 K) at the Fermi surface, which is a manifestation of the magnetic structure whose periodicity is incommensurate with the periodicity of the crystal lattice [171]. In the case of the family of compounds $RE_8Pd_{24}Al$ (RE = Gd, Tb, Dy and Ho), Singh and Dhar [169] reported that, since the minimum occurs at temperature below T_N, the increase in the resistivity for temperature range between T_N and T_{min} in the paramagnetic region cannot be attributed to the magnetic-superzone-induced gap effect.

Since the AFM order is associated with large reciprocal magnetic lattice vector, typically for temperatures above T_N, the large-*k* (*k* being the wave vector) fluctuations diminish while small-*k* fluctuations grow [169, 173] which should lead to a decreasing resistivity in AFM materials above T_N. Henceforth, the resistivity minima arise because the phonon contribution to the resistivity is increasing slower than the decrease of the critical resistivity in the paramagnetic region which results in a negative temperature coefficient for the resistivity in a certain range of temperature [169]. To further investigate the opening of the FM superzone pseudogap at the Fermi surface in CeCu($Ge_{0.9}Sn_{0.1}$), the plot of ρ(*T*) data of this alloy is shown in figure 4.16, together with the LSQ fit of the activated behaviour [171]:

$$\rho(T) = A + Bexp\left(\frac{\Delta_{sg}}{T}\right), \tag{4.7}$$

where A and B are constants and Δ_{sg} is the superzone band gap. LSQ fits of Eq. 4.7 to ρ (T) data in the temperature range $T_N < T < T_{min}$ yielded the values of A = 168.8 (5) μΩ.cm, B =0.5 μΩ.cm, and Δ_{sg} = 32 (2) K. Attempts to fit this activation behaviour for $CeCu(Ge_{0.7}Sn_{0.3})$ and $CeCu(Ge_{0.2}Sn_{0.8})$ alloys with the present ρ (T) of these samples which exhibit a very small increase below T_{min} was not successful.

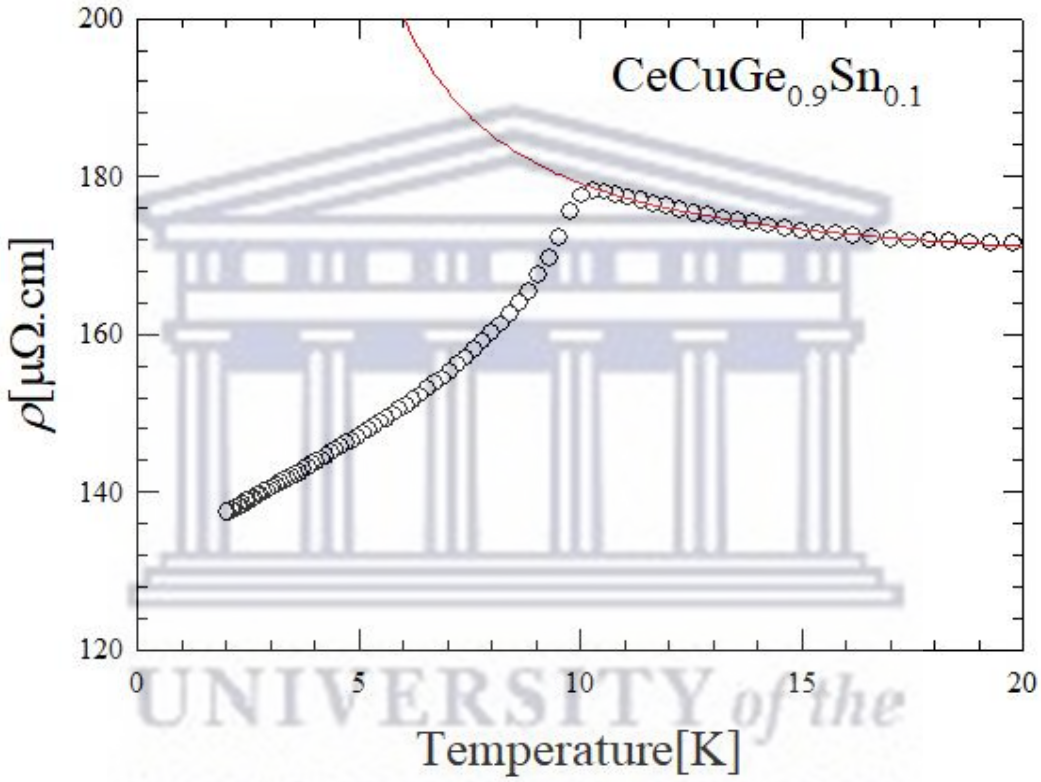

Figure 4.16: The FM superzone pseudogap at the Fermi surface in $CeCu(Ge_{0.9}Sn_{0.1})$, the red solid line present the LSQ fit of FM superzone band gap (Eq. 4.7).

4.3.5 Conclusion

XRD results confirm the hexagonal ZrBeSi-type crystal structure with space group *P6₃/mmc* for all investigated samples in the alloy series $CeCu(Ge_{1-x}Sn_x)$. The resulting unit cell volume increases linearly with increasing Sn content *x* as a result of the bigger atomic radius of Sn compared to Ge atom which suggest no valence change of Ce-ion across the series and confirm the Vegard's rule. The susceptibility, $\chi(T)$ data for all samples follow the Curie-Weiss law at high temperatures in the paramagnetic region, given an effective magnetic, μ_{eff} values close to that predicted within the Russell-Saunders coupling scenario for the trivalent Ce^{3+}-ion (2.54 μ_B). The negative values of the Weiss temperature, θp obtained for all samples in the FM and AFM states, indicate that this system is dominated by AFM exchange interactions of the Ce magnetic moments. At low temperatures, $\chi(T)$ data for all investigated samples in the series order magnetically below T_C and T_N due to the magnetic moments carried on trivalent Ce^{3+}-ion. The magnetization data, $M(\mu_0 H)$ exhibit metamagnetic behaviour for samples in the AFM regime.

The low temperature heat capacity, $C_p(T)$ and electrical resistivity, $\rho(T)$ data confirm the magnetic phase transition temperatures at T_C and T_N and revealed the occurrence of a second magnetic phase transition below T_C and T_N which may be attributed to spin reorientation or rearrangement of the magnetic moments of Ce ions. Furthermore, $C_p(T)$ and $\rho(T)$ data below T_C are well described by the spin-wave excitations with energy Δ_C and Δ_R in the FM spin-wave spectrum. The total entropy, $S(T)$ for all measured samples reaches a value of *Rln2* expected for doublet ground states above their respective phase transition temperature. $\rho(T)$ data of all investigated samples are well described by the BGM formula in the paramagnetic region at high temperature. Resistivities minima were observed for some samples and were attributed to FM superzone pseudogap at the Fermi surface in these samples. The overall measurements of the magnetization, magnetic susceptibility, heat capacity and electrical resistivity are unequivocal in their evidence of ligand substitution-induced transition of the magnetic ground state from ferromagnetic to antiferromagnetic order in CeCuGe**.** The FM order extends up to 60% Sn substitution which confirms the robustness of the FM state of CeCuGe compound.

Chapter 5

4*f*-electron substitution-induced transition of the magnetic ground state from antiferromagnetic to ferromagnetic order in $(Ce_{1-x}Nd_x)CuGe$

Abstract

This chapter reports the 4*f*-electron substitution-induced transition of the magnetic ground state from AFM to FM order in $(Ce_{1-x}Nd_x)CuGe$ by means of electrical resistivity, magnetic susceptibility and magnetization measurements. As found from the powder XRD studies, except for the parent compound CeCuGe which crystallizes in the ZrBeSi-type hexagonal crystal structure with space group *P6₃/mmc* (No. 194), all samples indicate the AlB_2-type hexagonal crystal structure with space group *P6/mmm* (No. 191). The temperature dependence of the electrical resistivity, ρ (*T*) of selected samples at high temperatures is characteristic of electron-phonon interaction (metallic behaviour) in the presence of *s-d* scattering assuming negligible crystal-electric field. In the ordering state, ρ (*T*) data for samples ordering ferromagnetically can be well described in terms of FM spin-wave dispersion with an energy gap. Above the ordering temperature and below the temperature of the resistivity minimum for some samples order antiferromagnetically, and ρ(*T*) data can be represented in terms of AFM superzone pseudogap with an energy gap.

The magnetic susceptibility, χ(*T*) at high temperatures follows the Curie-Weiss relation given an effective magnetic moment which increases from the value expected for the free Ce^{3+}-ion (2.54 μ_B) to that expected for the free Nd^{3+}-ion (3.62 μ_B) with positive and negative Weiss temperature, θ_p. χ (*T*) data at low temperature indicate AFM transition for alloys in the concentration range $0.7 \leq x \leq 1$ and FM for $x \leq 0.6$. The magnetization, $M(\mu_0 H)$ results for samples exhibiting AFM behaviour initially increases linearly at low field and deviate from linear behaviour characteristic of metamagnetic behaviour at low field. $M(\mu_0 H)$ results for samples exhibiting FM behaviour show saturation in high magnetic fields.

5.1 Introduction

Among the equiatomic ternary compounds of rare-earth, a number of recent reviews have highlighted their crystallographic and magnetic properties [1-5]. These compounds exhibit

a variety of magnetic behaviour depending on the ratio of exchange interactions to crystal field interactions [174]. Of these compounds, ternary equiatomic lanthanide copper germanides with the general formula RCuGe (R = rare earth metals), which crystallize in several different structure types have been intensively reported in the literature [69, 175, 176, 177]. The crystal and magnetic structures of this family of compounds was determined by neutron diffraction on polycrystalline samples [2]. The compound with R = Pr and Nd crystallized in the hexagonal AlB_2-type crystal structure while other compounds show hexagonal LiGaGe-type structure [2]. Goruganti *et al*. [174] report that NdCuGe compound adopted the AlB_2-type structure with space group *P6/mmm*, No. 191, with mixed occupation of Cu and Ge on B sites in the AlB_2 lattice also reported elsewhere in the literature [2, 153]. The magnetic properties studies of the NdCuGe compound in particular indicated that compound exhibited a collinear antiferromagnetic structure below T_N = 3.5 K with a unit cell dimension $a_m = \sqrt{(3a_h)}$, $b_m = a_h$, $c_m = c_h$ and magnetic moments parallel to the *a*-axis [152].

Electrical resistivity, heat capacity and dc magnetization measurements were reported on the intermetallic NdCuGe over a temperature range 2-300 K [173]. It is was reported that NdCuGe exhibited magnetization attributable to Nd^{3+} moments, with an antiferromagnetic transition at T_N = 3.1 K. The magnetization, heat capacity and resistivity results were used to determine the crystalline electric field (CEF) splitting of the Nd^{3+} magnetic sublevels. It was found that the ground state was a doublet composed of ±5/2 levels and the antiferromagnetic state was built from this magnetic doublet, with a reduction in the average sublattice magnetization attributed to the site disorder among Cu-Ge sites [174]. It was also reported that the low temperature electrical transport was dominated by spin – disorder scattering among CEF split levels and a small T^2 spin fluctuation term. This spin fluctuation term was almost two orders of magnitude smaller than previously observed isostructural CeCuGe which ordered ferromagnetically below T_C = 10 K.

The present chapter reports the 4*f*-electron substitution-induced transition of the magnetic ground state from antiferromagnetic to ferromagnetic order in $(Ce_{1-x}Nd_x)CuGe$, through measurements of electrical resistivity, magnetic susceptibility and magnetization.

5.2 Sample preparation and characterization

Polycrystalline samples of the alloys series $(Ce_{1-x}Nd_x)CuGe$ with $0 \leq x \leq 1$ were

synthesized by arc-melting stoichiometric amounts of the elements Ce, Nd, Cu and Ge as described in section 3.2. The purity of these elements is also indicated in section 3.2. The weight losses of all samples after final melting were always less than 1 wt. %. Subsequently the samples were subjected for heat treatment as described in section 3.2. The products were checked by powder XRD using a Bruker D8 ADVANCED diffractometer with CuKα radiation described in chapter 3. The X-ray diffraction pattern for members of all the alloy series were analyzed using the CAILS-Pawley refinement method and the full-profile Rietveld refinement method for the end product NdCuGe both from TOPAS ACADEMIC programme. XRD analysis of the compound CeCuGe are illustrated in chapter 4. All prepared samples were single phase with no evidence of parasitic phases or unreacted elements. Further characterization of the parent compound NdCuGe, by electron micro-probe and the scanning electron microscopy (SEM) analysis were performed to obtain the chemical sample and morphology of the samples.

5.3 Results and discussion

5.3.1 Scanning electron microscopy (SEM)

Figure 5.1 shows SEM micrograph of the NdCuGe compound magnified at 50 μm. The image shows microstructure with an uneven textured surface. Dislocations are observed at the surface. Atomic ratios of the elements as obtained from electron dispersive spectroscopy (EDS) analyses indicate the sample elemental sample normalized to the Nd content to be $NdCu_{0.941(2)}Ge_{0.996(2)}$ which is roughly in the 1:1:1 sample.

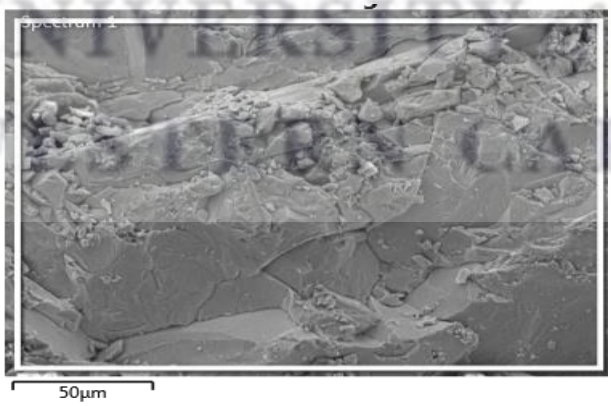

Figure 5.1: Cross section for NdCuGe with a scale of 50 μm**.**

5.3.2 Lattice parameters and crystallography

Figure 5.2 shows XRD spectra of the alloys $(Ce_{1-x}Nd_x)CuGe$ (x = 0, 0.3, 0.6 0.8), together with the CAILS-Pawley refinement results. Except for the CeCuGe compound which crystallize in the ZrBeSi-type hexagonal crystal structure with space group $P6_3/mmc$ (No. 194), all samples were found to crystallize in the AlB_2 – type hexagonal crystal structure with space group *P6/mmm* (No. 191).

The lattice parameters and unit cell volume (v = a. b. c sin 60^o) for the parent compound NdCuGe resulting from the fit were found to be $a = b$ = 4.279 (2) Å, c = 3.899 (3) Å, and V = 61.834 (8) Å^3 in good agreement with previously reported values in the literature [174]. The lattice parameters and the unit cell volume for all samples resulting from the fit are plotted as a function of Nd content in figure 5.3.

It is observed that the refined room-temperature lattice parameter (a) and unit cell volume (V) decrease linearly with increasing Nd content. The decrease of V with x result from the small atomic radius of Nd atom compared to that of Ce atom and amount to 51% change in volume. It should be noted that, this large change in the unit cell volume does not only result from the difference of atomic radii since they are comparable, but results from the difference in the two crystal structures of both parent compounds with CeCuGe being a double hexagonal close-packed (dhcp)) and NdCuGe being hexagonal close-packed (hcp) structure. This decrease in V also corroborates with Vegard's rule which suggests no sudden change in Ce and Nd valence across the series, as well as no change in the number of conduction electrons, which ensures metallic bonding of the alloy system. Figure 5.4 displays the XRD pattern of NdCuGe together with the full profile Rietveld LSQ refinement (solid black curve in figure 5.4).

The space group setting used in the refinement was the hexagonal P6/mmm (No. 191). In this space group, Nd atoms occupy the crystallographic sites 2*a* with atomic coordinate (0,0,0), Cu atoms occupy the crystallographic sites 2*c* with atomic coordinate (1/3,1/3,1/2) while Ge atoms occupy the crystallographic sites 2*d* with atomic coordinate (1/3,2/3,1/2). In this refinement the site occupancy (S.O.) and the isotropic temperature factor (beq) of all the atoms was kept fixed at 100%. The resulting refinement instrumental parameters of the Rietveld refinement (R_p, R_{wp}, R_{exp}, χ^2, DW, R_B and phase density) for NdCuGe are listed in Table 5.1 and the resulting atomic coordinates are gathered in table 5.2.

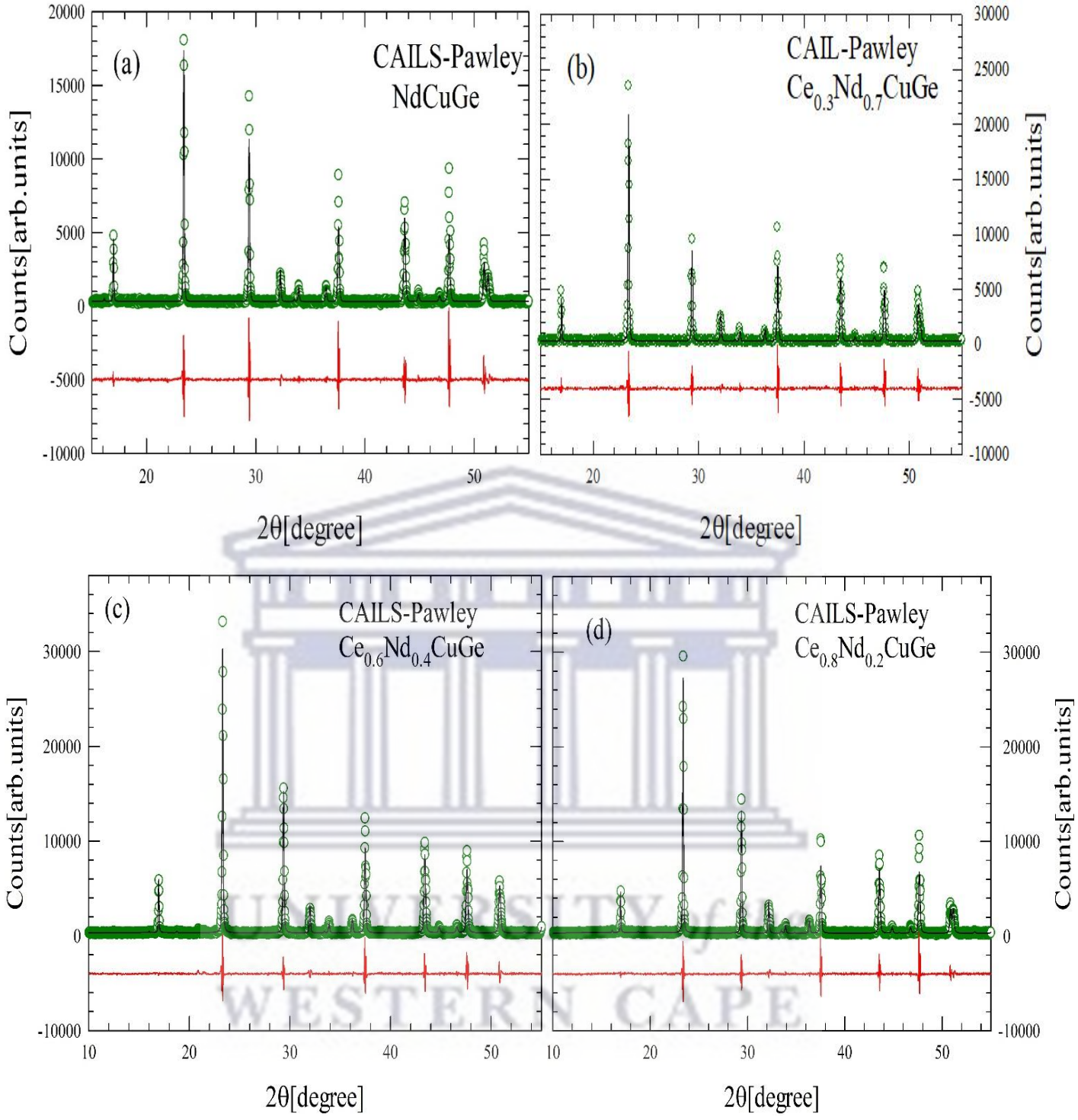

Figure 5.2: CAILS-Pawley analysed pattern of selected samples of $(Ce_{1-x}Nd_x)CuGe$. The observed data are shown by green symbols and the solid black lines through the data represent the result of the CAILS refinement. The lower red curves are the difference curves between the experimental data and the calculated curves.

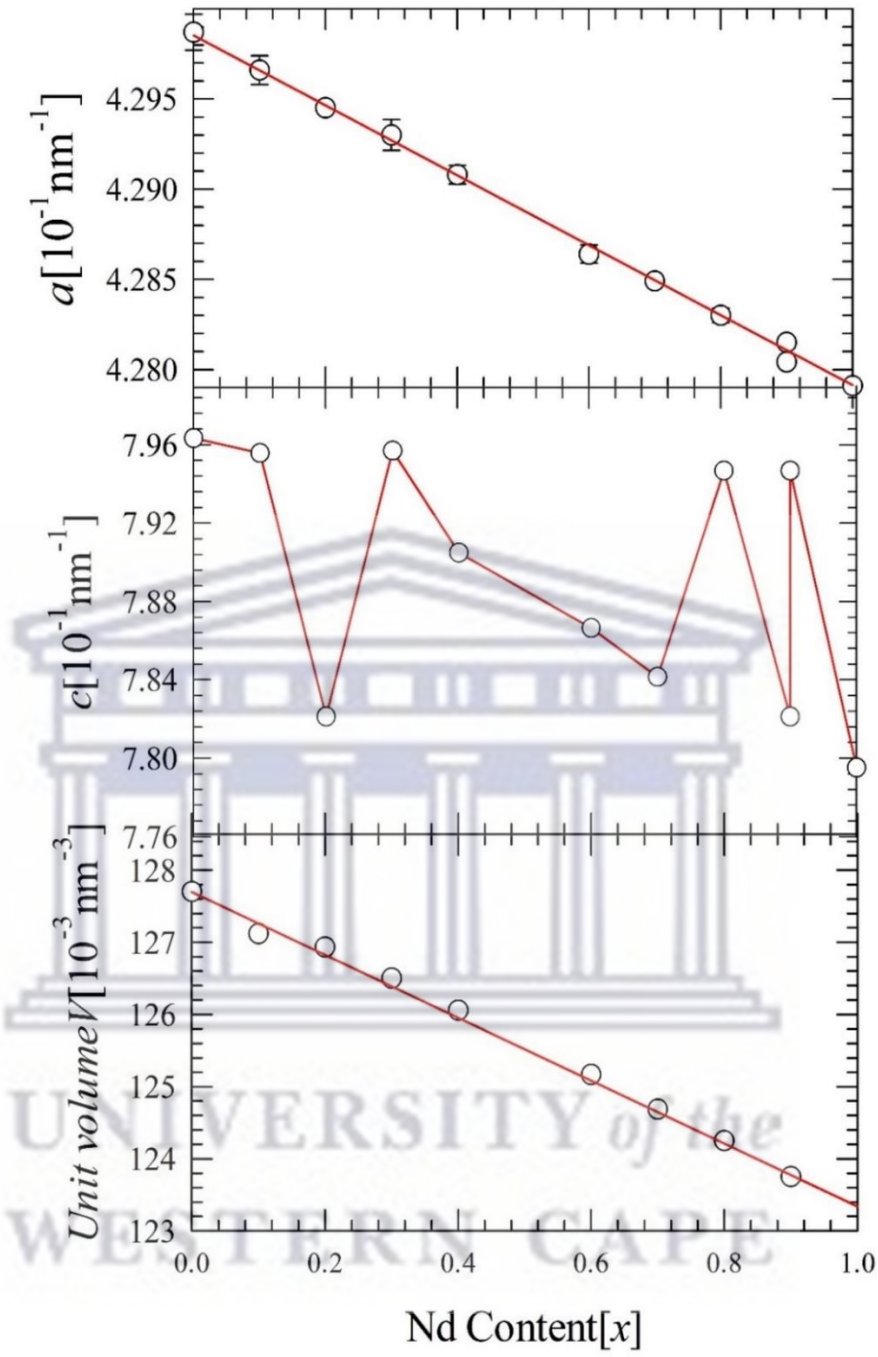

Figure 5.3: The figure shows the lattice parameters *a*, c and unit cell volume *V* in ($Ce_{1-x}Nd_x$)CuGe alloy series. The solid red lines in the lattice parameters *a* and the unit cell volume *V* are LSQ fits to the data. The red line in the middle panel is a guide to the eye.

Table 5.1: The refined instrumental parameters obtained from the CAILS-Pawley and the full profile Rietveld refinement methods for the NdCuGe.

Parameters	CAILS – Pawley	Rietveld
R_p [%]	16.005	4.651
R_{wp} [%]	20.325	6.596
R_{exp} [%]	4.344	1.875
χ^2	3.836	3.518
DW [%]	1.298	0.330
R_B [%]		8.954
Phase density [g/cm^3]		7.535

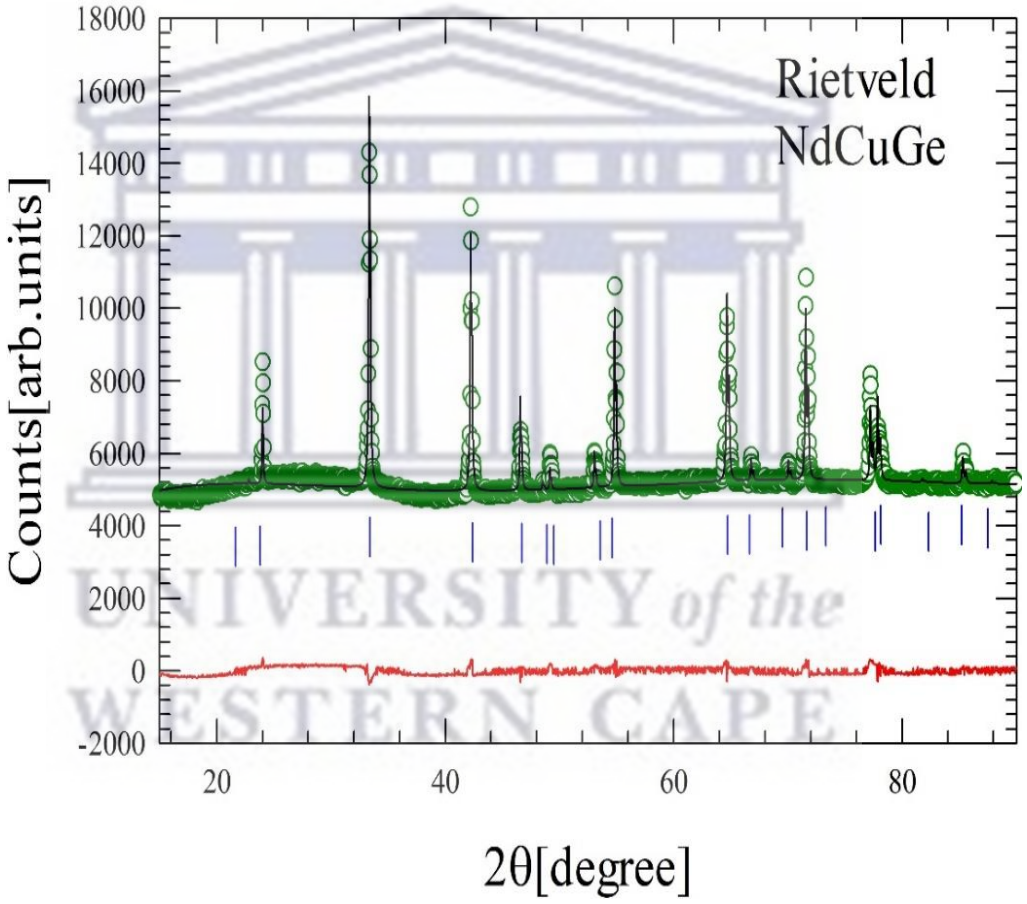

Figure 5.4: Rietveld analysed pattern of NdCuGe. The observed data are shown by green symbols and the solid black lines through the data represent the result of the CAILS refinement. The lower red curves are the difference curves between the experimental data and the calculated curves. The vertical blue ticks represent the Bragg's reflections.

Table 5.2: Atomic coordinates, site occupancy (S.O.) and the equivalent isotropic temperature factor (beq) for NdCuGe obtained from the full profile Rietveld refinement method using the space group *P6/mmm*. The S.O. and the beq were kept fixed.

Atoms	Wyckoff site	*x*	*y*	*z*	S.O.	beq
Nd	1a	0	0	0	1	1
Cu	2d	1/3	2/3	1/2	1	1
Ge	2d	1/3	2/3	1/2	1	1

The resulting hexagonal crystal structure of the AlB_2-type is depicted in figure 5.5. The observed values of the R-factors and χ^2 (goodness of fit) obtained from the CAILS and Rietveld refinement methods are indicative of good fits to the data. Furthermore, the values of *DW* for all investigated samples are less than the value of 2% in agreement with the ideal ranges of values of $0 < DW < 2\%$ [25, 26] which indicates that the quality of the fit model is correct.

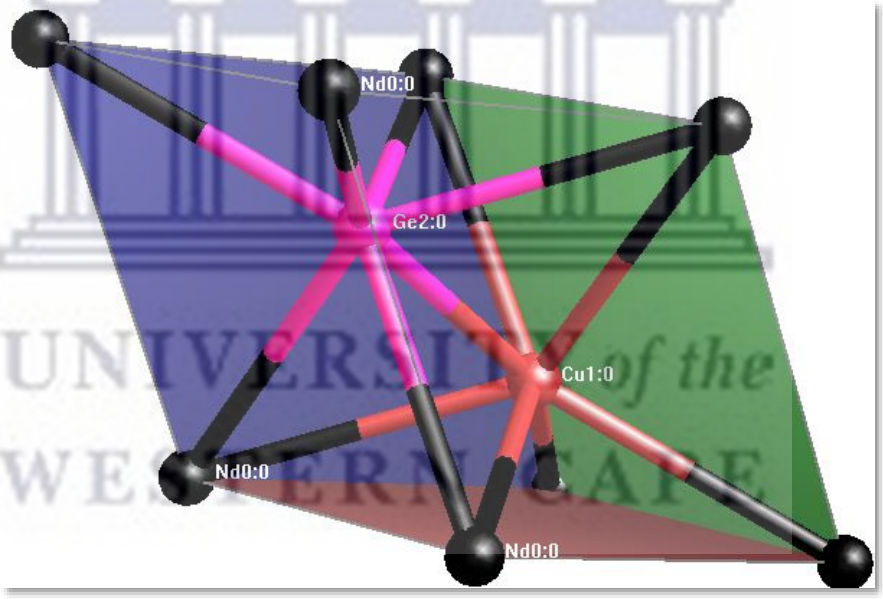

Figure 5.5: The hexagonal crystal structure of NdCuGe derived from Rietveld refinement method. The black circles represent the Nd atoms, the brown circles represent the Cu atoms and the pink circles represent the Ge atoms.

5.3.3 Magnetization and magnetic susceptibility

The field dependencies of the magnetization, M ($\mu_0 H$) measured at 1.7 K in fields up to 5 T are shown in figures 5.6 and 5.7 for samples of ($Ce_{1-x}Nd_x$)CuGe exhibiting AFM ($0.7 \leq x \leq 1$) and FM ($0.1 \leq x \leq 0.4$) behaviours respectively. It is observed that for samples exhibiting AFM behaviour, M ($\mu_0 H$) initially increase linearly at low field and exhibit a downward bending from linearity above 1 T. Hysteresis loops were observed for samples with $x = 1$ in low fields and $x = 0.9$ in field up to 4 T. On the other hand, for samples $0 \leq x \leq 0.7$, the shape of $M(\mu_0 H)$ are typical for FM materials. In fields stronger 0.5 T for Ce rich-alloys and 1 T for $x = 0.4$, $M(\mu_0 H)$ saturate at values less than 1.2 μ_B while the value of $M(\mu_0 H)$ at 5 T for samples exhibiting AFM behaviour is less 1.5 μ_B. These values of M ($\mu_0 H$) at 5 T for all samples are less than for both theoretical values of trivalent Ce (gJ = 2.14 μ_B) and Nd (gJ = 2.72 μ_B), likely due to combined effects CEF and magnetic anisotropy.

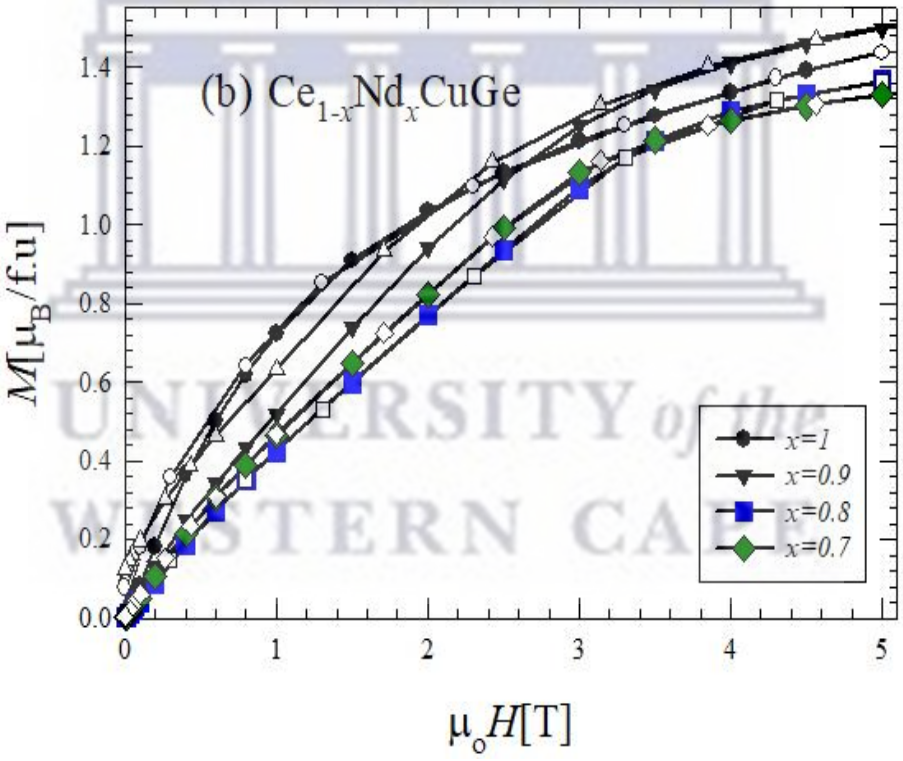

Figure 5.6: The field variation of the magnetization at 1.7 K for selected Samples of ($Ce_{1-x}Nd_x$)CuGe alloys with $0.7 \leq x \leq 1$ for increasing (closed symbols) and decreasing field (open symbols).

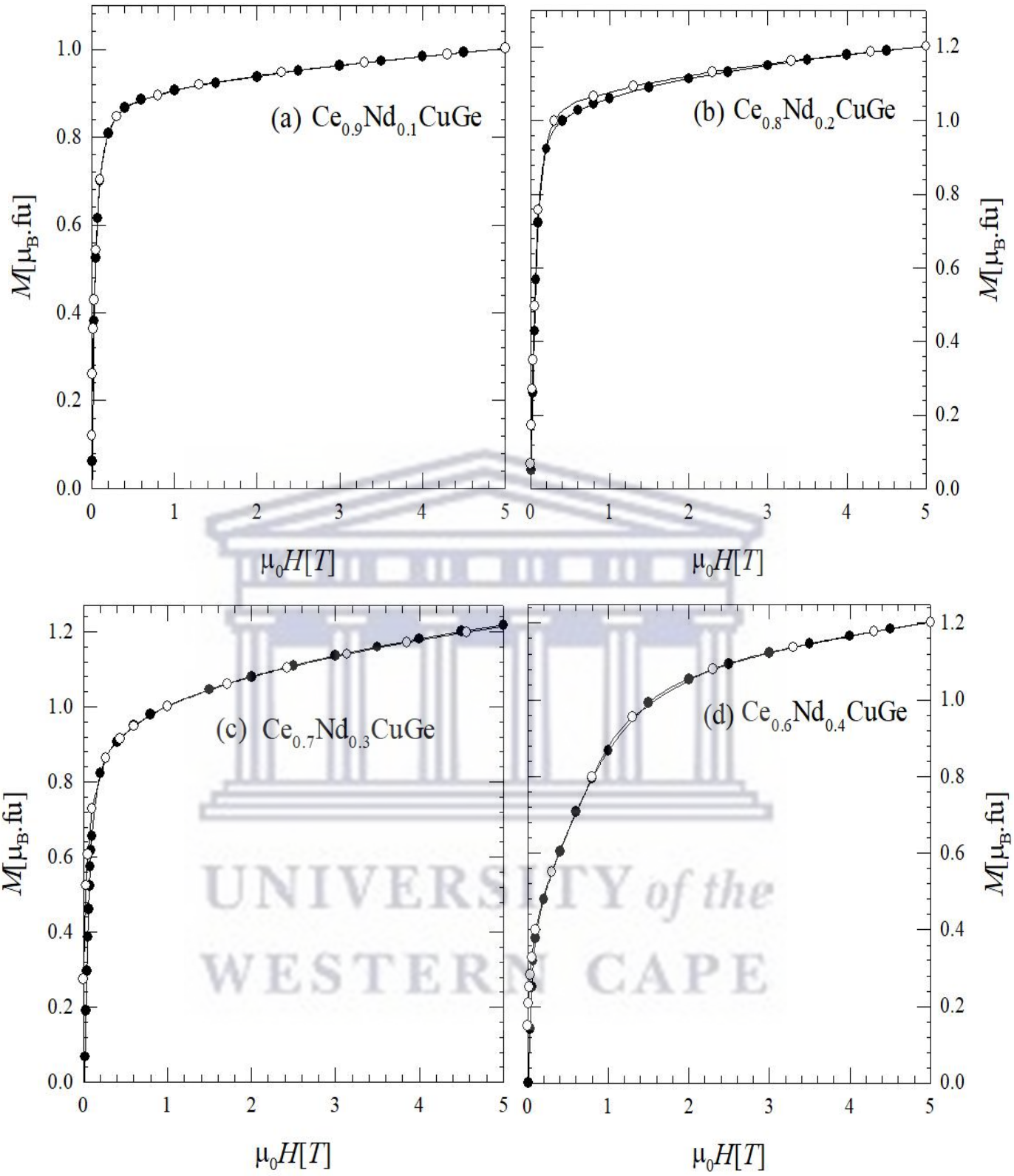

Figure 5.7: The field variation of the magnetization at 1.7 K for selected samples of ($Ce_{1-x}Nd_x$)CuGe alloys with $0.1 \leq x \leq 0.4$ for increasing (closed symbols) and decreasing field (open symbols).

The temperature variation of the dc-inverse magnetic susceptibility, $\chi^{-1}(T)$, measured in applied magnetic field of 0.1 T in the temperature range 1.7-400 K are depicted in figure 5.8 for the $(Ce_{1-x}Nd_x)CuGe$ alloys for $0 \leq x \leq 1$. The field of 0.1 T was chosen since M ($\mu_0 H$) was linear in this field range for all samples. It is observed that the reciprocal paramagnetic susceptibility follows the Curie-Weiss relationship (Eq. 4.1) over an extended temperature range above 100 K. LSQ fits of Eq. 4.1 against the experimental data are shown as solid red lines in figure 5.8. Parameters obtained from the LSQ fits are gathered in table 5.3.

The experimental effective magnetic moments, μ_{eff}^{Exp}, as well as the paramagnetic Weiss temperature, θ_p, were obtained from LSQ fits of the Curie-Weiss relation (Eq. 4.1) to the measured data in figure 5.8.

Table 5.3: Magnetic susceptibility data of the alloy system $(Ce_{1-x}Nd_x)CuGe$.

Nd Content x	$\mu_{eff}exp[\mu_B]$	$\mu_{eff}Calc[\mu_B]]$	$-\theta_P[K]$	$T_C^{\chi}[K]$	$T_N^{\chi}[K]$
1	3.632(1)		–2.27(1)		2.9
0.9	3.63(1)	3.508	2.44(2)		3.9
0.8	3.34(2)	3.396	–2.627(2)		2.7
0.7	3.444(1)	3.284	2.192(1)		3
0.6	3.264(1)	3.172	– 0.371(1)	7	
0.4	2.972(1)	2.948	3.066(2)	7.5	
0.3	2.947(3)	2.836	4.24(4)	9.5	
0.2	2.88 (3)	2.724	5.021(8)	9.8	
0.1	2.769(2)	2.612	– 19.86(4)	10.6	
0	2.500(3)		– 4.81(2)	11	

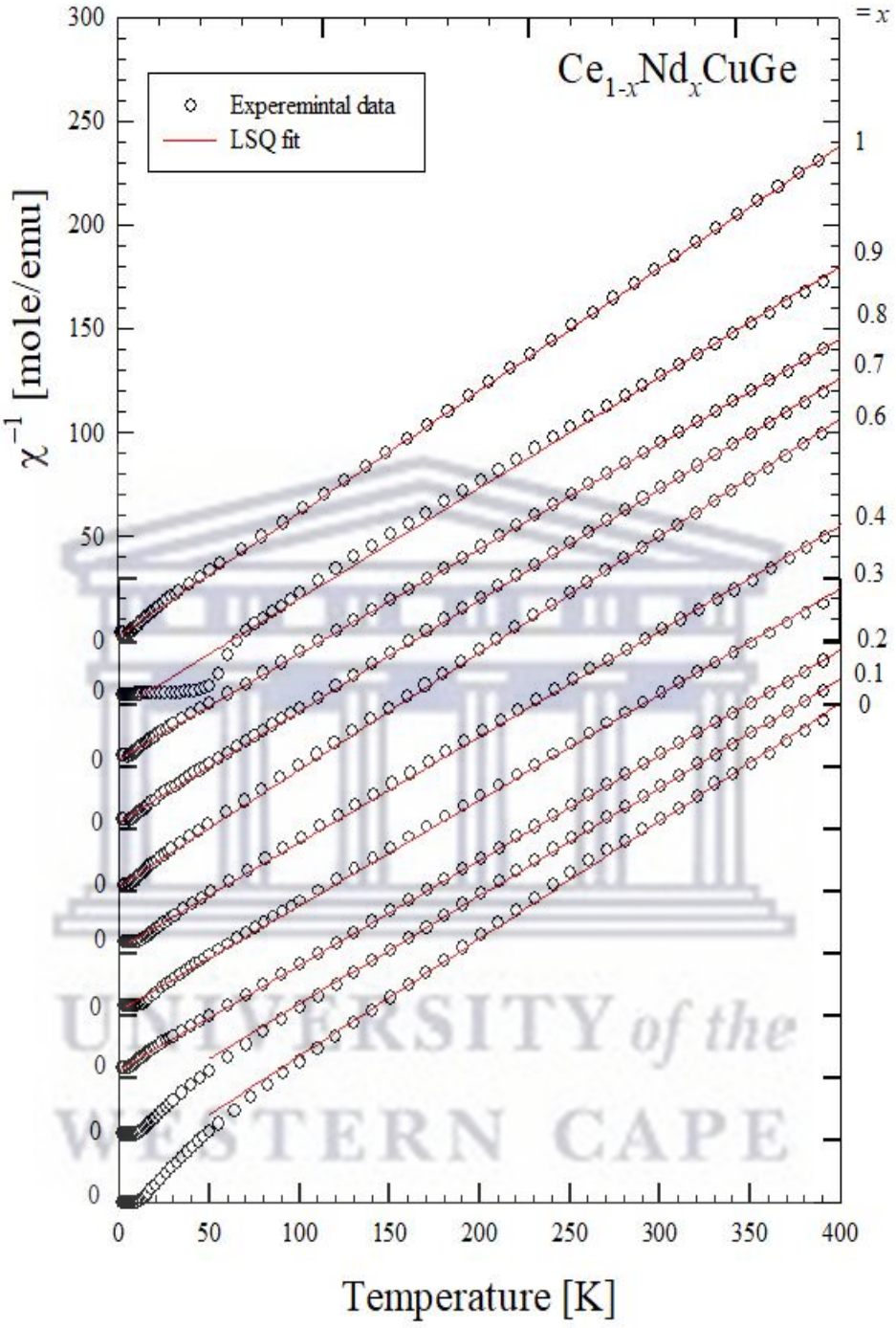

Figure 5.8: DC-inverse magnetic susceptibility, of ($Ce_{1-x}Nd_x$)CuGe alloys with the least-square (LSQ) fits of the Curie-Weiss law to the data points above 100 K.

Values of T_N were inferred from the positions of kinks as indicated by arrows in figure 5.10, while values of T_C were inferred from the positions of the minimum of $d\chi(T)/dT$ curves as indicated by arrows in figure 5.9. The calculated effective magnetic moment values were obtained from theoretical values of both free Ce and Nd ions of 2.54 and 3.62 μ_B respectively. The positive values of the Weiss temperature, θ_p, observed for sample with $x = 0.7$ exhibiting AFM behaviour indicated the presence of ferromagnetic exchange interactions in this samples, while the negative values of θ_p, observed for samples with $x = 0$ and 0.1 exhibiting FM magnetic behaviour, indicated the presence of antiferromagnetic exchange interactions as well. The effective magnetic moment values obtained for the two end compounds are in good agreement with the expected free-ion values of 2.54 μ_B for the Ce^{3+}-ion and 3.62 μ_B for the Nd^{3+}-ion. A gradual increase in the observed μ_{eff} values was evident between CeCuGe and NdCuGe suggesting that at high temperature the Ce and Nd atoms contributed independently to the total moment. We calculated the moment expected for all samples based on the assumption of independent contributions of the Ce and Nd atoms to the total moment. It is observed from table 5.6 that the calculated and observed values are in reasonable agreement.

Such behaviour was found in several systems such as $(Ce_{1-x}Tb_x)Pt_2Si_2$ [178], $(Ce_{1-x}Gd_x)Pt_2Si_2$ [179], $(Ce_{1-x}Gd_x)Cu_6$ [180], $(Ce_{1-x}RE_x)In_3$ [181]. As apparent from figure 5.9, the low temperature $\chi(T)$ data exhibited a behaviour characteristic of ferromagnets for samples in the range $0.1 \leq x \leq 0.4$. The magnetic phase transition temperature, T_C estimated from the midpoint of the abrupt rise in χ (T) curve that corresponds to the minimum in $d\chi(T)/dT$ amount to values of T_C listed in table 5.6. These values of T_C obtained from $\chi(T)$ data were in good agreement with the resistivity data (see section 5.3.3). Similarly, as observed in figure 5.10, the low temperature $\chi(T)$ data exhibited a behaviour that may be associated to antiferromagnets for samples in the range $0.7 \leq x \leq 1$. The magnetic phase transition temperature T_N estimated at the kinks of $\chi(T)$ curve amounted to values of T_N listed in table 5.6. Our value of T_N for the NdCuGe is in good agreement with previous reported value in the literature [182].

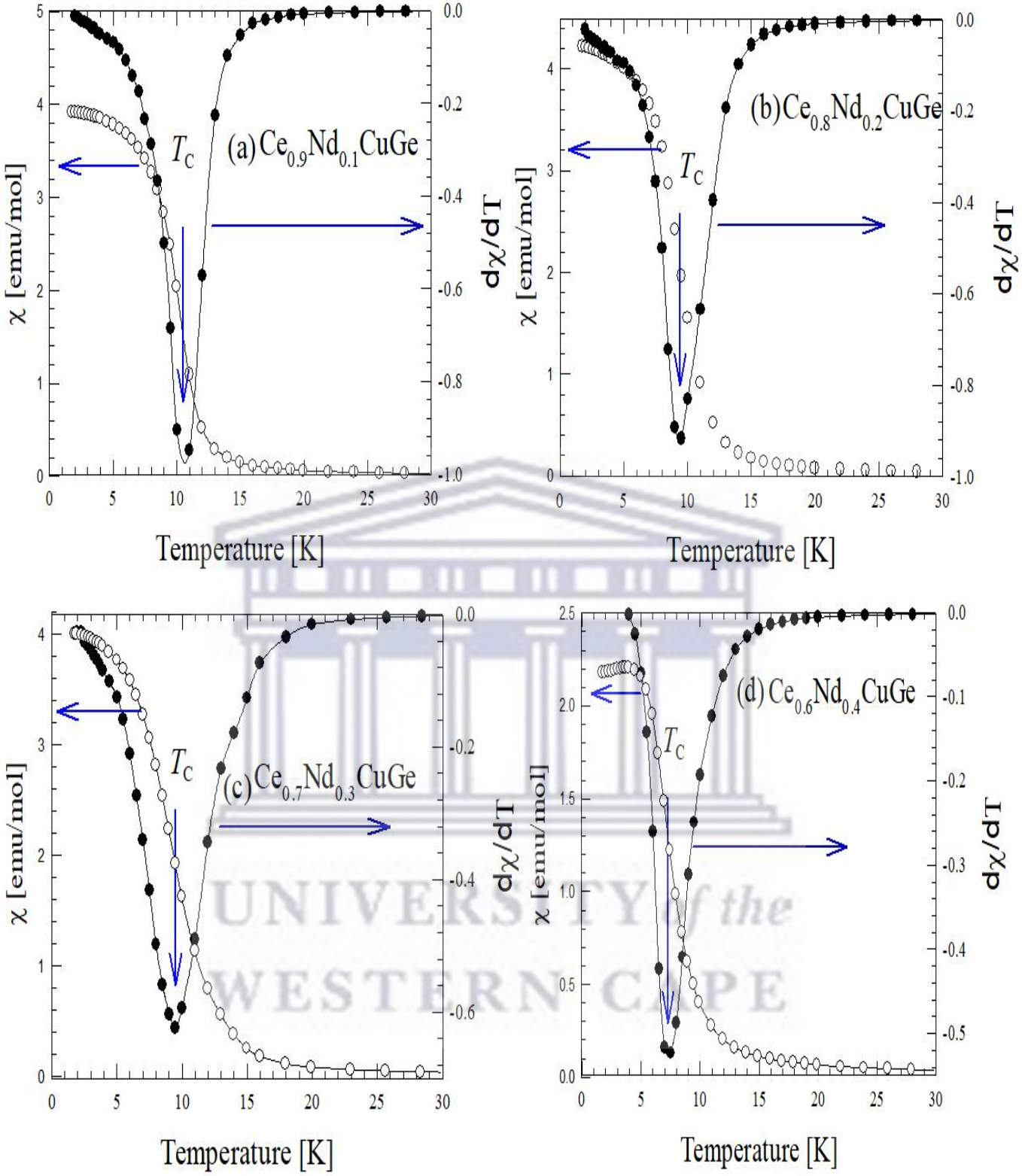

Figure 5.9: The low temperature, $\chi(T)$ data (left axis) and the derivative $d\chi(T)/dT$ curve (right axis) of selected samples of $(Ce_{1-x}Nd_x)CuGe$ alloys with $0.1 \leq x \leq 0.4$. The arrows indicate the ferromagnetic transition temperature T_C at the minimum of $d\chi(T)/dT$ curves.

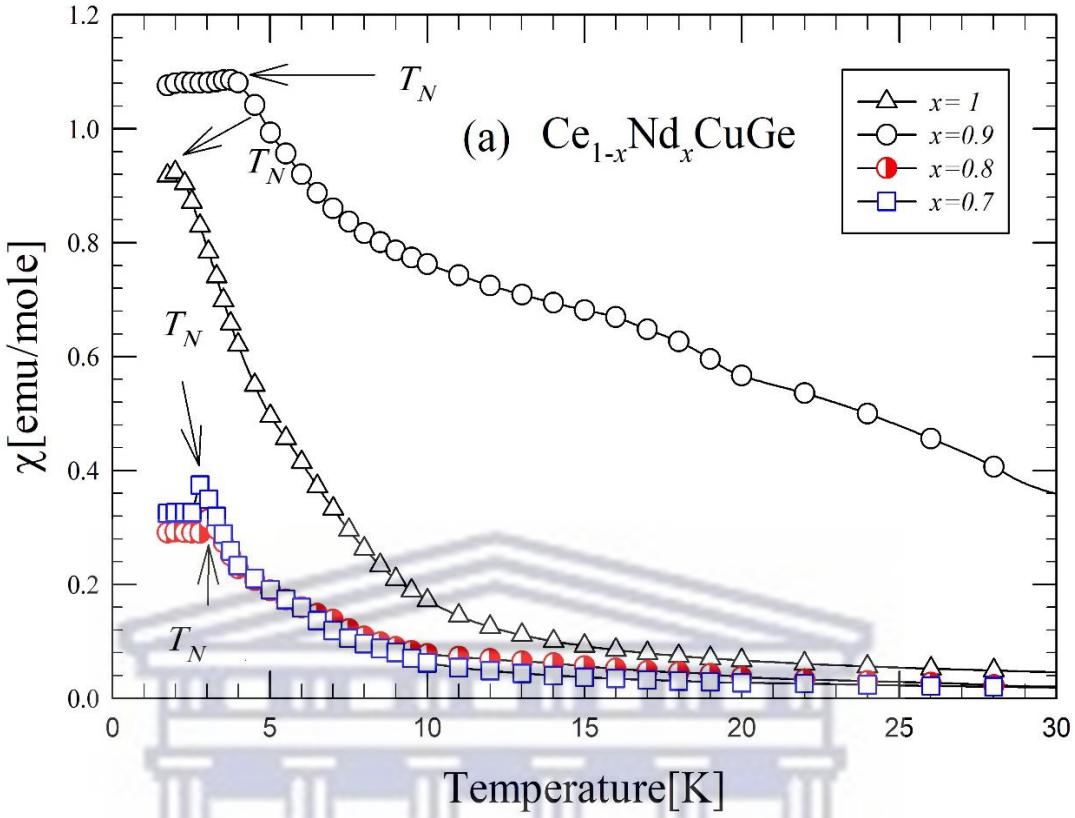

Figure 5.10: The low temperature, $\chi(T)$ data of selected samples of $(Ce_{1-x}Nd_x)CuGe$ alloys with $0.7 \leq x \leq 1$. The arrows indicate the positions of the kinks associated with the antiferromagnetic transition temperature T_N.

5.3.4 Electrical resistivity

The temperature dependence of the electrical resistivity, $\rho(T)$ for several samples of the alloy series $(Ce_{1-x}Nd_x)CuGe$ are depicted in figure 5.11. $\rho(T)$ was measured in the temperature range of 2 – 300 K in zero applied magnetic field. $\rho(T)$ for all samples show metallic conductivity with some bending of the $\rho(T)$ curve characteristic of the of *s-d* interband scattering and / or crystal-electric-field (CEF) effect. This behaviour is similar to several rare-earth intermetallic compounds such as Pr_2Pt_2In [183], Nd_2Pt_2In [184] La_3NiGe_2 [185]. Usually for Nd-bearing compounds, CEF was predominant in the electrical resistivity [186, 187], and a simple analysis in terms of the Bloch-Grüneissen-Mott (BGM) relationship (Eq.4.5) [166] similar to chapter 4 was not possible.

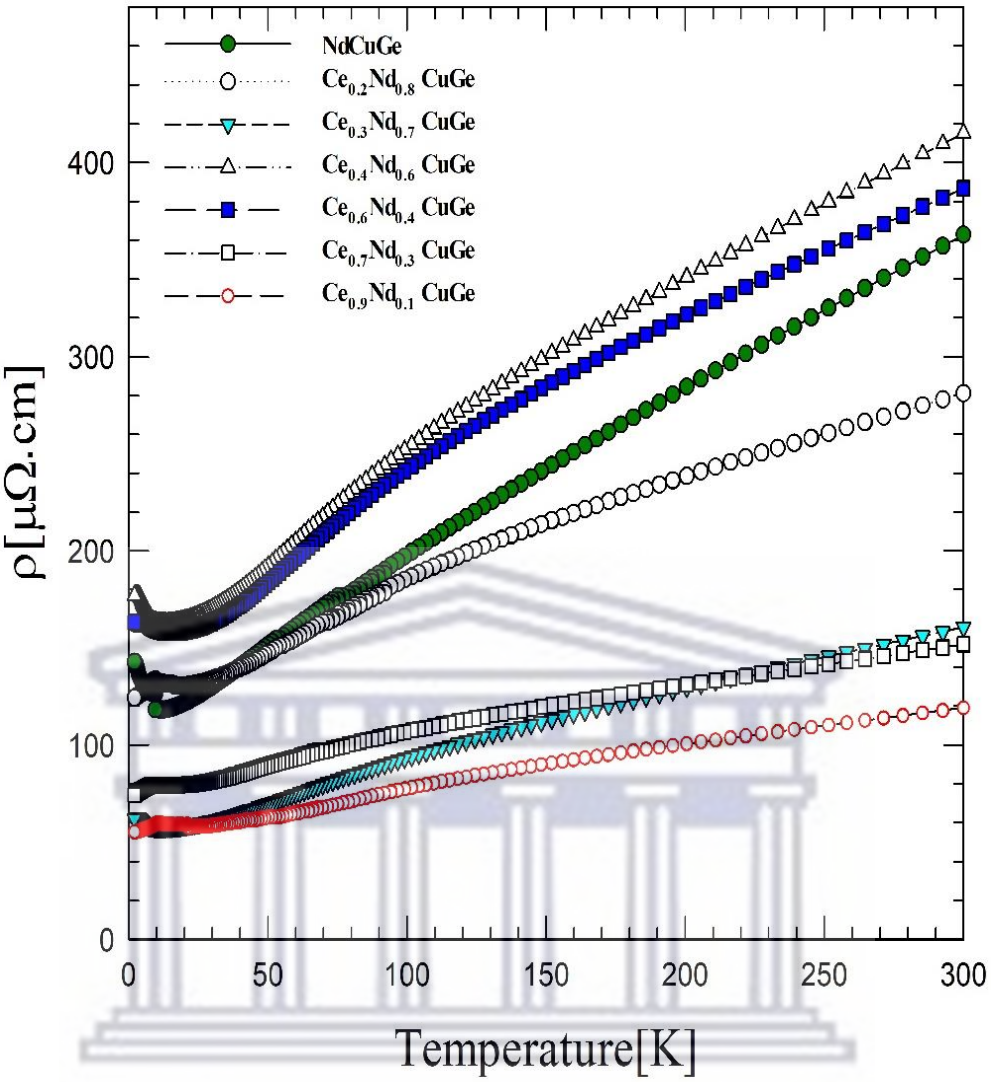

Figure 5.11: Temperature dependence of the electrical resistivity, ρ(*T*) of selected ($Ce_{1-x}Nd_x$)CuGe alloy series ($0.1 \leq x \leq 1$).

Figure 5.12 shown the low temperature ρ(*T*) data for selected alloy series of ($Ce_{1-x}Nd_x$)CuGe, that exhibit resistivity minima at T_{min}. As discussed in section 4.3.4, the resistivity for Gd and Tb based rare-earth compounds that exhibit AFM order, the observed upturn in ρ(*T*) for $T_N < T < T_{min}$ cannot be attributed to the magnetic-superzone-induced gap effect. Indeed, the AFM order is associated with large reciprocal magnetic lattice vector, typically for $T > T_N$ the large $-k$ (k is the wave vector) fluctuation diminish while small $-k$ fluctuation grow [169, 188, 189].

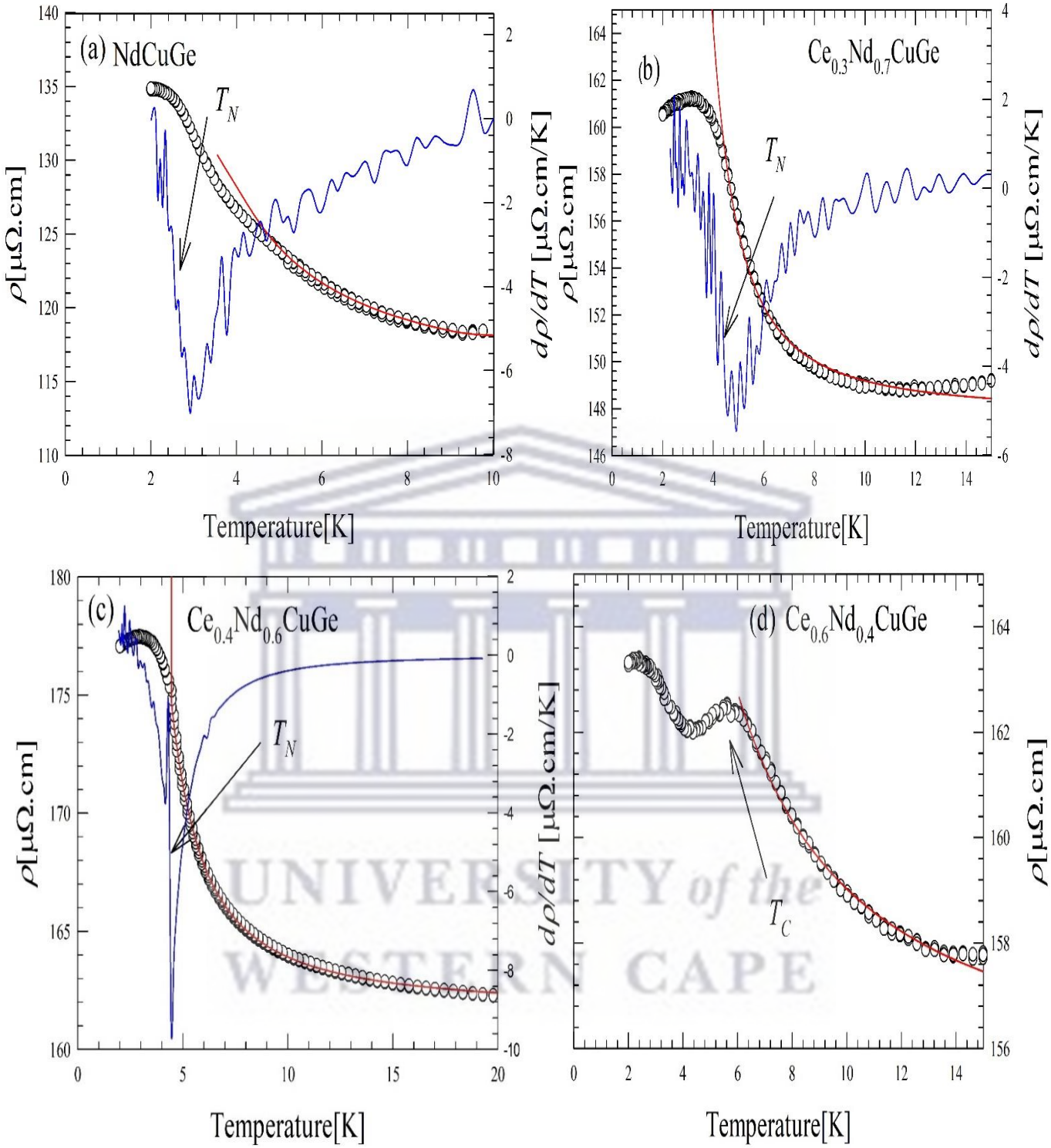

Figure. 5.12 The Low-temperatures, $\rho\ (T)$ data of (0.4≤x≤1) of the ($Ce_{1-x}Nd_x$)CuGe alloy series shows the antiferromagnetic superzone regions. The solid red curves are the least squares fits of Eq. 4.7.

In the case of compounds with x = 0.4 and 0.6 exhibiting FM behaviour, the upturn in $\rho(T)$ data was interpreted in terms of FM superzone pseudogap at the Fermi surface and described by the activated behaviour given by Eq. 4.3 [169] (solid curves figure 5.12). LSQ fits of Eq. 4.3 to ρ (T) data in the temperature range $T_C < T < T_{min}$ yielded the values of A = 144.92 (2) μΩ.cm, B = 10.414 (3) μΩ.cm, Δ_{sg} = 3.403 (6) K and A = 154.298 (1) μΩ.cm, B = 5.255 (9) μΩ.cm, Δ_{sg} = 6.289 (5) K for x = 0.4 and 0.6, respectively.

Figure 5.13 also displays the low temperature $\rho(T)$ data for selected samples of $(Ce_{1-x}Nd_x)CuGe$ with x = 0.1, 0.2 and 0.3. As mentioned in section 4.3.4, below the magnetic phase transition temperature T_C, a steep decrease in $\rho(T)$ bears testimony to the effects of long-range ordering in the spin sublattice on the electronic scattering. Similar to section 4.3.4, the sudden decrease in $\rho(T)$ data below T_C was well described in terms of ferromagnetic spin-waves excitation with energy gap Δ_{FM} in the magnon spectrum, (Eq 4.7, solid curve in figure 5.12) [168]. The resulting LSQ fit parameters are gathered in table 5.4. The sample with x = 0.3, $\rho(T)$ data below T_C decrease almost linearly with decreased temperature. Such a linear T-dependence of ρ(T) below T_C may have originated from the combination of magnetic, phononic and possible Fermi liquid contributions also observed in some rare-earth compounds such as GdCu4Au [189].

The magnetic phase transition temperature T_N and T_C obtained from the low temperature resistivity (figures 5.12 and 5.13) were estimated according to Sato criterion [167], which was at the midpoint of the anomaly in the $d\rho(T)/dT$ curve only for samples for which the resolutions of the performed $\rho(T)$ measurements were sufficient to resolve the phase transitions. For samples for which the resolutions of the performed $\rho(T)$ measurements were insufficient to resolve the phase transitions, the values T_C were estimated at the sudden drop of $\rho(T)$ data (note the arrows in figures 5.12 and 5.13).

Table 5.4: LSQ fits parameters of the spin-waves dispersion relation (Eq. 4.6) to the measured $\rho(T)$ data below T_C for sample with x = 0.1 and 0.2 in the alloys series $(Ce_{1-x}Nd_x)CuGe$.

Nd content (x)	ρ_0 [$\mu\Omega$.cm]	A [$\mu\Omega$.cm/K^2]	Δ_R[K]	T_C (T_N) [K]
0.1	55.20 (1)	0.025 (4)	1.91 (2)	10.6
0.2	124.36 (1)	0.061 (8)	1.435(1)	9.8

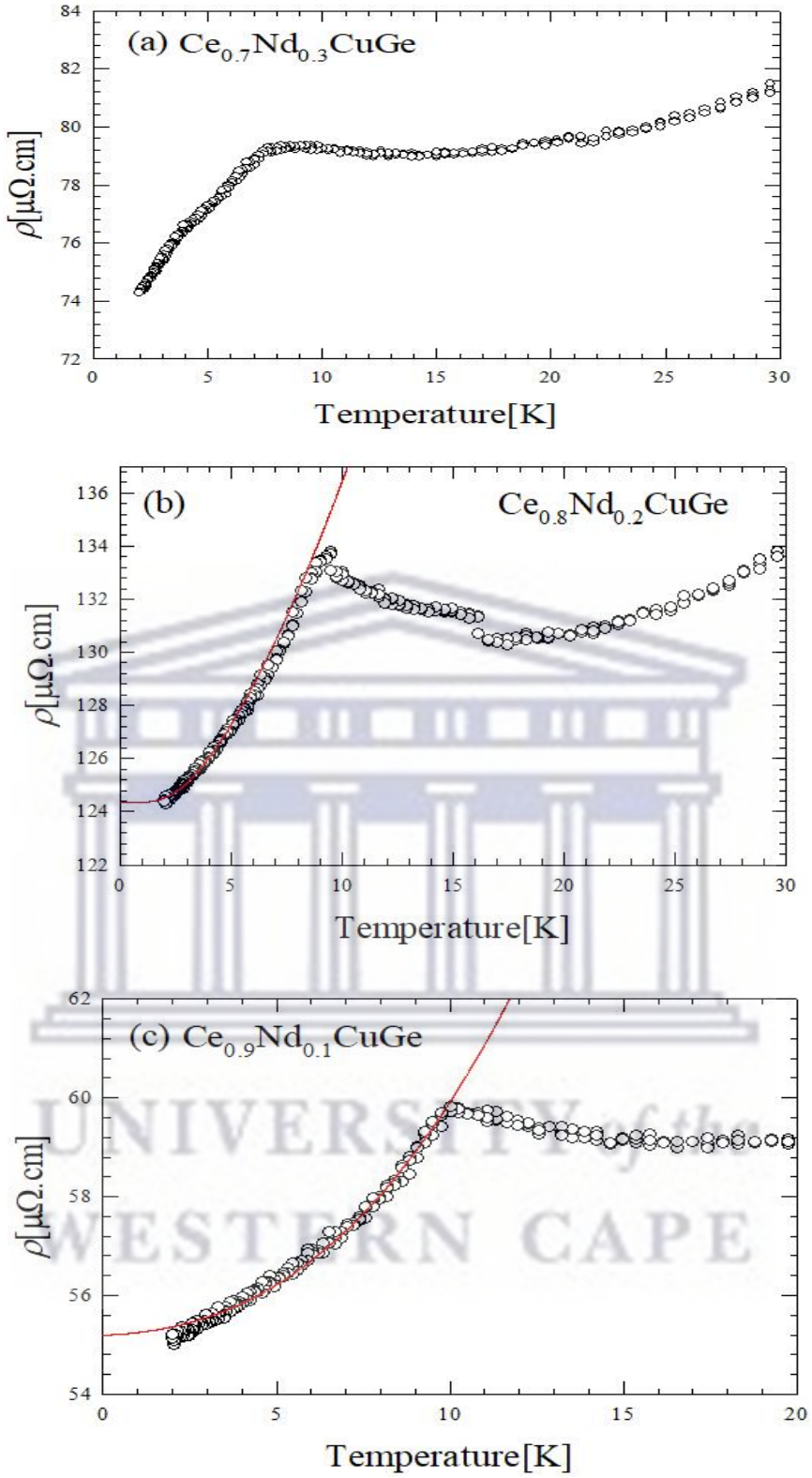

Figure 5.13: The low temperature ρ(*T*) data of selected samples in $(Ce_{1-x}Nd_x)CuGe$ alloy series ($0.1 \leq x \leq 0.3$). The solid red lines is LSQ fits of the spin-waves (Eq. 4.6).

5.3.4 Conclusion

The transition of the magnetic ground state from antiferromagnetic to ferromagnetic order in ($Ce_{1-x}Nd_x$)CuGe have been investigated from $\rho(T)$, $\chi(T)$ and $M(\mu_0 H)$ measurements. The results of these physical properties indicated that both FM and AFM states extended up to 50% substitution of Ce or Nd content. XRD results indicated that except for CeCuGe which crystallized in the ZrBeSi-type double-hexagonal-close (hcp) crystal structure with space group *P6$_3$/mmc* (No. 194), all samples indicated the AlB_2-type hexagonal crystal structure with space group *P6/mmm* (No. 191). $\chi(T)$ data at high temperatures follow the Curie-Weiss for all samples given an effective magnetic moment which increases gradually from CeCuGe to NdCuGe end compounds. In the ordered states, $\rho(T)$ variations for some samples can be well described by considering a gapped FM spin-wave spectrum. $\rho(T)$ data in the temperature range $T_C < T < T_{min}$ (T_{min} being the temperature of $\rho(T)$ minimum) for some samples can be well interpreted in terms of FM superzone pseudogap at the Fermi surface.

Chapter 6

3*d*-electron substitution-induced transition of the magnetic ground state from antiferromagnetic to ferromagnetic order in Dy($Cu_{1-x}Pd_x$)In alloy series

Abstract

Similar to the preceding chapters, this chapter reports on the 3*d*-electron substitution-induced transition of the magnetic ground state from AFM to FM order in Dy($Cu_{1-x}Pd_x$)In by means of magnetic susceptibility, $\chi(T)$, magnetization, $M(\mu_0 H)$, and heat capacity, $C_p(T)$, measurements. XRD results for all samples of Dy($Cu_{1-x}Pd_x$)In system indicate the hexagonal ZrNiAl-type structure with space group *P*-62*m* (No.189). $\chi(T)$ data at higher temperature follows the Curie-Weiss relation for all alloy samples and gives effective magnetic moment values μ_{eff} close to the expected value of 10.65 μ_B for the Dy^{3+}-ion. At low temperatures $\chi(T)$ exhibits antiferromagnetism at T_N in the concentration range $0 \leq x \leq 0.5$ and ferromagnetism at T_C in the concentration range $0.6 \leq x \leq 1$. Below T_C a second-order magnetic phase transition is observed at T_t signaling a spin orientation process which may occur. In concert, $C_p(T)$ data for alloys in this concentration range exhibit a similar second-order magnetic phase transition at low temperatures.

Furthermore, below T_C, $C_p(T)$ can be well described in terms of FM spin-wave dispersion with an energy gap Δ_C. The crystalline electric field (CEF) was observed at low temperatures in the $C_p(T)$ data which plays an influential role in the ground state for this system. The CEF parameters have been estimated from the LSQ fits of the Schottky anomaly to the $C_p(T)$ data. Furthermore $C_p(T)$ data confirm the FM and AFM phase transitions at T_C and T_N, respectively. On the other hand, the non-magnetic homologues YCuIn and YPdIn can be described by the Debye -Einstein model, giving Debye and Einstein temperature values of θ_D = 232.8(3) K and θ_E = 26.5(5) K and θ_D = 273.6(2) K and θ_E = 191.8(4) K, respectively. The 4*f*-electron specific heat, $C_{4f}(T)$, of the two end compounds DyCuIn and DyPdIn show Schottky-type anomalies around 55.1 K and 60 K, respectively associated with CEF, with energy splitting Δ_1 = 77(2) K, Δ_2 = 140(2) K and Δ_1 = 96(2) K, Δ_2 = 202(3) K, respectively of Dy^{3+} (J = 15/2) multiplet, that are associated with the first and second excited state of Dy^{3+} ion. The low temperature $C_{4f}(T)$

for samples exhibiting FM behaviour, can be well described assuming spin-wave excitations with an energy gap Δ_C.

6.1 Introduction

The group of compounds RCuIn (R = Ce, Nd, Gd, Tb, Dy, Ho, Er) and RPdIn (R = La, Ce, Pr, Nd, Ho, Er) have been the subject of several experimental investigations for the past two decades due to their interesting magnetic ground state properties [190 - 193]. Both groups of compounds crystallize in the hexagonal ZrNiAl-type structure with space group *P*-62*m*) [190 - 196] and exhibit various magnetic properties characterized generally by complex magnetic structures. An interesting property of the group of compounds RCuAl in particular, is that substitution of Cu with Ni retains the crystal structure, but the magnetic properties are modified from AFM to FM [197 - 199]. It was reported that in the RCuIn family, CeCuIn is paramagnetic down to 1.9 K, whereas the compounds with R = Nd, Gd, Dy, Tb, Ho, Er exhibit AFM order in which the magnetic structure for Nd, Tb and Ho is non-collinear and for Er it is collinear [190, 192, 200, 201, 202]. DyCuIn in particular order antiferromagnetically below T_N = 6.2 K [201].

On the other hand, the RPdIn family compounds were reported to exhibit ferrimagnetic ordering with an additional transition below their T_C except for GdPdIn, which is a ferromagnet, from magnetization measurements [203]. In the case of DyPdIn and TbPdIn in particular, Nishigori *et al*. [200] reported that these compounds are spin glasses due to the spin frustration of Gd and Tb ions forming a deformed Kagome lattice. Figure 6.1 shows the suggested deformed Kagome lattice forming by rare-earth ions in RPdIn (R = Dy, Tb).

Neutron diffraction experiments performed on DyPdIn indicates that this compound orders ferromagnetically below T_C = 31 K with an additional magnetic phase transition at T_1 = 14 K [191]. Furthermore, in the high – temperature phase $T_1 < T < T_C$, the Dy magnetic moments are aligned ferromagnetically along the c-axis and below T_1, basal-plane components of the Dy moments develop and order antiferromagnetically with the propagation vector $k = \left(\frac{1}{2}, 0, \frac{1}{2}\right)$ [191]. Metastable characteristics in ferromagnetic TbCuIn and DyCuIn were studied by means of DC magnetization, AC susceptibility, magnetic relaxation, specific heat and electrical resistivity measurements [190]. This study indicates that, the two compounds order ferromagnetically at T_C = 74

K for TbCuIn and T_C = 38 K with metastable magnetic properties, acting as the irreversibility of the temperature dependence of magnetization below a characteristic temperature T_{ir} and the long-time magnetic relaxation behaviour below T_C when changing the magnetic field at a constant temperature [192].

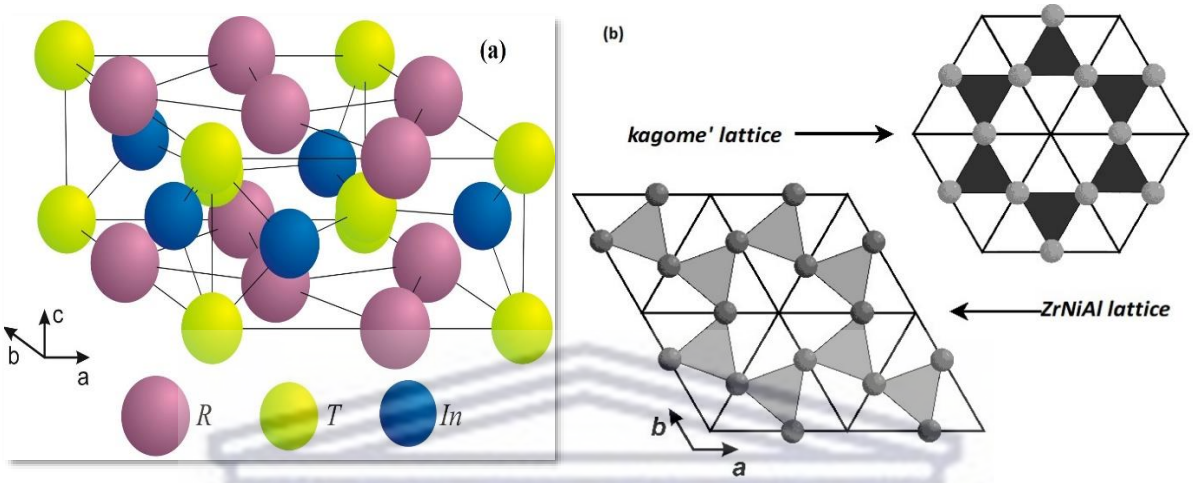

Figure. 6.1 (a) crystal unit cell of the RTIn compounds (ZrNiAl-type). (b) Shows distribution of the rare-earth atoms in a-a plane of ZrNiAl-type structure and comparison with the Kagomè lattice [204].

Furthermore, DyPdIn shows a second phase transition at T_N = 23 K, caused by the antiferromagnetic coupling [192]. For both TbPdIn and DyPdIn compounds, the ground states are not collinear ferromagnets, but are canted with antiferromagnetic component. Heat capacity study of CePdIn indicates a heavy fermion character for this compound and a sharp peak at 1.7 K signalling the onset of the AFM ordering [205]. On the other hand, magnetic susceptibility studies on PrPdIn compound does not indicate any magnetic ordering and furthermore, the large value of temperature independent magnetic susceptibility is of the order of those characteristics of strong spin fluctuators [206].

In view of these various magnetic properties characterized by complex magnetic structures of DyPdIn and DyCuIn, the present chapter investigates the 3*d*-electron substitution-induced transition of the magnetic ground state from AFM to FM order in $Dy(Cu_{1-x}Pd_x)In$ by means of magnetic susceptibility, $\chi(T)$, magnetization, $M(\mu_0 H)$, and heat capacity, $C_p(T)$, measurements. An interesting property of the DyCuIn compound is that the

gradual substitution of Cu by Pd retains the crystal structure, but the magnetic properties are modified from AFM of DyCuIn to FM of DyPdIn.

6. 2 Sample preparation and characterization

Polycrystalline samples of the alloy series $Dy(Cu_{1-x}\ Pd_x)In$ with $0 \leq x \leq 1$ were synthesized by arc-melting stoichiometric amounts of the elements Dy, Cu, Pd and In as described in section 3.2. The purity of these elements is also indicated in section 3.2. The weight losses of all samples after final melting were always less than 1 wt. %. Subsequently, the samples were subjected to heat treatment as described in section 3.2. The products were checked by powder XRD using a Bruker D8 ADVANCED diffractometer with CuKα radiation described in chapter 3. The X-ray diffraction pattern for all members of the alloy series were analyzed using the CAILS-Pawley refinement method and the full-profile Rietveld refinement method for the end compound DyCuIn and DyPdIn, both from TOPAS ACADEMIC programme. All prepared samples were single phase with no evidence of parasitic phasea or unreacted elements. Further characterization of the two end compounds DyCuIn and DyPdIn by electron micro – probe and the scanning electron microscope (SEM) analysis were performed to obtain the chemical sample and morphology of the samples.

6.3 Results and discussion

6.3.1 Scanning electron microscope (SEM)

Figure. 6.2 and 6.3 display the micrographs of DyCuIn, YCuIn and DyPdIn, YPdIn compounds magnified at 250 μm, 100 μm and 100 μm, 250 μm, respectively taken from SEM. The micrograph images of all four compounds show microstructure and region of uneven texture and smooth surfaces. The results of this analysis indicated the homogeneity of the four compounds with the uneven texture attributed to crystallites with different crystallography orientation. Atomic ratios of the elements as obtained from electron dispersive spectroscopy (EDS) indicate that the sample elemental sample normalized to the rare-earth atoms (Dy and Y) found to be $DyCu_{0.986(2)}In_{0.80(2)}$, $YCu_{0.974(2)}In_{0.881(2)}$, $DyPd_{0.967(2)}In_{0.80(2)}$, $YPd_{0.927(2)}In_{0.170(2)}$ which is roughly in the ratio 1:1:1 of the sample. The small offsets of the atomic rations are ascribed to the small mass loss that occurs during the sample preparation.

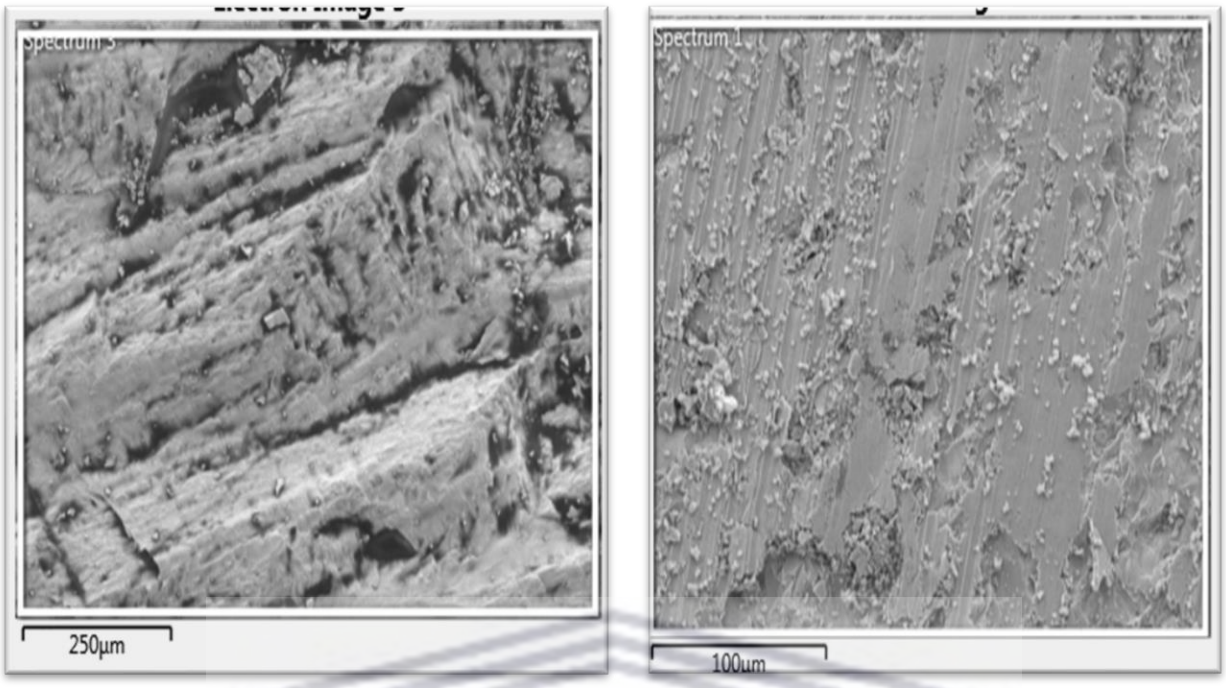

Figure 6.2: SEM micrographs of DyCuIn with a scale of 250 µm (left) and YCuIn with a scale of 100 µm (right).

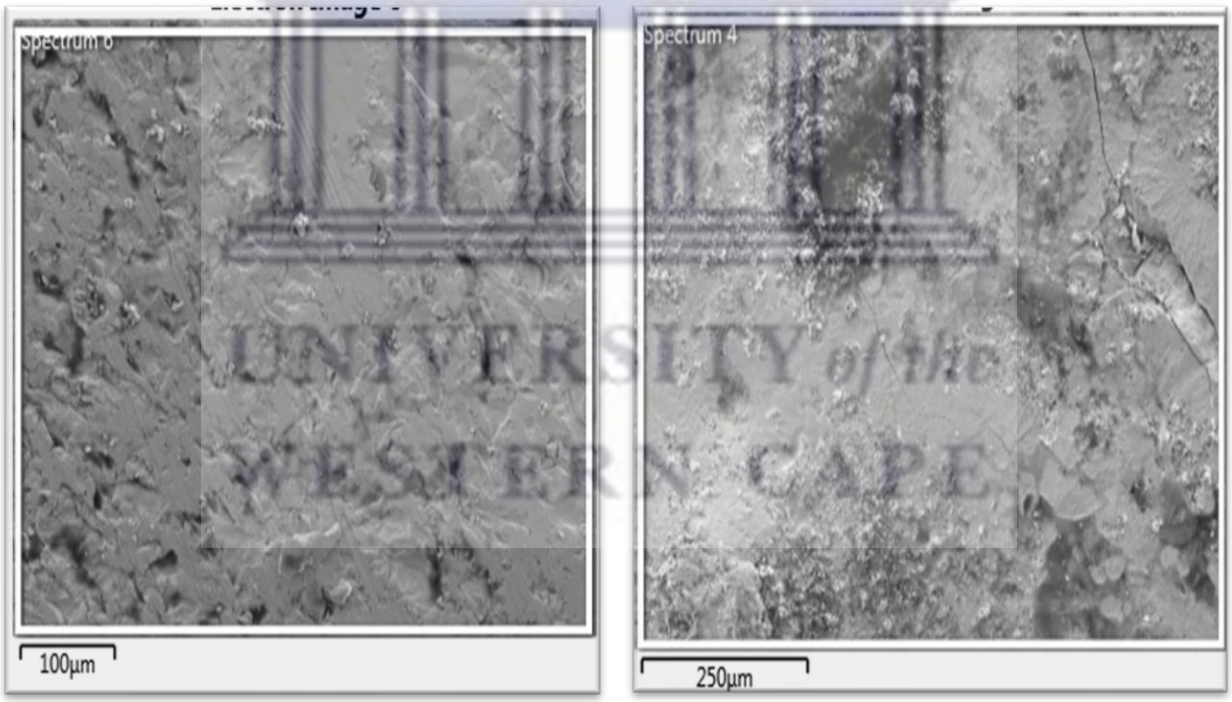

Figure 6.3: SEM micrographs of DyPdIn with a scale of 100 µm (left) and YPdIn with a scale of 250 µm (right).

6.3.2 Lattice parameters and crystallography

X-ray diffraction obtained for the two end compounds as well as four samples in the alloy series Dy($Cu_{1-x}Pd_x$)In and YTIn (T = Cu, Pd) together with the CAILS-Pawley refinement fits to the data, are shown in figure. 6.4, 6.5 and 6.6. All samples were found to crystallize in the ZrNiAl-type structure with space group *P*-62*m* (No. 189).

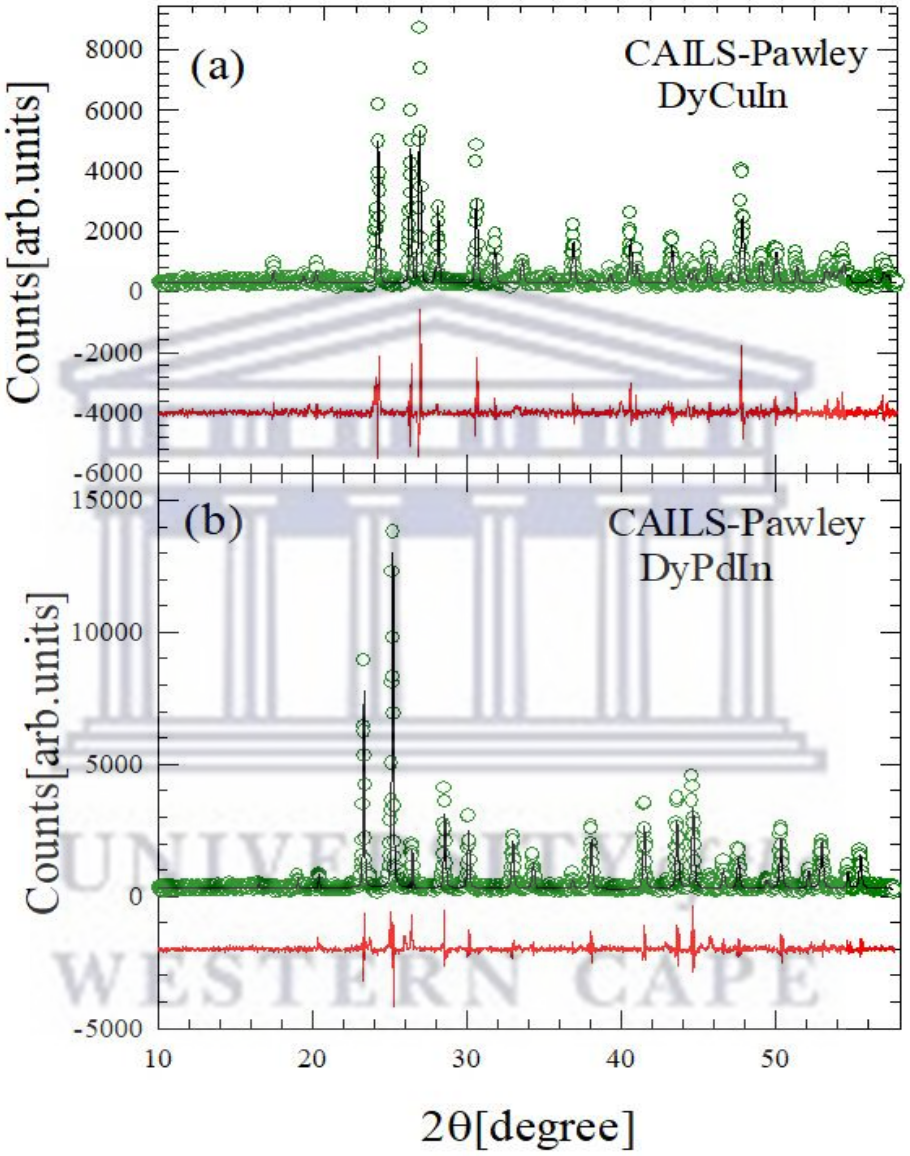

Figure 6.4: X-ray diffraction patterns (green symbols) of (a) DyCuIn and (b) DyPdIn collected at room temperature together with CAILS-Pawley refinement fits (black curves) through the data. The lower red curves are the difference between the experimental data and the calculated curves.

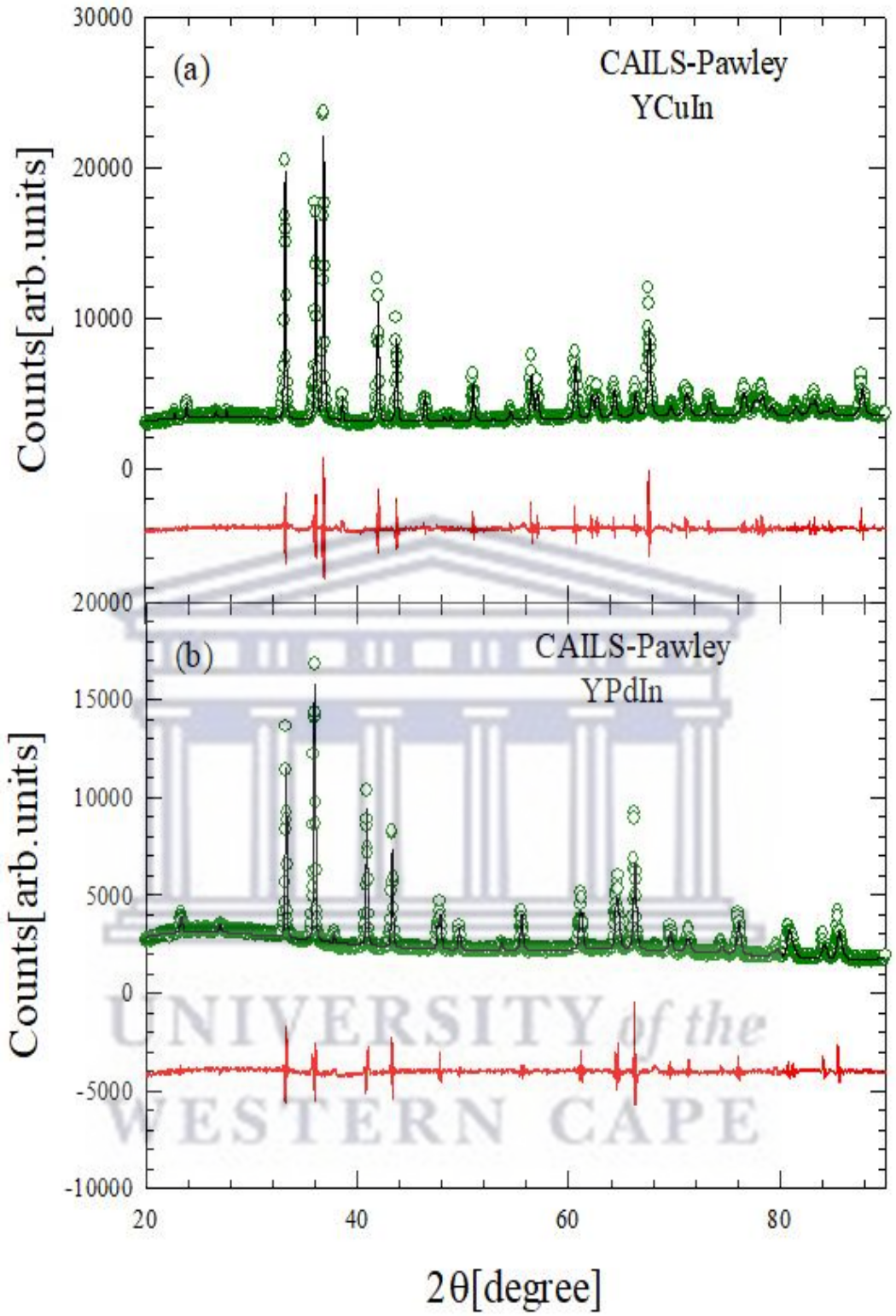

Figure 6.5: X-ray diffraction patterns (green symbols) of (a) YCuIn and (b) YPdIn collected at room temperature together with CAILS-Pawley refinement fits (black curves) through the data. The lower red curves are the difference between the experimental data and the calculated curves.

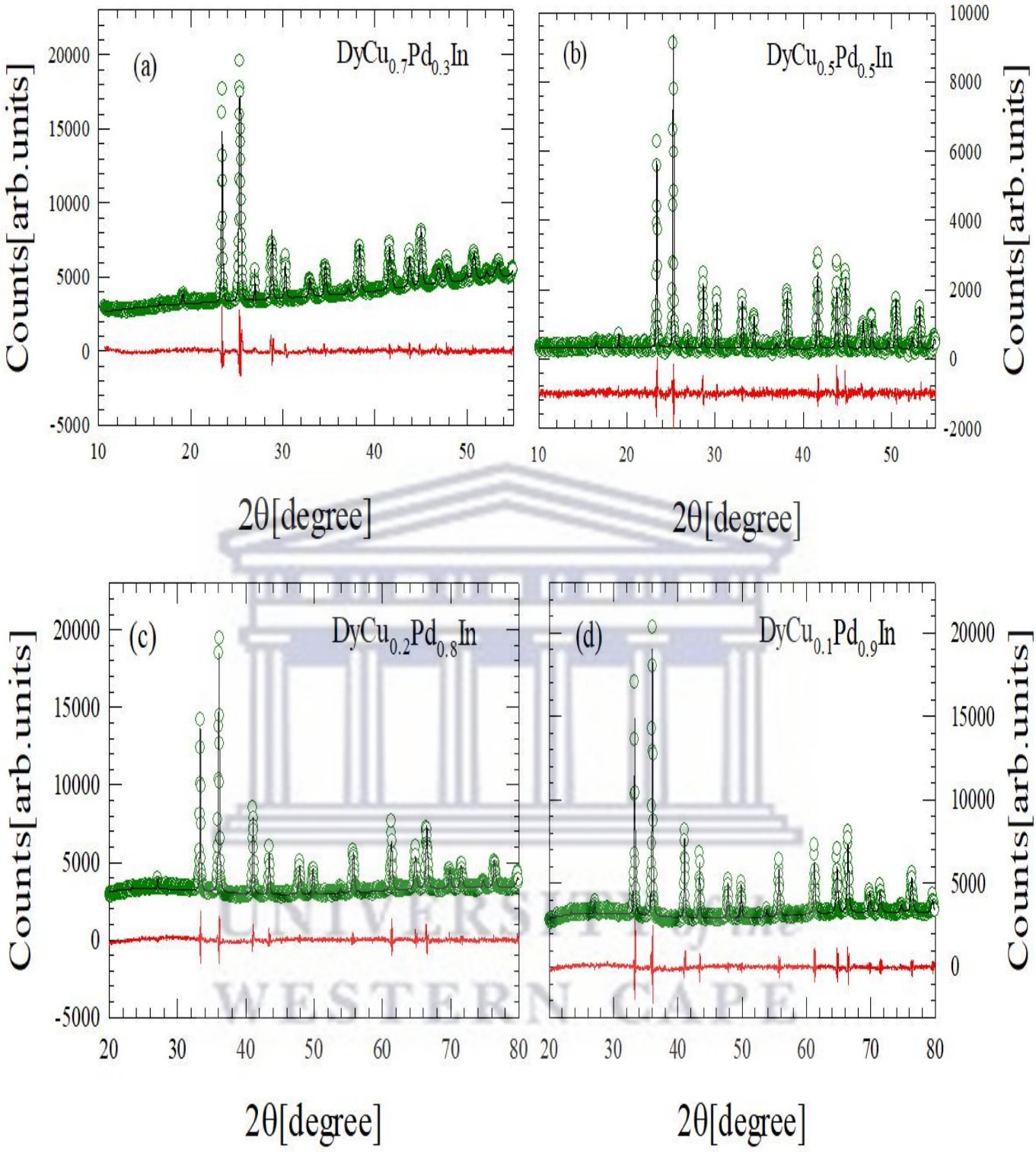

Figure 6.6: X-ray diffraction patterns (green symbols) of selected samples in the alloy series $Dy(Cu_{1-x}Pd_x)In$ with (a) $x = 0.3$ (b) $x = 0.5$ (c) $x = 0.8$ and (d) $x = 0.9$ collected at room temperature together with CAILS – Pawley refinement fits (black curves) through the data. The lower red curves are the difference between the experimental data and the calculated curves.

The room temperature lattice parameters and unit cell volume for the compounds DyCuIn and DyPdIn resulting from the fit were found to be a_{Cu} = 7.4220 (4) Å, c_{Cu} = 3.9018 (4) Å, V_{Cu} = 186.140 (2) Å^3 and a_{Pd} = 7.6280 (4) Å, c_{Pd} = 3.8043 (6) Å, V_{Pd} = 191.704 (3) Å^3 in good agreement with previously reported values in the literature [190, 191, 194]. On the other hand, the room temperature lattice parameters and unit cell volume for the non-magnetic compounds YCuIn and YPdIn resulting from the fit were found to be a_{Cu} = 7.448 (4) Å, c_{Cu} = 3.908 (6) Å, V_{Cu} = 187.762 (3) Å^3 and a_{Pd} = 7.638 (4) Å, c_{Pd} = 3.797 (4) Å, V_{Pd} = 191.817 (3) Å^3. The lattice parameters and the unit cell volume for all samples resulting from the fit are plotted as a function of Pd content x in figure. 6.7. It is observed that the refined room-temperature lattice parameter (a) and unit cell volume (V) increase linearly with increasing Pd content. The increase of V with x results from the small atomic radius of Cu atom (r = 1.57 Å) compared to that of Pd atom (r = 1.79 Å) and amount to 2.9%, the relative change in volume which is roughly 4.2 times smaller than the relative change of the atomic radius of Pd and Cu (12.3%). The relative change in the a-axis of 2.7% is in the same order of magnitude as that of the relative change in volume. The linear increase in V is consistent with Vegard's law which suggests the stability of the Dy valence across the series as well as no change in the number of conduction electrons, which ensures metallic bonding of the alloy system.

Figures 6.8 and 6.9 display the XRD patterns of the two end compounds DyCuIn and DyPdIn and the non-magnetic compounds YCuIn and YPdIn, together with the full profile Rietveld LSQ refinement (solid black curve in figure 6.6). The space group setting used in the refinement was the hexagonal P-62m (No. 189) also used for the CAILS-Pawley refinement method. In this space group, the Dy or Y occupy the crystallographic site 3f, Cu or Pd occupy two crystallographic sites 1a and 2d and In occupy the crystallographic site 3g. The atomic coordinates, the site occupancy (S.O.) and the equivalent isotropic temperature factor (beq) are gathered in table 6.1. In this refinement S.O. and beq of all the atoms was kept fixed at 100%. The resulting refinement instrumental parameters of the Rietveld refinement as well as the CAILS-Pawley refinement (R_p, R_{wp}, R_{exp}, χ^2, DW, R_B and phase density) listed in tables 6.2 and 6.3 and the crystal structure is shown in figure. 6.10.

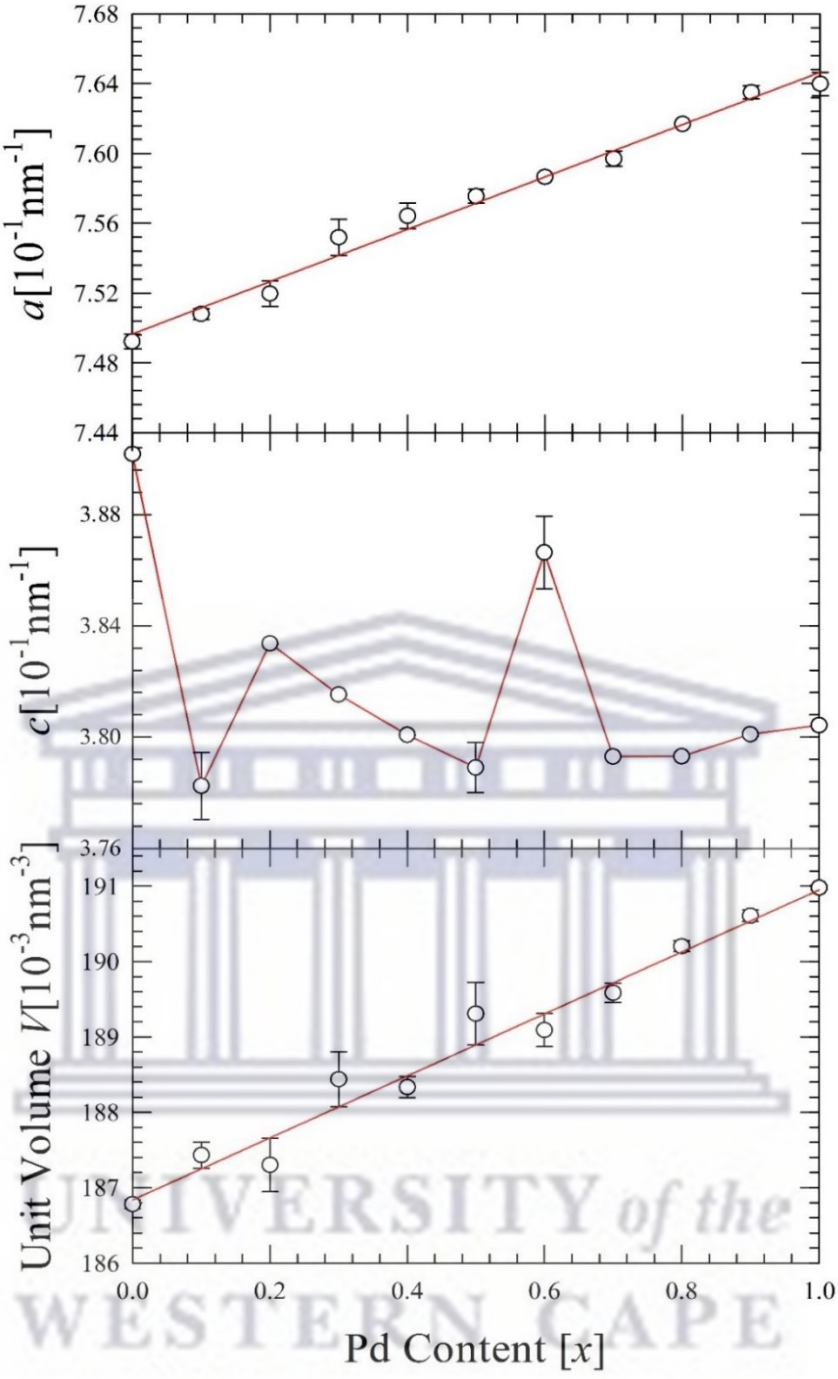

Figure 6.7: Lattice parameters ($a = b$) and unit cell volume V of the hexagonal $Dy(Cu_{1-x}Pd_x)In$ alloys system as function of Pd content x. The Solid red lines in the lattice parameters a and the unit cell volume V Panels is LSQ fit of the data to the linear equation. The red line in the middle panel is a guide to the eye.

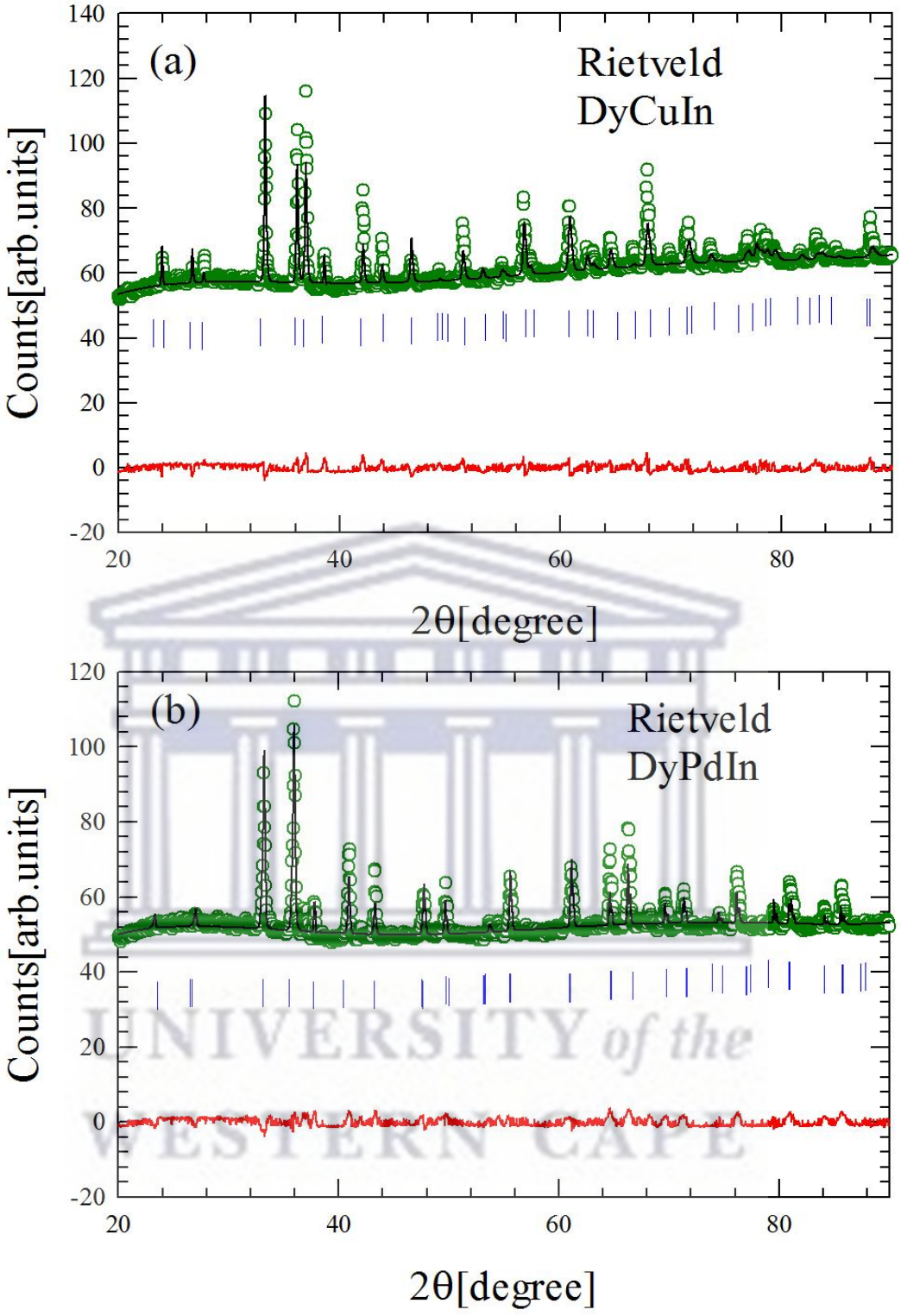

Figure 6.8: XRD patterns of the two end compounds DyCuIn and DyPdIn (green symbols) together with the full profile Rietveld LSQ refinement (solid black curve). The solid red curves are the difference between the experimental and calculated patterns. The vertical blue ticks represent the Bragg's reflections.

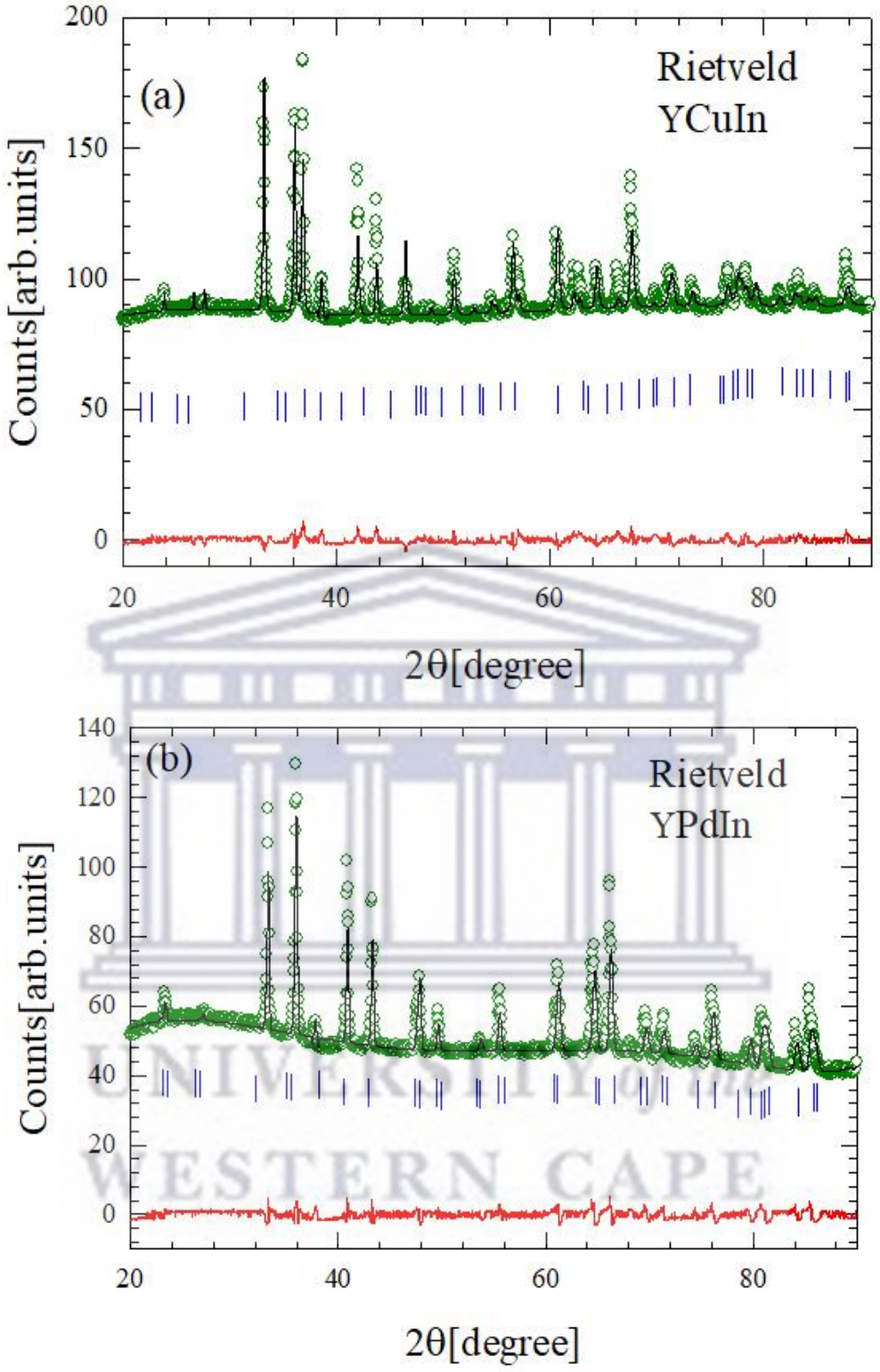

Figure 6.9: XRD patterns of the non-magnetic compounds YCuIn and YPdIn (green symbols) together with the full profile Rietveld LSQ refinement (solid black curve). The solid red curves are the difference between the experimental and calculated patterns. The vertical ticks represent the Bragg's reflections.

Table 6.1: Atomic coordinates, the site occupancy (S.O.) and the equivalent isotropic temperature factor (beq) for RTIn (R = Dy or Y; T = Cu or Pd) obtained for the full-structure Rietveld refinement method using the space group *P*-62*m*. The S.O. and the beq were kept fixed.

Atoms	Wyckoff site	*x*	*y*	*z*	S.O	beq
R0	3*f*	0.411	0	0.5	1	1
R1	3*f*	0	0.411	0.5	1	1
R2	3*f*	0.589 (1)	0.589 (3)	0.5	1	1
T3	1*a*	0.75	0	0	1	1
T4	2*d*	0	0.75	0	1	1
T5	2*d*	0.25	0.25	0	1	1
In6	3*g*	0	0	0.5	1	1
In7	3*g*	0.333	0.667	0	1	1
In8	3*g*	0.667	0.333	0	1	1

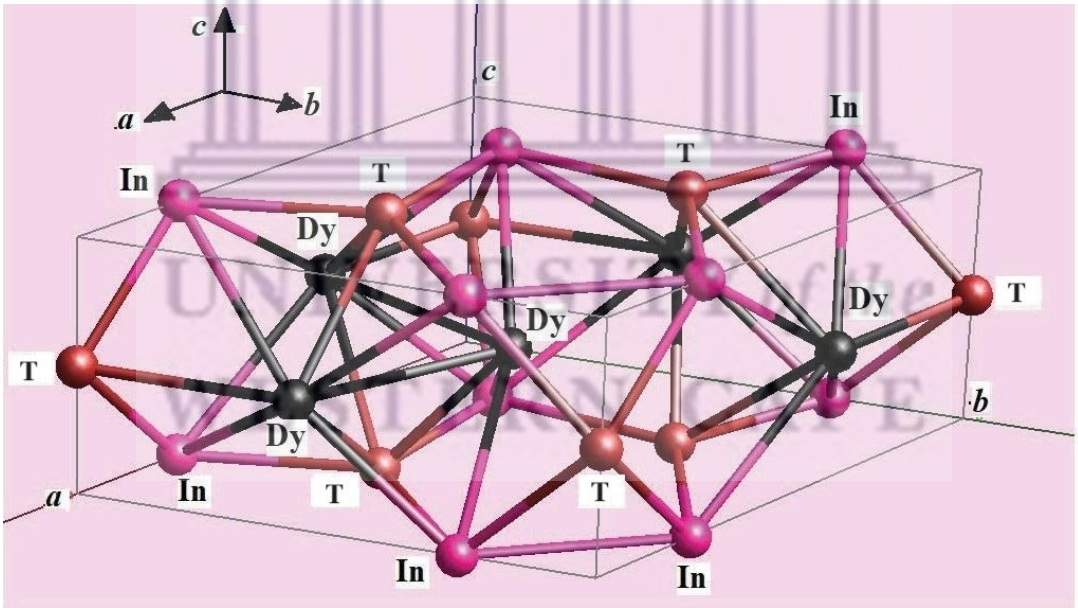

Figure 6.10: The hexagonal crystal structure of DyTIn (T = Cu or Pd) obtained from Rietveld refinement method. The black circles represent the Dy or Y atoms, the brown circles represent the Cu or Pd atoms and the pink circles represent the In atoms.

Table 6.2: The refined instrumental parameters of the (1) CAILS-Pawley and (2) Full-structure Rietveld refinement methods (for comparison only) for the two end compounds DyCuIn and DyPdIn.

Parameters	CAILS (1)		Rietveld (2)	
	DyCuIn	DyPdIn	DyCuIn	DyPdIn
Rp [%]	3.049	3.017	3.325	4.248
Rwp [%]	4.638	4.261	5.248	6.253
Rexp [%]	1.618	1.870	1.637	1.890
$X^2 = GOF$	3.902	2.279	3.207	3.309
DW [%]	0.759	0.727	0.345	0.290
R_B [%]			8.7583	9.232
Phase density [g/cm^3]			9.079	8.8

Table 6.3: The refined instrumental parameters of the (1) CAILS-Pawley and (2) Full-structure Rietveld refinement methods (for comparison only) for non-magnetic compounds YCuIn and YPdIn.

Parameters	CAILS (1)		Rietveld (2)	
	YCuIn	YPdIn	YCuIn	YPdIn
Rp [%]	3.856	4.172	6.409	5.705
Rwp [%]	5.926	6.183	11.180	9.097
Rexp [%]	1.613	1.934	1.631	1.952
$X^2 = GOF$	3.647	2.279	3.855	4.660
DW [%]	0.981	0.824	0.316	0.416
R_B [%]			11.825	7.845
Phase density [g/cm^3]			9.003	8.785

The observed values of the *R*-factors and χ^2 (goodness of fit) obtained from the CAILS and Rietveld refinement methods are in the same order of magnitude and relatively good as observed from the good quality of the fit (see figure 6.7). Furthermore, the values of *DW* for all investigated samples are less than the value of 2, in agreement with the ideal range value of $0 < DW < 2\%$ [25, 26] which indicates that the quality of the fit model is correct. The values of the phase density obtained for the two compounds are of the same order of magnitude.

6.3.2 Magnetization and magnetic susceptibility

The magnetic field dependence of the magnetization, $M(\mu_0 H)$, was measured for the $Dy(Cu_{1-x}Pd_x)In$ alloy system at 1.7 K and in fields up to 5 T. Figure 6.11 displays $M(\mu_0 H)$ for selected samples in the alloy system. It is observed that $M(\mu_0 H)$ data show hysteresis loops during the process of increasing and decreasing magnetic fields. Metamagnetic behaviour is observed around 2 T for the parent compound DyCuIn. For samples in the concentration range $0 \leq x \leq 0.5$, $M(\mu_0 H)$ initially increases linearly at low fields and exhibit downward curvature at high fields. For samples in the concentration range $0.6 \leq x \leq 1$, the shapes of $M(\mu_0 H)$ is typical for FM materials. In fields stronger than 1 T, $M(\mu_0 H)$ data for these samples saturate at value below $M_s = 8\ \mu_B$/f.u. The values of $M(\mu_0 H)$ for all investigated samples at 5 T are smaller than 8 μ_B/f.u., which are also smaller than the theoretical value of trivalent Dy ($g_J J = 10\mu_B$). This reduction is probably due to combined effects of CEF and magnetic anisotropy.

The dc-inverse magnetic susceptibility, $\chi^{-1}(T)$ of the $Dy(Cu_{1-x}Pd_x)In$ alloy series, measured in an applied field of 0.1 T in the temperature range $1.7 \leq T \leq 400$ K, are shown in figure 6.12. The magnetic field of 0.1 T was chosen, since at this field $M(\mu_0 H)$ for all samples was linear. At temperatures above 50 K, $\chi^{-1}(T)$ data follow the Curie-Weiss (CW) relationship (Eq. 4.1). The least squares (LSQ) fits of the CW relation against the experimental data are shown as red solid lines in figure 6.12. The obtained parameters from the LSQ fits are gathered in table 6.4. The observed μ_{eff} values across the series are close to that expected for the free Dy^{3+}-ion $\left(g_J\sqrt{J(J+1)} = 10.65\mu_B\right)$. The negative θ_p values obtained from the fits hint at the antiferromagnetic exchange interactions between the Dy moments, while the positive values hint at the ferromagnetic exchange interactions. Below 50 K, $\chi^{-1}(T)$ data for all samples deviate from the CW linear behaviour, likely due to magnetocrystalline anisotropy.

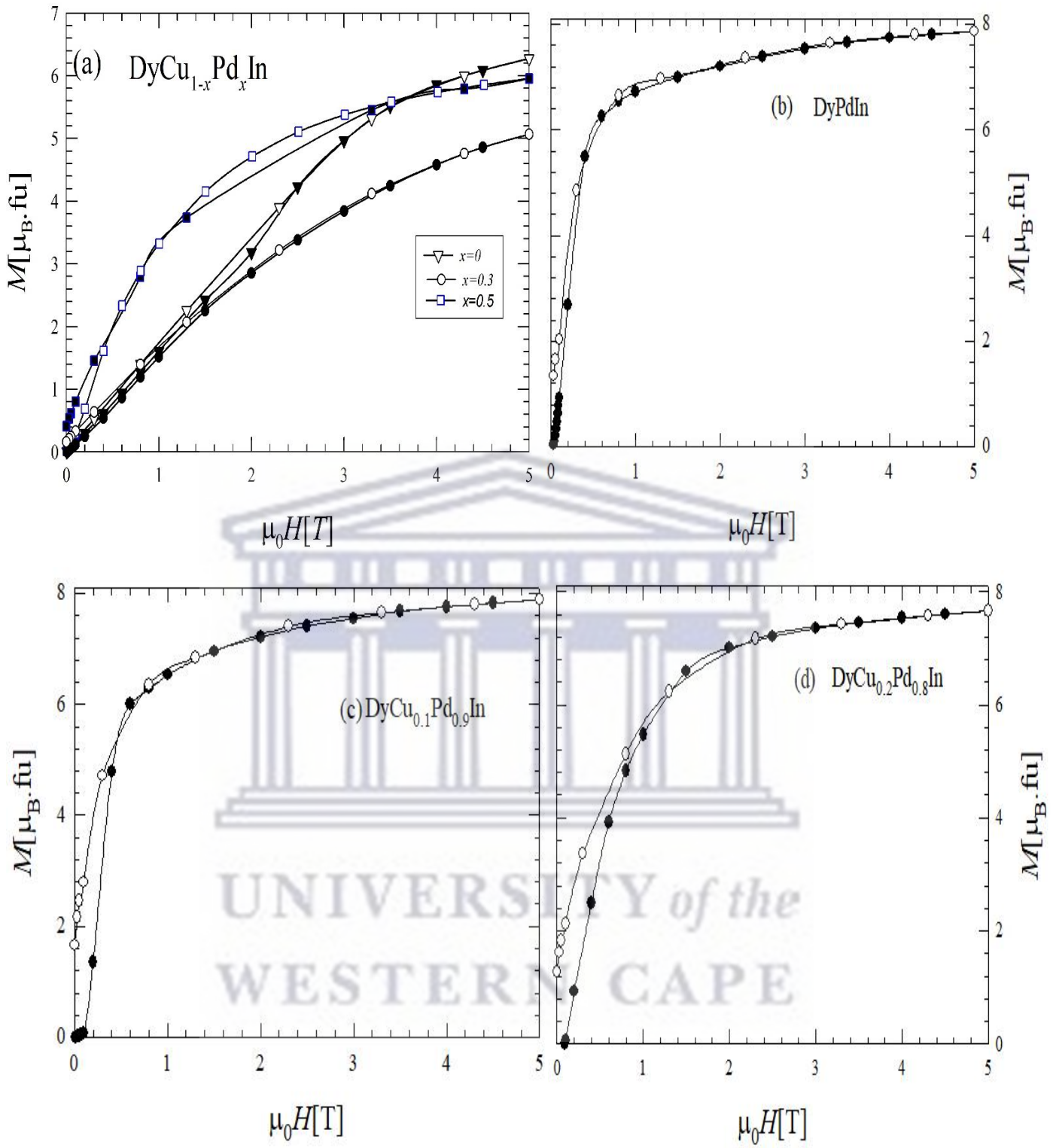

Figure 6.11: The field-dependence magnetization, M ($\mu_o H$) of selected samples in the alloy series $Dy(Cu_{1-x}Pd_x)In$ measured at 1.7 K in increasing (closed symbols) and decreasing (open symbols) magnetic fields.

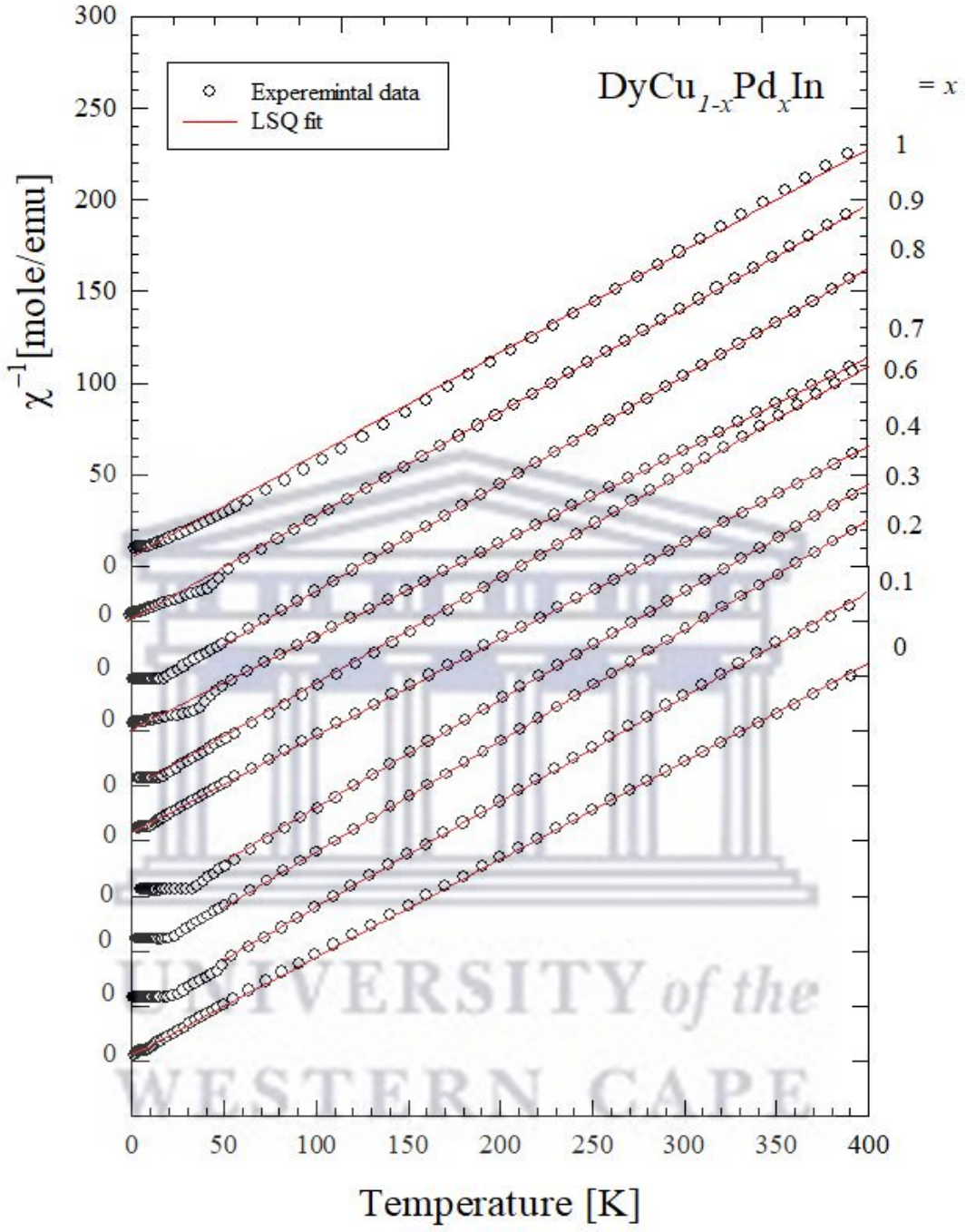

Figure 6.12: Dc-inverse magnetic susceptibility, $\chi^{-1}(T)$ of the Dy($Cu_{1-x}Pd_x$)In alloys with the least-square (LSQ) fits of the Curie-Weiss law to the data points above 50 K.

The low temperature $\chi(T)$ data for selected samples of the $Dy(Cu_{1-x}Pd_x)In$ alloy series are depicted in figure 6.13. For samples in the concentration range $0 \leq x \leq 0.5$, χ (T) data showed kinks at temperatures T_N as indicated by arrows in figure 6.13 (a), characteristic of AFM phase transitions. On the other hand, for alloys in the concentration range $0.6 \leq x \leq 1$, $\chi(T)$ data exhibit FM phase transitions at T_C as indicated by arrows in figures 6.13 (b), (c) and (d). The values of T_C were estimated at the minimum of the derivative of $\chi(T)$ data, $d\chi(T)/dT$ (right axis of figures 6.13(b), (c) and (d). Still in this concentration range, an additional magnetic phase transition was observed below T_C at T_1 (for x=1, 0.9, 0.8, 0.7 and T_1 observed at 10.6, 11.9, 12.1 and 9.5 K respectively). This second magnetic phase transition at T_1 was also reported for DyPdIn in the literature and was attributed to the AFM arrangement of the Dy moment [193]. The estimated values of T_C, T_N and T_1 are also listed in table 6.4. It is observed that the values of T_C, T_N and T_1 obtained for the two end compounds are in close agreement with the previous reported values in the literature [191, 207, 201, 193]. The occurrence of spin-glass transition or metastable magnetic properties in Pd-rich alloys cannot be discussed with present data.

Table 6.4: Magnetic susceptibility parameters: effective magnetic moment, μ_{eff}, Weiss temperature θp resulting from LSQ fits of the dc-inverse magnetic susceptibility to the Curie-Weiss law of the $Dy(Cu_{1-x}Pd_x)In$ alloys, as well as the observed magnetic phase transition temperature, T_C, T_N and T_1.

Pd Content (x)	$\mu_{eff}[\mu_B]$	$-\theta_P[K]$	$T_C^{\chi}[K]$	$T_1^{\chi}[K]$	$T_N^{\chi}[K]$
1	10.7(1)	12.2(1)	34.5	10.6	
0.9	11(3)	11.5(1)	24.3	11.9	
0.8	11(3)	9.63(8)	23	12.1	
0.7	11(4)	9.03(7)	20	9.5	
0.6	11(4)	7.18(6)	16		
0.5	10.8(2)	1.87(3)			9
0.4	10.6	–2.77(2)			8.3
0.3	10.5(2)	–8.32(2)			7.3
0.2	10.8 (1)	0.25(7)			6.9
0.1	11 (3)	–4.56(6)			6.7
0	11(1)	–7.30(4)			6.5

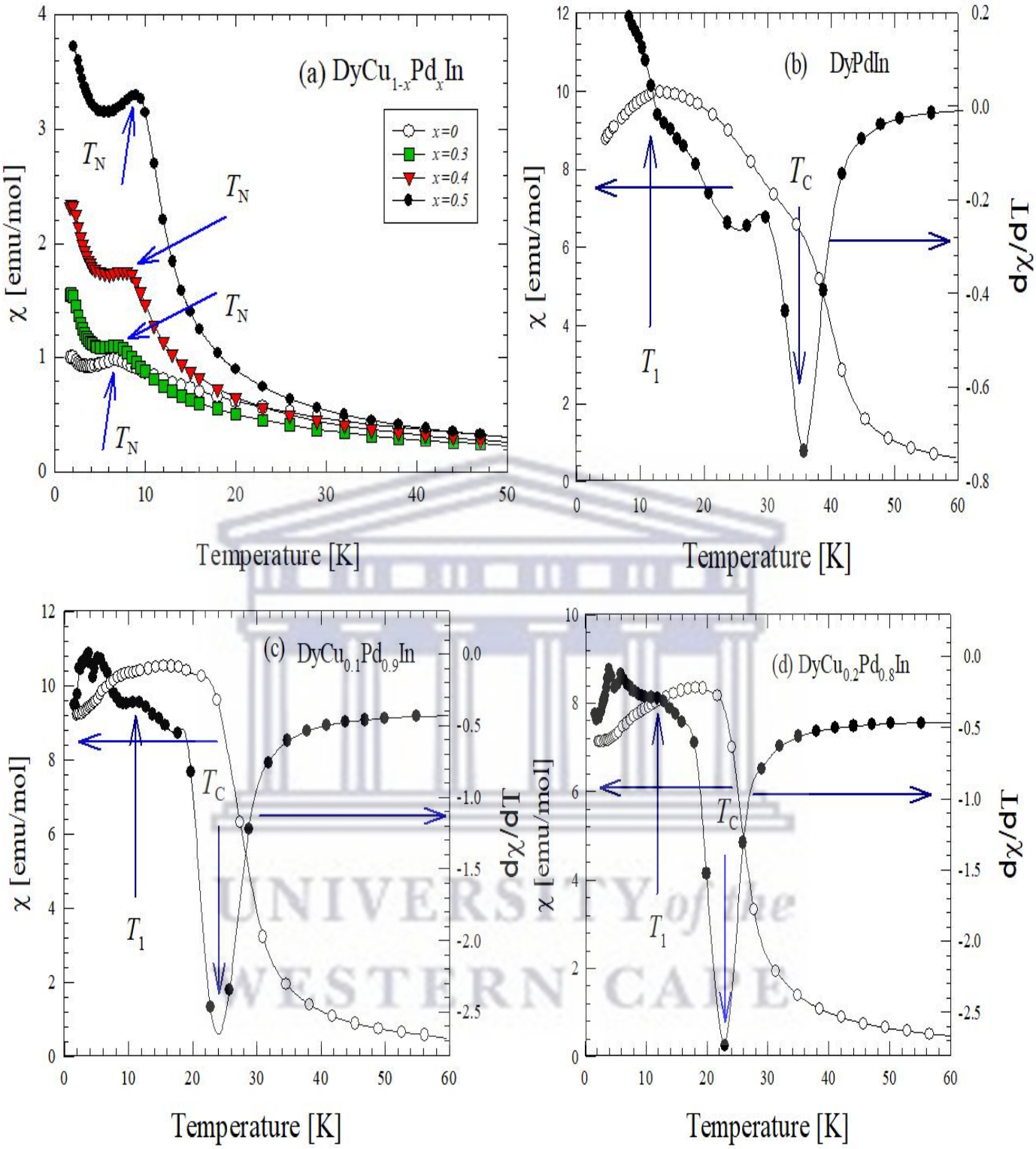

Figure 6.13: The low temperature χ (*T*) data of selected samples of the Dy($Cu_{1-x}Pd_x$)In alloys series in the (a) AFM regime, (b), (c) and (d) FM regime (left axis). The right axis of (b), (c) and (d) display $d\chi/dT$. The arrows indicate the magnetic phase transition temperature T_N taken at kink and T_C taken at the minimum of $d\chi/dT$ curves.

6.3.3 Heat capacity

Figures 6.14 (a) and (b) show the heat capacity, $C_p(T)$ results of the two end compounds DyCuIn and DyPdIn together with their isomorphous non-magnetic compounds YCuIn and YPdIn, measured in the temperature range 2 to 300 K at zero magnetic field. For the two isomorphous non-magnetic compounds, $C_p(T)$ varies monotonically with no anomaly down to 2 K, while $C_p(T)$ of the two magnetic compounds DyCuIn and DyPdIn show anomalies at the magnetic phase transition temperature T_N = 6.6 K and T_C = 30.4 K, T_1 = 11.6 K, T_2 = 3.6 K, respectively as indicated by arrows in figures 6.14 (a) and (b). These values corroborate with the magnetic phase transition temperatures observed from the susceptibility results except for the magnetic phase transition temperature T_2. At higher temperatures, the heat capacity curves of DyCuIn YCuIn in and YPdIn approach the classical value $3NR$ = 74.83 J/mole.K (N = 3 is the number of atoms per formula unit, R stands for the gas constant) of the Dulong-Petit law at 300 K (horizontal line in figures 6.14 (a) and (b) and above 300 K for the DyPdIn. In the whole temperature range measured, $C_p(T)$ data of both isomorphous non-magnetic compounds can be well described by the Debye-Einstein model [208]:

$$C_p(T) = \gamma T + 9NR(1-d)\left(\frac{T}{\theta_D}\right)^3 \int_0^{\frac{\theta_D}{T}} \frac{x^4 e^x}{(e^x-1)^2} dx + 3NRd\left(\frac{\Theta_E}{T}\right)^2 \frac{e^{\Theta_E/T}}{\left(e^{\Theta_E/T}-1\right)^2} \qquad (6.1)$$

where d is a number of Einstein modes, the first term represents the electronic contribution with γ being the Sommerfeld coefficient and the second and third terms are the standard Debye and Einstein expressions for the phonon contribution with θ_D and Θ_E being the Debye and Einstein temperatures, respectively. The LQS fit of Eq. 6.1 to $C_p(T)$ data (note the red curves in figures 6.14 (a) and (b) yielded the parameters: γ =2.0 (1) mJ/mole.K, d = 0.116 (2), θ_D = 232.8 (3) K and Θ_E = 26.5 (5) K for YCuIn and γ = 1.5 (3) mJ/mole.K, d = 0.27 (2), θ_D = 273.6 (2) K and Θ_E = 191.8 (4) K for YPdIn. It should be noted that the large value of θ_D obtained for the YPdIn results from the large atomic mass of Pd atom compared to the Cu atom and indicated a large vibrational spectrum of the YPdIn compound. The low temperature $C_p(T)$ data of DyCuIn, measured in zero magnetic field, 3 T and 5 T are shown in the inset of figure 6.14 (a). In contrast to typical antiferromagnet, the specific heat peak at T_N marking the onset of the ordered state shifts to higher temperatures with increasing magnetic field strength. Such behaviour is usually observed in ferromagnetic materials.

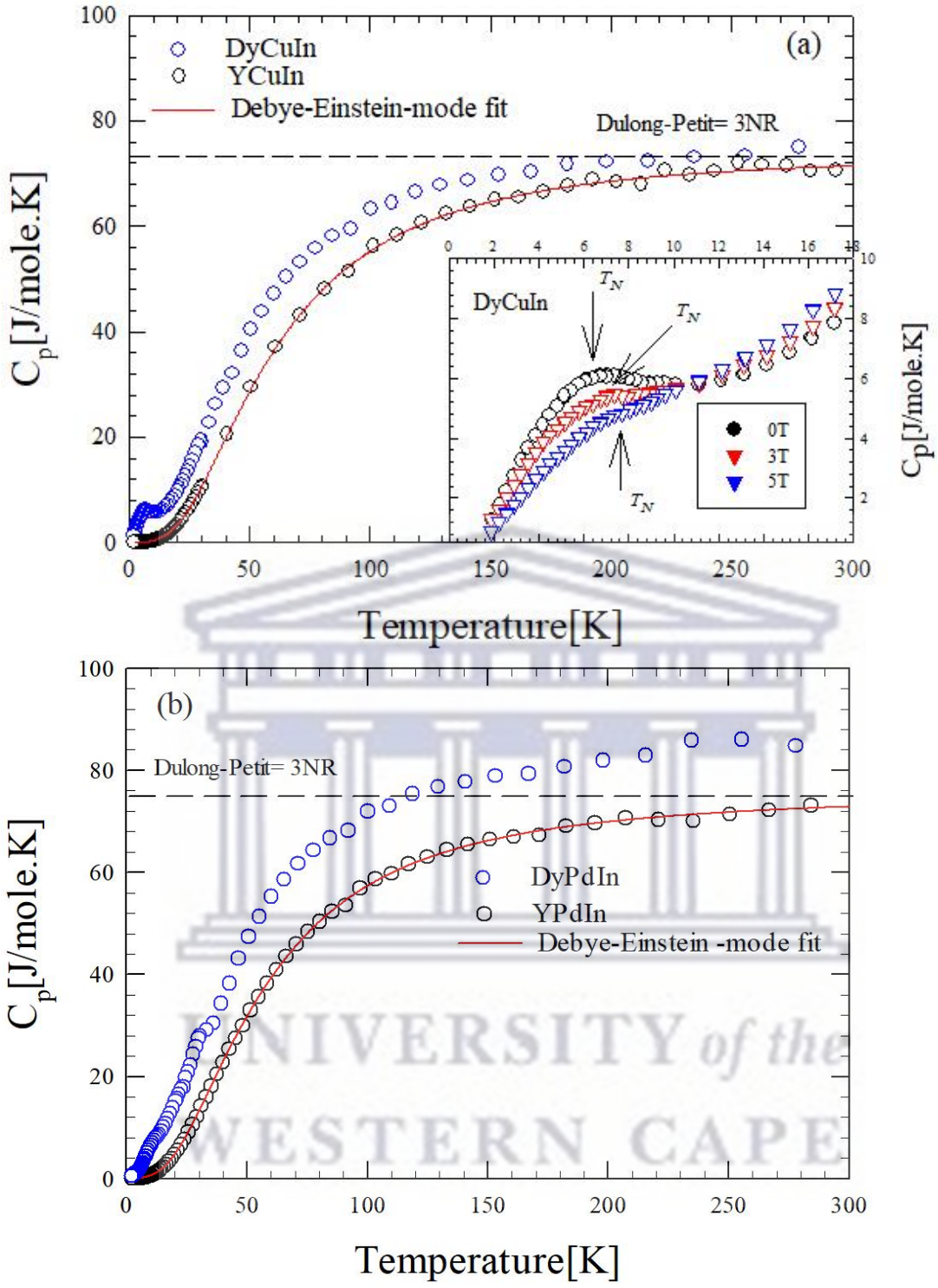

Figure 6.14: Temperature variation of the heat capacity, $C_p(T)$ of (a) DyCuIn and YCuIn with inset showing an expanded view of the low temperature $C_p(T)$ measured in 0, 3 and 5 T applied field; (b) DyPdIn and YPdIn. The solid red curves are the LSQ fit of Eq. 6.1 to the experimental data of both non-magnetic compounds YCuIn and YPdIn. The arrows in the inset indicate the position of T_N.

Figures 6.15, and 6.16 display the low temperature C_p (T)/T results of all measured samples. It is observed that all samples in the alloy series Dy($Cu_{1-x}Pd_x$)In order magnetically due to the magnetic moments carried on trivalent Dy ions. For some samples in the alloys series, C_p (T) data revealed the occurrence of two to three maxima and kinks as indicated by arrows in figures 6.15 and 6.16 which may be attributed to subsequent phase transitions of antiferromagnetic and ferromagnetic character. A cascade of features at similar temperatures were also found in the magnetic susceptibility of samples exhibiting FM behaviour. These additional magnetic phase transitions were attributed to the AFM rearrangement of the Dy moments. The observed magnetic phase transitions from C_p (T) data are listed in table 6.5.

Table 6.5: Magnetic phase transition temperatures observed from heat capacity data of the alloy series Dy($Cu_{1-x}Pd_x$)In.

Pd Content x	$T_C^{Cp}[K]$	$T_N^{Cp}[K]$	T_1^{Cp}	T_2^{Cp}
1	30.4		11.8	3.5
0.9	23.4		11.5	
0.8	18.3		9.9	
0.7	16.7		9.4	
0.6	9.9			
0.5		9.4		
0.4		8.6		
0.3		7.9		
0		6.6		

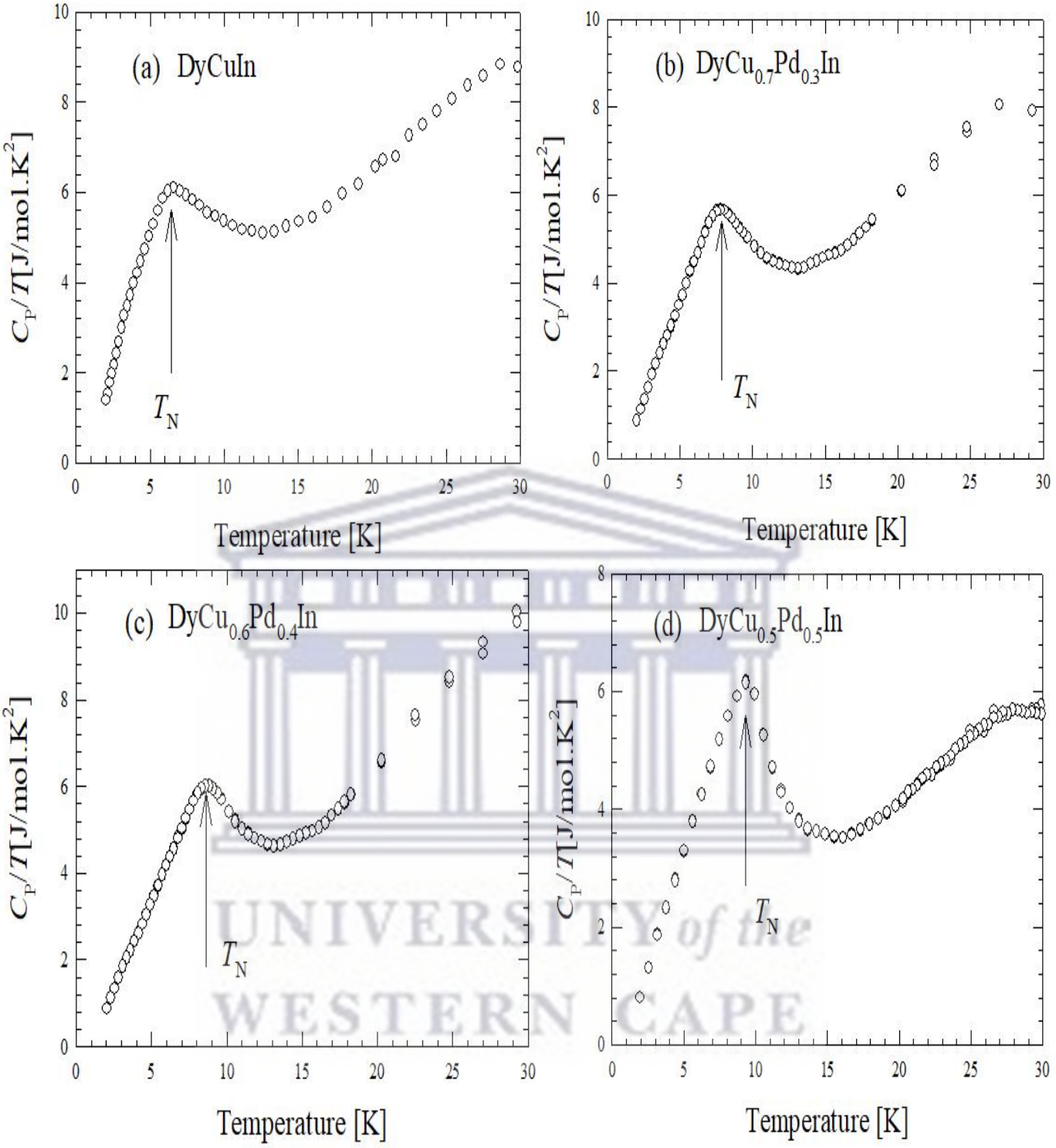

Figure 6.15: The low temperature $C_p(T)/T$ data of the alloy series $Dy(Cu_{1-x}Pd_x)In$. The arrows indicate the magnetic phase transition temperatures.

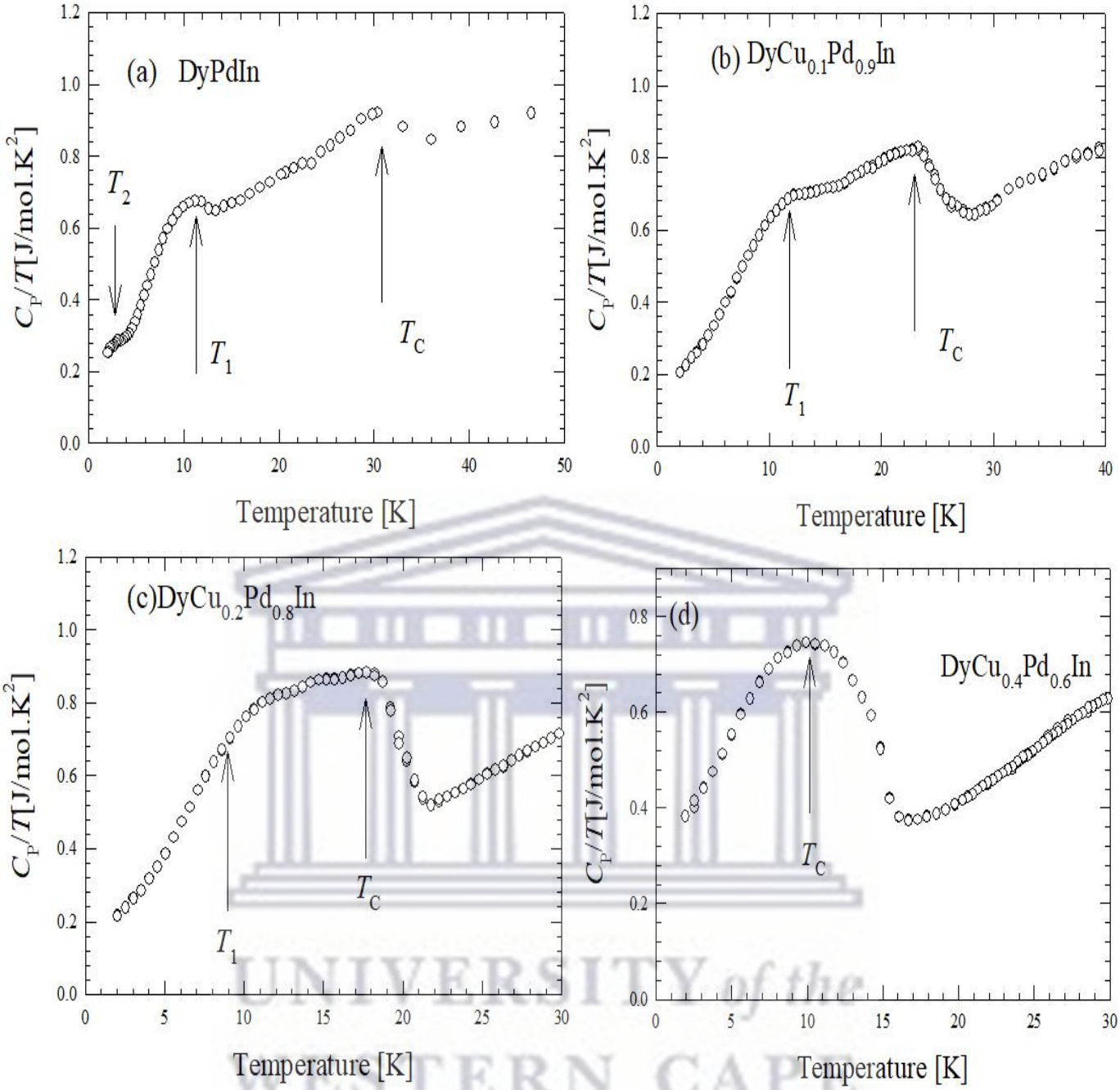

Figure 6.16: The low temperature C_p (T)/T data of the alloy series Dy($Cu_{1-x}Pd_x$)In. The arrows indicate the magnetic phase transition temperatures.

Figure 6.17 displays the magnetic 4*f*-electron contribution to the total heat capacity, C_{4f} (T) of selected samples of the alloy series Dy($Cu_{1-x}Pd_x$)In, obtained by subtracting the phonon contribution which was assumed to be the same as in the isostructural compounds YCuIn and YPdIn given by:

$$C_{4f}(T) = C_{p,Dy(Cu_{1-x}Pd_x)In}(T) - \left[(1-x)C_{p,YCuIn}(T) + xC_{p,YPdIn}(T)\right]. \quad (6.2)$$

As shown in figure 6.17, below T_C, $C_{4f}(T)$ data can be well approximated according to the ferromagnetic magnons with an energy gap Δ_C in the spin-wave spectrum (Eq. 4.3). LSQ fit of Eq. 4.3 to the data (solid red curves) yielded the parameter values listed in Table 6.6.

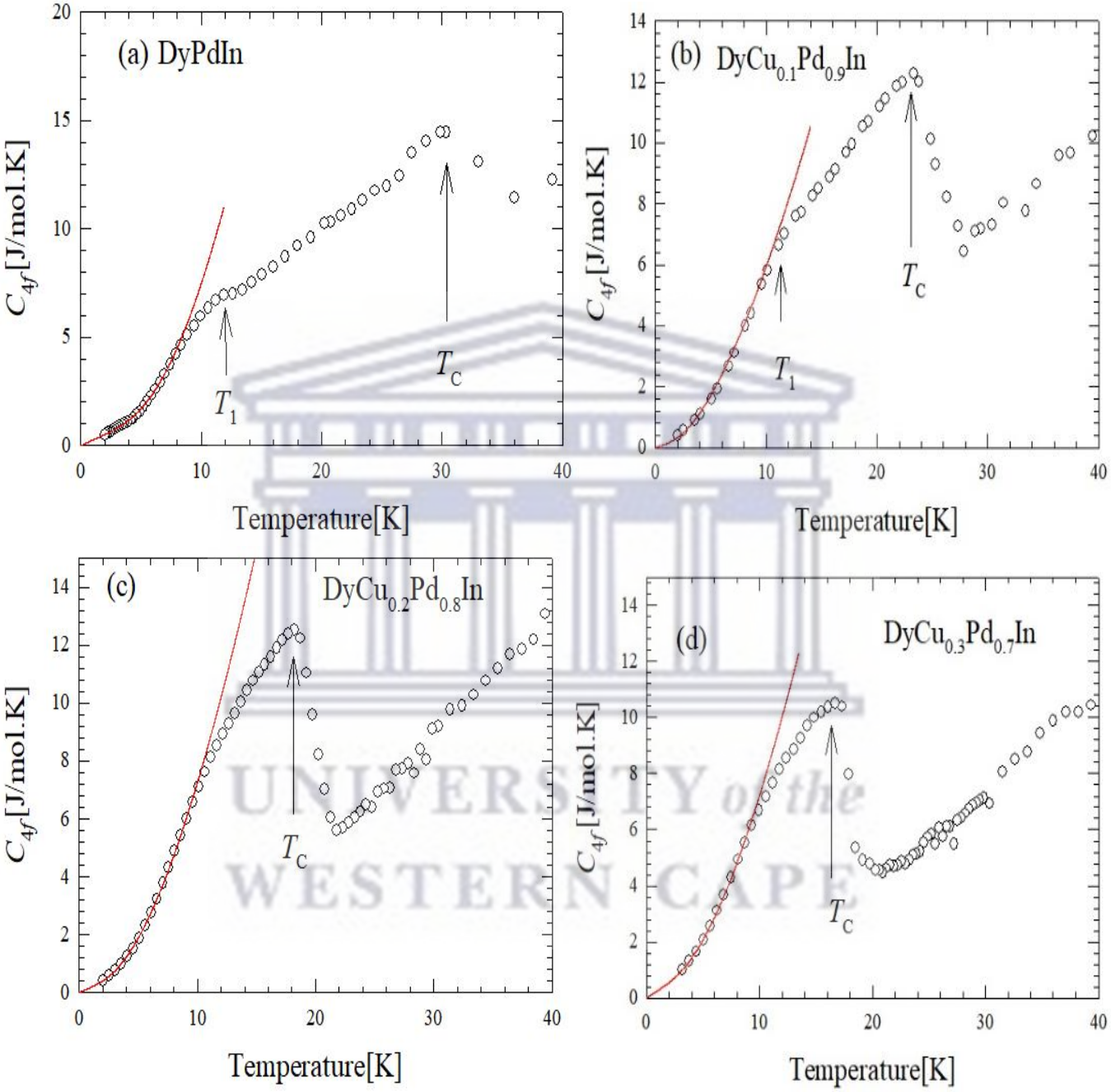

Figure 6.17: Temperature variations of the 4*f*-electron contribution to the total heat capacity, $C_{4f}(T)$ of selected samples in the alloy series $Dy(Cu_{1-x}Pd_x)In$ measured in zero applied magnetic field. The solid red curves are LSQ fits of the spin-wave dispersion relation Eq. 4.3 to the C_{4f} (T) data.

Table 6.6: Spin-wave parameters of selected samples of the alloy series $Dy(Cu_{1-x}Pd_x)In$ obtained from the LSQ fit of Eq. 4.3 to the data.

Pd content [x]	γ[J/mol.K^2]	A [J/mol.K$^{5/2}$]	Δ_C [K]
0.7	0.246(2)	0.273(1)	6.155(1)
0.8	0.137(3)	0.284(1)	4.693(9)
0.9	0.172(2)	0.238(9)	6.309 (7)
1	0229(1)	0.331(2)	9.246(1)

Figure. 6.18 displays the magnetic 4*f*-electron contribution to the total specific heat, C_{4f} (T) of selected samples of the alloy series $Dy(Cu_{1-x}Pd_x)In$ calculated, as above in Eq 6.2. It is observed that C_{4f} (T) for these samples above the magnetic phase transition region exhibited a broad maximum centered around T_{max} = 60, 61, 81 and 55 K for x = 1, 0.9, 0.8 and 0, respectively characteristic of a Schottky anomaly, due to the freezing out of CEF-split magnetic levels. This observed maximum is well described in absolute magnitude to a three-level CEF Schottky description:

$$C_{4f}(T) = \frac{R}{T^2}\left[\frac{\sum_{i=0}^{n-1}\left(\frac{g_i}{g_{i+1}}\right)\Delta_i^2 e^{-\Delta_i/T}}{\sum_{i=0}^{n-1} e^{-\Delta_i/T}} - \left(\frac{\sum_{i=0}^{n-1}\left(\frac{g_i}{g_{i+1}}\right)\Delta_i e^{-\Delta_i/T}}{\sum_{i=0}^{n-1} e^{-\Delta_i/T}}\right)^2\right]. \quad (6.3)$$

The most suitable fit of Eq. 6.3 to the data was obtained using the degeneracy ratio $\frac{g_0}{g_1} = \frac{1}{2}$ and $\frac{g_1}{g_2} = 3$ (for DyCuIn), $\frac{g_0}{g_1} = \frac{5}{2}$ and $\frac{g_1}{g_2} = \frac{7}{2}$ (for DyPdIn), $\frac{g_0}{g_1} = 2$ and $\frac{g_1}{g_2} = 3$ (for $Dy(Cu_{0.1}Pd_{0.9})In$), between the ground state and first excited state and between the first excited state and second excited state of Dy^{3+}-ion, respectively. The LSQ fits gave the estimations of the energy splitting taking the ground state Δ_0 = 0 K; Δ_1 = 77 (2) K and Δ_2 = 140 (2) K for DyCuIn; Δ_0 = 0 K; Δ_1 = 96 (2) K and Δ_2 = 202 (3) K for DyPdIn and finally Δ_0 = 0 K; Δ_1 = 82 (2) K and Δ_2 = 177 (3) K for $Dy(Cu_{0.1}Pd_{0.9})In$. LSQ fit of Eq. 6.3 to C_{4f} (T) of $Dy(Cu_{0.2}Pd_{0.8})In$ was not successful due to the shallow maximum observed for this samples.

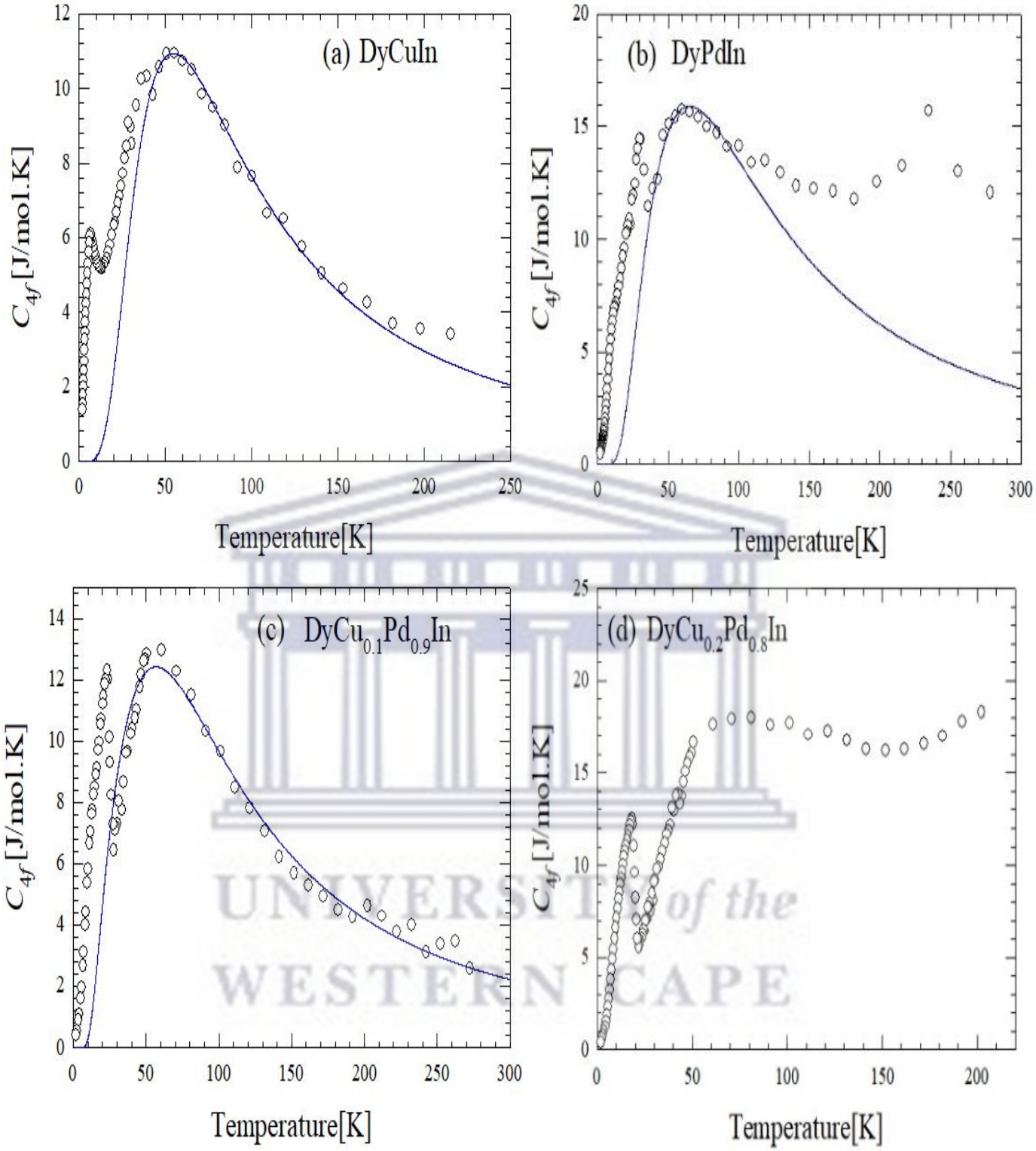

Figure 6.18: Temperature variations of the 4*f*-electron contribution to the total heat capacity, $C_{4f}(T)$ of selected samples in the alloy series $Dy(Cu_{1-x}Pd_x)In$ measured in zero applied magnetic field. The solid blue curves are CEF-derived Schottky anomaly using Eq 6.3.

The temperature variation of the magnetic entropy $S_{4f}(T)$ is shown in figures 6.19 and 6.20. $S_{4f}(T)$ were obtained from the magnetic 4*f*-electron specific heat, $C_{4f}(T)$ data of each sample in the alloy series $Dy(Cu_{1-x}Pd_x)In$ using the relation:

$$S_{4f}(T) = \int_0^T \frac{C_{4f}(T')}{T'} dT'. \tag{6.4}$$

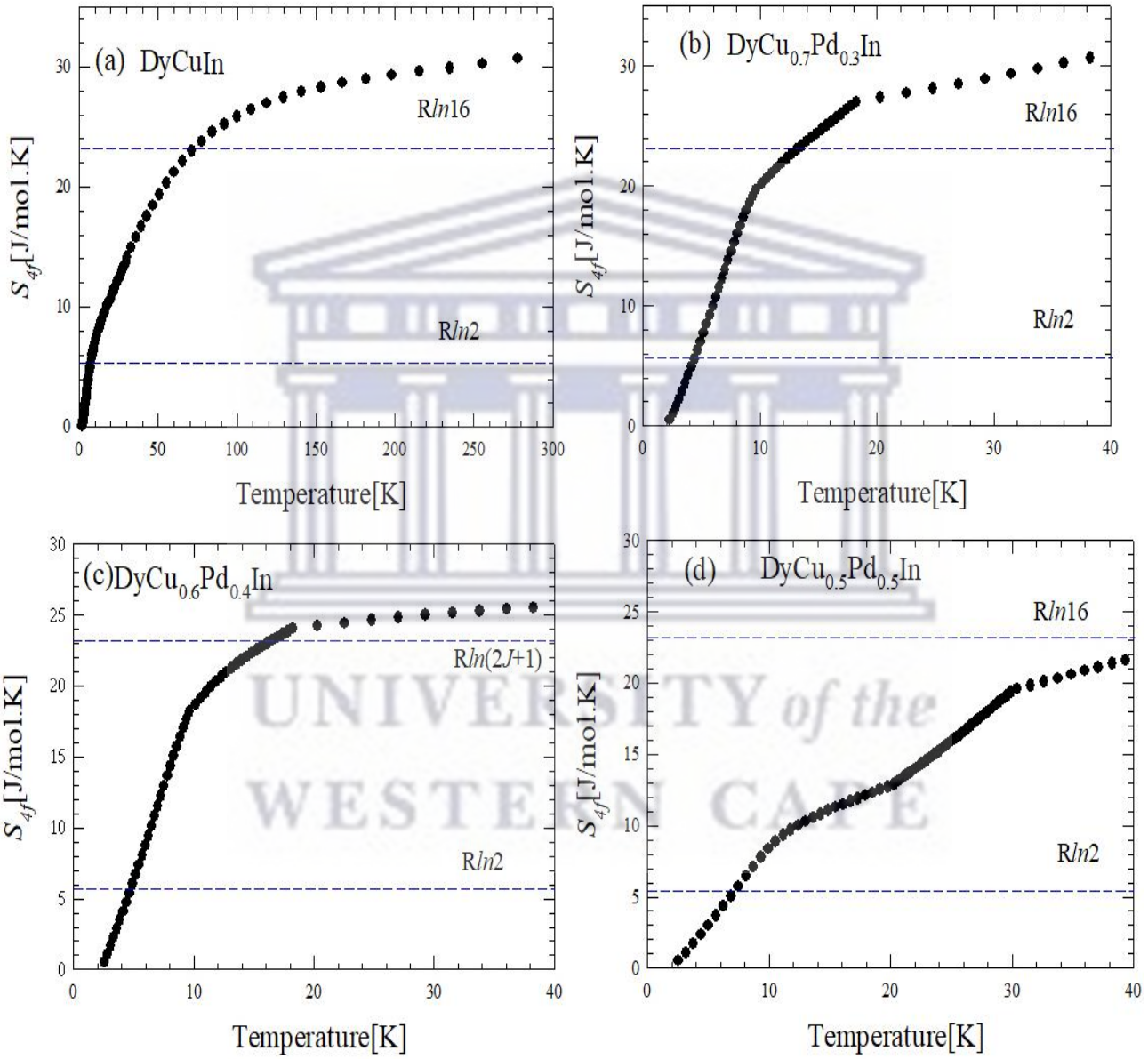

Figure 6.19: Temperature variations of magnetic entropy $S_{4f}(T)$ obtained from the magnetic 4*f*-electron specific heat, $C_{4f}(T)$ data of each sample in the alloy series $Dy(Cu_{1-x}Pd_x)In$ using Eq 6.4.

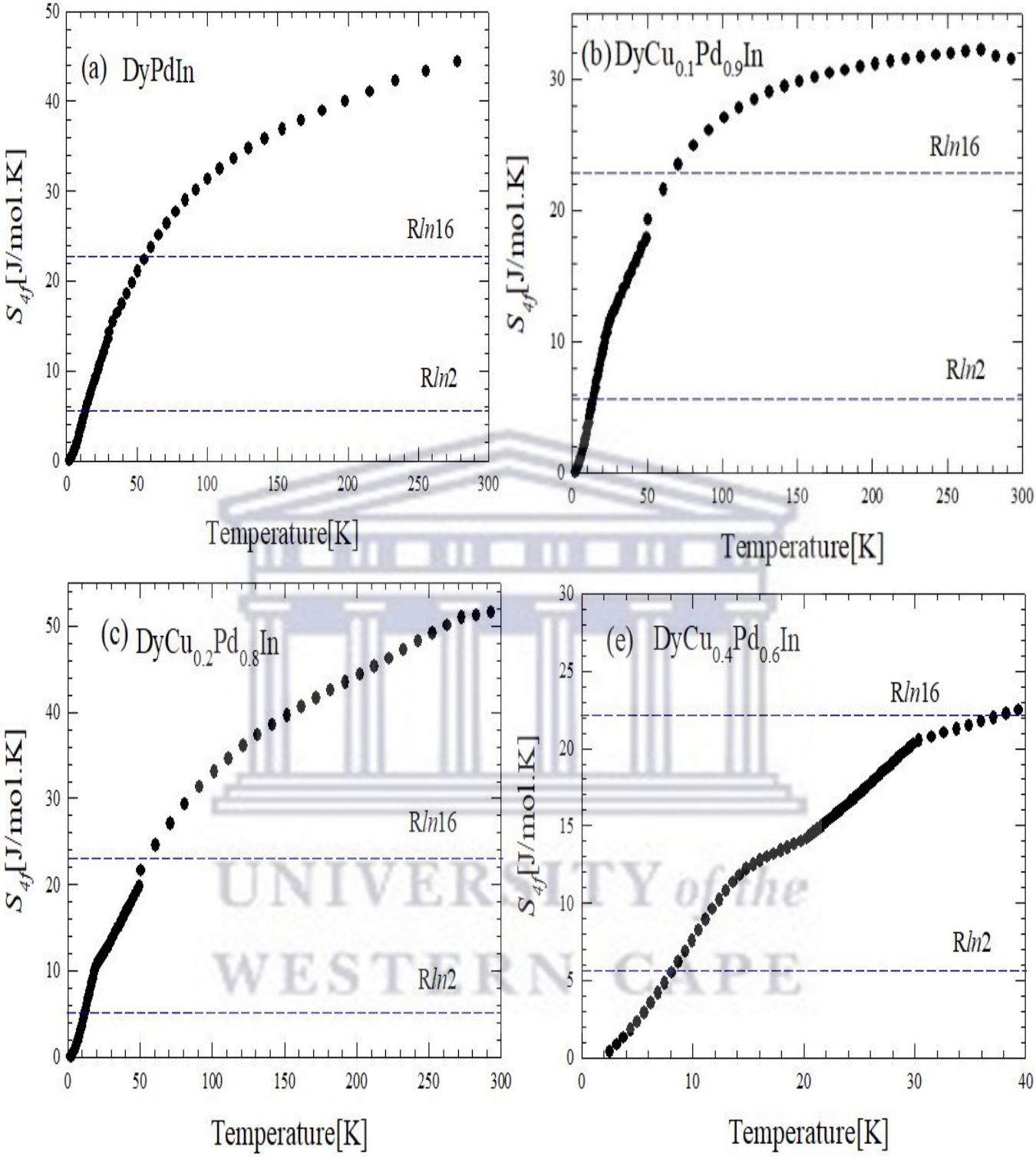

Figure 6.20: Temperature variations of magnetic entropy $S_{4f}(T)$ obtained from the magnetic 4*f*-electron specific heat, $C_{4f}(T)$ data of each sample in the alloy series $Dy(Cu_{1-x}Pd_x)In$ using Eq 6.4.

As shown in figures 6.18 and 6.19, $S_{4f}(T)$ has its largest drop around the temperature range corresponding to the Schottky-like broad maximum in $C_{4f}(T)$, while a further drop is observed near T_C and T_N. The values of $S_{4f}(T)$ at T_N and T_C are listed in table 6.7.

Table 6.7: The 4*f*-electron magnetic entropy $S_{4f}(T)$ values at the magnetic phase transition temperature T_N and T_C for $Dy(Cu_{1-x}Pd_x)In$.

Pd [x]	S_{4f} [J/mol.K] at T_N	S_{4f} [J/mol.K] at T_C
0	5.13	
0.3	15.36	
0.4	15.848	
0.5	8.091	
0.6		7.561
0.7		13.594
0.8		9.694
0.9		10.689
1		14.318

As inferred in table 6.8 for the DyCuIn compound, $S_{4f}(T)$ reaches the value of $Rln2$ expected for the two-level ground states at temperatures close to T_N while for all the other samples $S_{4f}(T)$ reaches this value well below their magnetic phase transition temperatures T_N and T_C. On the other hand, for all investigated samples, $S_{4f}(T)$ curves reach the value of $Rln(2J+1) = Rln(16)$ for J = 15/2 well above T_N and T_C. As mentioned above, the drop in $S_{4f}(T)$ of DyCuIn is comparable to the two-level ground states with the value of $S_{4f}(T)$ at T_N equal to 5.13 J/mole.K which is of the same order of magnitude as that of the theoretical value $Rln2$ = 5.76 J/mole.K. In contrast, the value of $C_{4f}(T)$ at T_N of 6.12 J/mole.K is roughly two times smaller than $\frac{3}{2}R = 12.74$ J/mole.K expected for the two-level ground states. However, the value of the $C_{4f}(T)$ at the Schottky-like maximum of 10.94 J/mole.K may be compared to $\frac{3}{2}R$ value.

It is worthwhile to summarize all the results obtained from these experimental investigations through a putative magnetic phase diagram of $Dy(Cu_{1-x}Pd_x)In$ alloy series as depicted in Fig 6.21. Remarkably all the results corroborated quite well from the different measurements. No dominance of the AFM or the FM state was observed across the series. Further investigations are needed in the concentration range $0.5 < x_C < 0.6$ for a possible coexistence of AFM and FM state, or a quantum critical concentration x_C, which mark the crossover from the AFM to the FM state.

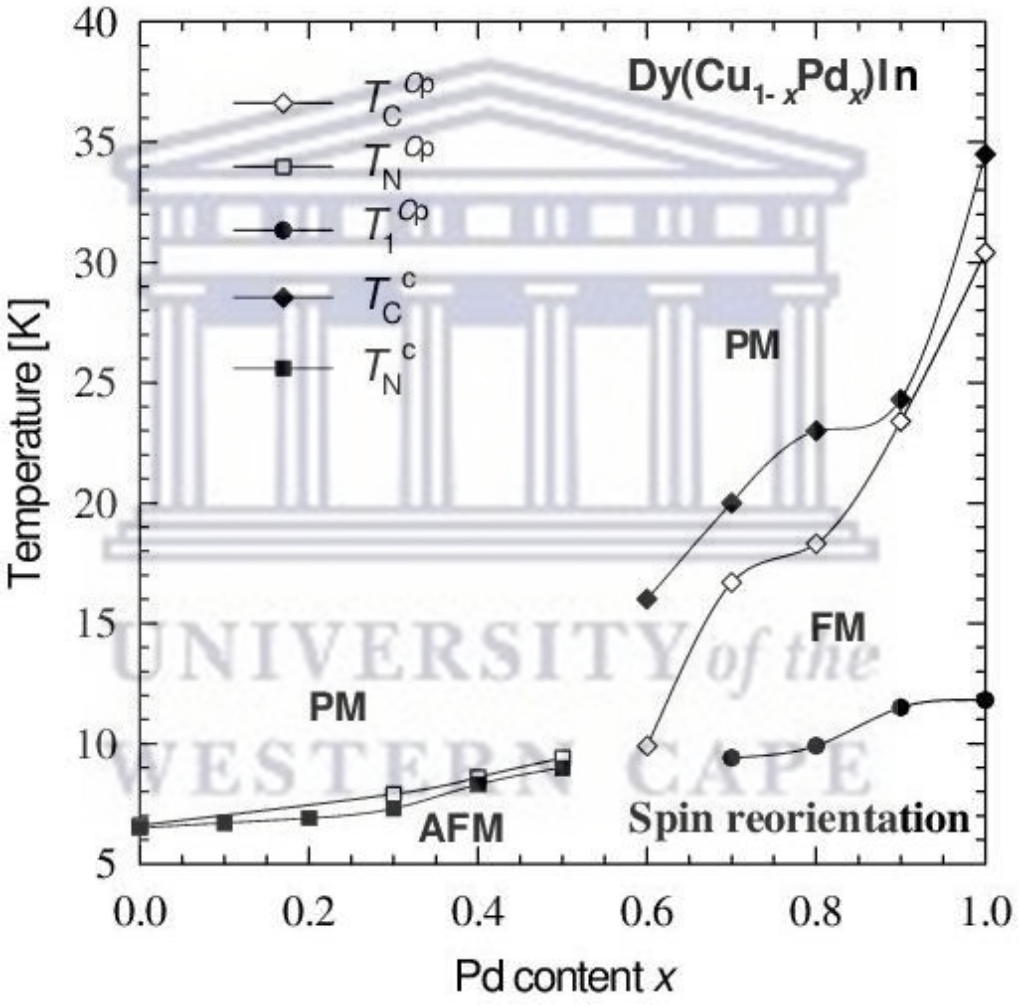

Figure 6.21: Tentative magnetic phase diagram of polycrystalline $Dy(Cu_{1-x}Pd_x)In$ alloy series. The lines are guide for the eye. PM- paramagnetic, AFM- antiferromagnetic and FM- ferromagnetic.

6.4 Conclusion

In summary, the study of the transition of the magnetic state from antiferromagnetic to ferromagnetic order in $Dy(Cu_{1-x}Pd_x)In$ under chemical substitution showed that the AFM state extended up 50% Pd content. The method used for this transition of magnetic state is that of the macroscopic method which relied on the temperature dependences of magnetization, magnetic susceptibility and specific heat measurements. XRD studies revealed that the gradual substitution of Cu with Pd retained the crystal structure but the magnetic properties were modified from AFM to FM. All samples as well as the non-magnetic YCuIn and YPdIn compounds were found to crystallize in the ZrNiAl-type structure with space group *P*-62*m* (No. 189). Magnetization behaviour for samples in the range $0.6 \leq x \leq 1$ are typical for FM materials while for samples in range $0 \leq x \leq 0.5$, M ($\mu_0 H$) behaviour may be attributed to AFM. χ (T) at high temperature all samples follow the Curie-Weiss behaviour giving an effective magnetic moment value in agreement with that expected for the Dy ion.

The low temperature $\chi(T)$ and $C_p(T)$ revealed the occurrence of two to three distinct magnetic phase transitions at T_C, T_N and T_1, which may be attributed to subsequent phase transitions of FM and AFM character. The additional phase transition observed below T_C and T_N indicated AFM rearrangement or spin reorientation of the Dy moment. $C_p(T)$ data of both non-magnetic counterparts can be well described by the Debye-Einstein model. The 4*f*-electron magnetic contribution to the total $C_p(T)$ indicated a CEF splitting of the $J = 15/2$ ground state of Dy^{3+}. $C_{4f}(T)$ below T_C are well described in terms of ferromagnetic spin – wave with energy gap Δ_C. The 4*f*-electron magnetic entropy, $S_{4f}(T)$ reached the value of $Rln(2)$ expected for the two-level ground state near T_N for the DyCuIn and well below T_N and T_C for the other samples.

Chapter 7

Conclusion and future works

Beside the conclusions given in each chapter, this chapter summarizes all the results obtained from the physical properties' measurements investigated in this research project including XRD analysis.

Evidence for magnetic ground state switching between ferromagnetic (FM) and antiferromagnetic (AFM) ordering driven by chemical substitution in *d*, *f* and *p*-electron compounds have been the unified term in this experimental research. The method used in particular for this transition is that of the macroscopic method which involves the temperature dependences of magnetization, magnetic susceptibility and specific heat measurements. The measurements of electrical resistivity were implemented to explore the magnetic behaviour and the scattering process at low temperatures below the ordering temperature for spin-wave description as well as the phonon scattering under the influence of crystal electric field effect (CEF) at high temperatures.

The alloy systems for which the transition from FM to AFM was investigated in this research project includes: $CeCu(Ge_{1-x}Sn_x)$, $(Ce_{1-x}Nd_x)CuGe$ and $Dy(Cu_{1-x}Pd_x)In$. An interesting property of the first and the third systems is that substitution of Ge in place of Sn and of Pd in place of Cu retains the crystal structure, but the magnetic properties are modified from FM to AFM. The parent compounds CeCuGe and DyPdIn adopt the FM ground state, while CeCuSn, NdCuGe and DyCuIn adopt the AFM ground state. The overall results of magnetization, magnetic susceptibility and heat capacity indicate that the FM ground state is predominant for the two former systems upon chemical substitution. For $CeCu(Ge_{1-x}Sn_x)$ and $(Ce_{1-x}Nd_x)CuGe$ alloys series, the FM ground state extend up to 60% Ge and Ce content, respectively, while for $Dy(Cu_{1-x}Pd_x)In$ alloy series, the AFM ground state extend up to 50% for both Cu and Pd content. The overall results of XRD for all three systems indicate a hexagonal crystal structure with different space groups. For $CeCu(Ge_{1-x}Sn_x)$ alloy series XRD indicates a hexagonal ZrBeSi-type crystal structure with space group $P6_3/mmc$ for all investigated samples, while for

$(Ce_{1-x}Nd_x)CuGe$ alloys series, XRD results indicated that except for CeCuGe which crystallized in the ZrBeSi-type double-hexagonal-close (hcp) crystal structure all samples crystallize in the AlB_2-type hexagonal crystal structure with space group *P6/mmm*. In the case of $Dy(Cu_{1-x}Pd_x)In$ alloy series, XRD results revealed that all samples as well as the non-magnetic counterpart YCuIn and YPdIn compounds crystallized in the ZrNiAl-type structure with space group *P-62m*.

For the $CeCu(Ge_{1-x}Sn_x)$, $Dy(Cu_{1-x}Pd_x)In$ and $(Ce_{1-x}Nd_x)CuGe$ alloys series, the magnetic susceptibility, χ (T) data at high temperatures follows the Curie-Weiss relation given and effective magnetic moment, μ_{eff} values reasonably close to that predicted within a Russel-Saunders coupling scenario for the trivalent Ce-ion (2.54 μ_B) and Dy-ion (10.65 μ_B) in the case of the first and the second systems, while a gradual increase of μ_{eff} values from 2.54 μ_B to the theoretical value of 3.62 μ_B expected for the Nd-ion in the case of $(Ce_{1-x}Nd_x)CuGe$ alloys series. At low temperature χ (T) data deviated from the Curie-Weiss relation due to magnetocrystalline anisotropy and exhibited a magnetic phase transition temperature at T_C and T_N for all samples in the three alloy systems. Furthermore, for some samples in the alloy series $CeCu(Ge_{1-x}Sn_x)$ and $Dy(Cu_{1-x}Pd_x)In$, an additional magnetic phase transition at T_1 was observed below T_C and T_N and was attributed to spin reorientation of the Ce or Dy magnetic moments. For samples exhibiting FM ordering, the magnetization, M (μ_0,H) behaviour was typical of FM materials.

In concert, the heat capacity, C_p (T) data at low temperature confirm the magnetic phase transitions at T_C and T_N. An additional magnetic phase transition below these temperature for the alloy series $CeCu(Ge_{1-x}Sn_x)$ and $Dy(Cu_{1-x}Pd_x)In$. C_p (T) data of both non-magnetic counterparts YCuIn and YPdIn are well described in terms of the Debye-Einstein model. For some samples in the alloy series $CeCu(Ge_{1-x}Sn_x)$ and $Dy(Cu_{1-x}Pd_x)In$, the 4*f*-electron magnetic contribution to the total heat capacity, C_{4f} (T) below T_C are well described in terms of ferromagnetic spin-waves with energy gap Δ_C. For some samples in the alloy series $Dy(Cu_{1-x}Pd_x)In$, C_{4f} (T) at high temperature exhibit a broad maximum characteristic of a Schottky anomaly which indicated a CEF splitting of the J = 15/2 ground state multiplet of Dy^{3+}. The 4*f*-electron magnetic entropy, S_{4f} (T) reached the value of $Rln(2)$ expected for the two – level ground states near T_N for the DyCuIn and well below T_N and T_C for some samples in the alloy series $CeCu(Ge_{1-x}Sn_x)$ and $Dy(Cu_{1-x}Pd_x)In$.

Results for the electrical resistivity, ρ (T) data of the alloy systems $CeCu(Ge_{1-x}Sn_x)$ and $(Ce_{1-x}Nd_x)CuGe$ also confirm the magnetic phase transitions at low temperature T_C and T_N and revealed the occurrence of a second magnetic phase transition below T_C and T_N which may be attributed to spin reorientation or rearrangement of the magnetic moments of Ce ions in the case of $CeCu(Ge_{1-x}Sn_x)$ alloy series. For some samples in the alloy series $CeCu(Ge_{1-x}Sn_x)$ and $(Ce_{1-x}Nd_x)CuGe$, ρ (T) data below T_C are well described in terms of FM spin-wave excitation with energy gap Δ_R. For some samples in the alloy series $CeCu(Ge_{1-x}Sn_x)$ and $(Ce_{1-x}Nd_x)CuGe$, ρ (T) data show a minimum at T_{min} above T_C and T_N and the increase of ρ (T) data between T_{min} and T_C or T_N are interpreted in terms of FM or AFM superzone pseudogap at the Fermi surface. For the alloy systems $CeCu(Ge_{1-x}Sn_x)$, ρ (T) data at high temperatures in the paramagnetic region are well described in terms of the Bloch-Grüneisen-Mott (BGM) formula, while for the alloy system $(Ce_{1-x}Nd_x)CuGe$, ρ (T) data at high temperature cannot be interpreted in terms of BGM formula due to the large influence of the CEF effect resulting from Nd atom.

Future experimental investigations of the magnetic ground state switching between FM and AFM orderings can be done using the microscopic method which involve neutron diffraction and Mössbauer effect. The magnetic structure of these alloys will result from these experiments. Furthermore, the nature of the ordered state of these alloy systems need to be performed through measurements of AC susceptibility. The critical concentration, x_c at which the transition occurs need to be investigated for synthesized samples in the border of the FM and AFM region.

References

[1]. K.H.J. Buschow, *Rep. Prog. Phys* 40, (1977) 1179.

[2]. A. Szytula, *Handbook of Magnetic Materials vol 6* (Elsevier, Amsterdam, 1991) 85.

[3]. A.M. Tishin, Y.I. Spichkin, *The magnetocaloric effect and its applications*, (Inst. Phys. Publ., Bristol, 2003) 322.

[4]. H. Szymczak and R. Szymczak. *Materials Science-Poland, 26* (2008) 807.

[5]. A.M. Tishin, *J. Magn. Magn. Mater*, 184 (1998) 62.

[6]. V. Pecharsky, K. Vitalij, K. Gschneidner, *J. Magn. Magn.Mater* 200, (1999) 44.

[7]. H. Feng-Xia, S. Bao-Gen, S. Ji-Rong, and Z. Xi-Xiang, *Chinese Phys.B*, 9 (2000) 550.

[8]. H. Feng-xia, S. Bao-gen, S. Ji-rong, C. Zhao-hua, R. Guang-hui, and Z. Xi-Xiang, *Appl. Phys. Lett.*, 78 (2001) 3675.

[9]. H. Wada, Y. Tanabe, *Appl Phys. Lett.* 79 (2001) 3302.

[10]. O. Tegus, E. Bruck, K.H.J. Buschow, F.R. De Boer, *Nature*, 415 (2002) 150.

[11]. J. G. Sereni, "Encyclopedia of Materials: Science and Technology", Eds: K. H. J. Busschov and E. Gratz, Elsevier Ltd., Oxford, 2001, p. 4986.

[12]. G. E. Bacon, "Neutron Diffraction", Clarendon Press, Clarendon, 1975.

[13]. F. von Rohr, A. Krzton-Maziopa, V. Pomjakushim, H. Gundmann, Z. Guguchia, W.Schnick and A Schilling, J. Phys.: Condens. Matter 28 (2016) 276001.

[14]. P. Kushwaha, P. Bag, R. Rawat and P. Chadda, J. Phys.: Condens. Matter 24 (2012) 096005.

[15]. Mrcin M. Wysokiński, Scientific Reports 9 (2019) 19461.

[16]. K. H. J. Buschow, F.R.de Boer, *Physics of Magnetism and Magnetic Materials*,(Kluwer Academic-NewYork, 2003) 4-9.

[17]. S. Cotton, *Lanthanide and actinide chemistry* (John Wiley & Sons, England, 2013) 9.

[18]. D.H. Martin, *Magnetism in Solids*, (M.I.T Press, Cambridge- Mass,1967) 145-148.

[19]. A.H. Morrish, *The Physical Principles of Magnetism*, (New York: John Wiley and Sons,1965) 36.

[20]. W.E. Henry, *Phys. Rev*. 88 (1952) 559.

[21]. S. Chikazumi, *Physics of Ferromagnetism*, (Oxford University Press Inc., New York,1997) 163.

[22]. J. Jensen, A.R. Mackintosh. *Rare Earth Magnetism*, (CLARENDON PRESS·OXFORD, 1991) 13.

[23]. A. Szytuła. K. H. J. Buschow (Eds), *Handbook of magnetic materials 6*, (Amsterdam: North Holland, 1991) 85.

[24]. K. Yosida, *Theory of Magnetism*, (Springer-Verlag, Berlin, 1996) 6-11.

[25]. B. D. Cullity, C. D. Graham, *Introduction to magnetic materials*, (Wiley-IEEE Press, 2011) 87-114.

[26]. R.E.Smallman, A.H.W.Ngan, *Modern Physical Metallurgy*, (Butterworth-Heinemann, 2014) 189-191.

[27]. N. W. Ashcroft, N. D Mermin, *Solid State Physics*, (Harcourt: Orlando, 1976) 644-649.

[28]. K.H.J. Buschow, *Rep. Prog. Phys*. 54 (1991) 1123.

[29]. C. Kittel, *Introduction to solid state physics* (John Wiley, New York, 2005) 305.

[30]. D. J. Craik, *Magnetism Principles and Applications* (John Wiley, New York, 1995) 59.

[31]. G.I. Likhtenshtein, J. Yamauchi, S. Nakatsuji, A.I. Smirnov, R. Tamura, *Fundamentals of magnetism* (John Wiley, Weinheim, 2008) 24.

[32]. H.E. Hall, J.R. Hook, *Solid state Physics* (Wiley, Chichester, 1994) 244.

[33]. B. M. Sondezi, PhD thesis, University of Johannesburg (2014).

[34]. J. Stohr and H.C. Siegmann, *Magnetism: from fundamentals to Nano scale dynamics* (Springer Science & Business Media, New York, 2007) 17.

[35]. R. J. Elliott, *Magnetic Properties of Rare Earth Metals* (Plenum Press. London, 1972)

4-22, 129.

[36]. R. M Bozorth, *Ferromagnetism*, (Wiley-IEEE Press, 1993) 190-196.

[37]. J. H. Van Vleck, *The theory of electric and magnetic susceptibilities* (Clarendon Press, Oxford,1932) 316.

[38]. W. R. Myers, *Rev. Mod. Phys.*, 24 (1952) 15.

[39]. A. Aharoni, *Introduction to the theory of ferromagnetism*, (Oxford: Oxford University, 1996) 16-32.

[40]. L. Pauling, *J. Chem. Phys.*, 4 (1936), 673.

[41]. C. G Shull, W.A. Strauser, E.O. Wollan, *Phys. Rev. APS* 83(1951) 333.

[42]. J.S. Smart, *AJP* 23 (1955) 356.

[43]. E. Vogt, *Magnetism and metallurgy* (ed. Berkowitz and Kneller, Academic Press, New York,1969) 7-22.

[44]. T. Tsushima, *J. Phys. Soc. Jpn*. 18 (1963) 1162.

[45]. K. H. J. Buschow, R.P.van Stapele, *J. Appl. Phys.*, 41, (1970) 4066.

[46]. J. A Mydosh, *Spin Glasses: An Experimental Introduction*, (CRC Press-london, 1993) 45.

[47]. E. Santucci, L. A. Ludovico, *ICMC* (2014) 94.

[48]. P.A Joy, P.S.A Kumar, *J. Phys.: Condens. Matter*. 10 (1998) 11049.

[49]. P. Nordblad, L. Lundgren, L Sandlund, *J. Magn. Magn.Mater*.54-57 (1986)185.

[50]. V. Dupuis, E. Vincent, J. Hammann, J. E. Greedan, A. S. Wills, *J. Appl. Phys*., 91 (2002) 8384.

[51]. P. E. Jonsson and H. Takayama, *J. Phys. Soc. Jpn*.,74 (2005) 1131.

[52]. P. Weiss, *J. Phys*. 6 (1907), 661.

[53]. R. Becker, W. Doring, *Ferromagnetismus, Nat. Physics, 145* (1940) 606-607.

[54]. A. Arrott, *Phys. Rev*., 108 (1957), 1394.

[55]. J. S. Kouvel, M. E. Fisher, *Phys. Rev*., 136 (1964), 1626.

[56]. J. S. Kouvel, D. S. Rodbell, *Phys. Rev. Letters*, 18 (1967), 215.

[57]. A. Arrott and J. E. Noakes, *Phys. Rev. Letters*, 19 (1967), 786.

[58]. W. Heisenberg, *Z. Physik*, 49 (1928), 619.

[59]. W. L. Bragg and E. J. Williams, *Proc. Ray. Soc*., 151 (1935), 540.

[60]. H. A. Bethe, *Proc. Roy. Soc*., A150 (1935), 552.

[61]. R. Peierls, *Proc. Camb. Phil. Soc*., 32 (1936), 477.

[62]. E. Ising, *Z. Physik*, 31 (1925), 253.

[63]. L. Onsager, *Phys. Rev*. 65 (1944), 117.

[64]. S. Blundell, *Magnetism in condensed matter*, (Oxford Series in Condensed Matter Physics,2001) 79.

[65]. F. Bloch, *Z. Physik*, 61 (1630), 206.

[66]. T. Kasuya, *Prog. Theo. Phys*, 16 (1956) 45–57.

[67]. W. Pauli, *Z. Physik*, 31 (1925), 765.

[68]. P. W. Kasteleijn and J. Van Kranendonk, *Physica* , 22 (1956) 317.

[69]. M.B. Fontes, J.C. Trochez, B. Giordanengo, S.L. Bud'ko, D.R Sanchez, E.M. Baggio- Saitovitch, M.A. Continentino, *Phys. Rev. B*, 60 (1999) 6781.

[70]. N.H. Andersen, H. Smith, *Phys. Rev. B*, 19 (1979) 355.

[71]. K.A. Gschneidner Jr., L. Eyring (Eds.), *Handbook on Physics and Chemistry of Rare Earths, Vol. 6*, (North-Holland, Amsterdam, 1984) 113.

[72]. J. C. Slater, Phys. Rev. 35, 509 (1930).

[73]. H. Yamada and S. Takada, *Prog. Theo. Phys* 49, (1973) 1401.

[74]. S.N. de Medeiros, M.A. Continentino, M.T.D. Orlando, M.B. Fontes, E.M. Baggio-Saitovitch, A. Rosch, and A. Eichler, *Physica B: Condens. Mat.*, 281 (2000) 340.

[75]. F. J. Dyson, *Phys. Rev*. 102 (1956)1217.

[76]. T. Oguchi, *Phys. Rev*. 117(1960) 117.

[77]. F. Keffer and R. Loudon, *Appl. Phys*. 32 (1961) 28.

[78]. M.S. Dresselhaus, G. Dresselhaus, A. Jorio: *Group Theory: Application to the Physics of Condensed Matter,* (Springer, Berlin Heidelberg, 2008) 349.

[79]. E. Pavarini, S. Biermann, A. Poteryaev, A.I. Lichtenstein, A. Georges, O.K. Andersen, *Phys. Rev. Lett*. 92 (2004) 176403.

[80]. E. Pavarini, E. Koch, F. Anders, M. Jarrell, *Correlated Electrons: From Models to Materials Modeling and Simulation Vol. 2* (Forschungszentrum Julich, 2012) 12-14.

[81]. A. Tari*: The Specific Heat of Matter at Low Temperatures* (Imperial College Press, 2003) 250.

[82]. E. Pavarini, E. Koch, and A.I. Lichtenstein, *Phys. Rev*. *Lett*. 101 (2008) 266405.

[83]. E. Pavarini and E. Koch, *Phys. Rev. Lett*. 104 (2010) 086402.

[84]. Ming-Xing Zhang, Patrick M. Kelly. *Crystallographic features of phase transformations in solids*, *Prog. Mater. Sci*. 54 (2009) 1101-1170.

[85]. C Domb, M. Green, *Phase transitions and Critical phenomena* (Academic Press, 1976) 394-406.

[86]. R. Baierlein, *Thermal Physics* (Cambridge University Press, 1996) 205.

[87]. H. von Lohneysen, *J. Phys.: Condens. Matter*, 8 (1996) 9689.

[88]. H. von Lohneysen, A. Rosch , M. Vojta , P.Wolfle, *Rev. Mod. Phys*. 79 (2007)1015.

[89]. VK. Pecharsky, KA Gschneidner, D Fort, *Scripta Mater,* 35 (1996) 843.

[90]. L. Landau, *Phys. Z. Sowjet.* 11 (1937)26; 11.(1937)545.

[91]. L. Landau, E. Lifshitz, *Phys. Z. Sowiet*, 8 (1935)113.

[92]. L.D. Landau, E.M. Lifshitz, *Statistical Physics*, (Addison-Wesley, 1969) 109.

[93]. J.C. Toledano, P. Toledano, *The Landau Theory of Phase Transitions,* (World Sci. press, 1986) 35-41.

[94]. D.R. Moore et al., *Phys. Rev. B*, 27 (1983)7676.

[95]. J. Hertz, *Phys. Rev. B,* 14 (1976) 1165.

[96]. M.A Manekar, S. Chaudhary, M. K. Chattopadhyay, K. J Singh, S. B. Roy, P. Chaddah, *Physical Review B*. 64 (2001) 104416.

[97]. B. Boechat, M.A. Continentino, *J. Phys: Cond. Matt*, 2 (1990) 5277.

[98]. S. Tripathi, *Phys, Rev. B*, 52 (1995) 6522.

[99]. B. Boechat, A. Saguia e M.A. Continentino, *Sol. St. Comm*,98 (1996) 411.

[100]. I. S. Jacobs. *Appl. Phys*, 32 (1961) 61S.

[101]. H. Kobayashi, T. Haseda,. *Phys. Soc. Japan*, 19 (1964) 765.

[102]. J. Kanamori, *Prog. Theor. Phys*., 35 (1966) 16.

[103]. R.J. Elliott, A.F. Gibson, *Introduction to Solid State Physics and its Applications* (MacMillan Press, London, 1974) 205-208.

[104]. E. Stryjewski, N. Giordano. *Metamagnetism, Adv. Phys*. 26 (1977) 487-650

[105]. E.P. Wohlfarth, P. Rhodes. *Collective Electron Metamagnetism, Philos. Mag.*7(83), (1962) 1817–1824 .

[106]. M.R. Ward, *Electrical Engineering Science* (McGraw-Hill Education, New York, 1971) 97.

[107]. F. J. Blatt, *Physics of Electronic Conduction in Solids*, (McGraw – Hill: New York (1968) 144.

[108]. J.M. Ziman, *Electrons and Phonons: the theory of transport phenomena in solids* (Oxford university press, 1960) 483–524.

[109]. P.G de Gennes and J.Friedel. J.*Phys.Chem.Solids*, 4, (1958) 71.

[110]. Meaden G.T. *Electrical Resistance of Metals*. (Plenum press: NewYork, 1965) 59-94.

[111]. Ek. Bringuier. *Eur. J. Phys.* 40 (2019) 025103.

[112]. E. GRATZ. *J.Magn. Magn. Matter*, 24, (1981) 1-6.

[113]. T. Kasuya, *Prog. Theo. Phys*, 16 (1956)45.

[114]. P.G. De Gennes, *J. Phys. Chem. of Solids*, 4 (1958) 71.

[115]. A.J. Dekker, *J. Appl. Phys*., 36 (1965) 906.

[116]. T. Kasuya, *Prog. Theor. Phys*. 22 (1959) 227.

[117]. A. R. Mckintosh, *Phys. Lett*. 4 (1963) 140.

[118]. I. Mannari, *Prog. Theor. Phys*, 22 (1959)335.

[119]. R.J. Elliott and F.A. Wedgwood, *Proc. Phys. Soc*, 81 (1963) 846.

[120]. H. Miwa, *Prog. Theor. Phys*, 28 (1962) 208.

[121]. H. Miwa, *Prog. Theor. Phys*, 29 (1963) 4466.

[122]. H. Yamada and S. Takada, *Prog. Theor. Phys*, 52 (1974) 1077.

[123]. S. J. Blundell, *contemp.phys*, 40 (1999) 175.

[124]. E.S.R. Gopal, *Specific heats at low temperatures* (Springer Science, New York, 1966) 5-109.

[125]. A.A. Coelho, *J. Appl. Cryst*, 36 (2003) 86.

[126]. D.B. Wiles and R.A. Young, *J. Appl. Cryst*, 14 (1981) 149.

[127]. H.M. Rietveld, *J. Appl. Cryst*, 2 (1969) 65.

[128]. R.A. Young, *The Rietveld method* (Oxford University Press., 1993) 23.

[129]. G. Will, *Powder diffraction: The Rietveld method and the two stage method to determine and refine crystal structures from powder diffraction data* (Springer, 2006) 41-70.

[130]. J. Durbin and G.S. Watson, *Biometrika*, 58 (1971)1.

[131]. R.J. Hill and H.D. Flack, *J. Appl. Cryst*, 20 (1987) 356.

[132]. Quantum Design Physical Property Measurement System (PPMS), San Diego (USA), User Manuel, (1988) 17.

[133]. B. Chesca, R. Kleiner, D. Koelle, and A.I. Braginski, *Fundamentals and technology of SQUIDs and SQUID systems* (Wiley–VCH, Germany, 2004) 29-92.

[134]. J.C. Gallop and F. Piquemal, *The SQUID Handbook, Vol. II Applications of SQUIDS and SQUID systems* (WILEY-VCH, Weinheim, 2006) 402.

[135]. J. Clarke and A.I. Braginski, *The SQUID handbook, Vol. I Applications of SQUIDs and SQUID systems* (John Wiley & Sons, Weinheim, 2004) 88.

[136]. S. Friedemann, W. Duncan, M. Hirschberger, T. Bauer, R. Küchler, A. Neubauer, M. Brando, *Nat. Physics, 14* (2018) 62.

[137]. V. Taufour, S. Kaluarachchi, , R. Khasanov, N. M. Cuong, Z. Guguchia, B. Zurab, P. Kumar, D. B Pietro, D. R. Roberto, Lin, Xiao, Kim, Stella K., Mun, Eun Deok, Kim, F. Hyunsoo, W. Yuji, C. Zhuang, L. Bud'ko, P.C. Canfield, *Phys. Rev. Lett*. 117 (2016) 037207.

[138]. U.S. Kaluarachchi, Bud'ko, S. L., Canfield, P. C. V. Taufour, W. Tricritical, *Nat. Comm*. 8 (2017) 546.

[139]. J. R. Jeffries, R.L. Stillwell, S.T. Weir, Y. K. Vohra, N. P Butch, *Phys. Rev. B,* 93 (2016) 184406.

[140]. J. Pospíšil, H. Yoshinori, S. Kambe, Y. Tokunaga, N. Tateiwa, D. Aoki, F. Honda, A. Nakamura, Y. Homma, E. Yamamoto, T. Yamamura, *Phys. Rev. B,* 95 (2017) 155138.

[141]. Lengyel, E. et al. Avoided ferromagnetic quantum critical point in cerupo. Phys. Rev. B 91, (2015) 035130.

[142]. M. W. Marcin, *Sci. Rep*. 9 (2019) 19461.

[143]. D. Belitz, T. R. Kirkpatrick, *Phys. Rev. Lett*. 119 (2017) 267202.

[144]. A.Szytula,. *Mat. Sci. Pol*, 25 (2007) 2.

[145]. S. Gupta, K. G. Suresh, *J. Magn. Magn. Mater*. 391 (2015) 151.

[146]. A. Szytula and J. Leciejewicz, *Handbook of Crystal Structures and Magnetic Properties of Rare Earth Intermetallics* (CRC Press, Boca Raton, FL, 1994) 83.

[147]. A.V. Morozkin, Yu.D. Seropegin, A.V. Leonov, I.A. Sviridov, I.A. Tskhadadze, S.A. Nikitin. *J. Alloys Compds*., 267 (1998) L14.

[148]. Y. Oner, O. Kamer, J. H. Ross, Jr., C. S. Lue, and Y. K. Kuo, *Solid State Commun*. 136 (2005) 533.

[149]. F. Yang, J. P. Kuang, J. Li, E. Bruck, H. Nakotte, F. R. Boer, X. Wu, Z. Li, and Y. Wang, *J. Appl. Phys*. 69 (1991) 4705.

[150]. B.M. Sondezi, D. T. Adroja, A. M. Strydom, W. Kocklemann, E. A. Goremychkin. *J.phys.; conf. series*, 200 (2010) 012190.

[151]. W. Rieger, E. Parthe Monatsh. *Chem*., 100 (1969) 439.

[152]. S. Baran, A. Szytuła, J. Leciejewicz, N. Stüsser, A. Zygmunt, Z. Tomkowicz, M. Guillot, *J. Alloys Compds*., 243 (1996) 112-119.

[153]. A. Iandelli, *J. Alloys Compds*., 198 (1993) 141.

[154]. S. Baran, M. Hofmann, J. Leciejewicz, M. Ślaski, A. Szytuła, *J. Phys.: Condens. Matter*, 10 (1998) 2107.

[155]. J. Sakurai, K. Kegai, K. Nishimura, Y. Ishikawa, K. Mori, *Phys. B*, 186 (1993) 583.

[156]. A. Landelli, *J less comm. Met.* 90 (1983) 121.

[157]. B. M. Sondezi, D. T. Adroja, A. M. Strydom, W. Kocklemann, E. A. Goremychkin. *Physica B: Condensed Matter* 404 (2009)3032.

[158]. S. Chang, Y. Janssen, V. O. Garlea, J. Zarestky, H. Nakotte, R. J. McQueeney, *J. Appl. Phys*. 97 (2005) 10A913-1.

[159]. B. M. Sondezi, J. L. Snyman, A. M. Strydom. *Conf. Sa. Inst. Phys*. 56 (2011) 324.

[160]. H. Nakotte, E. Bruck, K. Prokes, J. H. V. Brabers, F. R. de Boer, L. Havela, K. H. J. Buschow, H. Fu-ming, *J. Alloy. Compd*. 208 (1994) 245.

[161]. C. P. Sebastian, S. Rayaprol, R.-D. Hoffmann, U. Ch. Rodewald, T. Pape, and R. Pottden, *Z. Naturforsch*. 62b (2007) 647.

[162]. C. P. Sebastian, S. Rayaprol, R. Pottgen, *Solid State Commun*., 140, (2006) 276.

[163]. A. Altayeb, B. M. Sondezi, M. B. Tchoula Tchokonté, A. M. Strydom, T. B. Doyle and D. Kaczorowski, AIP ADVANCES, 7 (2017) 055714.

[164]. A. M. Strydom, *Euro. Phys. J. B*. 74 (2010) 9.

[165]. A. Bohm, R. Caspary, U. Habel, L. Pawlak, A. Zuber, F. Steglich and A. Loidl, *J. Magm. Magn. Mate*r. 76 (1988) 150.

[166]. N. F. Mott and H. Jones, *The theory of the Properties of Metals and Alloys*, (Oxford University Press, 1958) 274.

[167]. N. Sato, N. Aso, K. Hirota, T. Komatsubara, Y. Endoh, S.M. Shapiro, G.H.

Lander,and K. Kakurai, *Phys. Rev. B*, 53 (1996) 14043.

[168]. D. T. Adroja, B.D. Rainford, A. J. Neville, *J. Phys.:Condens. Matter*, 9 (1997), L391.

[169]. S. Singh and S.K. Dhar, *J. Phys.: Condens. Matter*, 14 (2002) 11795.

[170]. A.K. Bashir, M.B. Tchoula Tchokontè, and A.M. Strydom, *J. Magn. Magn.Mater* 414, (2016) 69.

[171]. A. Pandey, C. Mazumdar, R. Ranganathan, and D.C. Johnston, Sci. Rep 287, (2017) 42789.

[172]. J. J. Mboukam, MSC thesis, University of the Western Cape (2018).

[173]. I. Balberg, *Phys. Rev. B*, 91 (1977) 71.

[174]. V. Goruganti, K. D. D. Rathnayaka, J. H. Ross, Jr., Y. Öner, C. S. Lue, and Y. K. Kuo, *J. Appl. Phys*. 103 (2008) 073919.

[175]. A. Szytula, D. Fus, B. Penc, and A. Jezierski, *J. Alloys Compds*. 340 (2001) 317.

[176]. C. P. Sebastian, H. Eckert, C. Fehse, J. P. Wright, J. P. Attfield, D. Johrengt, S. Rayaprol, R. -D. Hoffmann and R. Pottgen, *J. Solid State Chem*. 179 (2006) 2376.

[177]. S. Baran, A. Szytula, J. Leciejewicz, N. Strüsser, A. Zygmunt, Z. Tomkowicz and M. Guillot, *J. Alloys Compds*, 243 (1996) 112.

[178]. M. B. Tchoula Tchokonte, Z. M. Mahlubi, A. M. Strydom, D. Kaczorowski, T. B. Doyle. *J. Alloys and Compds*. 696 (2017) 1004.

[179]. M. B. Tchoula Tchokonte, P. de V. du Plessis and D. Kaczorowski. *J. Phys.: Condens. Matter* 15 (2003) 3767.

[180]. S. B. Roy, M. R. Lees, G. R. Stewart, and B. R. Coles, *Phys. Rev*. B43 (1991) 8264.

[181]. M. B. Tchoula Tchokontè, K. G. Tshabalala, P. de V. du Plessis and D. Kaczorowski. *J. Phys. Chem. of Solids* 71 (2010) 181.

[182]. V. Goruganti, K. D. D. Rathnayaka, Joseph H. Ross, Jr. A Y. Öner, C. S. Lue, Y. K. Kuo, *J. Appl.Phys*. 103, (2008) 0739199.

[183]. M. B. Tchoula Tchokontè, J. J. Mboukam, A. K. H. Bashir, B. M. Sondezi, K. Ramesh Kumar, A. M. Strydom, D. Kaczorowski, *Physica B* 536 (2018) 418.

[184]. J. J Mboukam, B. M Sondezi, M. B. Tchoula Tchokontè, A. K. H. Bashir, A. M. Strydom, D. Britz, D. Kaczorowski, *J. Alloys Compds* 753 (2018) 41.

[185]. M. Falkowski, *J. Alloy Compds*. 689 (2016) 1059.

[186]. Z. Fisk, *Solid State Commun*., 221 (1976) 18.

[187]. Z. Kletowski, P.J. Markowski, and B. Stalin´ski, *Solid State Commun*, 293 (1986) 57.

[188]. I. Balberg *Physica B*, 91 (1977) 71.

[189]. A.K. Bashir, M.B. Tchoula Tchokont´e, and A.M. Strydom, *J. Magn. Magn.Mater* 414, 69 (2016) 69.

[190]. A. Szytuła, Yu. Tyvanvhuk, T. Jaworska-golab, A. Zarzycki, Ya. Kalychak, Ł. Gondek, N. Stüsser. *Chem. Met. Alloys* 1 (2008) 97.

[191]. P. Javorsky, H. Sugawara, S. Nishigori, B. Ouladdiaf. *Physica B: Condensed Matter*, 276-278 (2000) 730.

[192]. D.X. Li, Y. Shiokawaa, T. Nozueb, T. Kamimurab, K. Sumiyama, *J. Magn. Magn. Mater*. 241 (2002) 17.

[193]. Ł.Gondek, J.Czub, A.Szytuła, Z.Izaola, E.Kemnerd. *Solid State Commun*;149 (2009)

[194]. E. Parthé, B. Chabot, in *Handbook on the Physics and Chemistry of Rare Earths*, Eds. K. A. Gschneidner Jr., L. Eyring, Vol. 7,(North – Holland, Amsterdam 1984) 113.

[195]. A. Szytula, *Crystal Structures and Magnetic Properties of RTX Rare Earth Intermetallics*, (Wydawnictwo Uniwersytetu Jagiellońskiego, Kraków, 1998) 1-16.

[196]. G. Ehlers, H. Maletter, *Z. Phys. B* 99 (1996) 145.

[197]. J. Prchal, M. Míšek and O. Isnard, *J. Phys.: Conf. Series* 251 (2010) 012022.

[198]. L Prchal, P. Javorský, B. Detlefs, S. Daniš, O. Isnard, *J. Magn. Magn. Mater*. 310 (2007) 589.

[199]. S. Nishigori, Y. Horooka, T. Ito, *J. Magn. Magn. Mater*. 177 (1998) 137.

[200]. A. Szytuła, Yu. Tyvanchuk, Ya. Kalychak, A. Winiarski, B. Penc, and A. Zarzycki, J. *Alloys Compds*. 442 (2007) 279.

[201]. T. Fujita, K. Satoh, Y. Maeno, Y. Uwatoko, H. Fujii, *J. Magn. Magn. Mater*.76-77, 133

(1988).

[202]. M. Bałanda, A. Szytuła, M. Guillot, *J. Magn. Magn. Mater*. 247 (2002) 345.

[203]. K. Satoh, T. Fujita, Y. Maeno, Y. Uwatoko,H. Fujii, *J. Phys. Soc. Jpn*. 59 (1990) 692.

[204]. A. SzytuÃla, A. Arulraj, S. Barana, T. Jaworska-GoÃlb, B. Penc, N. Stusser, Yu. Tyvanchukc and A. Zarzyckia, *Acta Phys. Pol.A*, 113 (2008) 1185.

[205]. Ł. Gondek, A. Szytuła, D. Kaczorowski, K. Nenkov, *Solid State Commun*. 142 (2007) 556.

[206]. S. Gupta, K.G. Suresh. *J. Alloys Compds*, 618 (2015) 562.

[207]. P. Javorski, P. Svoboda, S. Nishigori, M. Hofmann, N. Stüsser, *Acta Phys. Slov*. 48 (1998) 767.

[208]. A. Tari, *The Specific Heat of matter at Low Temperature*, (Imperial College Press, London 2003) 24-32.